Micro-manufactured Rogowski coils for fault detection of aircraft electrical wiring and interconnect systems (EWIS)

Brian G. Moffat

Submitted for the degree of Doctor of Philosophy

Heriot-Watt University

School of Engineering and Physical Sciences

March 2014

Abstract

Aircraft wiring failures have increased over the last few years resulting in arc faults and high-energy flashover on the wiring bundle, which can propagate down through aircraft Electrical Wiring and Interconnect Systems (EWIS). It is considered cost prohibitive to completely rewire a plane in terms of man hours and operational time lost to do this, and most faults are only detectable whilst the aircraft is in flight. Temperature, humidity and vibration all accelerate ageing and failure effects on EWIS.

This research investigates methods of in-situ non-invasive testing of aircraft wiring during fight. Failure Mode Effects and Analysis (FMEA) was performed on legacy aircraft EWIS using data obtained from RAF Brize Norton. Micro-Electro-mechanical-Systems (MEMS) were evaluated for use in a wire monitoring system that measures the environmental parameters responsible for ageing and failure of EWIS. Such MEMS can be developed into a Health and Usage Monitoring MicroSystem (HUMMS) by incorporating advanced signal processing and prognostic software.

Current and humidity sensors were chosen for further investigation in this thesis. These sensors can be positioned inside and outside cable connectors of EWIS so that arc faults can be reliably detected and located. This thesis presents the design, manufacture and test of micro-manufactured Rogowski sensors. The manufactured sensors were benchmarked against commercial high frequency current transformers (HFCT), as these devices can also detect high frequency current signature due to wire insulation failure. Results indicate that these sensors possess superior voltage output compared to the HFCT.

The design, manufacture and test of a polymer capacitive humidity sensor is also presented. Two different types of polymer were reviewed as part of the evaluation. A feature of the sensor design is recovery from exposure to chemicals found on wiring bundles. Current and humidity sensors were demonstrated to be suitable for integrating onto a common substrate with accelerometers, temperature sensors and pressure sensors for health monitoring and prognostics of aircraft EWIS.

DEDICATION

To Nipper and Abbi.

DECLARATION STATEMENT

I hereby declare that the work presented in this thesis was carried out by myself at Heriot-Watt University, Edinburgh, and has not been submitted for any other degree at this, or any other institution.

Brian G. Moffat

March 2014

Acknowledgements

I would like to express my gratitude to my academic supervisor, Professor Marc Desmulliez, for the opportunity to do this PhD and his supervision, guidance and encouragement throughout my studies and beyond.

I would like to acknowledge the financial support of both the Engineering and Physical Sciences Research Council (EPSRC).

I would like to acknowledge the financial and technical support of BCF Designs Ltd. In particular, I would also like to thank my industrial supervisor, Dr. Alistair Sutherland for his supervision and facilitating visits to RAF Brize Norton to observe the challenges faced by military personnel to keep legacy aircraft safe and airworthy.

I would like to express my gratitude to the cleanroom manager, Mark Leonard, for his time and help to learn to use the range of processing equipment in the cleanroom and also for making any apparatus required to manufacture the devices discussed in this thesis. I would like to add thanks to Dr. David Flynn and Dr. John Carr for the assistance and advice they provided on manufacturing processes.

I would also like to thank all the past and present members of the Microsystems Engineering Centre, Dr Robert Kay, Dr Jack Hoy-Gig Ng, Jean-Baptiste Munier, Dr Yves Lacrotte, Dr Norbert Lorenz, Douglas Colliar, Stefan Wilhelm and Jens Kaufmann. I thank them all for their advice, support and friendship and during my studies.

I am especially grateful to my family and family-in-law for all their support during the highs and lows of completing this thesis. This last word of acknowledgment I have saved for is my partner Deirdre, for all her love and support throughout this time. I am blessed to have you by my side.

Table of Contents

List of Tables

List of Figures

List of Publications

Peer-reviewed Journal Publications

B.G. Moffat, E. Abraham, M.P.Y. Desmulliez, D. Koltsov and A. Richardson "Failure Mechanisms of Legacy Aircraft Wiring and Interconnect". IEEE Transactions on Dielectrics and Electrical Insulation, Vol. 15, Issue 3, pp. 808-822, 13th June 2008.

J.H.-G. Ng, M.P.Y. Desmulliez, M. Lamponi, B.G. Moffat, A. McCarthy, H. Suyal, A.C. Walker, K.A. Prior, D.P. Hand, "A direct-writing approach t the micro-patterning of copper onto polyimide", Circuit World, Vol. 35, no. 2, pp.3-17, 2009.

Conference Publications

B.G. Moffat, M.P.Y. Desmulliez, K. Brown, C. Desai, D. Flynn and A. Sutherland. "A micro-fabricated current sensor for arc fault detection of aircraft wiring", IEEE Electronics System Integration Technology (ESTC) Conference, 1st-4th September, 2008.

Z. Hu, S. Saha, A. Richardson, B. Honary, J. Hannu, A. Sutherland, B.G. Moffat, and M.P.Y. Desmulliez, "Embedded health monitoring strategies for aircraft wiring systems", IEEE Electronics System Integration Technology (ESTC) Conference, 1st-4th September, 2008.

J. N-G Ng, M.P.Y. Desmulliez, M. Lamponi, B.G. Moffat, A.C. Walker, A. McCarthy, H. Suyal, K.A. Prior and D.P. Hand, "UV direct-writing of metals on polymer substrates", IEEE Electronics System Integration Technology (ESTC) Conference, 1st-4th September, 2008.

Awards

First year PhD prize, School of Engineering and Physical Sciences, Heriot-Watt University.

Chapter 1 Layout and scope of the thesis

1.1 Introduction

Aircraft wiring technology has evolved over the years due to the introduction to digital systems as a result of advances made in semiconductor fabrication and digital signal processing. These advances led to the creation of the military standard, Mil-Std 1553, a digital transmission system and protocol, which enabled systems and subsystems linked into a network to communicate with each other. The system shares the wiring and electrical interconnects with other systems, subsystems and sensors, which enable the devices to share information. The system consists of a number of black boxes or Line Replaceable Units (LRUs), which cover a variety of functions ranging from converting signals from one format to another (Remote Terminal), data monitoring and recording of events such as errors in the system (Bus Monitor), to controlling data flow (Bus Controller), or subsystems, and sensors, as figure 1.1 illustrates.

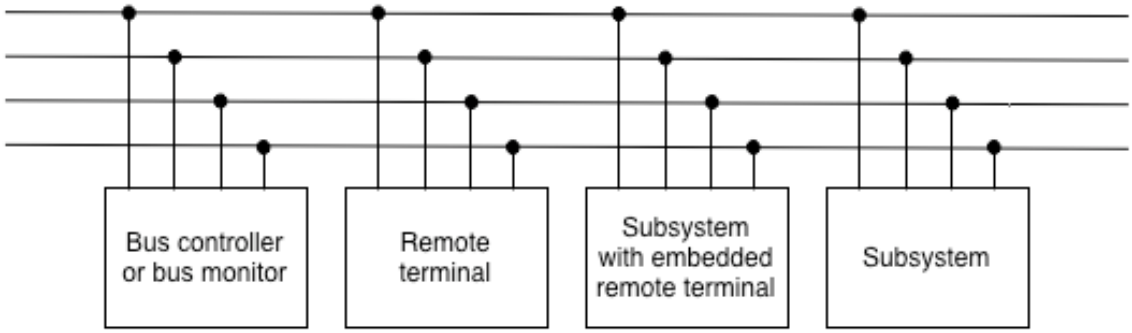

Figure 1.1 Mil-Std wiring, consisting of databus and LRU's

Even though systems in an aircraft have been upgraded over the years, the wiring that interconnect them is often neglected. Errors that have been reported by either the pilot or the system are sometimes undetectable during routine maintenance for two main reasons: either the Automated Test Equipment (ATE) cannot detect the faults until the device fails, or the faults only occur during flight. In the latter case, the aircraft wiring is immersed in harsh environments such as vibration, temperature, humidity and corrosive chemical agents. Wiring rubbing against other wiring or structures cause fraying of the insulation and moisture intrusion which leads to the loss of mechanical and electrical strength. This then leads to insulation rupturing, leaving the conductor vulnerable to short circuiting with other metallic structures and/or other exposed wiring covered in

moisture. This form of short-circuiting is called arcing, where a high-energy flashover takes place, which can lead to fire before the circuit breakers can act. Arcing also increases the amount of signal loss and distortion on live signals.

This thesis aims at designing, manufacturing and testing a sensor that detects the onset of arcing and the presence of humidity with a view to rapidly locate the fault within the cable harness of an airplane. In that respect this thesis has reviewed the detection of a variety of failure modes which could utilise MEMS sensors that are suitable for in-situ, in-flight testing of the wiring. Of particular importance is the possibility to diagnose ageing of the wiring before it becomes a safety issue. This research work was carried out in collaboration with BCF Designs Ltd., an English company specialising in wiring test systems and solutions. BCF Designs wished to create a test system to increase levels of safety and confidence and to aid aircraft operators in preventative maintenance and safety of the wiring. This increases aircraft availability, while man-hours and high cost of fault finding is decreased. Later on the company was taken over by the multinational company Ultra Electronics Precision Air and Land Systems (PALS) which continued the research programme.

The schematic of the research work carried in this project is given in figure 1.2, which illustrates how the various research activities can be linked together to form a prognostics system that not only senses failure in the wiring, but also can detect deterioration of the wiring by sensing the contributing effects that lead to failure. MEMS based sensors will enable the detection of faults and deterioration in the wire health. The information obtained by MEMS based sensors enables the correct decisions to be made concerning the wire health. This information can then be stored in a database with the purpose of scheduling maintenance and further processing. Later, more information can be found on the ageing effect if the aircraft is operating in a harsher environment than other aircraft.

1.2 Project Objectives

The objectives of this project are therefore to:

- Review the elements of aircraft wiring and perform FMEA (Failure Mode and Effect Analysis) to identify the contributory cause(s) of failure.
- Identify the contributory effects that lead to failures and review those which are

detectable.

- Analyse available MEMS sensors and techniques that enable new MEMS sensors to be designed that can detect either failure of the wiring and/or detect the deterioration of wiring so that preventative maintenance can be carried out.
- Design, model, micro-manufacture and test a current sensor that has a very small "sugar cube sized" form factor, is of low weight, low power consumption and is capable of measuring and detecting high frequency waveforms such as arcing or partial discharge signals.
- Design, model, manufacture and test of a suitable humidity sensor for incorporating into a multi-sensor system that can be embedded within key areas of aircraft electrical wiring and interconnect systems.

1.3 Organisation of the work

This thesis presents the work undertaken during the PhD studies of the author at the Microsystems Engineering Centre (MISEC) at Heriot-Watt University, Edinburgh.
The plan of the thesis is as follows:

Chapter 2 Failure mechanisms of aircraft wiring and interconnect systems (EWIS). This chapter introduces an overview of the history of aircraft wiring, the issues leading to a variety of failures, as well as an overview of the aircraft wiring system. It proceeds to describe all types of failure and the resulting effects. Some of the failure effects are more catastrophic than others and, in most cases, the minor failures lead in time to the ageing effect of wiring and then ultimately catastrophic failure. For this reason, Failure Mode Effects and Analysis (FMEA) was performed on the wiring system. This type of analysis breaks the wiring system down into smaller parts that are considered in terms of possible ways that the part may fail and the consequence of the failure(s). These failures are mapped out to see how they affect the overall system, and how detectable these failures are.

Chapter 3 Sensor based systems for fault monitoring of electrical aircraft wiring and interconnect. The rationale of developing Health and Usage Monitoring MicroSystems (HUMMS) for monitoring of the ageing and failure of legacy aircraft electrical wiring and interconnect systems is presented. The chapter looks at Health and Usage Monitoring Systems (HUMS) currently in the market-place and examines the

gaps in customer requirements where microsystems technology and smart sensor technology could be used. This chapter ends with the key focus of the thesis being outlined. It lays out the design challenge of using micro-manufacturing techniques for miniaturising a current sensor that is suitable for integration with other proposed sensors onto a common substrate with the necessary power, communications and processing electronics to monitor ageing, deterioration and fault detection of EWIS.

Chapter 4 Design and analysis of Rogowski sensors covers the theory of the Rogowski coil at a deeper level by considering the lumped element model of the sensor and its interaction with a wire to be monitored. It examines how its lumped element behavior satisfies second order behaviour and how this is used to understand how the device reacts to fast rise time signals. Sensor behaviour is derived from the calculated values of the sensor resistance, inductance and capacitance. The interaction of the device with a Wire Under Test (WUT) is described in terms of the mutual inductance that exists between wire and sensor.

Chapter 5 UV LIGA process for the manufacture of a planar Rogowski sensor. This chapter introduces the manufacturing processes for the micro-manufacture of a 2.5D Rogowski sensor along with methodology used to assemble and package the sensor die ready for test. A fused deposition manufactured (FDM) package is introduced for positioning the sense die close to the wire under test.

Chapter 6 Methodology for characterisation and test of Rogowski sensors. The two-part test methodology used for characterising the UV-LIGA Rogowski sensor and the Qudos manufactured Rogowski sensor is introduced along with justification via a brief literature review. This chapter covers current research used to examine the suitability of this sensor for partial discharge detection. The experimental setup discussed in this work is the basis for testing the sensors next to a current carrying wire. The waveforms used range from 1-100 MHz sine wave and charging and discharge waveforms. These mimic the shape of a typical Partial Discharge waveform.

Chapter 7 Test and discussion of Rogowski sensors. This chapter contains the data and analysis of both Rogowski sensor designs discussed in this thesis. The chapter starts by introducing the results for the inductance, capacitance and resistance measurements. Where appropriate, further statistical analysis of the measurements is provided. The second part of the chapter evaluates the sensors performance by testing

the capability to detect a range of high frequency waveforms next to a current carrying wire.

Chapter 8 Characterisation and test of a humidity sensor. The selection of a suitable humidity sensor for integration into a multi-sensor solution is discussed through a brief literature review. The selected sensor was manufactured by Qudos and presented for test and comparison to a simulated model in Comsol Multiphysics. The test setup used for characterisation is also discussed and summarised in context of the sensor design performance.

Chapter 9 Conclusions and future work. This chapter summarises the work described in this research, with comparison made to the performance of the sensor designs versus a more expensive off-the-shelf high frequency current transformer. An outlook of the future work of this research is also given in the context of further testing and design refinement.

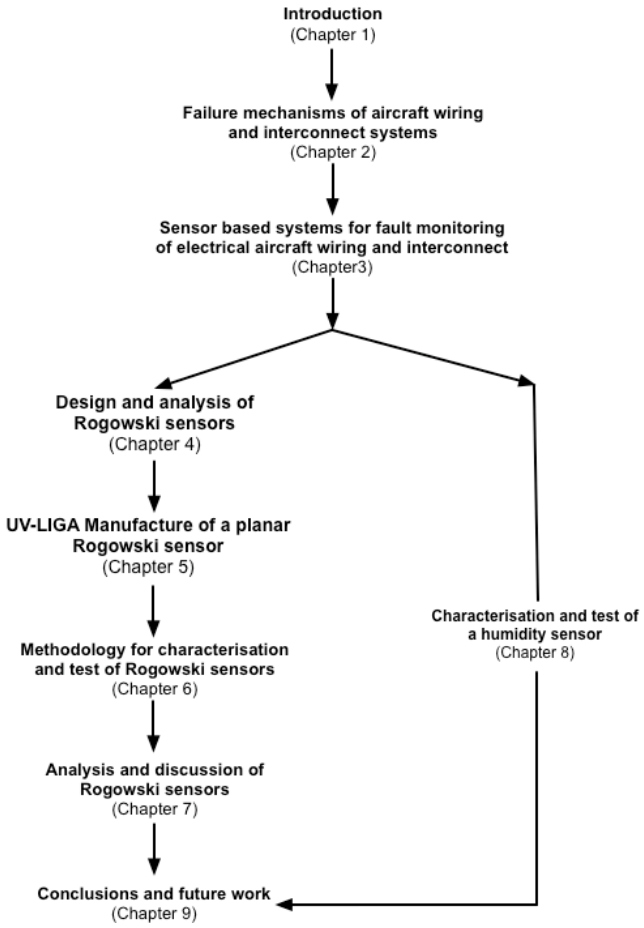

Figure 1.2 Synopsis of thesis

Chapter 2 Failure mechanisms of aircraft wiring and interconnects

2.1 Introduction

Electrical wiring and Interconnect Systems (EWIS) have become a major area of research and development for a variety of industries ranging from aerospace and defense to test equipment manufacturers. For many years attention was limited to the key electrical systems such as radar, hydraulics and control systems. Commercial and more importantly military aircraft now last way beyond their original predicted lifetime due to the retrofitting of new systems. Consequently increased lifetimes of up to 60 years have become commonplace [2.1,2.2]. Wiring and interconnect, are however, often neglected due to the high cost in terms of man-hours and time taken to rewire the aircraft [2.1-2.5]. One issue that still needs addressed is the linkage between ageing and failure of EWIS. The subsequent errors reported by either the pilot and/or the system are sometimes undetectable during routine maintenance for two main reasons: either the Automated Test Equipment (ATE) cannot detect the faults until they fail, or the faults only occur during flight.

Fatal accidents attributed to electrical failure over the last few decades have drawn increased concern from industry and government bodies. The 1996 Trans World Airlines crash cited arcing in the fuel tank as the primary reason for this catastrophe [2.2-2.4]. Research undertaken during this period has illustrated that this type of failure is not primarily due to key electrical systems but to the wiring and interconnect linking these key systems together [2.6]. Furthermore, most Line Replaceable Units (LRUs) have often been cited as the reason for failure in avionics systems. Two out of three LRUs that had been reported as failed were in fact not faulty or reported as “No Fault Found (NFF)” [2.6-2.8]. This is otherwise known as a false positive test result. Wiring and interconnect have not been considered as a key system itself and industry has now had to address this. The ageing and failure of electrical wiring and interconnect increase the probability of a variety of arcing faults occurring during flight. The drive by the aviation industry to make systems lighter has driven the specification of wire insulation to smaller thicknesses. This results in a quicker deterioration of the insulation [2.9] for higher gauge wire, and more opportunities for open or short conditions to occur [2.10] as insulation thickness decreases.

Wheeler et al. concluded in [2.11] that the broad range of failure categories is difficult to link with physics of degradation and the corresponding electromagnetic signatures. A

better way of approaching wire ageing and failure is to carry out further assessments of the effects experienced randomly whilst the aircraft is in flight, which is normally ignored in laboratory tests. Further investigation into the impact of varying humidity and vibration on the performance of wire fault detection systems has not been investigated at a deep enough level.

To understand how the environment and other factors influence the deterioration and failure of wiring and interconnect, it is necessary to classify these effects into certain categories so that the FMEA can be carried out for each type of failure mechanism [2.6]. In so doing, the root cause and severity of the failure can be ascertained and its contribution to the overall degradation mechanism quantified. Failures occur due to the ageing and degradation of the cable harness under mechanical, chemical or electrical duress. The taxonomy of failure modes also serve as a tool for future development of specialised *in-vivo* sensors that can monitor the wiring and interconnect for deterioration and failure. Each subsection describes the different modes of failure according to the domain of energy considered (chemical, mechanical, electrical).

This chapter presents a list of the causes and modes of ageing and failure in legacy aircraft wiring and interconnects. Taxonomies of the electrical, mechanical, chemical and thermal stresses that contribute to the various stages of ageing and/or failure are presented. A Failure Mode and Effect Analysis (FMEA) is conducted to categorise the most serious failures. The order of severity in the FMEA has been backed up by maintenance data gathered by the Royal Air Force (RAF) base Brize Norton during routine inspection [2.12]. This information is used subsequently in this thesis to develop a multi-sensor solution that can monitor these parameters as indication of ageing and the incipient and intermittent failure of EWIS.

2.1 Chemical Degradation and Failure

2.1.1 Hydrolytic scission

The process of hydrolytic scission in the degradation of wiring insulation is central to most of the failure modes outlined in this article. Impurities or abnormalities in the molecular structure of the polymer leave it vulnerable to moisture being absorbed. KAPTON™, an aromatic polyimide, is the primary insulating material used in MIL-W-

81381 wire. This material had originally been chosen for its good dielectric and mechanical strength at high temperatures. However, reports suggest [2.1-2.5, 2.13-2.24] that this type of insulating material is not as immune to the effects of harsh environment as initially thought. In [2.25], the author states that polyimide is still susceptible to humidity, which is believed to produce cracks in the insulation. This then leads to the onset of intermittent electrical malfunctions.

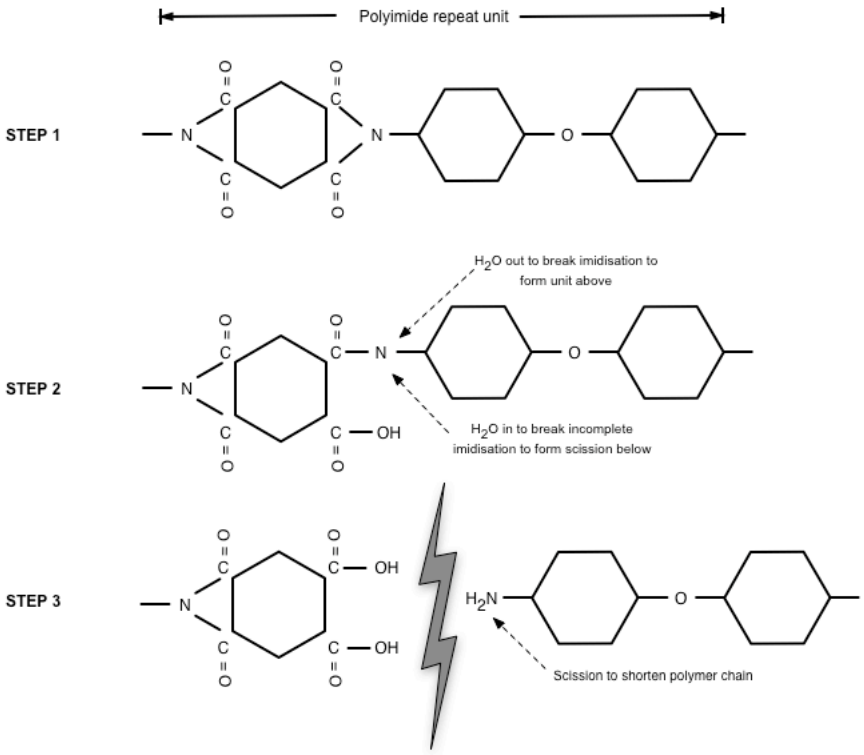

Figure 2.1 Polyimide chain scission.

The chemical structure of the aromatic polyimide as shown in figure 2.1 is a repeating chain resulting from the condensation polymerization of a dianhydride and diamine molecule [2.1,2.4,2.15-2.20]. At high humidity exposure, water is absorbed in the polymer chain through its imperfections resulting in the swelling of the insulating material [2.10].

This swelling allows a variety of liquids ranging from water and sea spray to cleaning fluids on the aircraft to be drawn into the insulation [2.1,2.4,2.5,2.13-2.20]. When the insulation absorbs moisture [2.25] the formation of polar groups occur within the polymer chain. Scission reactions occur at vulnerable parts of the polymer chain, which is believed to be caused by imperfections in the molecular chain. During the scission process, moisture reacts with side chains of the polymer structure that result in the chain being broken. This lowers the average molecular number of the polymer, during which

the chemical and electrical properties of the polymer degrade accordingly. The vulnerable parts of the polymer chain are thought to be the carbonyl side groups. The scission reaction slows with time as the number of vulnerable sites on the polymer decreases. During tests in [2.25], the authors observed the real part of permittivity and loss factor of polyimide film increase significantly during the first four days of immersion in water before slowing. This is attributed to the scission effect where initially there are a high number of available sites, before reducing as the scission effect progresses. As the rate of scission progresses there is a corresponding decrease in the electrical and mechanical properties of the polyimide insulation.

2.1.2 Corrosion

Corrosion is an electro-chemical reaction which predominantly occurs at the metal-metal interface of the interconnect. This degradation mechanism is caused by humidity getting into the connectors resulting in the oxidation of the metal. Imperfect connections can arise either through poor maintenance by aircraft technicians or through vibration and temperature cycling causing stress relaxation of the interconnect. The latter, in turn, causes the metal-metal contacts to rub against each other, often degrading any protective coating. This phenomenon is known as contact fretting and is cited as being responsible for intermittency issues that occur in the connectors [2.28-2.34].

Corrosion in connectors is the first sign of failure within the connector housing, after which it manifests itself into a serious electrical mode failure. The corrosion increases the contact resistance, which, in turn, causes an increase in temperature till a glowing terminal is observed prior to onset of fire or a smoldering connection. Twenty percent of electronic failures are caused by moisture induced corrosion [2.21]. Appendix 1.1 provides the comprehensive list of chemical degradation and failure occurring in wire and interconnects.

More generally, humidity is cited as being a major factor in the deterioration of wiring and interconnects. By solely using dehumidification equipment on aircraft, failures have been reported to drop by 24% [2.20,2.21].

2.2 Electrical Degradation and Failure

2.2.1 Degradation of Electrical Performance of Insulation

Wiring operating at high frequencies, such as signal systems, need to be designed carefully to enable maximum functionality and safety. This includes wiring such as digital bus, twisted pair and 2/3 phase [2.17,2.22]. To enable correct electrical operation of wiring at high frequencies, the impedances must be balanced otherwise reflections will occur where impedance discontinuities are located. This degradation of the dielectric function decreases the resistance and hence increases the leakage current of the insulation [2.17].

As the polyimide chain shortens as a consequence of hydrolytic scission, the electrical characteristics of the insulation change through the modification of the real and imaginary part of the permittivity [2.3]. The leakage current is dissipated through the insulation, which cannot cope with the additional stress caused by the heating effect from Joule losses. The heating effect increases the hydrolytic scission rate and also dries out the insulation leaving it brittle, where small cracks and micro voids will occur more frequently. In [2.25] the authors show that, as polyimide is subjected to temperatures higher than 475°C over five hours, it became more brittle, darker in colour and thicker. The increase in thickness is thought to be due to the formation of oxidised layers forming over the polyimide surface. The increase in brittleness will leave the insulation more vulnerable to further cracking. When the cracks are close enough together and/or linked by a conductive path via moisture then an electrical discharge will occur. The OH- groups from the water molecule react with any of the carbonyl side groups and the H+ bonds react with the amine groups. This produces ionic side groups in the shortened polymer chain that promotes charge transport.

This is thought to accelerate the reduction of the electrical breakdown strength of the insulation as well as the increase in the variation in electrical breakdown strength of a selection of polyimide samples.

Figure 2.2 Low level arcing (<10A), prior to high energy flashover [2.5].

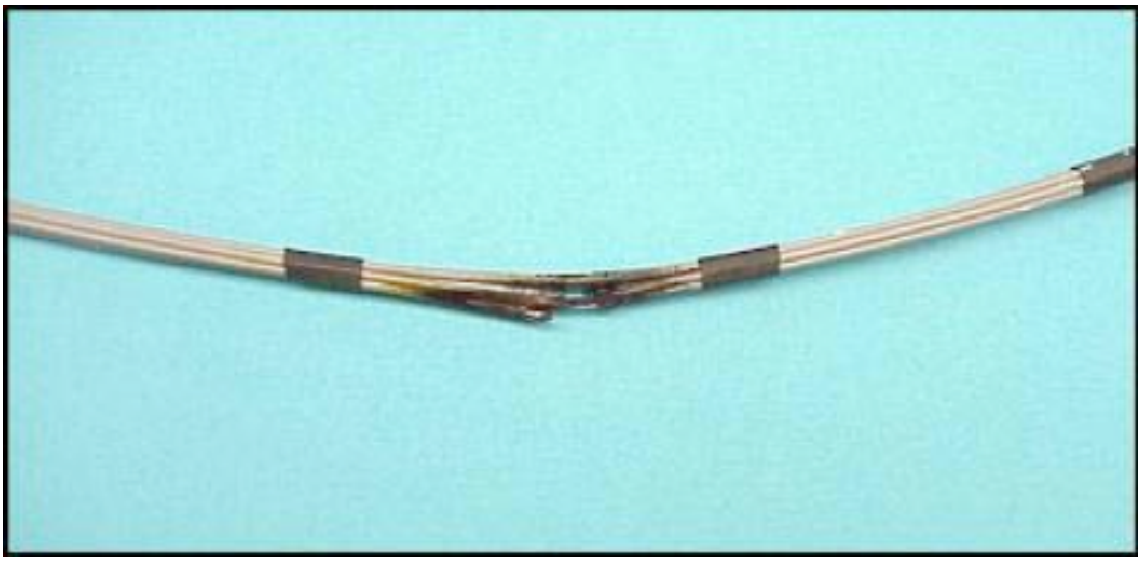

Figure 2.3 Effects of low level wire arcing for 5 mins [2.5].

Figure 2.4 High level wire arcing (>100A)

There have been other types of wiring used in the aircraft over the last 30 years, which exhibit dangerous failure effects. Polyvinyl-Chloride (PVC)/Nylon wiring fails the Federal Aviation Regulations (FAR) Part 25: Airworthiness Standards: Transport Category Airplanes. This was first used in the 1950s, and has since been banned by the US Air Force due to a variety of undesirable qualities.The softness of the material makes it vulnerable to chaffing as the cable rubs against wiring comprising harder insulation [24,26]. Hydrochloric acid is produced when the insulation is burning and brought in contact with moisture. Additionally, the insulation releases flammable gases during degradation. Another material, alphatic polyimide, has also been banned from insulated wires by the US Navy. It is brittle insulation, known for visible cracks as well as its poor chafe resistance to other wires/objects. Initially the lifetime of the insulation was estimated as 60,000 hours but investigations by the US Navy suggest that cracks appear after 4,000 hours. Tefzel and cross-linked Tefzel fail the FAR Part 25 test as this material is very soft and unsuitable for wire bundles. Cross-linked Tefzel is known for wet arc tracking and will produce dense smoke when on fire that severely impairs visibility.

2.2.2 Wet arcing

Wet arcing, also known as wet arc tracking, is the creation of a bright electrical discharge across a gap and/or insulation, which sustains itself through a form of conductive path such as carbonised insulation. There are many ways that arcing can occur. One way is in the presence of moisture or fluids on the insulation, where leakage currents present on the deteriorated insulation create small electrical discharges across closely spaced cracks or voids. The pyrolysis of the insulation at this point creates a carbonised track, which, due to its graphitic structure, is very conductive. At the next arcing event an even greater explosive flashover occurs and propagates down and/or across adjacent wire bundles. Recent studies carried out by Lectromech indicate that 34% of wire failures have two or more faults at the original fault location [2.23].

The heating effect of the insulation caused by carrying normal current loads can also create arcing by vaporising the moisture and dirt lying on the insulator and forming then a dry path. This path produces an increased resistance to current flow, which causes small random discharges to be produced on the surface of the insulation. This charring of the insulation provides a carbonised path. The insulation degrades to form carbide

crystals at the effected area and, on contact with water, releases a highly flammable gas that will ignite at the arc onset as shown in Figures 2.2 to 2.4 [2.5].

A fully sustained arc will burn fiercely at temperatures around 5000˚C due to the aromatic structure of Kapton [2.1,2.4]. The seriousness of this type of arcing is most emphasised in aromatic polyimides, though it also occurs in other insulation types such as Polytetrafluoroethylene (PTFE) and Ethylene/Tetrafluoroethylene (ETFE). The arc extinguishes at every null of current in the load current, and then restarts. It can be explosive enough to propagate onto other wire bundles. This is caused by the circuit breakers failing to trip as a consequence of the current flowing through the track being below the threshold trip point.

2.2.3 Parallel arcing

Parallel arcing occurs when a wire with exposed insulation connects with the metallic airframe or another wire with bare metal exposed [2.35,2.36]. Such a condition can occur when the insulation wears away from chaffing and/or rupturing to expose a significant part of the insulation [2.6]. During this fault, the current of the arc is equal to or less than the impedance of the voltage source, the wire and the arc. This version of arcing usually produces a current of sufficient magnitude to activate the circuit breaker.

For conditions where the energy liberated during parallel arcing is sufficiently high the wires become forced further apart and the arc voltage increases. Following such a condition, the fault current decreases below the critical current level required to activate the circuit breaker, which is thought to be one reason for the ticking faults often heard. Total destruction of a wire bundle has been witnessed [2.2-2.5,2.13] due to a wire with broken insulation touching another wire at another potential of a part of the aircraft structure. In a NASA report on arcing, inspection of a bolt-head involved with dry arcing found there was an area where metal ejection has occurred due to the sputtering effect of the arc [2.13]. This was attributed to paint having been removed with time from the bolt-head, leaving it as an exposed conductor instead of the insulated painted surface. The energy generated by parallel arcing is believed to reach up to 10,000 °F, which explains why sputtering of metal debris has been observed. These high temperatures also contribute to the charring of the wire insulation that could later experience wet arc tracking.

2.2.4 Series arcing

Series arcing is defined in [2.35] as a condition that occurs when a faulty wire is connected in series with a load. The fault is due to a break in this connection that could be in the wire or at the wire and connector interface. Other examples are loose terminal plugs and cross threaded electrical plugs. The voltage drop inside a loose connector begins at a few hundred mV's and slowly heats or pyrolises the surrounding media [2.1,2.5]. The voltage increases then to a few volts, where a glowing connection is most probable and smoke is emitted from the surrounding insulation. This may present itself in the cabin as flickering lights. The reason for the increased heating effect is partially attributed to vibration levels within the aircraft. Vibration serves to create many connections and disconnections to the electrical supply [2.23], which results in small arcs occurring as the contacts move away from each other. This will dissipate a reasonably small amount of energy for one arcing cycle; however, if vibration is producing many broken connections to occur within sufficiently short duration then the result is a build up of localised dissipated energy and hence rapid temperature increase to the point of fire ignition. Carbon powder inside the connector is also found at this stage. The current waveform of a series arc is observed as a variation in the normal load current. The current in this instance is limited by the impedance of the electrical load that is connected to the circuit, where the power is also far less than for the parallel case [2.1,2.5]. The dangerous part of this type of arcing is that the current remains below the limit that will trip the circuit breaker. The symptoms associated in this case are load voltage drops, heating of the wire, pin and sockets, which result in the failure of the component and source of ignition. Appendix 1.2 provides an exhaustive list of failure modes and degradation due to electrical effects.

In work by Schweickart et al., [2.37] the authors examined the relationship between pressure and arcing behavior on aircraft wiring systems. The pressures ranged from 0.27 to 101 kPa, which represented the pressure experienced by the electrical wiring system at an altitude of 40 km and at sea level, respectively. The authors concluded that the rise times and duration of PD signals at low pressure (40 km) was longer than the characteristics seen at higher pressures. This is because the breakdown strength of air varies with gas pressure.

2.3 Mechanical Degradation and Failure

2.3.1 Degradation and failure due to maintenance

Aircraft technicians must be able to test a large amount of often inaccessible wiring without actually making the situation much worse. Even with correct training, stresses of sufficient magnitude to cause the insulation to crack can still be translated through the wiring. As the insulation deteriorates, the minimum required mechanical strength cannot be guaranteed to prevent cracking. More precisely, hydrolytic scission and thermal cycling render the insulation brittle, i.e. the insulation will not flex back to its original position and will rupture. In some instances although these ruptures are microscopic in size, the damage is already done and at this stage the failure will be system critical and/or fatal. Up to 80% of induced faults in the wiring have been produced due to maintenance errors [2.16]. In some instances trying to disconnect a part of wiring is enough to cause a variety of failure modes. Research undertaken in [2.27-2.29] illustrates how up to 43% of electronics failures are attributed to the wiring and interconnect.

2.3.2 Mechanical ageing

Mechanical ageing of the wire insulation is achieved by vibration, shock, and repeated flexing of the wire or the wire bundle being placed under too much tensile strain [2.3,2.14,2.15,2.30]. Repeated flexing, especially in moist environments, will accelerate the ageing process. The cracks grow as the insulation is exposed to cycles of water ingress and drying, which increases the probability of arcing at a later stage.

The insulation loses its mechanical strength as the scission rate increases due to the scission reaction. The polymer chain of the insulator decreases to such an extent that the mechanical strain created from the insulation being wrapped and bent reaches the actual breaking strain. When this condition occurs, the insulation ruptures spontaneously, exposing it to the harsh environment surrounding it and leaving it vulnerable to future arcing events.

Lectromec [2.23] identify delamination as an issue that affects fluoropolymers and aromatic polymers. Some insulation manufacturing is based upon successive layers being wrapped and glued on top of each other by an adhesive such as melted plastic.

This bond is responsible for holding the insulation together, and when this adhesion is lost, the mechanical strength of the insulation is lost in terms of chafe resistance and from moisture intrusion. Subsequent corrosion of the conductor and/or arcing is likely to occur afterwards. The mechanical strain becomes significant in wiring failure modes in two other ways [2.3,2.14- 2.18]:

1. In a bent wire, strain decreases the effective activation energy for the reaction with water at defective weaker sites of the polymer. Wiring in bent positions will therefore age at a far quicker rate than wiring in a normal straight position. The greater the bend of the wire, the higher the molecular energy created by the strain and hence the quicker the ageing process. Specific maintenance guidelines are given to the maximum bend radius that wiring must have in an aircraft.

2. Rupture of insulation depends on the amount of strain within insulation at the moment of rupture. If wiring is left to age without additional impact of the strain, it will last longer until it is moved or flexed by maintenance engineers, causing it to rupture.

2.4 Intermittency and Contact Fretting of Electrical Connectors

Intermittency is a vast problem in aircraft electrical systems. Recent advances have been made by Furse et al. [2.34,2.38,2.39] using reflectometry techniques such as spread spectrum for locating faults of intermittent nature. Before such advances were made, correct detection in the early stages of failure was difficult. Additionally, differentiation between intermittency and the case of no faults when using test equipment was also problematic. The issue with intermittency is that existing digital methods only sample for a certain period of time or are able to detect the fault once it has manifested itself in its final failure mode as a hard fault. Intermittency has a variety of contributing mechanisms from vibration to temperature gradients.

If the boundary of the connector interface is considered at the micro-scale, the problem becomes more apparent as shown in Figure 2.5. As two contacts move relative to one another the micro-protrusions at the highest peaks on the surface of the connector collide and resist further motion until a shearing force breaks off these protrusions as loose particles [2.31-2.33]. Vibration and shock levels in aircraft are of sufficient magnitude to provide these shearing forces.

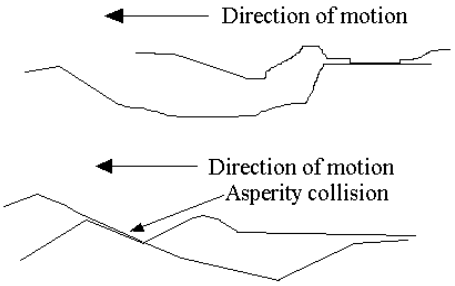

Figure 2.5 Asperity interaction due to horizontal motion [2.31].

The other mode of deterioration that occurs at the connector surface is adhesion of the micro-protrusions. This causes micro-welding of certain contacting points of the connector surfaces. Electrical continuity relies on micro-protrusions on the surface continually making contact. Processes such as oxidation, thermal expansion, galvanic corrosion and fretting serve to degrade the contact area and increase the contact resistance [2.33]. Both these modes of failure present themselves electrically as random changes in resistance since the contacting surfaces change relative to one another.

In Mano et al., [2.33,2.40] corrosion beginning at the ends of a contact can further prevent micro-protrusions establishing full contact between connectors. This has the effect of corroding the whole contact area and cutting off the supply of current. This type of failure could take up to 300 years at 25^{o}C and 3 years at 125 ^{o}C. These figures could be even less due to the nonlinearities not accounted for in their model. Other explanations for contact fretting include the presence of corrosive particles generated on the connector electrode boundaries and being dragged into the shallow areas of the conductor surface. A particle thickness of 20 nm at the interface stops electron tunneling from occurring, hence stopping current flow [2.40,2.41]. These explanations serve to explain why there are transient changes in the connector resistance over its operating lifetime, and why Automatic Test Equipment (ATE) can detect it only before connector failure. Aircraft wiring is immersed in high thermal gradients, humidity changes and corrosive elements such as chlorine and hydrogen. It then becomes justifiable to link fretting issues within the FMEA of wiring.

Bare metal contacts subjected to high amounts of vibration have the ability to fail due to fretting corrosion by increase of the contact resistance. When enough wear at the conductor surfaces has occurred, there will again be removal of particles and the formation of abrasive insulating oxides, which serves to increase the rate of wear. At low vibrational frequencies fewer cycles are required for an increase in the contact

resistance. In an ideal case wires are electrically lossless and source and load impedances match the characteristic impedance of the cables. Signal and power systems operating at high frequencies suffer additional degradation due to the system being unmatched and unbalanced. This creates multiple reflections at all points in the circuit where there are changes in impedance. As a result, signals are distorted and an increase in signal error rate is witnessed.

Baisheng et al. have shown that fretting resistance can be modeled as a capacitance in parallel with a resistance at high data transmission rate [2.42]. As mentioned previously, the contact area is made up of a number of loci where actual electrical contact is made. These spots allow the flow of current, and cause an increase in resistance, aptly named the constriction resistance. Since these spots are smaller than the non-conducting area of the contact area and the distance between conducting spots being small, the parasitic capacitance at high frequencies becomes dominant. In the situation where contaminants have entered the conducting surfaces at thicknesses of around 20 nm, the contact approximates a capacitor.

2.5 Repeated Load and Fatigue

Failure can be caused by progressive fracture or fatigue, whereby fatigue is defined as the deterioration of a material under repeated cycles of stress and strain resulting in a fracture [2.44]. In normal fatigued failure, a microscopic crack forms at the point of high stress, which increases in size as the loads are repeated. This effect can be found in wiring that is in a bent position or stressed state as the ageing process of the wiring is accelerated to point of failure. It is therefore judicious to monitor vibration levels throughout the wiring and the interconnections. As the interconnections begin to fail, they become relaxed and therefore do not maintain as much force to enable a full electrical contact. This causes poor electrical connections to be made and leads to problems such as contact fretting and series arcing.

2.6 Causes of failure due to maintenance

Selinski [2.28] shows that damage suffered by wiring located in wheel wells caused by excessive flexing can also occur from the opening and closing of circuit breaker panels. Excessive loading of wiring can also be caused by inadequate support of wire bundles,

especially near the connector. Use of inadequate terminations of connectors results in moisture intrusion and subsequent corrosion. Unused connectors need to be environmentally sealed and attached to the structure by clamping or stowing [2.29].

When locating faults, care must be taken so as not to induce additional faults into other parts of the aircraft wiring and interconnect. To help address these issues the Federal Aviation Administration (FAA) produced Advisory Circular (AC) 120-YY [2.44]. This sets guidelines as recommended by the Ageing Transport Systems rulemaking Advisory Committee (ASTRAC), for creating training and best practices for a variety of EWIS inspections, maintenance and designs for personnel ranging from technicians and inspectors. In AC 120-84 [2.45], the FAA introduced safety requirements for aircraft over 14 years in service by requiring aircraft to have inspections and record reviews. In addition all parts that have high failure rates or are age sensitive will be observed and maintained within guidelines.

Harnesses need to be well routed and supported in the correct manner to ensure that the wire does not flex or vibrate against other wiring or parts of the aircraft structure. Some insulation materials such as Kapton have straight line memory and flex back to their originally unstrained position. Insulators can abrade, chafe and eventually cut through softer materials. By twisting the wiring (one to two turns per foot), the harness keeps more flexibility by allowing the wiring to bend through rotational motion rather than it being stressed by the occurring stretching.

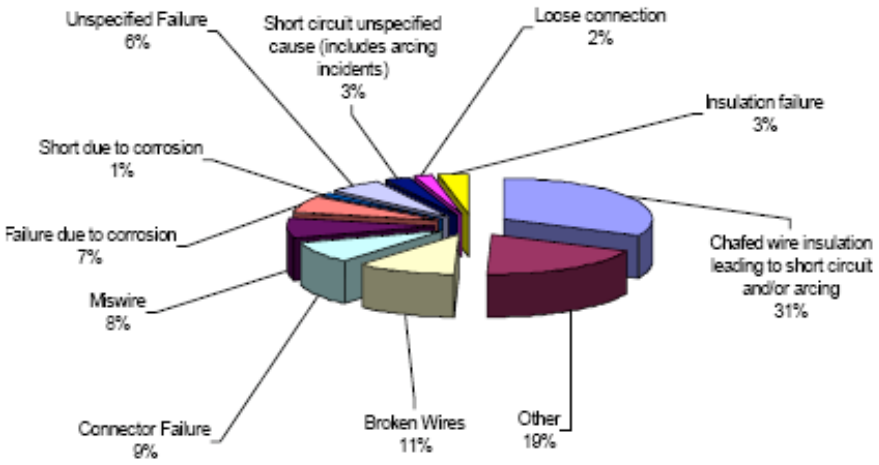

Figure 2.6 Typical wire system failure modes for aircraft for 1997-2001 [2.27].

Wiring failures due to maintenance are not the dominant cause of failure though a thorough understanding of these failures is required to avoid any damage to the wiring. The pie chart shown in figure 2.6 [2.27] illustrates the typical failure modes of wire and interconnects. A loose connection could be attributed to incorrect connection procedures being applied by the technician or it could be stress relaxation of the connector. This is caused by a series of amount of disconnections/connections of the connector during maintenance. Chafed wire insulation could be due to routing harder insulated wires next to softer wires, leading to extended periods of time rubbing against each other.

In addition this could also be due to insufficient cable ties being used on a wire bundle and subsequent sections being allowed to rub against sharp metal openings of the airframe. Failures due to corrosion again could be due to incorrect fittings of the connector or for unused connectors being covered incorrectly. This allows moisture intrusion and subsequent corrosive attack of the connector [2.29].

2.7 Navy Safety Centre Hazardous Incident Data

Specific data from failure analysis carried out by the Navy indicate the following [2.46]:

- 90% of faults repeated from aircraft to aircraft are of a single type by kind and location.
- 10% of faults are seldom encountered and are hard to detect.
- Visual inspection is 25% effective.
- Faults may have to be inspected many times before being fully resolved as they initially show when in flight.
- Advanced wire inspection techniques are 90% effective.

These findings are also supported in AC 25-YY [2.47], who have responded by providing “guidance for developing electrical system standard wiring practices” for a broad range of operators ranging from air operators to maintenance technicians. EWIS is categorised in terms of wire, connectors, connector accessories, grounding and bonding devices, splices, shields or braids, clamps, cable ties and pressure seals. Advice is given for cleaning, identification, installation, clamping and routing of EWIS plus repair/replacement and inspection procedures. The FAA produced AC 25.17xx [2.30] to give guidance on compliance and certification of electrical wiring systems. EWIS must be installed according to their limitations, such as maximum operating temperature,

moisture resistance, tensile strength and current carrying capabilities. Furthermore, component selection should be related to operating environment, i.e. vibration, moisture, insulation type, etc. Aromatic insulation is not to be chosen if the environment is subject to vibration and flexing in a moist environment such as in the landing gear harness [2.26,2.30].

AC 25-16 states that during maintenance, technicians should always make sure that, when the connectors are being removed, supports are installed to ensure no additional stress is placed on the rest of the wiring and connectors. When wiring is to be bent to curve round bends, the radii of the curve should not exceed the stated amount. The bend should be very slight as excessive bending of the wire to turn round a corner will cause the insulation to crack. When new wiring is installed, care should be taken to ensure that it is not fixed in a stressed state by the length of wire being too short. An ample length should be chosen to ensure it can flex slightly, hence avoiding additional stress on the wire and connector. Most faults are indeed found close to a connector in the wiring harness. Wire bundles should also "be routed along heavier structure members where possible to reduce the opportunity for maintenance technicians to step or climb on them" [2.26,2.30,2.44,2.45,2.47]. Wires should be bundled together according to hardness and separated and supported at certain distances to reduce the chances of chafing occurring.

Wiring should never be stood on to reach harder areas for inspection as this creates additional unplanned stress on the wiring that could cause it to fail. In some cases when wiring can be inspected there can be failed areas that cannot be noticed due to the small size of the flaw. Appendix 1.3 provides the comprehensive list of cause of failure and degradation due to mechanical causes.

In [2.27] Yang highlighted the need for a wire diagnostic and verification system that finds and locates hard faults such as opens/shorts, and intermittent faults caused by chafing, corrosion and loose connections. In addition, this information is to be stored for scheduled preventative maintenance. One solution is thought to incorporate embedded sensors and advanced algorithms. The benefit of this type of approach is that the amount of time spent on corrective maintenance is decreased, costs are reduced and availability of aircraft increases.

2.8 Failure Mode and Effect Analysis of Wiring and Interconnect

Failure Mode and Effect Analysis (FMEA) is defined in BS 5760-5:1991 as a "systematic and structured study of potential failures that may occur in any part of a system to determine the probable effect of each on all other parts of the system and on operational success, with the aim of improvement in the design, product and process development" [2.48,2.49]. It is a preventative analytical technique that has been around for about 40 years and was initially used in the aerospace industry. The motivation for using this method is to establish the prevalent contributors to wire failure. It also aims to map out the opportunities to design specific sensors and signal processing to detect aging and/or failure modes within wire and interconnect before producing severe failure effects. In this study, the aircraft wiring has been considered in terms of electrical, mechanical and chemical failure modes. The steps taken are as follows:

Step 1: *Break down the electronics into the wiring and interconnect*.

Step 2: *Consider the chemical, electrical and mechanical forms of failure*. Focus on one subsystem or manageable subsection to ensure that all effects of failure are found.

Step 3: *List the effects of each failure mode*. There are specially designed FMEA sheets for performing this analysis so that each failure mode and these effects are listed. Sometimes there is only one effect, more often multiple effects exist. A system should therefore be broken down into manageable sections to ensure that full analysis is performed.

Step 4: *Assign a severity rating to each effect of the failure effect.* This is one of the most complicated steps alongside step 5. A failure can cause more than one effect to the overall system, often with varying levels of severity. For this reason, all effects of a failure must be logged separately. It may be easier to assign a severity rating from prior expertise or available knowledge to a specific failure mode because of lack of available data. In that respect, estimations should be based on the understanding of the failure and how it contributes to the performance of the overall system. This chapter uses data in the available literature and reports on the various failure modes of wiring and interconnects as cited in each section. The severity rating starts at 1 for "no impact", and progresses to 10, which typifies "very critical". The full outline of an example of severity ratings is given in Appendix 1.4 and in [2.6].

The classification of the failure conditions is given in [2.31] and is performed by assigning a term according to the seriousness of the effect and an explanation, which sets out how this compromises the aircraft integrity and the chance of fatality in the form of operational capability and safety margins. These terms are given as (1) no safety effect, (2) minor, (3) major, (4) hazardous and (5) catastrophic.

When specifying severity in this FMEA, the worst case scenario is always assumed in the sense that the energy released during the failure of the wire is in contact with flammable substances or adjacent to system critical equipment.

Step 5: *Assign an occurrence rating for each failure mode*. This should be determined from the available data of the failure mode. If this data is not available then estimations should be made based on understanding of the failure mode. Details on the occurrence rating are given in Appendix 2.4. For the purpose of this chapter, ratings were based on available research in the area of wire aging and failure on aircraft. Specifically the data from references [2.12,2.51] were used as they are obtained during the maintenance of military aircraft. The value "1" depicts occurrence that is unlikely to occur, whereas "9-10" is very probable.

Step 6: *Assign a detection rating for each failure mode and/or effect.* This assignment is based on available information from current research. The value "1" is assigned to failure modes that are thought likely to be detected, and the values 9-10 for failure modes difficult to detect. Two sets of values assigned to each detection rating are provided and are in standard and bold fonts as shown in Appendix 2.4. The standard font considers the probability of detecting the fault whilst the aircraft is not in flight; the bold font considers the probability of detection whilst the aircraft is in flight.

An exemplar of FMEA is given in Appendix 1.4. The analysis of wet arc tracking shows values of "9" and "1" under the detection rating. Number "9" indicates that the detection of wet arcing events is unlikely whilst the aircraft is not flying. Wet arc tracking events are more likely to be detected when the aircraft is in flight where high humidity and vibrational cycling are common. Sensors developed by Furse et al., can check the wiring and interconnect when the aircraft is in flight using spread spectrum techniques [2.34,2.38,2.39]. The sensors operate whilst the wiring is live without interfering with the signals and can locate the fault location with a specific amount of wire branches within the wiring loom. Sensata have developed novel signal processing

techniques for analysing live wire signals and be able to locate arcing within these signals using the ARC Fault Circuit Breakers [2.13]. Advances in Spread Spectrum and Signal Processing Techniques mean that "1" is used as wet arc tracking is likely to be detected whilst the aircraft is in flight.

Step 7: *Calculate the risk priority number for each failure effect.* This number is calculated as follows: Risk Priority Number (RPN) = Severity rating times occurrence rating times detection rating.

Step 8: *Consider means of eliminating failure or detecting it before the failure modes becomes fatal to the subsystem or system.* The failure effects with the higher RPN are given high priority for corrective actions so that their RPNs can be decreased. All calculated RPNs are added so that the original system can be compared to the upgraded system to see how much improvement has occurred and if further work must be done to increase reliability and functionality of the system.

2.9 Summary of FMEA

FMEA of aircraft wiring is a necessary tool to save time and money during cable maintenance. Navair spent $94 million on No Fault Found (NFF) equipment removals due to wire faults being undiagnosed [2.27]. In addition, surveys undertaken from US Navy highlighted that fives times as much maintenance time was devoted to unscheduled or corrective maintenance compared to planned maintenance in 2004, with a third of this being wiring specific.

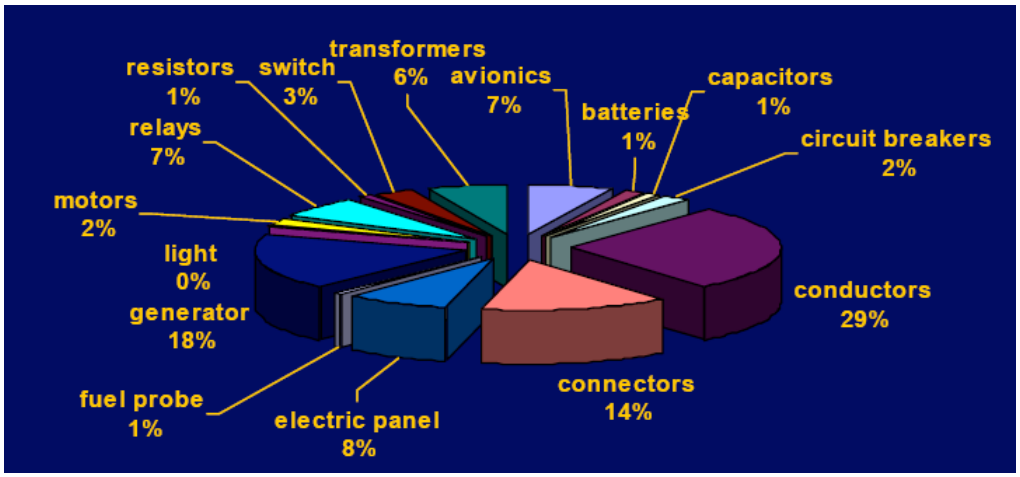

Figure 2.7 AF Mishap Data for Electronic Failures (1989-99). Navy Safety Centre Hazardous Incident data [2.28].

Most time is spent trouble shooting and trying to locate faults within aircraft wire as shown in figure 2.7. However, these faults are essentially soft faults such as chafing, corrosion manifestation or loose terminals, which are mostly only detectable when the aircraft is in flight. Even planned maintenance in most cases does not resolve the problem. Collins reports in [2.29] that the total amount of flight hours of all US Navy aircraft in 2005 was 921,658. Of this amount there was 637 hours between wiring failures occurring or 4 failures per day. Time spent by maintenance technicians trying to rectify these failures amount to 7.3 hours per flight hour for aircraft older than twenty years. Other reports, such as [2.52,2.53], confirm that the Department of Defense (DoD) spend 1.8 million work hours per year troubleshooting and repairing aircraft. Kiptiness [2.24] reports that using Smart Wiring Systems can produce massive savings for the Navy by:

- Reducing in flight fires and subsequent loss of aircraft by 80%.
- Reduce maintenance man-hours by between 200,000 to 400,000 per year.
- Generate savings of around $34.5 million annual savings from mission aborts and increase mission capable hours.

The design of sensors that enable monitoring and detection of the most important failures obtained from the FMEA will result in cost savings to maintain an ageing aircraft fleet. Smart wiring is composed of embedded sensors, reflectometry techniques, processor and wireless capability integrated into a single miniaturised unit. It can detect and pinpoint failures in wiring including intermittent faults such as arcing. By introducing arc fault circuit breakers maintenance would be reduced by up to 80%. This would provide a saving of $12 million per year.

NASA reported in [2.53] that more advanced techniques such as smart wiring are required for efficient testing of wire and interconnect. They include advanced signal processing techniques such as wavelets or edge detection algorithms for detection of transient signals. Moreover, in [2.28,2.51] failure data for fighter aircraft showed that 46% of it was broken wire.

A maintenance report from the Royal Air Force base Brize Norton [2.12] and work by Failure Analysis Associates [2.51] have shown that the vast majority of aircraft wiring problems lie with faulty wiring and interconnection (72%). Half of these issues (36%)

were attributed to interconnection [2.51]. Routine maintenance carried out by RAF illustrate that P-clips were either damaged, distorted or of incorrect size.
Poor/incorrect routing of cable looms were causing undue stress on the connectors, with bends in the wiring out with the recommended angle noted as well as abrasion to the insulation.

It was also found that the cable looms offered insufficient support. Fraying of outer cable insulation and dirty/contaminated cables were also observed. 18% of connector and conductor failures were also noted in this survey [2.51], all of which caused mechanical aging/failure of the wiring and could have been avoided through correct maintenance procedures. This supports earlier work [2.16] that claims that 80% of failures are induced by human error. Had these errors not occurred then the wiring would have aged due to the hydrolytic scission of insulation and increase in connector resistance.

2.10 Summary

This chapter has introduced the background of ageing and failure of electrical wiring and interconnects, the contributing factors towards ageing/failure and the different failure modes and effects experienced. The primary effects of the ageing wiring are its loss of mechanical and electrical strengths. This is attributed to the large fluctuations in temperature and humidity, resulting in the moisture being absorbed into the wiring and breaking up the polymer chain of the insulation into smaller parts. Temperature fluctuations dry out the insulation leaving it prone to cracking due to accelerating effect on the scission rate.

Mechanically, the insulation can be degraded by excessive fatigue, i.e. vibration, or by a sudden mechanical load. This could be due to technicians standing on wire bundles to reach often inaccessible areas of wiring. Failure will tend to occur in areas where the wire is bent, hence decreasing the strength of the insulation far quicker than areas where the wire is left in a straightened position.

FMEA has shown that chemical and mechanical strains exacerbate the ageing process by the decomposition of the material characteristics, yet extreme failure such as fire or

fire induced damage of other wiring or structures derive from electrical origins. When an aircraft is in flight the electrical systems are in operation and hence the problems are present. Once current is flowing within the system, failure modes present themselves by excessive standing waves, loss of signal transmission and wet arcing, leading to fire and/or loss of control of the aircraft.

The taxonomies of failure modes in Appendices 1.1 to 1.3 and the *Exemplar of FMEA* given in Appendix 1.4 highlight that wiring can fail from a wide range of effects. Whilst one cause of failure can start the accelerated ageing of the wiring (i.e. hydrolytic scission), it can ultimately be another source of failure that causes the wiring to catastrophically fail; for example, the bending the wire past the specified bend radii causing the insulation to crack and eventually cause an arcing event.
Other forms of arcing, such as series and parallel arcing, are the result of broken wires and wires being grounded against the airframe or exposed wires at different potentials. This leads to differences in the observed waveforms and the amount of energy that is expelled at the point of occurrence. The duration and rise-times of arcing are known to vary with pressure and humidity hence there appears to be an opportunity for developing a multi-sensor system to monitor these parameters along with the arcing waveform. This will enable a better understanding of the faults that occur and probability of occurrence. Using a wide-band current sensor for monitoring fast rise-time signals on wiring will increase the chance of detecting these signals among normal transients that occur from onboard electrical equipment.

MEMS coupled with advanced signal processing techniques appear as an attractive proposition in order to monitor the impact of environmental changes due to the small size, low weight and low power consumption of integrated circuits. Embedding humidity sensors inside and outside of the wire connectors will enable, for example, the monitoring of the surrounding environment as well as the detection of moisture penetrating into the connector seal.

This thesis will explore the development of a system capable of monitoring these parameters, with focus mainly on the development of a wide-band current sensor and a capacitive humidity sensor.

References

[2.1] F. Drichot and H.J. Reher, “Survey of Arc Tracking on Aerospace Cables and Wires”, IEEE Trans. Dielectr. Electr. Insul., Vol. 1, pp. 896-903, 1994.

[2.2] MD-11 Corrective Action Plan: A Case Study in Reactive Safety, Air Safety Week, Dec 13th 2004.
Available: http://findarticles.com/p/articles/mi_m0UBT/is_47_18/ai_n8581512.

[2.3] L.C. Brinson, S. Carr, T. Mason, K. Skull, T. Bai, N. Nunalee et al, Northwestern University. “Aging Characteristic and Lifetime Assessment of Polymeric Insulation in Aircraft Wiring”. Semi-annual Report, October 2002.
Available:
http://www.mech.northwestern.edu/fac/brinson/faawire/Semi_annualoct2002.pdf.

[2.4] W. Shawlee, Aviation Today, Column: “Avionics System Design-How Parts and Systems Age”. 1st November, 2000.
Available:
http://www.avionicsmagazine.com/cgi/av/show_mag.cgi?pub=av&mon=1100&file=column2.htm.

[2.5] T. Potter, M. Lavado and C. Pellon, “Methods of Characterizing Arc Fault Signatures in Aerospace Applications”, in Proc. 6th Joint FAA/DoD/NASA Conf on Aging Aircraft, September 8th-11th, 2003.
Available: http://www.sensata.com/files/AgingAircraftConf-Sept2003.pdf

[2.6] B.G. Moffat, E. Abraham, M.P.Y. Desmulliez, D. Koltsov, A. Richardson, "Failure mechanisms of legacy aircraft wiring and interconnects," *IEEE Transactions on Dielectrics and Electrical Insulation,* vol.15, no.3, pp. 808-822, June 2008.

[2.7] Kenneth G.Blemel and Peter A. Blemel, Management Sciences Inc., “Smart Wiring Prognostic Health Management” JAWSSS 2000, May 13th.
http://www.engineering.usu.edu/ece/furse/COE/wiring/Jawss2000.html

[2.8] S. Khan, P. Phillips and I. Jennions et al, ”No Fault Found events in maintenance engineering Part 1: Current trends, implications and organizational practices”, Reliability Engineering & System Safety, Volume 123, March 2014, Pages 183-195.

[2.9] Y. Wang, E. Dong and J. Cong et al, "Arc tracking properties of the aging wires in aircraft," *2nd International Symposium on Systems and Control in Aerospace and Astronautics,* pp. 1 - 5, 10-12 Dec. 2008.

[2.10] Z. Ma, P. Wang and N. Xiao, "Research on the factors contributing to aircraft wiring failures", Procedia Engineering, Vol. 17, pp. 433-439, 2011.

[2.11] K.R. Wheeler, D.A. Timucin and I.X. Twombly et al, "Aging aircraft wiring fault detection survey", *Aviation Safety program Aircraft Aging and Durability Project: Wiring Fault Detection Challenge, 2007*.

[2.12] RAF Norton Brize, Wiring Survey Report - Tri-Star Aircraft, 10-16 Oct., 1999.

[2.13] S.J Daniels, "Space Shuttle Columbia Aging Wiring Failure Analysis", in Proc. of 8th Joint FAA/DoD/NASA Conf. on Aging Aircraft, Florida, USA, 2005.

[2.14] A.M. Bruning, F.J. Campbell, "Aging of Wire under Multifactor Stress", IEEE Trans. Electr. Insul., Vol. 28, pp. 729-754, 1993.

[2.15] A.M. Bruning, F.J. Campbell, "Insulation Aging from Simultaneous Mechanical Strain, Polymer-Chemical and Temperature Interactions", in Proc. of International Symposium on Electrical Insulation (ISEI), Baltimore, USA, pp. 74-78, 7-10 June, 1992.

[2.16] F.J. Campbell, A.K. Brewer, R.J. Orr, T.A. Janicke and A.M. Bruning, "Hydrolytic Deterioration of Polyimide Insulation on Naval Aircraft". In Proc. of Conf. on Electrical Insulation and Dielectric Phenomena, pp. 180-188, 16-20 Oct 1988.

[2.17] C. Teal, W. Larsen, "The Phenemology of Wire, Dielectrics and Frequency", in Proc. of 21st IEEE Digital Avionics Systems Conf, vol. 2, pp. 12E6-1-12E6-9, 27-31 Oct, 2002.

[2.18] P. Connor, J.P. Jones, J.P. Llewellyn and T.J. Lewis, "A Mechanical Origin for Electrical Aging and Breakdown in Polymeric Insulation", Proc. of IEEE International Conf. on Breakdown in Solid Dielectrics, pp. 434-438, June 22-25, 1998.

[2.19] T.J. Lewis, J.P. Llewellyn, M.J. van der Sluijs, J. Freestone and R.N. Hampton, "A New Model for Electrical Aging and Breakdown in Dielectrics", 7th Conference on Dielectric Materials Measurements and Applications, pp.220-224, 23-26 September, 1996.

[2.20] J. Martin, "Maintenance Affordability and Readiness Improvements through Asset Redistribution and Corrosion Prevention", DoD Maintenance Symposium and Exhibition, October 27th, 2003.

[2.21] S. Benavides, "Dehumidification of Operational US Coast Guard Aircraft". Aging Aircraft Branch, 9th Joint FAA/DoD/NASA Conf on Aging Aircraft, March 6-9th, 2006. Available: www.agingaircraftconference.org/all_files/20/20a/90_doc.pdf

[2.22] C. Teale and D. Sorenson. "Balanced Circuits Improved Performance [aircraft wiring system]. In Proc. DASC, vol. 1, pp. 3B1/1-3B1/6, 14-18 October 2001.

[2.23] Lectromec Design Co. Website
www.lectromec.org

[2.24] Susan Kiptiness, Masters Thesis, "An Analysis of the Conventional Wire Maintenance Methods and Transition Wire Integrity Programs used in the Aviation Industry" East Tennessee State University, August 2004.

[2.25] N. Bowler, M.R. Kessler and L. Li et al, "Electromagnetic Nondestructive Evaluation of Wire Insulation and Models of Insulation Material Properties". NASA/CR-2012-217330, January 2012.

[2.26] Federal Aviation Administration Advisory Circular 25-16. "Electrical Fault and Fire Prevention and Protection". May 4t 1991.

[2.27] Andy Yang, "Accurate Data Collection: Roadmap to Proactive Aircraft Wiring Maintenance". In Proc. Aging Aircraft IPT, 19th July 2006.

[2.28] George Slenski, "Aging Wiring System Integrity Initiative".
Available:
www.wire.nasa.gov/participating_orgs/RTO%20BF%20on%20**Aging**%20**Wiring**%20final%20PA%20approved.pdf

[2.29] J. Collins, "The Challenges Facing US Navy Aircraft Electrical Wiring Systems". In Proc. 9th Joint FAA/DoD/NASA Conference on Aging Aircraft, March 2006. Available: www.aging**aircraft**conference.org/all_files/46/46b/152_doc.pdf

[2.30] Federal Aviation Administration Advisory Circular 25-17xx, "Certification of Electrical Wiring and Interconnection Systems on Transport Category Airplanes".

[2.31] J. Moran, M. Sweetland and N.P. Suh, "Low Friction and Wear on Non Lubricated Connector Contact Surfaces", Proc. of 50th Holm Conference. on Electrical Contacts and the 22nd International Conference. on Electrical Contacts, pp. 263-266, 20-23 Sept. 2004.

[2.32] M.D. Bryant, "Resistance Buildup in Electrical Connectors due to Fretting Corrosion of Rough Surfaces", *IEEE Trans. Compon., Packag., Manuf. Technol. A**, vol. 17, pp. 86-95, March 1994.

[2.33] E. Takano and K. Mano, "Theoretical Lifetime of Static Contacts", IEEE *Trans. Parts, Mater., Packag.*, vol. 3, pp. 184-185. December, 1967.

[2.34] C.Furse, P.Smith, M. Safavi, C. Lo," Feasibility of Spread Spectrum Reflectometry for Location of Arcs on Live Wires," *IEEE Sensors J.,* Vol.5, No. 6, pp.1445-1450, Dec 2005.

[2.35] Y. Wang, E. Dong and F. Cheng et al, "Simulation of arcing fault in aircraft wiring system", *IEEE 1st International Conference on Electric Power Equipment-Switching Technology*, pp. 582 – 585, 23-27 Oct., 2011.

[2.36] R. Spyker, D.L. Schweickart and J.C. Horwath, "An evaluation of diagnostic techniques relevant to arcing fault circuit interrupters for direct current power systems in future aircraft", *Proceedings Electrical Insulation Conference and Electrical Manufacturing Expo,* pp. 146 -150, 26-26 Oct. 2005.

[2.37] D.L. Schweickart, D.F. Grosjean and D.G. Kasten et al, "Low-Pressure Partial-Discharge Measurements: Monitoring the Insulation Integrity of Aircraft Power Wiring Systems," *Proceedings of the IEEE International Power Modulators and High Voltage Conference,* pp. 568 - 571, 27-31 May 2008.

[2.38] P. Smith, C.Furse and J.Gunther, "Fault Location on Aircraft Wiring Using Spread Spectrum Time Domain Reflectometry," *IEEE Sensors J,* Vol. 5, pp. 1469-1478, 6th Dec. 2005.

[2.39] C.Lo and C.Furse, "Noise Domain Reflectometry for Wire Fault Location," *IEEE Trans. Electromagn. Compat.*, Vol. 47, pp. 97-104, Feb. 2005.

[2.40] E. Takano and K. Mano, "The Failure Mode and Lifetime of Static Contacts", *IEEE Trans. Parts, Mater., Packag.* vol. 4, pp. 51-55, 1968.

[2.41] M.D. Bryant, "Assessment of Fretting Failure Models of Electrical Connectors", Proc. of the 40th IEEE Holm Conf. on Electrical Contacts, pp. 167-175, Oct. 17-19, 1994.

[2.42] B. Sun, "Effects of Electric Contact Failure on Signal Transmission in Unmatched Circuits", in Proc. 47th IEEE Holm Conference on Electrical Contacts, pp. 186-191, 10-12 Sept., 2001.

[2.43] B.A. Sorenson, P.W. Sorenson, G. Kelly and A. Sajecki, "An Analyzer for Detecting Aging Faults in Electronic Devices", in Proc. AUTOTESTCON, pp. 417-421, Sept. 20-22, 1994.

[2.44] Federal Aviation Administration Advisory Circular 120-YY, "Aircraft Electrical Wiring Interconnection Systems Training Program". February 8th 2002.

[2.45] Federal Aviation Administration Advisory Circular 120-84, "Aging Airplane Inspections and Records Reviews". October 22nd 2004.

[2.46] C. Teal and W. Larsen, "A Planned Maintenance Program for Aircraft Wiring". in 21st Proc. Digital Avionics Systems, Vol. 2, pp. 12D3-1 - 12D3-6, 27-31 Oct., 2002.

[2.47] Federal Aviation Administration Advisory Circular 25.YY. "Development of Standard Wiring Practices", 28th Oct., 2002.
Available:
http://www.mitrecaasd.org/atsrac/final_reports/Task_7_Final_Report_Advisory_Circula-10-31-2002.pdf

[2.48] Lavu S. 1st Year Report in FMEA of MEMS Micromotor. Heriot-Watt University, 2004.

[2.49] BS 5760-5:1991. Reliability of systems, equipment and components. Guide to failure modes, effects and criticality analysis (FMEA and FMECA). ISBN 0580196607.

[2.50] RAF Norton Brize, Wiring Survey Report - Tri-Star Aircraft, 10-16 Oct., 1999.

[2.51] D. Galler and G. Sienski, "Causes of Aircraft Electrical Failures ", in Proc. NAECON, vol. 3, pp. 1012-1018, 20-24th May, 1991.

[2.52] NSTC, "Review of Federal Programs for Wire Safety", Final Report, Nov. 2000. Available: http://www.ostp.gov/html/wire_rpt.pdf

[2.53] NASA, "Wiring Integrity Research (WIRE) Pilot Study A0SP-001-XB1, August 2000.

Chapter 3 Sensors and sensor systems for fault monitoring and ageing in aircraft wiring and interconnect

3.1 Introduction

Chapter 2 presented the theory behind ageing and failures of aircraft wiring and interconnects. This chapter focuses on the identification and selection of a cluster of sensors that could be integrated into a non-standard package. This cluster of sensors forms a miniaturized Health and Usage Monitoring System (HUMS) that is capable of monitoring the ageing parameters of Electrical Wiring and Interconnect Systems (EWIS), along with the detection of partial discharge or arcing fault signals. The initial customer (BCF Designs Ltd.) requirements for the system solution are also outlined and further specified to cover autonomous operation in harsh environment.

3.2 BCF Designs Ltd. customer requirements

BCF Design Ltd. is the leader on health management and prognostics of wiring systems for a number of projects such as DTI's Aerospace Innovation and Growth team and the Health Management And Prognostics (HMAP) programme. The research of this thesis is funded by BCF Designs Ltd. as part of their five to ten-year strategy of progressing beyond their current market offering in ground-based test systems to online monitoring diagnostic and prognostic systems, with the aim of increasing competitiveness and ensuring future growth of the company. Consequently BCF Designs Ltd has initiated a programme of research and development to progress beyond its current test equipment capabilities and that of its competitors. BCF envisage that the development of an online diagnostic and prognostic system will result in a new generation of aircraft testing devices that meet the demand of current and future market requirements of the defense and civil aviation industries.

The ultimate objective of such a programme is the development and commercialisation of smart miniature electronic devices that possess the ability to intelligently monitor the electrical health and surrounding environment of aircraft EWIS. The system envisioned will address the gaps of current products by facilitating online data storage and analysis,

communication with ground based maintenance and support systems, thereby providing ongoing condition monitoring.

In essence, what BCF Designs Ltd. would like, is a miniaturised version of the current ground based test system with the added capability to operate on-line while the aircraft is in flight and with further functionality such as being able to locate the location of the wiring fault. Such a system would be the size of a sugar cube, allowing it to be embedded within key problem areas of an aircraft for sufficient periods of time that require little maintenance or servicing. This would permit the implementation of a system on multiple aircrafts at a cost effective price point to roll out over various aircraft platforms.

This research aims to contribute towards the BCF strategy by designing and developing smarter test technology specifically for aircraft wiring systems. The technology must be capable of being embedded on the aircraft for continuous real time monitoring and diagnostics and meet the stringent technical, quality and safety specifications required by the military and aerospace industries. One of the key challenges in this research is establishing a system that is capable of monitoring different aircrafts and their associated systems. The wiring routes, wire types and areas of aircraft used for EWIS vary from aircraft to aircraft, and manufacturer to manufacturer. The problem of identifying arcing faults in particular may not be repeatable across a fleet. Therefore further experimental analysis is required to understand where the problem areas lie.

In the US, NASA's Wire Health Management Technology Development group [3.1] have conceded that lots of different types of test hardware have been developed to address EWIS challenges but that ultimately, there are knowledge and capability gaps in the following areas [3.2-3.5]:

- Algorithms that assess reflections that arise from partial discharge (PD) signals propagating down a wire for different wire types.
- No attention yet focused on detectability and uncertainty.
- Understanding how the electrical signals that characterize the PD signal change as the chafe size increases and/or changes shape with time.
- Little wire fault data available publicly to the scientific community that could be used

for developing such algorithms.

Two of the main drivers for further aerospace research are reducing operational costs and asset downtime as the visual, interval driven aircraft inspections and maintenance are time consuming and labour intensive. Other market drivers include the reduction of the system weight as well as safety and environmental concerns through full life cycle management of these systems. Consequently, such a system not only needs to be miniaturised for weight reduction but also be able to be fixed permanently in difficult areas requiring minimum maintenance support. Therefore powering of such a miniaturised system is a key feature such that it can be left for long periods of time without requiring to strip areas of the aircraft structure to access these microsystems.

The architecture of generic monitoring systems for aerospace would include a range of sensors such as temperature, strain, vibration, corrosion and wind velocity. Although damage detection is a key requirement of such systems, detection of damage early on in the degradation process prior to the larger scale failure of the component is still challenging. Such prognostic systems are able to calculate the remaining useful life (RUL) of an aircraft component. RUL looks at the deviation from normal operating conditions of a component in addition to its associated failure modes, early signs of ageing and fault detection. The data gathered from a prognostic system requires some form of post processing for decision making to be made with high levels of statistical confidence. This adds a further energy burden; therefore, sensor selection should be carried out with this in mind. Sensor components will drift over time, so the ability to auto-calibrate and be resistant to harsh environments will also be beneficial for verifying the system suitability in a stringent industry such as aerospace. The impact of this is examined and addressed throughout the course of this chapter.

3.3 Health and Usage Monitoring Systems (HUMS)

Health and Usage Monitoring Systems (HUMS) were initially developed for helicopter operators working in the North Sea in response to reliability issues and increasing accidents with their helicopter fleet [3.6], [3.8]. This was the result of accelerated ageing and failures of mission critical components such as the gearboxes. In discussions at the 2005

International Helicopter Symposium, goals were set at reducing the number of accidents by 80% in ten years through the introduction of novel Health Monitoring Systems. Although these systems have been around for the past 30 years, there has been an improvement to their diagnostic capabilities and reduction to their actual size by non-traditional HUMS providers.

HUMS are generally considered as more than a system, but rather as a collective group of avionics equipment, ground support equipment and changes to the way that aircraft are operated and maintained. An overview of a typical HUMS [3.7, 3.8] system is presented in figure 3.1.

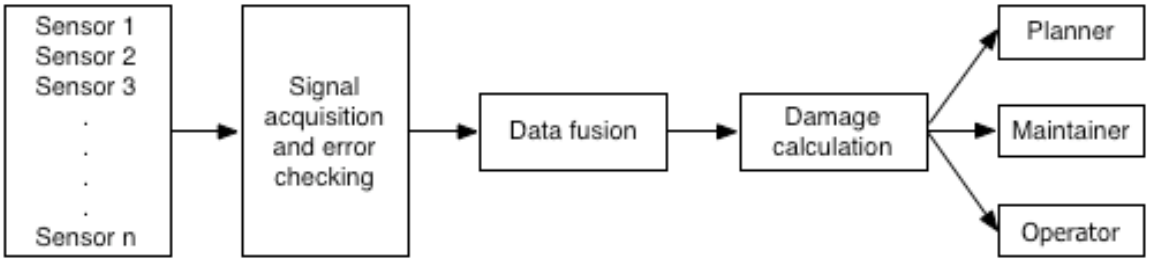

Figure 3.1 Functional overview of HUMS [3.7].

- The **H**ealth aspect is a measure of the flight readiness or worthiness of the aircraft and is assessed through examination of parameters related to the remaining life usage of the components or systems being monitored [3.8].
- The **U**sage aspect is the examination of how far into the finite lifetime of operation the parts currently are. This enables decisions to be made regarding when preventative maintenance can be performed.
- The **M**onitoring aspect is the method or means of evaluating the parameters related to the state in lifetime of the parts and/or system.
- The **S**ystem aspect is the collection of sensors, data acquisition, signal processing, data fusion and maintenance program(s) that run together to improve the management of aircraft fleets in terms of operating costs, flight safety and fleet readiness.

The sensors monitor multiple parameters and also convert the sensor output to a common signal that can be processed by some form of error checking before performing data fusion.

This allows then an estimate of the damage to be calculated and shared with operator(s) of the aircraft, the maintenance engineers, supply chain management and planning team. Due to every aircraft component having a safe limit of operation, the current standard of maintenance is time based. In addition to the safe limit of operation being defined in terms of hours of usage, an additional amount of hours is added to satisfy safety tolerances. This leads to maintenance being performed according to time based intervals, resulting in components or systems being replaced when there is still adequate lifetime in the parts. Over recent years, HUMS gained acceptance as a solution for providing predictive maintenance or Condition Based Monitoring (CBM) in helicopters and fixed wing aircraft [3.6–3.8]. At present there is a large focus on mission critical components on helicopters such as the gearbox, engine and rotors. HUMS systems typically possess the required sensors such as accelerometers, signal conditioning electronics and data processing to monitor these critical components.

In the case of legacy aircraft, 50% of current wiring issues are the result of chafing. The current method of detecting chafes to the wire insulation is through visual inspection. These inspections are not cost effective due to the large volume of wiring and the lack of accessibility to some areas of the wiring. Other challenges to address include the requirement of disconnecting wiring at the connector for ground based testing. This introduces stress to the wiring and interconnects such that the constant opening and closing of the wiring increases crack propagation along the insulation and may also crack internal conductors of the wire bundle. Fault identification and location using these methods is often unsuccessful due to the problem only presenting itself while the aircraft is in flight. This supports the requirement of modern HUMS systems being capable of being operated in situ so that faults can be detected and analysed to provide meaningful data and facilitate corrective decision-making.

HUMS come in typically two modes of device, known as prognostic or diagnostic [3.7].

3.3.1 Prognostic HUMS

The Prognostic version predicts the remaining useful life based upon monitoring the level of damage to the component. This usually involves monitoring parameters relative to its operating environment such as load or temperature. These parameters are then used to predict what the estimated remaining life is. The drawback of this type of system is that a priori knowledge of the component is required to be able to make a meaningful estimate of the remaining lifetime [3.7]. Prognostic HUMS is used for condition based monitoring, with the value proposition being demonstrated on figure 3.2.

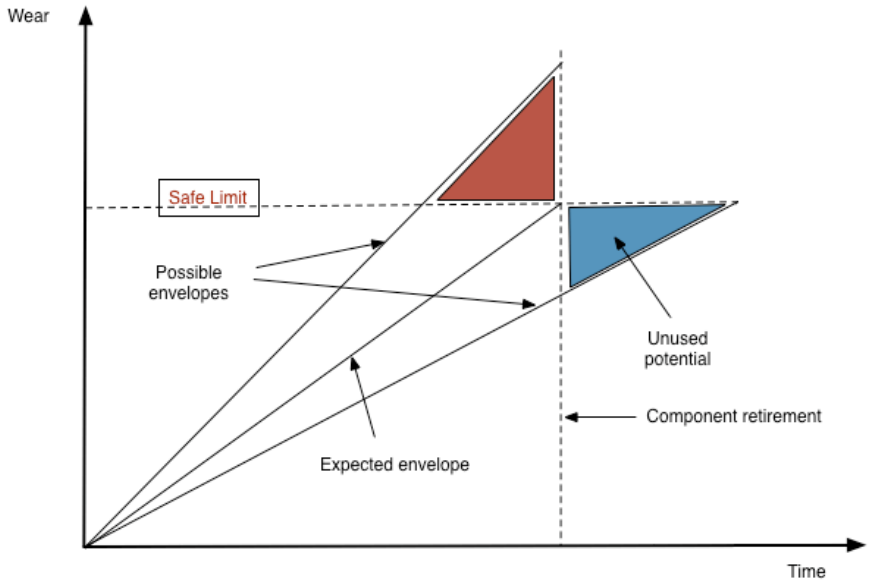

Figure 3.2 Condition based monitoring trade off [3.7].

Depending on the usage of a component or system on an aircraft, the part may reach end of life earlier or later than the expected envelope of operation. Some aircraft will have milder usage, and the component or system will last beyond the expected envelope. In the "expected envelope" there is an intercept from the y and x-axis that represents the safe limit cut-off and component retirement. This limit is calculated from an expected usage spectrum [3.6] with a margin added on top to account for variances. For the case of milder use, the component retirement point is extended further along the x-axis until it intercepts the safe limit of the part. This then allows the full life to be achieved for the part or system before maintenance is scheduled. On the other hand, for systems or components that have been exposed to more aggressive usage, the safe limit will be reached well before the average (expected) limit. Prognostics therefore provide an opportunity to decide whether there is

further unused potential (blue zone) or whether it falls in the dangerous region (red zone). For ageing wire and interconnect, these regions could be specified by ranges of humidity, temperature and vibration of particular sections of wiring and interconnect.

Some aircraft will not have experienced such harsh environments and others will have been exposed to larger exposures resulting in a higher probability of failure of the component and/or system.

3.3.2 Diagnostic HUMS

The diagnostic versions of HUMS are systems that look at the signs of symptoms of a fault and make a diagnosis based on this information. This involves comparison of sensor output signals against a healthy baseline signal to enable a decision to be made about the current state of health. This data allows decisions to be made about scheduled maintenance and corrective repairs on a required basis instead of time scheduled slots being made on an arbitrary basis.

The main challenge yet to be fully addressed using diagnostic HUMS is the identification of a set of sensors that can provide consistent and accurate indication of component health. The variation that exists in sensors as a result of the manufacturing steps means that the cumulative effects of the sensor outputs make it difficult to provide early warning of failure [3.7]. The 2008 Nexus report for structural health monitoring [3.9], which is a subset of the generic Health and Usage Monitoring Systems (HUMS) sector, identified that the key areas of focus were aeronautics, transportation, civil engineering and energy. These industries are now looking at HUMS due to the increasing availability of miniaturised smart sensors and increasing integration of those sensors onto smaller packages with the additional functionalities such as data storage and processing, energy scavenging and wireless communication. An example of two MicroHUMS or Health and Usage Monitoring Microsystems (HUMMS) is shown in figures 3.3 and 3.4 [3.10]. In this paper, Kavanagh et al. present a combined sensor and actuator for inflatable space structures that uses temperature, strain and accelerometer sensors. The HUMMS is used to monitor these structures for parameters such as deployment of the device, structural stresses and the assembled state.

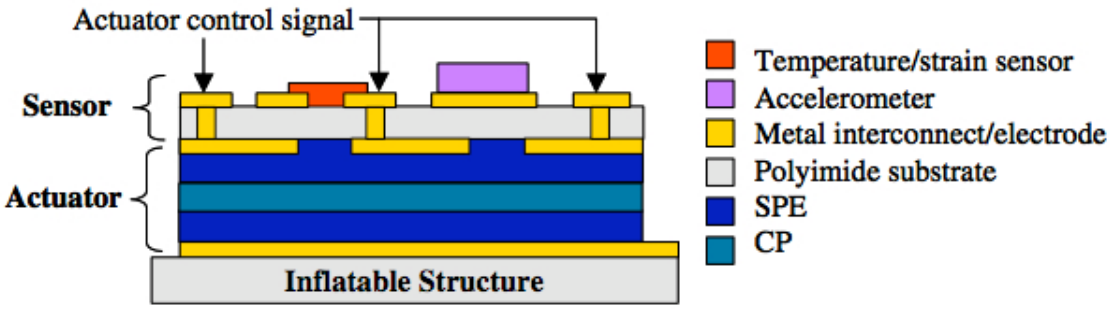

Figure 3.3 Side die profile of HMCS [3.10].

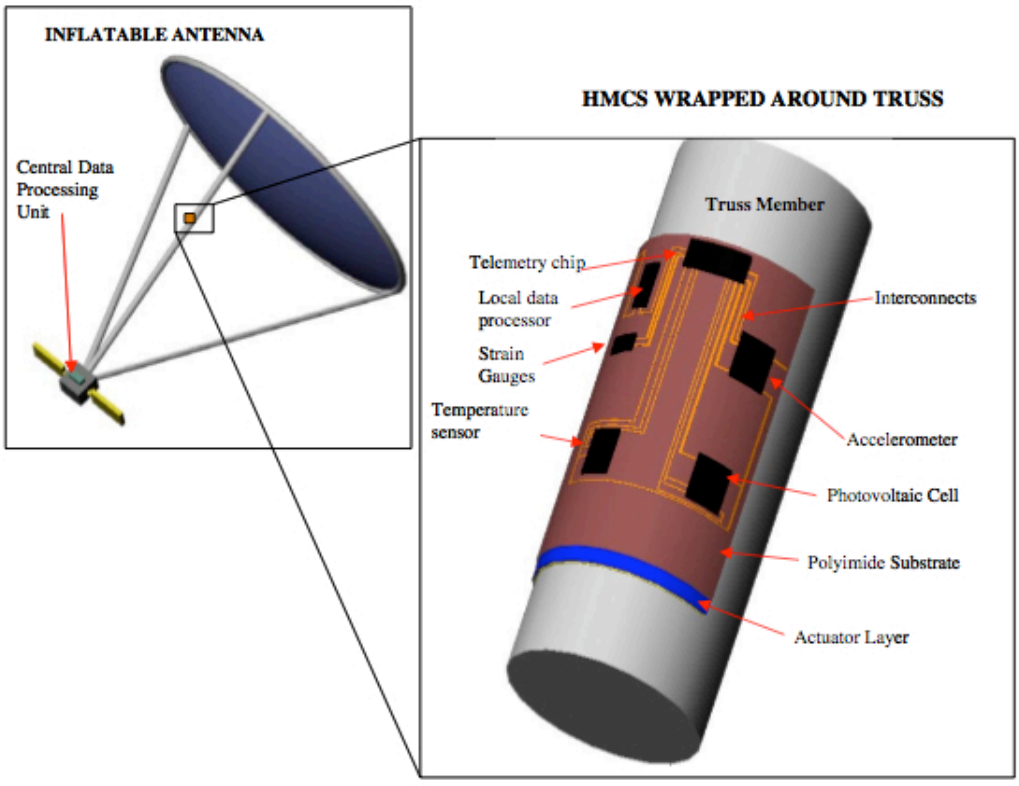

Figure 3.4 Application of an HMCS in an inflatable antenna [3.10]

The main driver for such devices stems from the increasing levels of system complexity and sophistication, which, in turn, has placed greater demands on flight performance requirements, ability to recover from a failure or serious system degradation event, increased reliability and reductions on overall system costs. Achieving these requirements meant incorporating the sensing and control capabilities into the system, resulting in local information such as its immediate environment being monitored and related to health of the system. This allowed measurements of material stress and temperature to be logged, analysed and transmitted and/or dealt with as necessary.

3.4 Smart Sensors

To appreciate the benefits of smart sensors, the definition of a traditional integrated sensor is provided first. A traditional sensor is defined as a device that can acquire information/energy from an object and transform it into an electrical signal as shown in figure 3.5. The operation is broken into three functions:

1. A sensing element (e.g. piezo-electric, magnetic, capacitive, photodiode, etc.)
2. A signal conditioning/processing component. (e.g. amplification, filtering, compensation and linearization).
3. Finally, the sensor interface (e.g. the wires and interconnects).

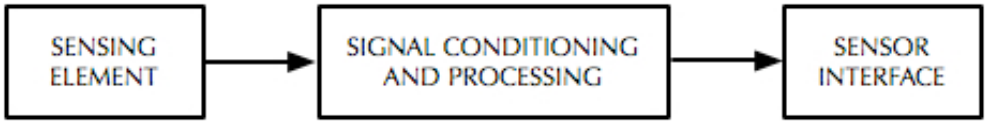

Figure 3.5 Traditional integrated sensor [3.10,3.11].

In [3.12] the authors define a smart sensor as "a smart sensor is one chip, without external components and including sensing, interfacing, signal processing, self validation and self-adaption functions". A smart sensor has more intelligence compared to its traditional counterpart in terms of on-board microprocessing capabilities [3.10,3.12,3.13]. Smart sensors can provide digital signal processing, analogue to digital conversion, and interfacing. MEMS has enabled smart sensors to be shrunk further in footprint; the integration of MEMS and electronics using very large scale integration technology (VLSI) and MEMS compatible process steps has produced devices capable of possessing

chemical/mechanical and electrical functionality.

The integration of a set of smart sensors for health monitoring and fault detection of aircraft wiring on a non standard package would realize a level of minaturisation to allow their location in multiple sections along a wiring loom and at the interconnect level. A collection of suitable chosen sensors could be installed that are of low power and can self calibrate in order to minimise non-linearities and drift. Such a system, if coupled with wireless capabilities, on-board battery and energy scavenging could monitor and report on key parameters such as humidity, temperature, pressure and acceleration. Further benefits of this system is that the sensor data could be transformed from analogue output to a digitized output, enabling decisions to be made at ground level based on the data that was being transmitted to the maintenance crew. A challenge is designing and manufacturing with a good yield a current sensor that can detect fast rise-time signals such as arcing i.e. a sufficiently large bandwidth in the MHz range.

3.5 Introduction of HUMS sensor platform for EWIS

This section introduces the thought process used to design a solution based on the customer criteria and the understanding of the FMEA carried out earlier in this thesis. The proposed solution will have a cluster of sensors organized in a small form factor, that will measure all parameters related to the ageing and failure of aircraft wiring and interconnect.

The first concept, shown in figure 3.6, is a plaster type solution where the HUMS is wrapped around the wire insulation. This solution uses a flexible polymer for the substrate to enable it to be wrapped around the wire under test. The substrate is T-shaped with sensors lined up along the bar of the T. The stalk of the T has a zig-zag cut to the outer edges for wrapping around the wire and inserting through a machined hole in the polymer, enabling it to be securely closed without coming loose and/or chaffing the wire insulation. The proposed sensors to be included are a humidity sensor, accelerometer, temperature sensor and pressure sensor. As mentioned earlier in this thesis, humidity levels can severely impact the lifetime of the EWIS. Some areas will be more at risk than others, therefore monitoring humidity in the immediate area of the wire under test will determine if a greater

level of maintenance is required. This may be in the form of de-humidifying problem areas of the aircraft that are shown to suffer from greater levels of humidity changes. The temperature sensor is required for monitoring the temperature changes in the local environment. Such data can be correlated to the planes travel history and to assign a level of probability that the wire insulation has degraded to a certain extent. The accelerometer was included for monitoring the range of vibration that is present on the wire cable loom bundles. Levels of vibration present are thought to accelerate the crack propagation and chafing present in the wire insulation and also put stress in the metal interconnects. The vibration levels are strong enough to induce arcing in wires next to each other or in metallic sections of the aircraft structure. Further exploratory tests would be required to enable a correlation of vibration patterns and low level arcing signals before they progress into a higher level arcing failure. The pressure sensor was included for a number of reasons. Firstly, it enables the monitoring of the pressure in the local environment of the wiring and interconnect. This helps to predict the likelihood of arcs self-sustaining or self-extinguishing due to the pressure levels that are present. Secondly, the sensor can be used to calculate the partial pressure of the environment at a particular temperature. This helps verify the functionality of the humidity sensor, and allows additional features to be designed to help auto-calibrate the humidity sensor over time. Finally, if the humidity sensor were to fail, then it is possible to still make relative humidity measurements with just the pressure sensor and the temperature sensor. The final sensor to mention is a current sensor for detecting the arcing signals, which consists of high frequency waveforms that are estimated from the rise-time of the arc signal. To ensure an arcing event is captured, analysis of the rise-time and frequency spectra of the signal is performed. This will help avoid falsely identifying a fault in the present of an electrical motor switching. Further post processing of the acquired waveform using signal processing techniques such as wavelet analysis will enable detection of a true fault in the presence of background noise.

The second concept of the HUMS solution, presented in figure 3.7, shows a selection of sensors on a disk shaped substrate. This substrate could again be a flexible polymer substrate or also a Low Temperature Co-fired Ceramic (LTCC).

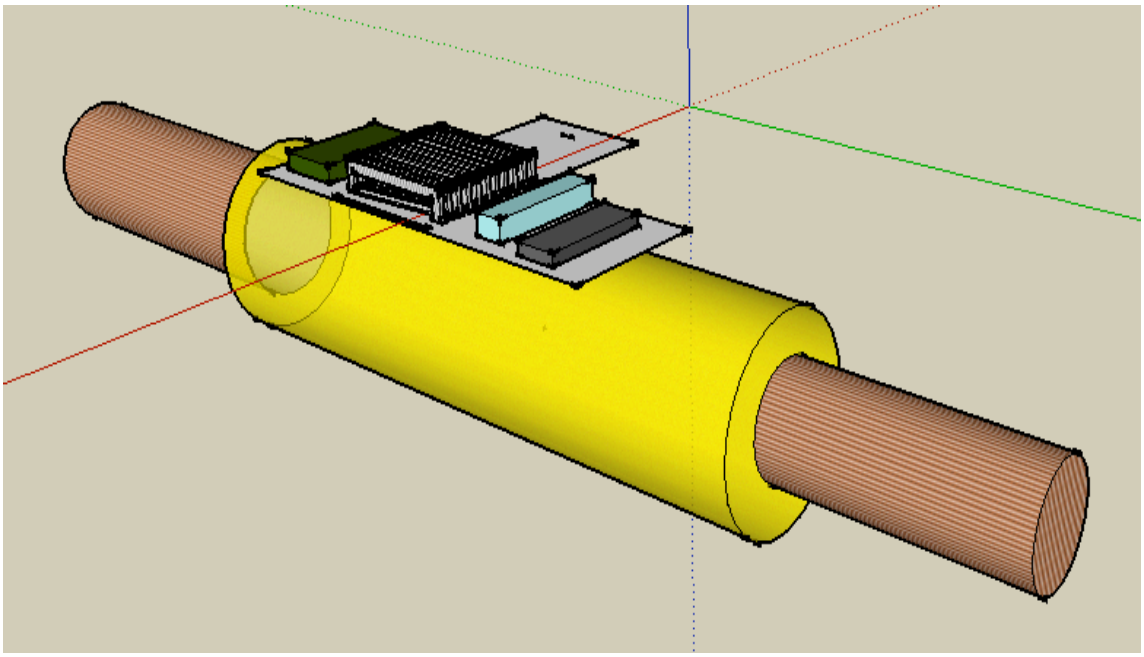

Figure 3.6 Concept 1 of HUMMS for EWIS.

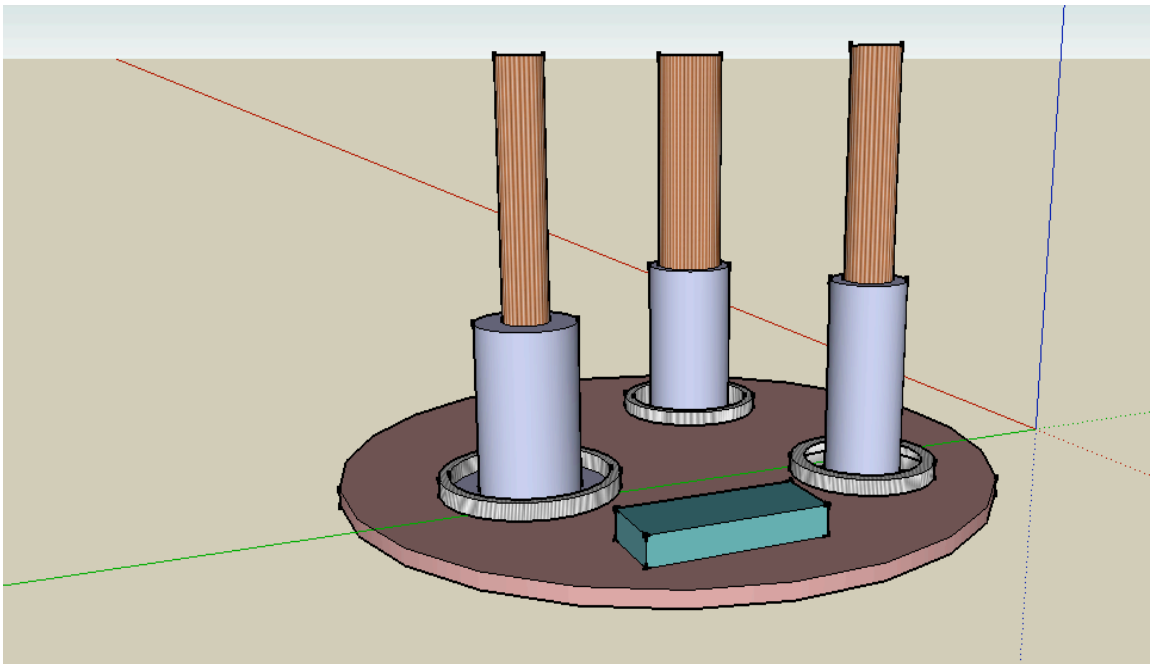

Figure 3.7 Concept 2 of HUMMS for EWIS

The sensor selection is the same for this case, but the solution also offers a number of additional benefits. These benefits are dependent on this solution being embedded within a smart connector, like that shown in [3.14]. Sensors would be located and sealed inside the smart connector used for connecting sections of wire bundles together. A humidity sensor would be used to ensure that the connector was properly connected to the mating surface of each wire bundle such that it sealed out the environment from ingressing inside the metal interconnects. The humidity sensor would therefore be used as a leak detector in addition to monitoring the level of moisture present in the connector after it had been opened after maintenance has been performed. As shown earlier, specific ranges of relative humidity are thought to accelerate the ageing process. Electronic failures are known to accelerate under this regime of humidity, therefore this would help calculate the remaining useful lifetime of operation. Accelerometers would be used to monitor vibration levels of the smart connector, which could be used to infer the likelihood of producing an arcing fault between the pins of a connector and also on the wire bundle. Additionally, this would also be used as an indicator that specific regions of wiring were not being supported at the ends.

A temperature sensor supports the calculation of relative humidity inside the connector along with the relative humidity sensor. Since a relative humidity sensor is being chosen for integration in the HUMS solution, temperature is required to enable the calculation of relative humidity. The temperature sensor can also be used to determine if there is onset of series arcing. At vibration levels that encourage contact fretting, there will be a gradual increase in the contact resistance depending on how bad the effect has grown. Temperature should also have an impact on this, therefore testing should examine this relationship with a wide temperature envelope that extends down to at least -40°C and as high as possible.

The accelerometer will again monitor the levels of vibration present on the wiring and interconnect. This can be compared to the other sensor data when the ingress of moisture inside the connector begins, and/or when arcing starts too occur. All of the data generated by these sensors can be stored and analysed further offline to see if there are patterns to the ageing and failure of the wiring and interconnect. The relative humidity sensors will need calibrated to operate to maximum accuracy despite extended periods of time in dry or wet

conditions. Such conditions can cause a greater long-term drift; this is subject to the chemistry of the polymer used as the moisture sensitive element.

Some of the sensors will be used to calculate the usage of the EWIS by monitoring the exposure of the wiring bundles to the key environmental parameters. This data is not limited to when the aircraft is in flight, but also the environmental data when grounded. To make such estimations will require testing of the wire bundles sections in conditions that replicate the environment that they are normally exposed to. This would involve doing some design of experiments to establish the mean life of the wiring and interconnect. For detection of arcing or partial discharges, another type of sensing arrangement is required in order to identify the occurrence and also the location on the wire bundle. This is examined in the following section.

3.6 Current sensing for high voltage applications

A technique called traveling wave fault detection is used to detect and locate faults on transmission lines in the high voltage industry. This technique has recently been applied to distribution lines [3.15]. When a fault occurs on a single section of transmission line, high frequency waves with fast rise times propagate away from the location of the fault in opposite directions. The waveforms are expressed in terms of the forward propagating (S_1) wave, backward propagating (S_2) wave and the characteristic impedance (Z_0) [3.10].

$$S_1 = v(x, t) + Z_0\, i(x, t)$$
$$S_2 = v(x, t) - Z_0\, i(x, t) \qquad \text{Eqn. 3.1}$$

Where v and i are the voltage and current at the time t and position x. The travelling waves will reach an impedance discontinuity such as an interconnect, bus bar or fault location; reflections and refractions will then occur, whose magnitude depends on the difference in impedance at the particular location. The size dependency of the signals generated at the discontinuities is given as the reflection and refraction coefficients. The distance to the fault location is calculated by measuring the time difference between the original fault signal at one end of the cable and the subsequent arrival of the reflected part of the signal. It is calculated as:

$$x = ((t2 - t1) \times u)/2 \qquad \text{Eqn. 3.2}$$

Where u is the velocity of propagation down the cable, t1 is the time for the signal to reach the sensor and t2 is the time for the reflected signal to reach the sensor. This method has shown good levels of success once data processing of the fault signal is performed to determine if the signal is a fault or a natural transient signal. Examples of natural transient signals are inrush currents from a motor switching on or off. Thus this method of identifying and locating faults can be extended to usage on aircraft wiring and interconnect systems.

In the presence of a noisy environment, there are more advanced signal processing methods such as wavelets, that can identify the features of a faulty signal while submerged below the noise margin. The selection of a current sensor for partial discharge detection will have an impact on the received signal and the classification of a partial discharge or normal switching transient signals. Current sensors are evaluated in the following section.

3.7 Current sensors for partial discharge detection

As current sensing is a viable method for detecting fast rise-time signals such as transients and partial discharge signals, a current sensor that satisfies all the requirements must be low cost, reliable, accurate and not require frequent calibration, in addition to being manufactured as part of a miniature sensing system that could be located in small hard to reach locations and impervious to harsh environments.

Table 3.1 Properties of current sensing technologies

Current sensing technology	Current shunt	Current Transformer	Hall Sensor	Rogowski coil
Cost	Very low	Medium	High	Low
Linearity	Very good	Fair	Poor	Very good
Power consumption	High	Low	Medium	Low
Saturation	No	Yes	Yes	No
Output variation with temperature	Medium	Low	High	Very low
DC Offset	Yes	No	Yes	No
Hysteresis	No	Yes	Yes	No

Firstly, recent current sensing technologies were reviewed to see if there was anything adaptable from a manufacturer. The main technologies outlined in Table 3.1 were current transformers, hall effect sensing and air-cored current transformers that are otherwise known as Rogowski sensors. The sensors need to be low cost to manufacture and have low consumption of energy. Sensor performance in terms of linearity, saturation, offset and hysteresis have an impact on the level of post processing of the signal and/or additional circuitry required in situ of the sensor to output a meaningful data signal. A desirable option is a sensor that operates passively and is immune from hysteresis and non-linearities across the bandwidth of operation.

3.7.1 Current transformers

Current transformers (CT) are used to measure alternating currents, and are used mostly in high voltage applications, as shown in figure 3.8. The CT is made up of a magnetic core, and one or two windings depending on the circuits operating current. The additional winding is used to step down the current to an acceptable level, as shown in the schematic of figure 3.9A. The magnetic core typically encompasses the wire (circuit) being tested. The arrangement will have a single turn on one side of the current transformer and an arrangement of multiple wire turns on the secondary coil, which is again wrapped around the magnetic core.

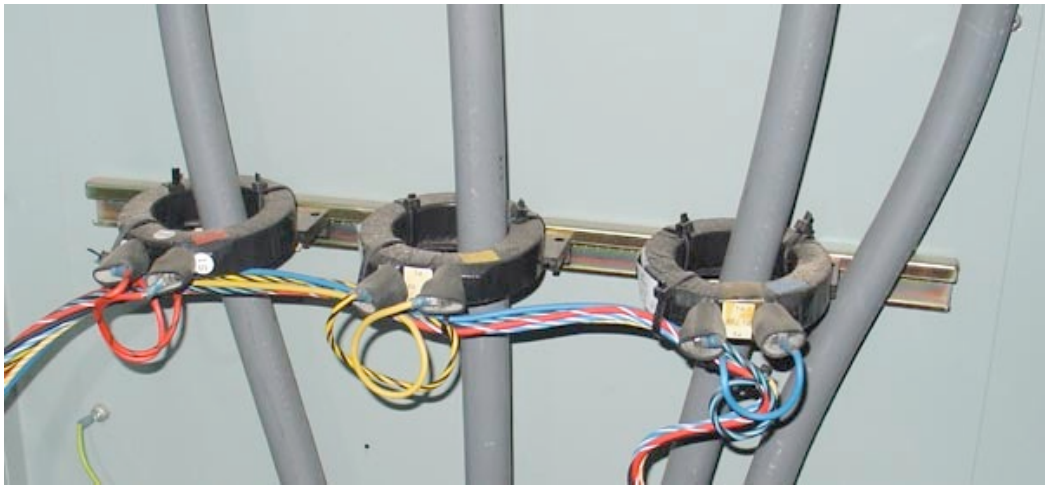

Figure 3.8 Example of a current transformer arrangement used for metering 3 phase 400A power supply.

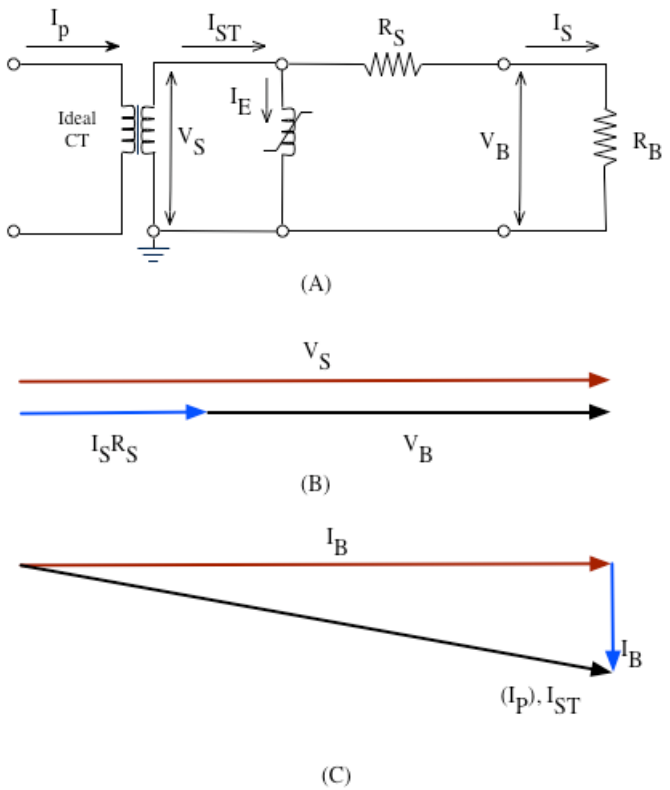

Figure 3.9 Schematic and vector diagram of current transformer [3.16].

(A) Vector diagram (B) Voltage phase diagram (C) Current phase diagram

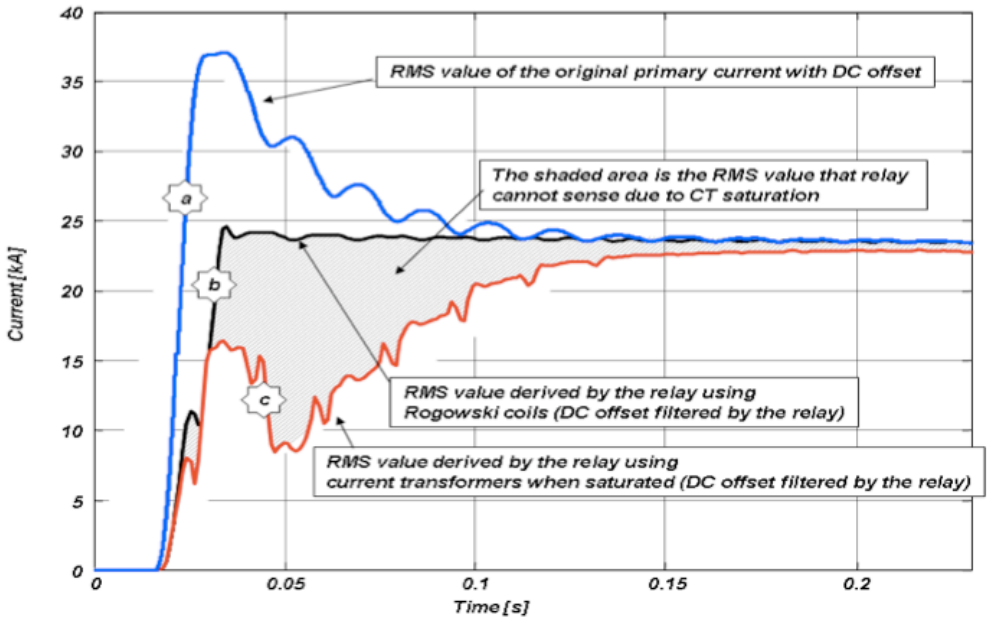

Figure 3.10 Comparison of output signals for the CT and Rogowski sensor [3.16].

The CT has a series resistance from the coil windings and a burden resistance, which is connected across the coil output where the sensor output is provided. The challenge of maintaining a reasonable level of coupling of the primary signal to the secondary coil winding is achieved through the incorporation of a magnetic core, which is shown for the ideal case in the same figure 3.9.

In [3.16], CTs are compared to other devices such as gapped CTs and Rogowski coils. One of the drawbacks of using a magnetic core is the core remanence. If the CT measures a fault current signal where the flux induced in the magnetic core is in the same direction as the remanent flux then this hinders the creation of magnetic flux in that direction [3.16]. This leads to a quicker time to saturation. If the fault current is in the opposite direction to the remanent flux then this results in an extension to the time to saturate. The impact of remanence is examined further in figures 3.9B and 3.9C, which show the voltage phasor diagram for the induced voltage in the CT is in phase with the output voltage that appears across the burden load resistance. For the current phasor diagram that is shown in figure 3.9C, the output current (I_S) that flows across the burden load resistance is not in phase with the primary current (I_P) or the current induced in the windings of the CT. The reason for this is that the current that is induced by the remanence (I_E) is 90° out of phase with the current flowing through the burden resistance (I_S). Removal of the remanence effect is achieved through saturating the CT secondary winding while the primary winding is left open. Other CT designs such as gapped current transformers have a gap in the magnetic core to reduce this remanent effect. The three waveforms in figure 3.10 represent the primary current (A), the current flowing through a Rogowski sensor (B) and the current flowing through the CT (C). The figure shows a grey shaded area for the CT that is the portion of the transient waveform that is lost due to the remanence of the magnetic core of the CT. This loss of waveform data leads to a reduced current value that, if faulty, would not trip the relay of the protection equipment. If this were a low level (low energy) arcing fault then this too would not be detected, allowing the carbonisation of the insulation to occur and further increases to the energy emitted from an arc fault signal. The signal processing for fault identification and location requires the information of rise-time and spectral content to be able to diagnose the fault signal and also to be able to discriminate from normal operating transient signals. Although the remanence can be reduced through periodic maintenance, this type of sensor would not be suitable for placing on an aircraft for

long periods of time to act as part of a HUMS system. What is required is a sensor that can detect the fast time transient signal without modifying the waveform itself.

3.8 Hall effect current sensors

Edwin Hall discovered this type of measurement in 1879 [3.17,3.18,3.19] during an experiment that investigated the impact of aligning a magnetic field perpendicularly to a thin rectangle shaped piece of thin gold. The measurement showed that this arrangement generated a difference in potential at the opposing edges. This difference in potential increases with the current that is generating the magnetic field across the sensor. The miniaturized version of this arrangement uses a thin layer of semiconducting material to detect this effect. As shown in figure 3.11A and in the absence of a magnetic field, the current distribution is uniform and no potential is generated across the output terminal. In the presence of a magnetic field, a Lorentz force is created that results in the disturbance of the current distribution of the material. This produces a change in potential across the output of the sensor due to the electron flow from the current being moved due to the Lorentz force, resulting in one side being more charged than the other. The output is amplified allowing a gain compensated output that is proportional to the current being measured from the magnetic field. The direction of voltage flow depends on the type of majority current carriers (n- or p-type) for semiconductor versions of Hall effect sensors [3.17-3.19]. The voltages produced at the edge of the semiconducting material will be positive for one type and negative for the other type. Hall sensors are used in detection of position or displacement of objects [3.19].

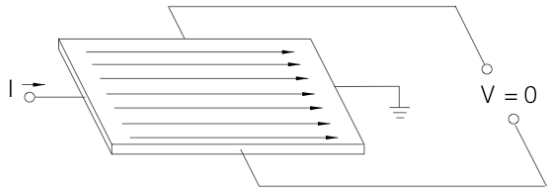

Figure 3.11A: Hall effect sensor. No magnetic field present.

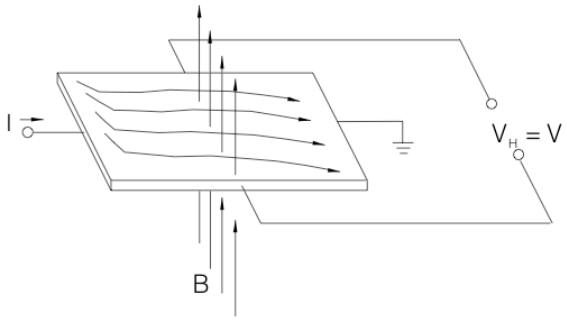

Figure 3.11B: Hall effect sensor with magnetic field present. [3.17]

Figure 3.11 Hall effect current sensor

These sensors are used as proximity sensors and also to sense the position of pistons and angles of throttle in the automobile industry [3.20]. Some Hall effects do not produce a great enough magnetic field unless it is positioned inside a slotted magnetic torroid [3.17]. The magnetic core focuses the magnetic field within the core material, resulting in the field being focused perpendicularly onto the face of the semiconducting thin film. The voltage output of Hall sensors is known to be sensitive to temperature and pressure [3.18], therefore compensation is usually provided with on-board electronic circuitry. In addition to this there is also a null offset to be calibrated out of the measurements. The null offset is the voltage output that is present even when there is no magnetic field present. This arises from manufacturing and material variations in terms of dimensions of elements used in the sensor. Some manufacturers overcome this by injecting an additional current to remove this. Other manufacturers use two Hall sensing elements in parallel and with opposing bias currents.

Closed loop Hall sensors use a similar setup as shown in figure 3.12, except that the magnetic core has multiple wire turns placed around it. The magnetic flux created in the Hall sensor element is amplified then used to drive an additional secondary current through these coil windings to oppose the original current. This enables a wider frequency range, improved accuracy, low temperature drift and excellent linearity. Other benefits of this type of sensor are that it is insensitive to environmental parameters such as humidity, dust and vibration.

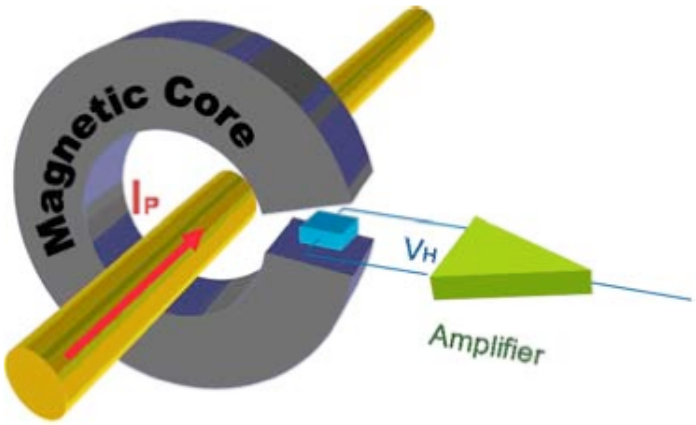

Figure 3.12 Current measurement using a Hall-effect current sensor

The drawbacks of this type of sensor is that a magnetic core is required to be placed around the wire to be tested, which adds weight and cost to a complete HUMS system located in multiple locations throughout the aircraft.Finally, although enhanced frequency ranges are reported, the typical operating bandwidth is reported to be 100 KHz in [3.17] and up to 1 MHz in [3.18]. This frequency range is not high enough for looking at the frequency content of PD or arcing fault type signals; therefore it will not be considered in this scope of work.

3.8.1 Rogowski coil

The Rogowski coil is an example of an inductive pickup coil that consists of a helical coil uniformly wound around a torroidal ring structure [3.22-3.25]. The operating principle of this sensor was first presented by Chattock in 1887 [27], although its common name as ”Rogowski Coil’ resulted from the description given by Rogowski and Steinhaus in 1912 [3.28] when they were evaluated for measuring magnetic fields. It is also known as a Chattock coil or Rogowski-Chattock potentiometer, RCP. At this time, Rogowski sensors could not be used for current measurements since the coil output voltage was insufficient to drive measuring equipment [3.29-3.31]. Instead, current transformers were traditionally favoured is this role due to their ability to provide the required high output voltage to drive the electromechanical equipment used for protective relaying functions.

Figure 3.13A: PEMUK split-core Rogowski sensor.

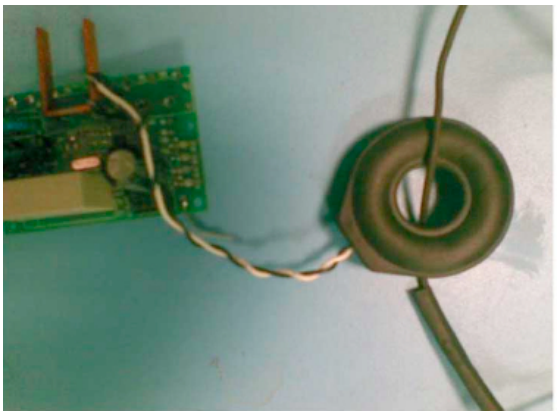

Figure 3.13B: Rogowski sensor by ST Microelectronics.

Figure 3.13 Commercial Rogowski sensors

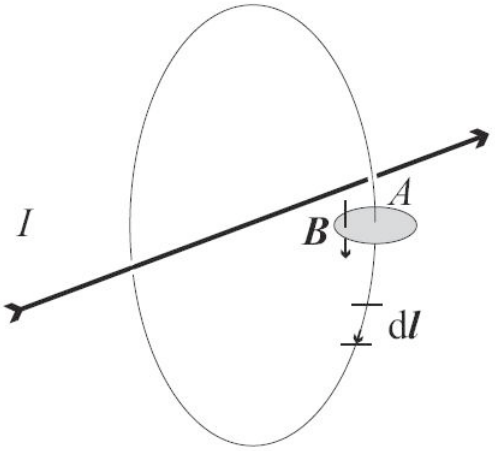

Figure 3.14A: A magnetic field line encircling a current carrying wire [3.32].

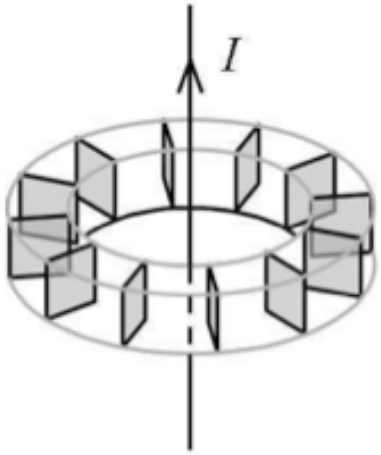

Figure 3.14B: Closed surface loop of each coil turn [3.33].

Figure 3.14 Ampere's Law around a current carrying wire

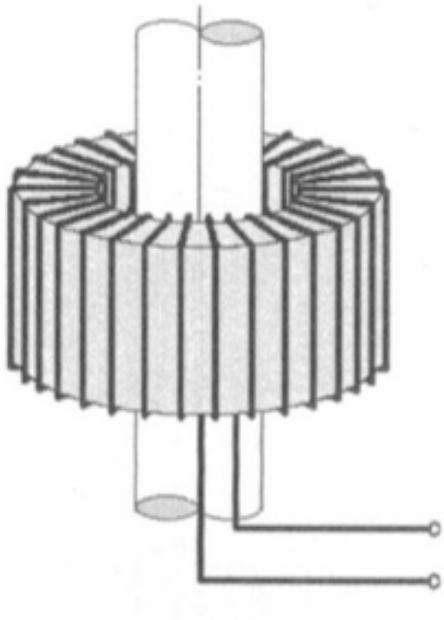

Figure 3.15A: WUT passing through torroidal Rogowski coil [3.38].

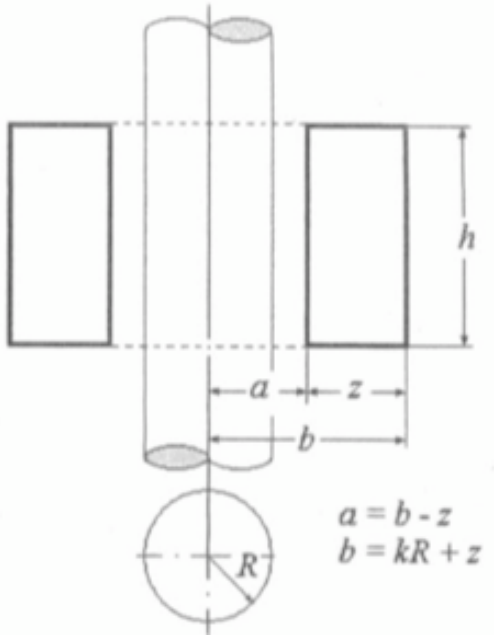

Figure 3.15B: The cross sectional area of each coil turn that cuts the magnetic field density [3.38].

Figure 3.15 The relationship between Rogowski coil construction and WUT.

Conventional Rogowski sensors such as those by PEMUK or ST Microelectronics (figure 3.13) have a large separation from the wire being tested to the coil turns of the Rogowski sensor.

$$\oint H.dL = I_{enclosed} \qquad \text{Eqn. 3.3}$$

This equation shows that the closed loop integral of the magnetic field intensity is equal to the current enclosed, where *dL* is the line element or small segment of the closed line integral around the loop. The equation can be rewritten to show the impact of the radial distance from the wire centre as a function of the magnetic field generated by the wire. This relationship is shown in equation 3.4, which shows that the magnitude of the magnetic field detected is inversely proportional to the distance, *r*, away from the wire under test (WUT).

$$H_{\Phi} = \frac{I}{2\pi r}\left(A/m\right) \qquad \text{Eqn. 3.4}$$

The magnetic field detected by a Rogowski sensor depends how close the sensor can be placed to the wire. As the radial distance from the wire centre increases, the magnitude of the magnetic field decreases [3.36]. This is further clarified in figures 3.15A and 3.15B, which shows how a Rogowski sensor is positioned around the wire under test (WUT). In these figures, the Rogowski sensor is centred with respect to the midpoint of the wire under test. If the Rogowski sensor is not centred then this contributes a measurement error, which is discussed further in [3.37].

The effective closed loop area of each coil turn of the Rogowski sensor is shown in figure 3.15B. It describes a coil turn by the height of the turn (h), the width of the coil turn (z), and the radial distance between the inner coil turn and the radius of the wire (a – R). As equation 3.4 points out, the magnetic field decreases radially outward from the wire. From figures 3.15A and 3.15B, the magnetic field is at a maximum in position R and decreases slightly to the inside of the coil (a); beyond this point the field decreases further to the outer edge of the coil turn (b) and beyond. This presents a conundrum for manufacturers of

Rogowski sensors, as they have to provide a range of sizes of the height (H) of the sensor, the width (z), inner diameter (2a) and the outer diameter (2b) suited to a range of applications having different sizes of wire diameter and accessibility.

If the wrong sensor size is chosen relative to the WUT, then inner diameter (a) could be large enough that it only detects weaker levels of the magnetic field. In terms of aircraft wiring, the best selection of sensor would have the inner diameter as small as possible so that it could pick up a larger overall magnetic field.

In addition to the magnetic field intensity (H), there is also the magnetic field density, B which takes into account the impact of material choice on the magnitude of the field. The magnetic field intensity is adjusted by a factor known as the permeability of free space, μ_0, as shown in equation 3.5.

$$B_{\Phi} = \frac{\mu_0 I}{2\pi r} \left(A/m\right) \qquad \text{Eqn. 3.5}$$

The reason that μ_0 is chosen is that the coil turns of the Rogowski sensor are positioned around an air filled core. For a current transformer, the coil windings are wrapped around a magnetic core then μ_0 would be multiplied by the permeability, μ_r, of the material under question. Despite sharing similar geometrical designs and construction, the current transformer has a higher output signal but suffers from distorted output signals if the signal has high frequency components. In contrast, the Rogowski sensor has a lower output signal yet reproduces the output signal with better fidelity due to possessing none of the high frequency saturation of the core magnetic material [3.16].

If the wire in figure 3.14A is turned so that it is pointing upward like figure 3.14B, the area cut by the magnetic field density field lines in 3.14A lie in the same plane as the closed surface loop of each coil turn in 3.14B. This shows that the magnetic field density from the wire couples to each coil turn of the Rogowski sensor. If the magnetic field enters and leaves the surface of each coil turn in the normal direction, then this will generate the maximum output signal for the closed loop on the condition that the current flowing down

the wire is changing with respect to time [3.35].

Faraday's law states that a changing magnetic field through a closed loop surface [3.35,3.39], such as a coil turn of the Rogowski sensor, produces a voltage at the terminals of the closed loop such that

$$V = \oint E \cdot dL = -\iint \frac{\partial B}{\partial t} \cdot ds = -\frac{d\psi}{dt} \quad \text{(V)} \qquad \text{Eqn. 3.6}$$

Where E is the electric field around each loop. The magnetic flux, ψ, is the product of magnetic field density, B, and the area it penetrates, A, such that:

$$\psi = \iint_s B \cdot ds \qquad \text{Eqn. 3.7}$$

The voltage output of each coil is related to the magnetic flux that passes through each coil turn. This aspect of Faradays Law is known as the transformer induction equation [3.39]. There is a 1:N coupling of the magnetic field from a 1-turn coil (WUT) to an N turn coil which is the Rogowski sensor. Any increase or decrease of the coil turns number of the sensor results in an increase/decrease of the voltage output of the sensor. Similarly if the magnetic field changes quickly then the output of the sensor increases. This concept is derived in the following equations. If equations 3.6 and 3.7 are applied to the models shown in figures 3.16 and 3.17, then we can derive the magnetic flux in each coil turn based on the key parameters of the Rogowski sensor. This is shown in equations 3.8.

$$\psi = \int_o^l \int_b^c \frac{\mu_0 I}{2\pi r}\, dr\, dl = \frac{\mu_0 I}{2\pi} \int_o^l dl \int_b^c \frac{1}{r}\, dr = \frac{\mu_0 I l}{2\pi}\, \ell n\left(\frac{c}{b}\right) \qquad \text{Eqn. 3.8}$$

The total magnetic flux around all the coil turns is calculated by summing all the magnetic fluxes of the Rogowski sensor [3.32], which provides the magnetic flux linkage, Λ :

$$\Lambda = N\psi = \frac{\mu_0 N I l}{2\pi} \ell n\left(\frac{c}{b}\right) \qquad \text{Eqn. 3.9}$$

Dividing equation 4.9 by the current, I, flowing through the WUT provides the mutual

inductance between the whole Rogowski sensor and the wire under test. The voltage output of the sensor is the mutual inductance between the sensor and WUT multiplied by the time rate of change of the current flowing through the wire under test [3.23,3.24,3.26,3.31,3.36,3.40,3.41]:

$$V_{SENSOR} = \frac{\mu_0 Nl}{2\pi} \ell n\left(\frac{c}{b}\right) \cdot \frac{di}{dt} = M \cdot \frac{di}{dt} \qquad \text{Eqn. 3.10}$$

At low frequencies, the output of the Rogowski coil is low. However, partial discharge signals possess a fast rise time that results in significant high frequency content [3.40], which is better reproduced than other types of current sensors. The magnetic field can be further amplified in the sensor by increasing the amount of coil turns. This would be like forming a number of loops around the wire shown in figure 3.14 and 3.15. For maximum amplification, the coil turns must be aligned normal to the flow of the magnetic field lines.

With advances in recent years in microprocessor based protection and measuring equipment, industry has started to view Rogowski coils as a sensible alternative to current transformer based protection and diagnostic equipment [3.29, 3.31, 3.42]. In [3.29, 3.31] the authors present Rogowski coils that incorporate multifunction relays and fibre-optic communications. This in turn provides faster responses times to faults, with the added benefit of being adaptable to changes in the load or power system configurations. Two PCB Rogowski coils are presented in their work, which consist of a torroidal design constructed with two PCBs. This was achieved through a series of conductive traces mapped across both sides of a ring shaped PCB, as shown in figure 3.16. Electrical interconnections to the traces at each side of the PCB were achieved by conductive electroplated holes, known as vias. This innovative approach brings the benefit of more accurately being able to wind the coil turns, hereby resulting in higher precision and less measurement error [3.30, 3.34]. A 3D PCB Rogowski sensor is presented in figure 3.17. The 3D design is achieved by inserting a number of small Printed Circuit Boards (PCB) that have a series of planar coil turns into a larger circular PCB. This overcomes the non-uniformity of coil turns that is experienced with conventional wire wound devices. In addition to this, the conductor can be centered inside the sensor and the manufacturing costs are lower.

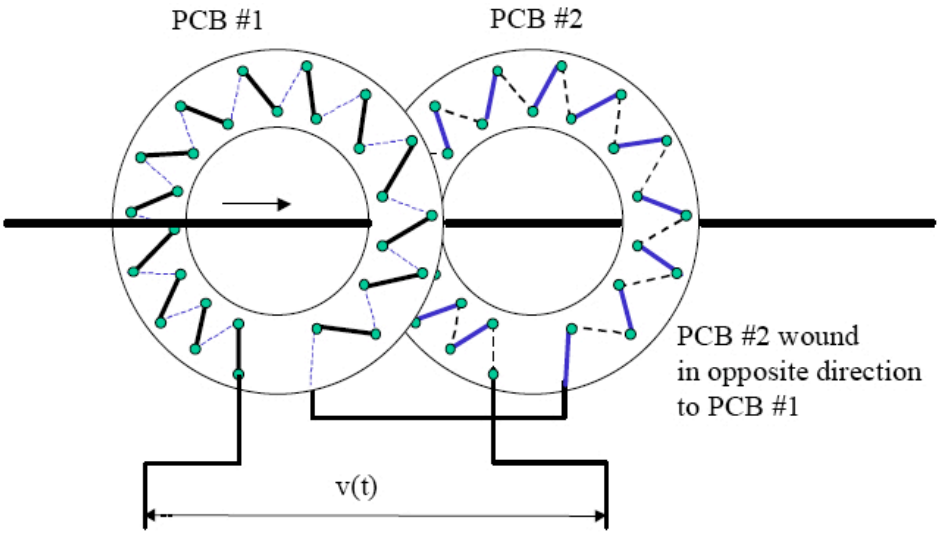

Figure 3.16 PCB Rogowski coil [3.30].

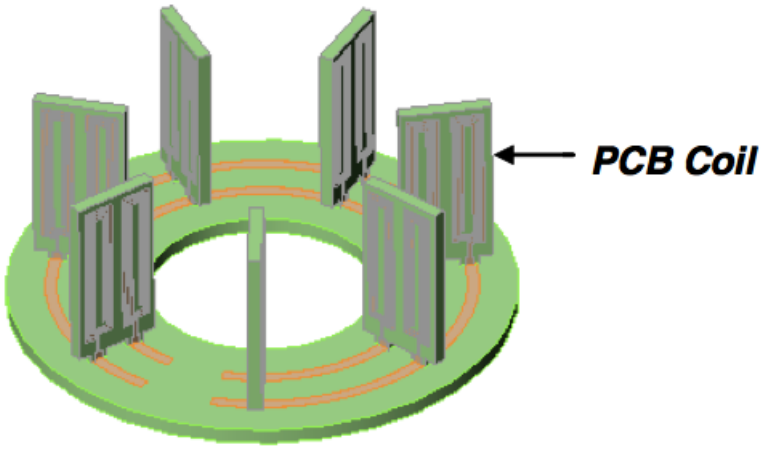

Figure 3.17 3D PCB Rogowski sensors with planar sub-sections.

As Rogowski coils do not saturate, this allows fault current threshold levels of the sensor to be set to higher limits. In figure 3.10, a comparison is shown between the Rogowski sensor and CT. It shows that the CT does not detect the higher current level, resulting in the relay not triggering. This benefits the protection equipment as it reduces the amount of stress it would have to withstand if a current transformer were to be used. This means less costly reactive maintenance as a consequence to being able to deal with the failure mode earlier in its operating lifetime. The PD signals that are to be detected by Rogowski coil sensors have a very steep wave front and a short duration. The rise time of the discharge pulse is a few nano-seconds, and its duration is in the order of tens of nano-seconds. This fast rise time means that the signal has a wide frequency spectrum of up to several hundreds of MHz [3.43]. Cheng et al [3.45] analysed the energy in a PD signal after ageing has occurred in power cables. The bandwidth of such PD signals were in the range of 3 to 15 MHz, suggesting that the bandwidth of the Rogowski sensor must be high enough to detect PD signals with up to 15 MHz frequency content. Li et al [3.46] designed the Rogowski coil magnetic sensor for the PD monitoring of XLPE cables from 1 to 60 MHz. Robles et al [3.36] made a Rogowski sensor manually using wire and a core to wrap it around. The ends of the coil turns were connected across a resistance to self-integrate the signal measured at the output of the sensor, which is the time rate of change of current. The author examined the relationship between the parameters of the Rogowski coil and its ability to detect partial discharge signals. They examined the impact of varying the inductance, capacitance and resistance of the Rogowski sensor. The results showed that they had an impact on the frequency response, as these parameters define the second order behaviour of the Rogowski sensor. The resistance affects the amount of damping, and the inductance and capacitance affect the frequency range where the sensor self-integrates. This condition allows the sensor to accurately reproduce the input signal because the Rogowski sensor differentiates it without the self-integrating resistance being connected across the output terminals. Increasing the Inductance increases the bandwidth by moving the low frequency pole further to the left. In contrast, increasing the capacitance moves the high frequency pole further to the right. The trade-off with such increases is that the sensitivity decreases as the bandwidth increases.

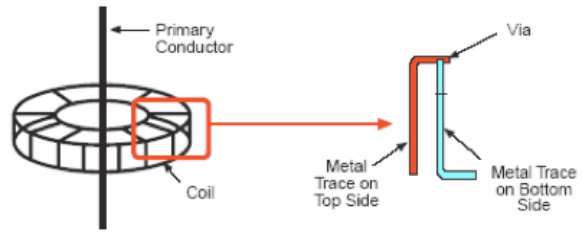

Figure 3.18A: Comparison of conventional Rogowski sensor and the proposed flexible Rogowski [3.43].

Figure 3.18B: Rogowski sensor layout on flexible substrate [3.43].

Figure 3.18 Comparison of conventional Rogowski sensor and Rogowski sensor on flexible substrate.

Companies such as GE [3.43] have manufactured and tested a flexible Rogowski sensor on thin polyimide substrates called Uniplex. The sensor is different to conventionally made devices as this version can be wrapped around a WUT instead of having to disconnect the wire bundle. The flexible sensor demonstrated the potential for detecting partial discharge signals on aircraft wiring. The metal traces (windings) for the coil arrangement were created through a subtractive etching process on copper covered polyimide sheets that were 127 µm thick. The traces were 25 µm in width with 25 µm spacing between the traces. The etched copper traces were connected on each side of the polyimide by laser drilling holes in the polyimide at the end points of each trace. Electrical connection between the traces is achieved by plating inside the etched via as shown in figure 3.18. Interestingly, GE called the sensor a Rogowski sensor even in the presence of a magnetic film deposited on the polymer substrate. This magnetic film was a soft Nanocrystalline material that consisted of around 73 % ferrous alloy. The magnetic material had an impact on the flat frequency response of the sensor output.

An innovative aspect of this thesis is that much smaller, lighter and cheaper sensors with higher sensitivity have been produced that use electrical conductors of smaller width than GE have reported.

3.9 Signal Processing for fault detection and location

Signal processing in this work relates to the post-processing of the current sensor output for diagnosis of a faulty signal and its location along the wire bundle. The current sensor must

capture the signal with a high amount of fidelity so that signal analysis can be performed with conclusions made with a high level of confidence. Making decisions based on statistical analysis of the data in both the short term and long term requires robust system design, in order that false positives and false negatives be avoided, which requires measurements to be repeatable and subjected to minimum levels of drift over time. Detection of arc faults is made more difficult in practical applications due to the signal being small in size and located within the noise floor of the system [3.48]. Additionally, there will be interference from other sources of transient signals present as a result of periodic switching of other devices or power sources. Switching of these types of systems produce fast rise time transient signals. Being able to separate these waveforms from faulty signals is essential to minimise the number of false fault warnings. This is a similar challenge that is being addressed by the high voltage industry when testing transmission lines and apparatus for arc faults or precursors to this type of failure. Earlier methods used to detect small amplitude signals in the noise floor were focused on having prior knowledge of the noise levels expected, such as the characteristics of a thyristor firing.

Conventional digital PD pulse detection is based on research in [3.49, 3.50]. Information was collected relating to PD signal amplitude and phase versus the number of PD pulse occurrences, with information provided in 3D plots. The stochastic analysis of PD pulse height and phase is discussed in [3.51,3.52] for diagnostic purposes. Other information such as pulse rise-time and the associated frequency content of these signals will help in the separation, identification and location of PD sources [3.49]. A measurement system that allows the digital acquisition of partial discharge signals (PD) was proposed by [3.49]. The separation of signals to allow correct identification of faulty transients from non-faulty transients used a fuzzy classifier; the classification of the signals was achieved through measuring information such as the PD pulse height and phase. The PD signals are gathered by sampling the signal at a high enough sampling rate to avoid high frequency aliasing and with a sufficient amount of PD pulses gathered to allow the stochastic analysis. Sampling rates of up to 4 Giga-samples per second GS/s were used for the signal acquisition, and the time and frequency context of each PD pulse were analysed with the fuzzy classifier. Fuzzy systems require an element of learning and require a high amount of computation, so they can be slow. In real world applications this may be an issue unless testing has been carried out previously. Large computational requirements would hinder this type of solution being

used while the aircraft was in flight.

A signal possessing a specific rise-time will have a range of frequency components when viewed using a Fourier transform. The faster the rise-time the greater the amount of higher frequency spectra that will be present when viewed in the frequency domain. The problem with using this type of signal processing is that while it can express a waveform in terms of constituent waveforms of specific frequency, it cannot tell us when they occurred in the time domain. The Fourier Transform has only frequency resolution and no time resolution. Multi-resolution time frequency analysis techniques have shown that small magnitude fault signals can be extracted in the presence of noise and other data signals. This technique has also been utilized for identifying non-standard behaviour in signals to monitor patient epileptic EEG signals. The signals are spikes in the waveform taken from normal brain signals [3.47]. Time-frequency signal processing techniques therefore provide frequency resolution and time information, which enable the reconstruction of the signal after these techniques have been applied.
Work by Ma et al [3.53,3.54] focused further on the implementation of wavelets for PD recognition. This work focused on the separation of noise from PD signals, which was successfully demonstrated. Shim [3.55,3.56] used wavelets to improve the ability to detect and locate PD signals in shielded distribution cables. Of major interest to this research is the work done by Tian, which looked at the application of the Wavelet Transform (WT) to de-noise signals that were being detected on a cable joint using a High Frequency Current Transformer (HFCT).

The definition of a wavelet transform, is a waveform of limited duration [3.48], that when averaged is equal to zero. The WT breaks up a signal in the time domain to a scale version of the time domain waveform in terms of a set of time shifted and scaled versions of the original waveform. The Fourier Transform can break up a time domain signal into a set of sinusoidal waves with different frequencies, though the downside is that the original time information of the signal is lost. This means that the Fourier Transform may be able to detect a PD signal but cannot determine when in time this fault may have occurred. The WT can however recover the original information of the signal after the wavelet transform has been performed. Wavelets come in two types, which are Continuous Wavelet Transform (CWT) and Discrete Wavelet Transform (DWT). The CWT is computationally

more expensive and generates more redundant data. The DWT overcomes these issues and is created by analyzing the signal at different frequency groups through digitally filtering the signal. This is performed by passing the waveform data through a series of high pass and low pass Quadrature Mirror Filters (QMF) to resolve the data into high frequency and low frequency groups. After this, the data is then sub-sampled. Error free reconstruction of the waveform can be done at a later time.

This method of feature extraction has now been extended beyond high voltage applications to partial discharge monitoring in aircraft wiring and interconnect in [3.58-3.60]. The work showed that the signals could be analysed using the wavelet transform. The choice of wavelet determines the scaling functions used for chopping up the waveform into low scale and high scale frequency groups. The low frequency aspect of the analysis is suited to detecting rapidly changing details such as the high frequency content. This provides the details of the waveform that would be used for analysing fast rising signals and establishing whether the occurrence was natural to the performance of the system or whether it occurred more by chance and required further investigation. The high scale aspect looks at the slowly changing and coarse features of a waveform that are attributed to the low frequency components of the waveform. In [3.58, 3.59] the authors concluded that the discrete wavelet transform could detect low-level damage arcing and also find the fault location. The continuous wavelet is computationally more expensive, and can only find the fault location.

3.10 Conclusions.

This chapter introduced the motivation of BCF Designs Ltd. for funding research into the design and manufacture of a miniaturised test system that enables the usage monitoring and remaining life of EWIS belonging to legacy aircraft in addition to fault identification and location. A review of current test solutions in the wider aircraft arena was then performed, which identified test solutions employed on aircraft in response to failures of mission critical components earlier than the expected life envelope. The response to this crisis was the deployment of health and usage monitoring systems (HUMS) in key areas of the

helicopter that impacted its ability to safely remain airborne. Such a system monitored parameters such as vibration levels in the gearbox as an indication that the component was at a compromised stage in its product life cycle and now required to be overhauled. This system could be used as part of a condition-monitoring program that enabled the deployment of carrying out servicing of these parts according to its actual usage instead of across time based intervals, saving costs according to the perceived usage of each helicopter.

The HUMS concept was applied to the challenge faced with monitoring EWIS in that the ageing and failure mechanisms of such systems occurred at different rates. The rates for the insulation is related to factors such as humidity and temperature due to this accelerating the rate of deterioration of the insulation such that it changed from being a flexible and compliant material to now become highly brittle and cracking. Other environmental parameters such as pressure and vibration impact the level of severity of such failures of the insulation. Vibration on the aircraft bundle can promote arcing of the wiring, which can initiate a sequence of small discharges that manifest into a high-energy flashover that can cross wire bundles and influence other mission critical systems. These micro discharges are challenging to detect and locate in a noisy environment. A similar issue is presented for the metallic interconnect. Stress relaxation over time and usage can allow the connectors to make and break electrical contact according to the level of vibration. This leads to localised levels of temperature increases over time that can promote series arcing. A connector assembly that is not fully closed will allow the ingress of humidity and salt water that promote and accelerate corrosion at specific ranges of relative humidity.

Development of a miniaturised solution that can monitor for lifetime usage and fault monitoring can be realized through the integration and assembly of a selection of smart sensors onto a common electronic package. Such sensors can have their analog output digitized and processed to deliver highly accurate and reliable output signals that can be used for necessary prognostic decision-making that enables a picture of the remaining lifetime to be monitored. Such a system would be known as a Health and Usage Monitoring Micro-System (HUMMS) that could be integrated into the connector assembly and also on specific points of the wire cable bundle in areas that are known problem zones and/or difficult and costly to access on a time based maintenance interval. The output of such

sensors could be communicated wirelessly to a central node that is capable of transmitting from the main communications system of the aircraft to ground based maintenance personnel for further decision making. One challenge still to be addressed is certifying wireless communication systems by the Federal Aviation Authority (FAA). This will focus on resolving a number of factors such as the allocated frequency range, RF power and electromagnetic interference. At present there is no specified radio spectrum provided for wireless systems on aircraft. The amount of data generated by clusters of sensors would require careful management to avoid network congestion and poor channel performance. Although there are protocols such as IEEE 802.15.4 and IEEE802.11 for limiting energy consumption and computational resources of wireless sensors, there are not yet protocols available that focus on communication delay or communication dropouts.
The drive for wireless sensor systems in aircraft is favoured due to system redundancy, weight saving and fuel reductions as well as maintenance costs. This should help maintain focus on implementing such systems for key areas of the aircraft where there is a strong benefit and low risk.

The sensor selection would involve integration of a polymer capacitive relative humidity sensor, temperature sensor, pressure sensor, accelerometer and current sensor. All measurands apart from the current sensor can be used to estimate the remaining lifetime of the EWIS, whereas the current sensor would be used for identifying the fast rise time transients that are indicative of fault like (arcing) behaviour.

The challenge of monitoring arc faults on aircraft in situ where the cables are carrying data or load signals mean that small level arcing is likely to be hidden in the electrical noise floor. Specific signal processing using wavelets would be needed to extract the signal features from the noise floor. Due to the signals possessing high bandwidth as a consequence of the fast rise time that is characteristic of arc fault signals, the current sensor needs to possess a high bandwidth that extends far into the MHz region. If the sensor is being used for the cable loom then being able to wrap this around the wire without pulling at the cable loom or disconnecting the interconnect is desirable in order to avoid introducing stresses that are sufficient enough to induce further cracks or breaks in the insulation. Size and weight are a key parameter to focus on in sensor selection. Lots of these sensors are required across wiring that stretches all over the aircraft. Weight is

therefore a consideration for our sensor. After evaluating the current sensors on offer in the market place, it was found that there was nothing available that met all the needs. Although commercial Rogowski coils and current transformers met the signal bandwidth criteria, the weight, size and cost of these parts would be too prohibitive. The GE sensor is not yet available to buy due to it being a prototype development stage. In addition, it still possesses too large a footprint to be considered for use in fault monitoring of aircraft wiring. Current transformers could easily saturate, leading to loss of fidelity in the high frequency region, meaning that it can impact the response time of circuit breakers to respond to a fault condition. In addition, there could be an opportunity for a current transformer to fail to identify such a condition had occurred due to the signal not being picked up by the current transformer. The current transformer would require additional electronics to cope with offset drift induced from the magnetic material and any DC component that may be present on some wires. The Rogowski coil possesses a better bandwidth yet provides an output that is smaller than the current transformer. However, the positional error of conventional sensors is a result of generic sensor types being used on small wire diameters. If the wire is not centred within the Rogowski sensor then an error is present. The Rogowski sensor output may be analysed using the wavelet transform to detect the sharp features of the transient signal in the presence of noise and also identify the fault location. The post-signal processing is not carried out in this thesis. Handling the large amount of data generated from multiple sensors and their high bandwidth is another challenge that would need addressed. Some form of data compression would be required before transmitting in order to consume low energy and limit the channel congestion. Powering of such systems could be performed through a combination of energy scavenging systems and battery technology. This would need further input from the FAA to use such technologies in flight on an aircraft. The design, modeling, manufacturing and testing of the sensor is investigated in the main body of the thesis.

References

[3.1] K.R. Wheeler, D. A. Timucin and I.X. Twombly et al. "Aging Aircraft Wiring Fault Detection Survey", *Unpublished Technical Report*, June 2007.

http://ti.arc.nasa.gov/m/profile/kwheeler/papers/wirefaultsurvey.pdf

[3.2] S.R. Schuet, D.A. Timucin and K.R. Wheeler. "Shielded-twisted-pair cable model for chafe fault detection via time-domain reflectometry". NASA Technical Report NASA/TM-2012-216001, National Aeronautics and Space Administration, March 2012.

[3.3] S. Schuet, K. Wheeler and D. Timucin et al. "Model based Inference for Wire Chafe Diagnostics". Ageing Aircraft Conference 2009.

[3.4] D. Timucin, S. Schuet, K. Wheeler, "Electrical Wire Chafe Fault Detection Analysis," Aircraft Airworthiness and Sustainment Conference, Austin TX, May 10-13, 2010.

[3.5] S. Schuet, D. Timucin, K. Wheeler, "Modeling and Detecting Wire Faults," NASA Aviation Safety Program Annual Technical Meeting, St. Louis MO, May 10-12, 2011.

[3.6] J. WIIG, **"**Optimization of Fault Diagnosis in Helicopter Health and Usage Monitoring Systems. PhD Thesis, 2006.

[3.7] R. Heine, "Role of on-board sensors in remaining life prognostic algorithm development for selected assemblies as an input to a health and usage monitoring system for military ground vehicles". PhD Thesis, 2008.

[3.8] J.E. Land. "HUMS – The Benefits: Past, present and future". IEEE Proceedings of Aerospace Conference, Vol. 6, pp. 3083 – 3094, 2001.

[3.9] S. Neylon, A. Richardson and H. Van Heeren. "Expert workshops in Microsystems for Structural Health Monitoring", 2008 Nexus Report.

[3.10] L. A. Roe A. Silano D.P. Maynard S. Tung, S. R. Witherspoon and N. Ferraro. "A MEMS-based flexible sensor and actuator system for space inflatable structures". In Smart Mater. Struct., volume 10, pp. 1230 – 1239. Institute of Physics Publishing, 2008.

[3.11] N.V. Kirianki, S.Y. Yurish and N.O. Shpak et al. "Data Acquisition & Signal Processing for Smart Sensors", Chapter 1, 2002. Wiley Publications.

[3.12] S.Y. Yurish and M.T.S.R. Gomes. "Smart Sensors and MEMS". Feb. 2005.

[3.13] B.F. Spencer, M.E. Ruiz-Sandoval and N. Kurata. “Smart sensing technology: Opportunities and Challenges”, 2004.

[3.14] C. Furse and P. Smith. “ASIC implementation of live arc fault SSTDR tester”, *Ageing Aircraft Conference*, April 21-24, 2008.

[3.15] B. Hayes-Gill Y. Zhu E.T.Pereira D. Coggins, D. Thomas and S.H.L. Cabral. “Initial experiences with a new FPGA based traveling wave fault recorder installed on a MV distribution network”, In Joint International Conference on Power System technology and IEEE Power India Conference 2008, pp. 1– 8, 2008.

[3.16] L.A. Kojovic. “Comparative Performance Characteristics of Current Transformers and Rogowski Coils used for Protective Relaying Purposes”, IEEE Power Engineering Society General Meeting, 2007. Pp. 1 – 6.

[3.17] “Hall Effect Sensing and Application”, Honeywell Microswitch Sensing and Control, product application notes.

http://serge77.rocketworkshop.net/hall/hallbook.pdf

[3.18] R. Pallas-Areny and J.G. Webster. “Sensors and Signal Conditioning’, 2nd Ed., Wiley-Interscience, Nov. 2000.

[3.19] J. Fraden. “Handbook of Modern Sensors: Physics, Designs and Applications”. Third Edition, Springer Publications.

[3.20] J. Wilson. “Sensor Technology Handbook”. Newes publications.

[3.21] B. Hayes-Gill Y. Zhu E.T.Pereira D. Coggins, D. Thomas and S.H.L. Cabral. “Initial experiences with a new FPGA based traveling wave fault recorder installed on a MV distribution network”, In Joint International Conference on Power System technology and IEEE Power India Conference 2008, pages 1– 8, 2008.

[3.22] C. Wang, Y. Chen and G. Zhang et al. “Design of Printed-Circuit board Rogowski Coil for accurate current measurement”. IEEE Proceedings on International Conference on Mechatronics and Automation, pp. 3801 – 3806. August 5th – 8th, 2007.

[3.23] G. Robles, J.M. Martinez, and J. Sanz et al. “Designing and tuning an air-cored current transformer for partial discharge pulse measurements”. *IEEE Instrumentation and Measurement Technology Conference*, pp. 2021 – 2025. May 2008.

[3.24] “Practical aspects of Rogowski coil applications to relaying”. Sponsored by the Power System Relaying Committee of the IEEE Power Engineering Society, September 2010.

[3.25] V. Skendzic and B. Hughes. “Using Rogowski Coils inside Protective Relays”. 2013 Conference for Protective Relay Engineers.

[3.26] S. Tumanski. “Induction coil sensors – a review”. *IOP Measurement Science and Technology*, vol. 18, pp. R31 – R46, 2007.

[3.27] A.P. Chattock. “On a magnetic potentiometer”. Phil. Mag. 24 94 – 96, 1887.

[3.28] W. Rogowski und W. Steinhaus: ‘Die Messung der magnetischen Spannung’, Arch Elektrotech*.,* 1912, 1, Pt.4, pp.141-150.

[3.29] L.A. Kojovic. “Rogowski coils suit relay protection and measurement”, *IEEE Computer Applications in Power*, vol.10, no.3, pp.47- 52, Jul 1997.

[3.30] L.A. Kojovic. “PCB Rogowski coil designs and performances for novel protective relaying”. *In Power Engineering Society General Meeting*, vol. 2, pp.609 – 614, July 2003.

[3.31] C. Xianghu; Z. Xiangjun; D. Feng; L. Ling. “Novel PCB based Rogowski coil for transmission lines fault detection”. *In Power Energy Society General Meeting*, pp. 1– 4, July 2009.

[3.32] S. Pleslic and Z. Andreic, “Application of Rogowski coil in fast pulsed measurements of capillary discharge”, FIZIKA A –ZAGREB, pp. 232-242, Dec. 2007.

http://fizika.hfd.hr/fizika_a/av07/a16p233.htm

[3.33] G. Becherini, S. Di Fraia et al. “Critical Parameters for Mutual Inductance between Rogowski Coil and Primary Conductor”, IEEE Trans. on Instrumentation and Measurement, vol.60, no.2, pp.625 - 632, Feb. 2011.

[3.34] M.N.O Saduko. “Elements of Electromagnetics”, Fifth Edition, Oxford Publications, 2009.

[3.35] J.D. Kraus and D. Fleisch. “Electromagnetics”, Fifth Edition. McGraw-Hill Publishers, 1999.

[3.36] G. Robles, M. Argueso, J. Sanz, R. Giannetti, B. Tellini, "Identification of parameters in a Rogowski coil used for the measurement of partial discharges," IEEE

Instrumentation and Measurement Technology Conference Proceedings, 2007. pp. 1-4.

[3.37] L. Ferkovic, D. Ilic, and R. Malarić, "Mutual Inductance of a Precise Rogowski Coil in Dependence of the Position of Primary Conductor," *IEEE Transactions on Instrumentation and Measurement,* vol.58, no.1, pp.122-128, Jan. 2009.

[3.38] H.M. Wang, F. Liu, and H.L. Zhang et al. "Analysis of the Thermal Expansion Effect on Measurement Precision of Rogowski Coils," Power Electronics and Drives Systems, 2005. PEDS 2005. International Conference on, vol.2, no., pp.1658 - 1661.

[3.39] N. Karrer and P. Hofer-Noser, "PCB Rogowski coils for high di/dt current measurement," Power Electronics Specialists Conference, 2000. PESC 00. 2000 IEEE 31st Annual, vol.3, pp.1296 - 1301, 2000 PCB.

[3.40] G.M. Hashmi. M. Lehtonen and M. Nordman, "Modeling and experimental verification of on-line PD detection in MV covered-conductor overhead networks", Dielectrics and Electrical Insulation, IEEE Transactions on, vol.17, no.1, pp.167 - 180, February 2010.

[3.41] B.G Moffat, M. P Y Desmulliez and K. Brown et al. "A micro-fabricated current sensor for arc fault detection of aircraft wiring," Proc. of the Electronics System-Integration Technology Conference, pp. 299 - 304, 1 - 4 Sept. 2008.

[3.42] L. A. Kojovic. "Novel low-power current sensors for relay protection systems (part 1)", In Eighth IEE International Conference on Developments in Power System Protection, volume 2, pp. 510 – 513. April 2004.

[3.43] S.B. Bulumulla, and N.A. Evers, "Flexible, lightweight sensor for monitoring wiring in aircraft," Sensors, 2005 IEEE, pp.790 – 793. Oct. 30 - Nov. 3, 2005.

[3.44] Z.S. Zhang, D.M. Xiao and Y. Li, "Rogowski air coil sensor technique for on-line partial discharge measurement of power cables," Science, Measurement & Technology, IET, vol.3, no.3, pp.187 - 196, May 2009.

[3.45] Y. Cheng, W. Li, and J. Y. Jisong, X. Hengkun, et al. 'Study on the detection of partial discharge with ultra wideband technique', J. Xi'an Jiaotong Univ. pp. 19–23, 1997,

[3.46] L. Xin, L. Chengrong and W. Wei, "Partial discharge measurement in XLPE cable joint by using VHF sensor," Solid Dielectrics, 2004. ICSD 2004. Proceedings of the 2004 IEEE International Conference on, vol.2, pp. 669 - 671, 5-9 July 2004.

[3.47] L. Pon; M. Sun and R.J. Sclabassi, "The bi-directional spike detection in EEG using mathematical morphology and wavelet transform," Signal Processing, 2002 6th International Conference on, pp.1512 – 1515, vol.2, 26 - 30 Aug, 2002.

[3.48] G.M. Hashmi. "Partial discharge detection for condition monitoring of covered-conductor overhead distribution networks using a Rogowski coil". PhD dissertation, Helsinki University of Technology, 2008.

[3.49] A. Contin, A. Cavallini, and G.C. Montanari et al "Artificial intelligence methodology for separation and classification of partial discharge signals," Electrical Insulation and Dielectric Phenomena, 2000 Annual Report Conference on, pp. 522 - 526 vol.2, 2000.

[3.50] B.H. Ward, "Digital Techniques for PD measurements", IEEE Trans. On Power Delivery, vol. 7, no. 2, pp. 649 – 479, April 1992.

[3.51] A. Contin, G.C. Montanari and C. Ferraro et al, "Partial discharge source recognition by weibull processing of the pulse-height distribution", IEEE. Trans. On Dielectrics and Electrical Insulation, vol. 7, no. 1, pp. 48 – 58, Feb 2000.

[3.52] E. Gulski, "Computer-Aided Recognition of PD using Statistical Tools", Ph.D Thesis, Delft University Press, 1991.

[3.53] X. Ma, C. ,Zhou and I.J. Kemp, "Automated wavelet selection and thresholding for PD detection". Electrical Insulation Magazine, IEEE, vol.18, no.2, pp.37 - 45, March-April 2002.

[3.54] X. Ma, C. Zhou and I.J. Kemp, "Interpretation of wavelet analysis and its application in partial discharge detection". Dielectrics and Electrical Insulation, IEEE Trans. Dielectr. Electr. Insul., vol.9, no.3, pp. 446 - 457, Jun 2002.

[3.55] I. Shim, J.J. Soragan and W.H. Siew. "Digital signal processing applied to the detection of partial discharge: an overview", Electrical Insulation Magazine, IEEE, vol.16, no.3, pp. 6 - 12, May-June 2000.

[3.56] I. Shim, J.J. Soragan and W.H. Siew. "Detection of PD utilizing digital signal processing methods part 3: open loop noise reduction". Electrical Insulation Magazine, IEEE, vol.17, no.1, pp.6 - 13, Jan. - Feb. 2001.

[3.57] A. Kyprianou, P.L. Lewin and V. Efthimiou**, "**Wavelet packet de-noising for online

partial discharge detection in cables and its application to experimental field results" IOP, Meas. Sci. Technol., pp. 2367–2379, 2006.

[3.58] C. Buccella, M. Feliziani and G. Manzi. "Accurate detection of low entity cable faults by wavelet transform," International Symposium on Electromagnetic Compatibility, (EMC) vol.3, pp.936 – 941, 9-13 Aug. 2004.

[3.59] H. Zhang, T. Chen; W. Li, "Arc Fault Signatures Detection on Aircraft Wiring System," The Sixth World Congress on Intelligent Control and Automation, (WCICA), vol. 2, pp.5548 – 5552, 2006.

[3.60] C. Desai, K. Brown and M. Desmulliez et al. "Selection of Wavelet for De-noising PD waveforms for Prognostics and Diagnostics of Aircraft Wiring," *Annual Report Conference on Electrical Insulation and Dielectric Phenomena (CEIDP)* pp.17-20, 26-29 Oct. 2008.

Chapter 4 Design and analysis of Rogowski coils

4.1 Introduction

Micro-manufacturing techniques allow the fabrication of planar Rogowski coils and the benefit from economy of scale whereby a large number of sensors per wafer can be fabricated provided that the individual footprint of such sensors is small. A high performance level of these sensors can be attained through the control, at the design stage, of critical parameters needed to be traded off, such as number of coil turns, turns width, length, spacing, height and overall device footprint.

To fully answer this series of trade-offs, this chapter studies the transfer function of the sensor by identifying how the parameters described above impact on the transfer function. The transfer function provides an understanding of how quick the sensor detects a fast rise time signal such as a partial discharge signal, which is indicative of cable failures. The methodology used to model the sensor is shown in figure 4.1. Selection of the sensing area, the number of coil turns, the coil turn width, inter-turn spacing and coil turns height provides the parameters needed to derive the inductance (L), capacitance (C), resistance (R) and mutual inductance (M) between the wire-under-test (WUT) and the sensor.

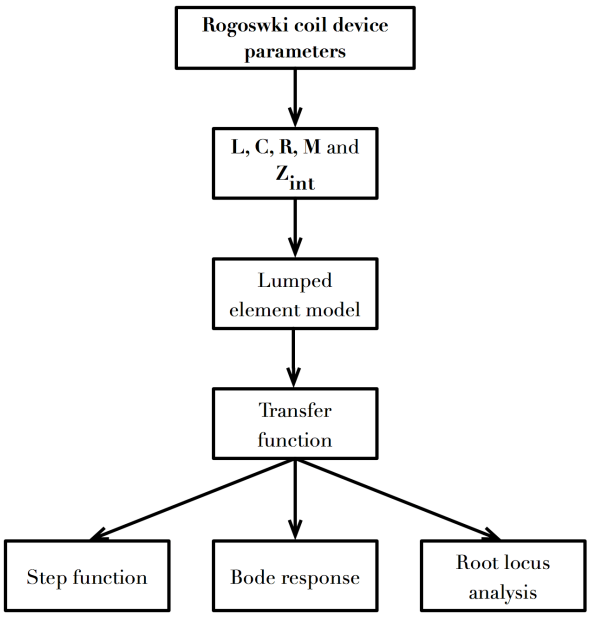

Figure 4.1 Methodology used in this chapter for the design and modeling of the Rogowski sensor

Signal responses of the sensor to input waveforms similar to the fast rise-time arcing and/or partial discharge signals will be derived. Through this derivation, the resistive, capacitive, and inductive components that form the lumped element representation of the sensor are linked to the manufacturing parameters.

4.2 Lumped element sensor model

A lumped electrical parameter model simplifies the mathematical analysis of the Rogowski coil in terms of its behaviour and responses to a variety of electrical inputs. Lumped parameter modeling results in a topology of discrete elements that approximate the behaviour of a discrete or spatially distributed system. When using the lumped model in electronics, the simplifying assumption is that elements are considered as black boxes connected with wires considered as perfect conductors. This type of model is valid when $L_c << \lambda$, where L_c is the characteristic length of the circuit and λ represents the operating wavelength. The lumped parameter model of the planar Rogowski coil is based on a series inductance and resistance in parallel with a capacitance. The inductance L_L represents the inductance of the multiple coil turns, the resistance $R_{L,}$ is resistance over the entire length of the multiple turns and the capacitance of the sensor, C_L, is the capacitance of the conductor turns.

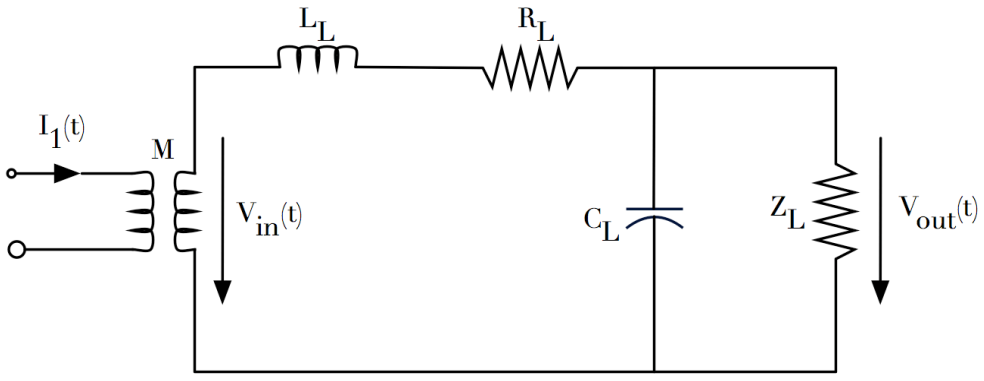

Figure 4.2 Lumped parameter representation of a Rogowski sensor (self-integrating) coupled to a wire under test [4.1].

The Rogowski coil is presented for the self-integrating (Figure 4.2) and differentiating (Figure 4.3) configurations. The only difference is the integrating resistance, Z_L, which is

connected in parallel across the capacitance of the sensor for the integrating case; the differentiating mode does not have this resistance. The Rogowski output, V_{out}, is obtained from the current flowing through the primary conductor, I_1, of a poorly coupled transformer.

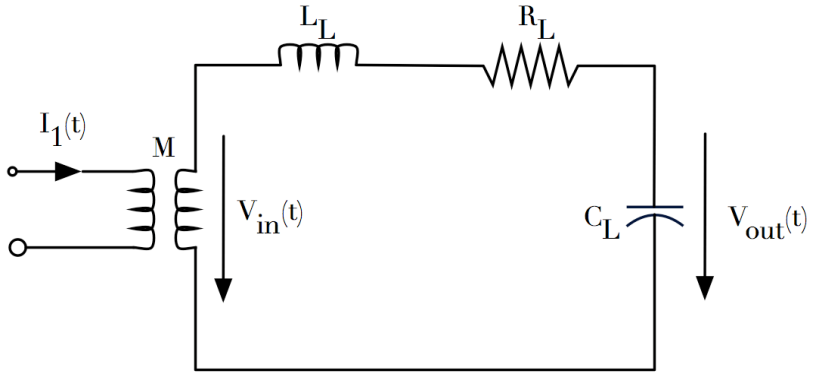

Figure 4.3 Lumped parameter model of a Rogowski sensor in the differentiating mode

4.2.1 Self-integrating mode

In the self-integrating mode the voltage gain transfer function, *H(s)* is expressed by the following equation [4.1-4.3]:

$$H(s) = \frac{V_{out}}{V_{in}} \qquad \text{Eqn 4.1}$$

The input voltage, V_{in}, is the voltage induced across the coil turns of the Rogowski coil from the time varying magnetic field emanating from the Wire-Under-Test (WUT). This is discussed further in section 4.2.2 and 4.2.3. The output voltage, V_{out}, is seen across the terminals of the integrating impedance Z_L that forms a voltage divider arrangement with the rest of the circuit. Calculation of the parallel contribution of C_L and Z_L in figure 4.2 is provided in equation 4.2.

$$Z_L \parallel C = \frac{Z_L/sC}{Z_L + 1/sC} = \frac{Z_L}{sCZ_L + 1} \qquad \text{Eqn 4.2}$$

The equation for V_{out} is completed by adding the contribution from the resistance (R_L) and inductance (L_L) from the lumped parameter model (figure 4.2) to equation 4.2 to and applying the voltage divider principle to solve for H(s). Rearranging equation 4.1 and solving for V_{out} provides the solution for V_{out}.

$$V_{out} = \frac{Z_L/(sC_LZ_L+1)}{R_L + sL_L + (Z_L/sC_LZ_L+1)} \cdot V_{in}$$ Eqn 4.3

Dividing both sides by V_{in} provides the transfer function:

$$\frac{V_{out}}{V_{in}} = \frac{Z_L/(sC_LZ_L+1)}{R_L + sL_L + (Z_L/sC_LZ_L+1)}$$ Eqn 4.4

The transfer function can be further simplified by multiplying the numerator and denominator by the common factor ($sLCZ_L + 1$) [4.1-4.5]:

$$\frac{V_{out}}{V_{in}} = \frac{Z_L}{s^2(L_LC_LZ_L) + s(L_L + C_LR_LZ_L) + (R_L + Z_L)}$$ Eqn 4.5

This equation is the basis for the modeling work carried out for the self-integrating condition. It is shown later how to solve the characteristic equation and use this information to analyse the sensor design in terms of rise-time, bode plots and step response.

4.2.2 Differentiating mode

For the differentiating mode, the output voltage, V_{out}, across the capacitance of the sensor is derived from the voltage divider principle:

$$H(s) = \frac{1/sC_L}{R_L + sL_L + 1/sC_L}$$ Eqn 4.6

The input voltage, V_{in}, can be expressed in terms of the mutual inductance of the sensor and the rate of change of current. This is shown in equation 4.7.

$$V_{in} = M \cdot \frac{di}{dt}$$ Eqn 4.7

Maintaining as high a coupling M as possible between the sensor and the Wire Under Test (WUT) influences the voltage generated over the sensor when rapid changes of current are present. This is achieved by positioning the sensor very close to the wire-under-test. In equation 4.8, the output voltage is derived in terms of R_L, L_L, C_L and V_{in}:

$$V_{out} = \frac{1/sC_L}{R_L + sL_L + 1/sC_L} \cdot V_{in}$$ Eqn 4.8

Dividing both sides of equation 4.8 leads to an expression of H(s). Further simplification is achieved by dividing the numerator and denominator by sC_L such that:

$$\frac{V_{out}}{V_{in}} = \frac{1}{s^2 + s\frac{R_L}{L_L} + \frac{1}{L_L C_L}} \qquad \text{Eqn 4.9}$$

The characteristic equation will be used for calculating the characteristics roots of the second order differential equation for the Rogowski coil. The rise-time, step response, root locus diagram and bode response of the sensor will also be described.

4.2.3 Mutual inductance

For traditional Rogowski coils, the mutual inductance is obtained from the coil turns on the non-magnetic torroid of the Rogowski coil. In the case of the planar Rogowski coil, the coil turns do not fully encircle the WUT as the sensor is placed to its side, as shown in figure 4.4. In this configuration, the magnetic field encircling the WUT penetrates the cross sectional area of each coil turn. The expression of the mutual inductance between the coil and WUT is given in equation 4.10 [4.2,4.3].

$$M = \int_{d+(k-1)p}^{d+D-(k-1)p} \frac{\mu_0}{2\pi x}\left[D - 2(k-1)p\right]dx \qquad \text{Eqn 4.10}$$

The terms of the integral take into account how the area of each coil turn decreases as you progress from the outer turn inwards by *k* turns. As the area decreases between each coil turn of figure 4.4, the distance between the sensor and WUT increases by a factor of (k-1)p. This is due to the magnetic field decreasing radially as the distance *d* is increased from 0 to a finite value. The modifications in this equation take into account the sensors parameters which include the width of the coil turns (w), the spacing between coil turns (s), the pitch (w + s), the height of the coil turns (h), the outer diameter of the sensor (D) and the inner diameter of the sensor (D_i) as shown in Figure 4.4. This equation represents the summation of all the mutual inductances that exist between all of the coil turns and the WUT. In contrast to traditional Rogowski coils, the coil turn area remains constant due to it being wrapped around a non-magnetic former. However, there is difficulty in achieving uniform coil turns and spacing, which results in measurement errors.

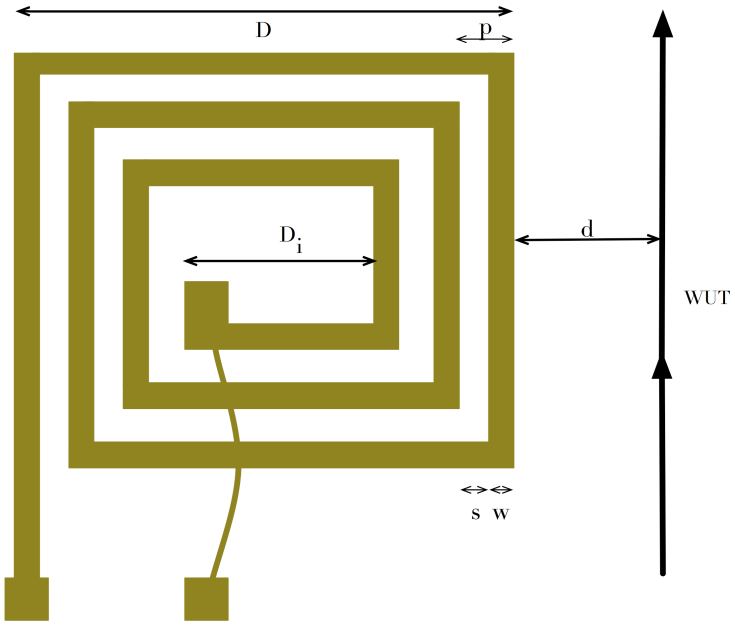

Figure 4.4 Interaction between the planar UV-LIGA manufactured Rogowski sensor and the WUT.

More importantly, the limitation with the positioning of the traditional coil very close to the WUT imposes restrictions to the maximal achievable mutual inductance. The size of the former required to maintain a good coil turns area means that the distance from the WUT and the sensor is often much larger than desired. If the size of the non-magnetic former is decreased to allow closer placement to the WUT, the coil turns area decreases further and larger measurement error is introduced as a result of WUT not being threaded through the middle of the sensor.

The proposed solution is presented in figure 5.12 of chapter 5, whereby a manufactured sensor package has been made that clips around the WUT. The planar Rogowski sensor is positioned inside this package and a smaller distance to the WUT is maintained by including a groove in the package design for the WUT to be held in. There is therefore little risk of introducing measurement error as a result of the WUT moving during everyday operation. As a result the mutual inductance is maximised, whilst retaining a very small footprint.

4.2.4 Inductance

The inductance of the planar Rogowski sensor can be calculated from a variety of methods [4.4,4.5] although the calculation is based on a square shape inductor. The work by Grover can be used in the case where the inductor layout is rectangular in shape [4.6,4.7].

Greenhouse developed an approximation for the inductance based on the breakdown of the planar coil into straight-line segments and computing the total summed inductances and the sum of the positive and negative mutual inductances. The following analysis presents how the inductance of a segment of the coil turns is calculated based on the cross section area of the coil turn being rectangular. The self-inductance at DC, L_{self}, expressed in nH, is:

$$L_{self} = 2l_{seg}\left(\ell n \frac{2\ell}{w+h} + 0.5 + \frac{w+h}{3\ell}\right) \quad \text{Eqn 4.11}$$

Where ℓ is the segment length in cm, w is the width in cm and t is the thickness in cm.

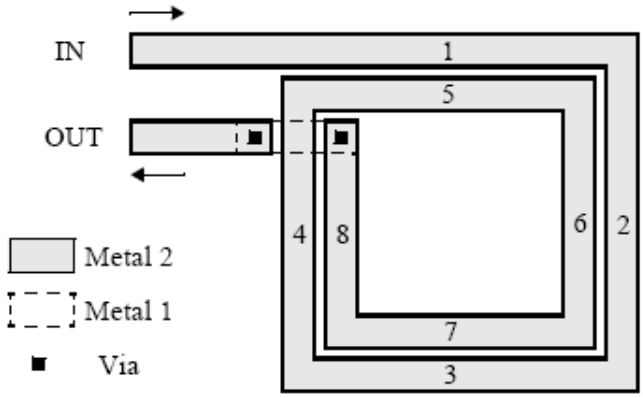

Figure 4.5 Calculation of the inductance of Rogowski sensor by breaking design into segments [4.6].

The next step in is to include the inductive coupling that exists between adjacent wire segments. The total inductance of the coil, L_{total}, is the sum of the inductances of all wire segments plus the difference in positive and negative mutual inductances between parallel-orientated segments.

$$L_{total} = L_0 + M_{positive} - M_{negative} \quad \text{Eqn 4.12}$$

where L_0 consists of the self-inductances of all the segments.

$$L_0 = \sum i^{NS} L_{self}(i) \qquad \text{Eqn 4.13}$$

Where i is the segment number and NS is the total number of segments in the spiral inductor. For the two turn planar inductor shown in [4.6] and Figure 4.5, there is a total of 8 segments.

The contributions of the positive mutual inductance between segments is:

$$M_{positive} = 2\left(M_{1,5} + M_{2,6} + M_{3,7} + M_{4,8}\right) \qquad \text{Eqn 4.14}$$

The negative mutual inductance contributions from the anti-phased segments is:

$$M_{negative} = 2\left(M_{1,5} + M_{1,7} + M_{2,4} + M_{2,8} + M_{3,5} + M_{4,6} + M_{5,7} + M_{6,8}\right) \qquad \text{Eqn 4.15}$$

Segments of the coil that lay orthogonally to one another have no magnetic coupling, as their fluxes do not link. The mutual inductance of parallel segments depends on the length of the conductors and the geometric mean distance (GMD) and is given as:

$$M = 2\ell Q \qquad \text{Eqn 4.16}$$

where M is the mutual inductance in nH, Q is the mutual inductance parameter; ℓ is the length of the wire segment.

$$Q = \left[\frac{\ell}{GMD} + \sqrt{1+\left(\frac{GMD^2}{\ell}\right)}\right] - \sqrt{1 + (\frac{GMD}{\ell})^2 + \frac{GMD}{\ell}} \qquad \text{Eqn 4.17}$$

The GMD is described by the following equation:

$$\ell n\ GMD = \ell n\ d - \frac{w^2}{12d^2} - \frac{w^4}{60d^2} - \frac{w^6}{168d^6} - \frac{w^8}{360d^8} - \frac{w^{10}}{660d^{10}} - \ldots \qquad \text{Eqn 4.18}$$

where w and d are the wire width and pitch in cm.

In [4.8] the inductance for a square planar micro-coil can be calculated differently from the derivation given by equations 4.11 to 4.18 [4.8]. For the case of a square spiral coil the inductance L is given by:

$$L = \left[\frac{\mu D^3}{4\pi p^2}\right]\left(1-\alpha^2\right)(1-\alpha)\left[\ell n\,\frac{(1+\alpha)}{(1-\alpha)} + 0.2235\,\frac{1-\alpha}{1+\alpha} + 0.726\right](Henries) \qquad \text{Eqn 4.19}$$

Where α is the ratio of the inner to outer diameter, D is the outer diameter and p is the pitch.

This equation saves a lot of calculation steps compared to the method presented by Greenhouse [4.6], and has been modified for use in this thesis for rectangular designs by deconstructing the rectangular designs into two sets of square coils. One set of the coils corresponds to the short side of the rectangular design and the other set of coils corresponds to the long side of the Rogowski sensor design. The values of these designs is halved and then added to provide the total inductance for the case of the rectangular design. The α value will be different for the short sided and long sided versions of the square coils, with the short sided square coil possessing a lower α value than the long sided square coil.

4.2.5 Capacitance

For a traditional Rogowski coil that has been manufactured through winding many coil turns around a toroid shaped former, capacitance is created between coil turns in the high frequency lumped model [4.9,4.10]. For the planar Rogowski coils manufactured either using UV-LIGA or on silicon substrates by Qudos Technology Ltd, the capacitance is based on the substrate choice, spacing between coil turns, capacitance through the substrate and also the material around the coil turns.

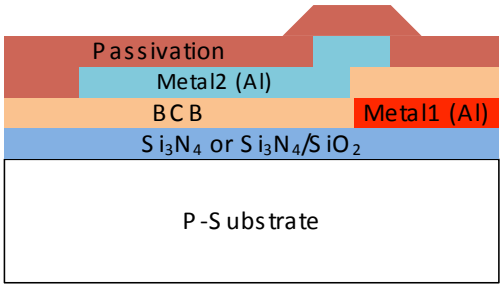

4.6a: Structure of the Rogowski coil manufactured by Qudos Technology Ltd.

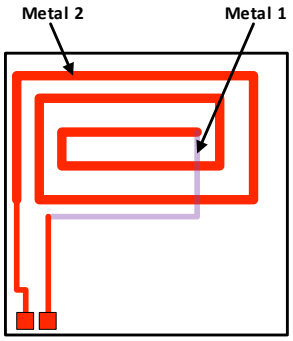

4.6b: Rogowski coil layout on silicon substrate

Figure 4.6 Structure and design layout of Qudos manufactured Rogowski sensors.

The UV-LIGA manufactured Rogowski coil uses a wire bond that is connected between the inner and outer contact pads, therefore its impact on the lumped capacitance is smaller compared to the Rogowski coil fabricated by Qudos Technology Ltd. Due to the wire bond bridging the inner and outer contact pads without shorting the coil turns, the permittivity of

the surrounding environment is air; therefore the permittivity of free space is used in the capacitance calculation. In contrast, for the Qudos coils, the return path connecting the inner and outer contact pads is created through depositing an additional metal layer that passes under the coil turns on top of the silicon nitride layer and surrounded by BCB layer. The function of the BCB layer is to provide a suitable mould for the metal layer 1 deposition in addition to the inter-dielectric layer function for the metal 2 layer resting on top of this for the formation of the coil turns. This is shown clearly in figures 4.6a and figure 4.6b. The capacitance of the underpass is therefore influenced by the dielectric permittivity of silicon nitride (ε_r=7) and the BCB inter-dielectric layer (ε_r = 2.7).

In [4.8], in the case of a square coil, the capacitance between turns, C_{tt}, shown in figure 4.7, is expressed by equation 4.20. This equation describes the capacitance based on the outer diameter of the coil or the length of one side of the coil, the number of turns, the height of the coil turns (h), the distance between the coil turns (s), pitch (p), length (l) of all the coil turns, and the ratio between the inner and outer diameter (α).

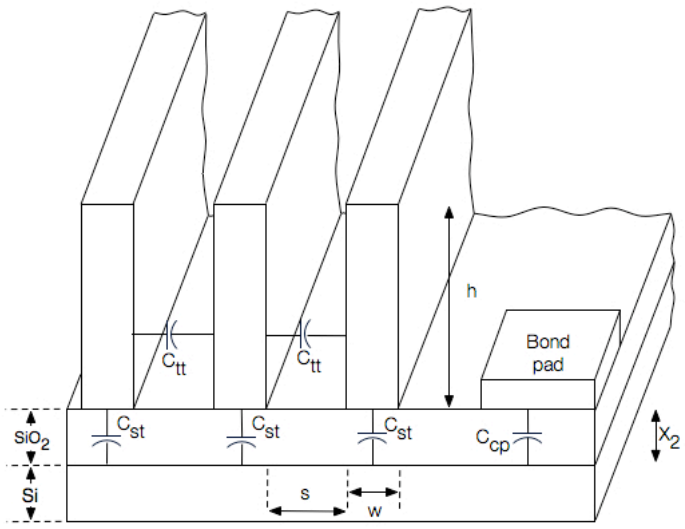

Figure 4.7 Cross section of planar coil showing the origin of the three types of parasitic capacitance that exist [4.8].

Neagu in [4.8] advocates that the impact of C_{tt} is to be minimal when compared to the substrate capacitance, C_{st}. This is due to the distance between the coil turns (s) and the coil turn height (h) being similar but the impact of the SiO_2 insulating layer beneath the micro-coil is dominant due to the smaller thickness and resultant capacitance to the substrate.

There is a passivation layer, polyimide (ε_r=3.2), deposited on top of the electroplated coil turns of the Qudos coil. This results in the capacitance between coil turns increasing by a factor of the relative permittivity of the passivation. The UV-LIGA manufactured Rogowski coils are to be manufactured on glass wafers that have no passivation layer, therefore the capacitance is expected to be much smaller. Additionally, as the substrate is glass instead of silicon, negligible capacitance is introduced between the coil turns to the substrate.

$$C_{tt} = \frac{\varepsilon h(l - 4D)}{Nx_1} = \frac{2\varepsilon hD}{x_1}\left(1 + \alpha - \frac{4p}{D(1-\alpha)}\right) \quad \text{Eqn 4.20}$$

By designing different sizes of UV-LIGA coils and using CMOS compatible fabrication steps, the impact of maximizing the mutual inductance through using different sensor layouts becomes evident when considering the overall R, L and C parameters. The number of turns is increased through decreasing coil turn width and spacing between turns, which, in turn, provides the greatest level of inter turn capacitance.

The next capacitance to be considered is between the coil turns and the substrate, C_{st}. This is a key component of devices that are manufactured on silicon and comprise of polymer and nitride insulating layers.

$$C_{st} = \frac{\varepsilon wl}{x_2} \quad \text{Eqn 4.21}$$

where w is width of the coil turn (l) is the length of the coil from outer turn to inner turn and x_2 is the thickness of the silicon dioxide layer between the silicon substrate and the coil turns. The total parasitic capacitance of the coil when on a silicon substrate is:

$$C_{sc} = 2\,\frac{\varepsilon A_{cp}}{x_2} \quad \text{Eqn 4.22}$$

The total capacitances of the Rogowski sensors are expressed as the sum of the capacitance between turns, the capacitance between the coil turns and substrate and the capacitance of the bond pads to substrate as shown in equation 4.23.

$$C_{par} = C_{tt} + \frac{1}{4}C_{st} + \frac{1}{2}C_{sc} \quad \text{Eqn 4.23}$$

4.2.6 Resistance

The DC resistance of the sensor is governed by the physical dimensions of the coil such as the width w_{turn}, height h_{turn}, length l_{turn} and the resistivity of the metal. The outer/inner diameter of the sensor and the desired turn width and spacing between turns will determine how many coil turns can be achieved and the total length of the coil turns. The height of the coil turns affects the area of the coil turn; subsequently this determines the resistance of the sensor and will have an immediate influence on the acquired signal levels and the presence of higher frequency components of a partial discharge or arc fault signal. This becomes more apparent when looking at the lumped or distributed sensor response: higher frequency components of the fast rise time signal become attenuated far quicker than the lower frequency components. This leads to a lower fidelity reproduction of the signal, which is viewed as a signal of lower magnitude and slower rise time. These higher frequency components are of more interest when it comes to using signal processing techniques for establishing if it is a fault signal or a transient signal during normal system operation. The resistance is given by:

$$R = \frac{\rho l}{w_{turn} h_{turn}} = \frac{\rho L}{A} \qquad \text{Eqn 4.24}$$

The prior equation can be expanded [4.8] to include a greater range of variables such as outer diameter D, ratio of inner to outer diameter α, pitch and number of turns N when considering a square shaped planar coil:

$$R = \frac{\rho L}{w_{turn} h_{turn}} = \frac{\rho L}{A} = \frac{\rho D^2}{h_{turn}} \frac{1 - \alpha^2}{w_{turn} p} \qquad \text{Eqn 4.25}$$

The length of the coil can also be expressed in a more intuitive form if the coil is square shaped [8.8, 8.9]:

$$l(metres) = 8aN = \frac{D^2}{p}\left(1 - \alpha^2\right) \qquad \text{Eqn 4.26}$$

Skin effect

Research by Neagu [4.8] and Dubickas [4.12] shows that there are two components of resistance that exist in planar micro coils and conventional Rogowski sensors. The first component is the DC component and is independent of frequency; the other part is frequency dependent and is determined by the frequency of operation of the planar inductor and its geometric values. At high frequencies it is common to consider both micro fabricated planar inductors and macro-scale inductors as distributed transmission lines. In this circumstance, eddy currents cause reduction of the current flow through the conductor cross sectional area. This is due to the alternating current that flows through a conductor causing currents that are normal to the magnetic flux of the conductor and opposing the direction of the normal current flow [4.8]. At high frequencies the eddy currents created at the centre of the conductor are at their strongest, which prevents normal current flow from occurring [4.13]. This AC resistance becomes more pronounced at higher frequencies. Quantification of the reduction in effective cross sectional area available for current conduction is described as the ”skin effect” and is dependent on the magnetic permeability, electrical conductivity and frequency of operation [4.13]:

$$\delta = \sqrt{\frac{2}{\omega\mu\sigma}} \qquad \text{Eqn 4.27}$$

The rule of thumb is that if the skin depth is much larger than the conductor thickness at a specified frequency then the skin effect is negligible at that frequency in the conductor. In [4.8], the effect of skin effect on the overall resistance is shown as:

$$R = \rho D^2 \cdot \frac{1-\alpha^2}{p} \cdot \left(\frac{1}{hb} + \frac{1}{2\delta(h+b)} \right) \qquad \text{Eqn. 4.28}$$

4.3 Second order behaviour of the Rogowski coil

The planar Rogowski coil displays inductive, resistive and capacitive effects and its transfer function has usually been modeled by a second order differential behaviour as shown in [4.14]. The lumped element transfer function, whose lumped elements electrical parameters

were obtained in the previous section, can be resolved in the form of G(s) in figure 4.8, which depicts the output response, C(s), of a second order system to a step input signal, R(s).

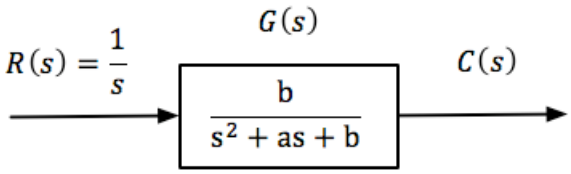

Figure 4.8 General response of a second order system to a step input.

This model helps build an understanding of how the sensor responds to fast rise-time signals such as arcing or partial discharge. The form of a general second order system takes the form of equation 4.28 [4.15]:

$$a_2 \frac{d^2y(t)}{dt^2} + a_1 \frac{dy(t)}{dt} + a_0 y(t) = f(t) \qquad \text{Eqn. 4.28}$$

In addition to equation 4.28, a second order system, excited by a harmonic input signal, can be expressed in terms of its damping factor and natural frequency:

$$\frac{d^2y(t)}{dt^2} + 2\zeta\omega_n \frac{dy(t)}{dt} + \omega_n^2 y(t) = f(t) \qquad \text{Eqn. 4.29}$$

where ω_n is the natural undamped frequency and ζ is the damping factor. In addition to modifying equation 4.29, the transfer function, G(s), can also be modified from the original expression in figure 4.8 to that of eqn. 4.30 by taking into account the expression of equation 4.29 instead of equation 4.28. This leads to 'a" in figure 4.8 being equal to $2\zeta\omega_n$ and "b" being equal to ω^2_n [4.16].

$$G(s) = \frac{\omega_n}{s^2 + 2\zeta\omega_n + \omega_n^2} = \frac{\omega_n^2}{(s + p_1)(s + p_2)} \qquad \text{Eqn. 4.30}$$

The denominator of the transfer function forms the characteristic equation, which, once solved, enables the derivation of the response of the coil to an input signal, such as a step input. The terms damping factor ζ, damping ratio α, natural frequency ω_n and damped natural frequency ω_d are introduced in figure 4.9 and explained below. The damping ratio is the ratio of the exponential decay frequency of the envelope of the response to the natural

frequency, ω_n, which is the frequency of oscillation in the absence of any damping in the system.

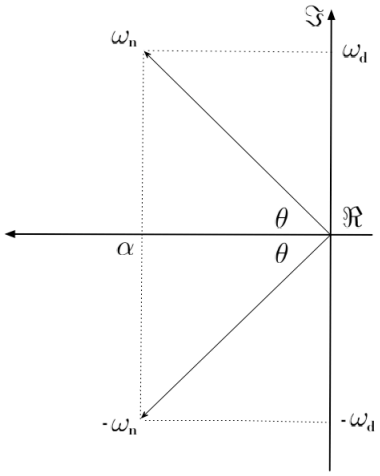

Figure 4.9 Relationship between pole location and damping/settling time in the s-plane [4.9].

It is shown in figure 4.9 as the radial distance from the roots of the characteristic equation to the origin of the s-plane. The damped natural frequency, ω_d, is the frequency of the system in the presence of damping. The sensor response is under-damped, if the damping factor ζ is less than unity and the roots given on the right hand side of equation 4.30 can be expressed as:

$$s^s + 2\xi\omega_n s + \omega_n^2 = \left(s + \alpha + j\omega_d\right)\left(s + \alpha - j\omega_d\right) \qquad \text{Eqn. 4.31}$$

with

$$s_1, s_2 = -\alpha \pm j\omega_d \qquad \text{Eqn. 4.32}$$

The damping ratio (α) is equal to $-\zeta\omega_n$ and lies on the negative real axis. The imaginary part of the roots is equal to $\omega_d=\omega_n\sqrt{1-\zeta^2}$, and lies on the imaginary part of the imaginary axis of the s-plane. The natural frequency is given in equation 4.33.

$$\omega_n = \sqrt{\alpha^2 + \omega_d^2} \qquad \text{Eqn. 4.33}$$

The roots of the characteristic equation can now be expressed in terms of the damping factor and natural undamped frequency for $0 \leq \zeta \leq 1$.

$$s_1, s_2 = -\zeta\omega_n \pm j\omega_n\sqrt{1-\zeta^2} \qquad \text{Eqn. 4.34}$$

In the case of the differentiating configuration Rogowski coil, the roots of the characteristic equation is expressed as follows [4.17]:

$$s_1, s_2 = -\frac{R}{2L} \pm \sqrt{\left(\frac{R}{2L}\right)^2 - \frac{1}{LC}} \qquad \text{Eqn. 4.35}$$

Where $\alpha = -R/2L$, $\omega_n = \sqrt{(1/LC)}$ and $\omega_d = \sqrt{((R/2L)^2 - 1/LC)}$[4.13]. For the self-integrating configuration, the roots of the characteristic equation are

$$s_1, s_2 = -\frac{L + CRZ_L}{2LCZ_L} \pm j\sqrt{\left(\frac{L + CRZ_L}{2LCZ_L}\right)^2 - \frac{R + Z_L}{LCZ_L}} \qquad \text{Eqn. 4.36}$$

Where $\alpha=(L+CRZ_L)/(2LCZ_L)$ [18,19], $\omega_n=\sqrt{(R+Z_L)/(LCZ_L)}$ and $\omega_d=\sqrt{(L+CRZ_L/2LCZ_L)^2 - (R+Z_L/LCZ_L)}$. The damping factor ζ is expressed in equation 4.37 as [4.16]:

$$\zeta = \frac{a_1}{2\sqrt{a_2 a_0}} \qquad \text{Eqn. 4.37}$$

For the differentiating and self-integrating [4.20, 4.21] cases, the damping ratio is provided by equations 4.38 and 4.39, respectively.

$$\zeta_{Differentiating} = \frac{CR}{2\sqrt{LC}} \qquad \text{Eqn. 4.38}$$

$$\zeta_{self-integrating} = \frac{L + CRZ_L}{2\sqrt{LCZ_L(R + Z_L)}} \qquad \text{Eqn. 4.39}$$

The output response to a step input signal, 1/s, is found by multiplying the transfer function by the input signal. The output response is composed of a transient or forced state, Y_f, and a steady state or natural response, Y_{ss}, such that [4.22]:

$$Y_{total} = Y_f + Y_{ss} \qquad \text{Eqn. 4.40}$$

The part of the response of most interest is the forced or transient response when the sensor responds to fast rise time signals. Specific characteristics of the sensor in that state, rise-time, settling time, bandwidth and Q-factor, are obtained by calculating the response of the system to a unit step input function:

$$C(s) = \frac{\omega_n}{s\left(s^2 + 2\zeta\omega_n s + \omega_n^2\right)} = \frac{K_1}{s} + \frac{K_2 s + K_3}{s^2 + 2\zeta\omega_n s + \omega_n^2} \qquad \text{Eqn. 4.41}$$

Taking the inverse Laplace transform [4.16]:

$$C(t) = 1 - \frac{e^{-\zeta\omega_n t}}{\sqrt{1-\zeta^2}} \sin(\omega_n \sqrt{1-\zeta^2}\, t + \cos^{-1}\zeta) \qquad \text{Equation 4.42}$$

where $\phi = \tan^{-1}\left(\zeta \Big/ \sqrt{1-\zeta^2} \right)$

4.4 Modeling of the UV-LIGA Rogowski coil in the differentiating mode

4.4.1 Bode response

A number of designs have been proposed in this thesis for manufacture using the UV-LIGA process. The designs are similar in form to the Qudos manufactured sensors (planar spiral coil turns), but greater freedom has been allowed when choosing the sensing footprint area and the accompanying shape. This variation in design parameters has led to different values of mutual inductance, inductance, capacitance and resistance being derived from the equations presented in sections 4.2.3-4.2.6, These values are summarised in table 4.1 and are used for simulating the second order lumped parameter responses for bode analysis and step response analysis.

The bode response of the planar Rogowski coil manufactured by the UV-LIGA process is presented in figure 4.10, with the main parameters of interest, resonant frequencies and magnitude at these points indicated in table 4.2. Looking at table 4.1, the resonant frequencies of sensors UV-1, UV-2, UV-3, UV-4, UV-5, UV-6, UV-9 and UV-10 are located at the lower end of the bode plot and range from 86.2 MHz to 340 MHz. Sensors UV-11 and UV-12 are in the middle of the bode plot, and sensors UV-7 and UV-8 are located at the higher end.

The sensors UV-3 and UV-4 that have the lowest resonant frequency also have the greatest sensor footprint at 20 x 10 mm and the largest number of turns. Next are the sensors UV-1 and UV-2, which correspond to a sensor footprint of 10 mm x 10 mm and turns ranging from 43 to 69; sensor UV-2 has the least amount of coil turns and the highest of resonant frequencies for this particular footprint. The actual performance of this design is presented

and discussed in **Chapter 7**. The final set of sensors that have a lower resonant frequency are sensors UV-5 and UV-6, with sensor footprints of 20 mm x 5 mm, followed by sensors UV-11 and UV-12 with footprints of 10 mm x 5 mm. Sensors with the lower amount of turns have higher resonant frequencies; sensor UV-6 had 24 turns vs. sensor UV-5 with 38, whereas sensor UV-11 had the lower amount of turns (12) in comparison to 19 turns for sensor UV-12.

Table 4.1 Calculated parameters for the planar Rogowski sensors manufactured by UV-LIGA.

Results are for the differentiating case.

Coil Dimension	**Turns**	**Resistance** (Ω)	**Inductance** (μH)	**Capacitance (pF)**	**3dB Bandwidth (MHz)**	**Natural Resonant Frequency** (MHz)	**Mutual Inductance** (μH)
10 x 10mm (UV-1)	66	237.5	36.5	0.0 3	76.1	105	35.
10 x 10m (UV-2)	43	70	14.5	0.06	110	170	22.5
20 x 10mm (UV-3)	66	437.5	77.4	0.11	3	55.3	80
20 x 10mm (UV-4)	43	107.5	31	0.11	62.1	87.8	49.7
20 x 5mm (UV-5)	38	181.25	24	0.081	80.4	114	51.2
20 x 5mm (UV-6)	24	55	11.7	0.089	110	155	33.6
5 x 2.5mm (UV-7)	9	18.75	0.62	0.026	885	1.25	3.7
5 x 2.5mm (UV-8)	14	50	1	0.027	689	974	7.1
5 x 10mm (UV-9)	37	115.7	6.6	0.052	191	272	24.4
5 x 10mm (UV-10)	23	27.5	4.3	0.051	240	339	15.3
2.5 x 10mm (UV-11)	12	12.5	1.5	0.039	468.3	661.4	8.8
2.5 x 10mm (UV-12)	19	50	1.5	0.047	417	590	13.7

From a design perspective, for a fixed sensor footprint, to maximize the voltage induced across the Rogowski coil requires an increase of the number of coil turns. This increases the capacitance as the distance between coil turns becomes smaller to accommodate the larger number of coil turns. As the number of turns increases, the overall inductance and

resistance increase as a result of the increase of the overall length of the Rogowski coil.

Table 4.2 Summary of bode response for Rogowski sensors manufactured through UV-LIGA.

Sensors are in differentiating mode

Sensor	UV1	UV2	UV3	UV4	UV5	UV6	UV7	UV8	UV9	UV10	UV11	UV12
Peak Magnitude	40.1	46.9	35.7	43.9	39.6	46.4	48.4	41.7	39.8	50.5	53.9	41.2
Resonant Frequency (MHz)	105	171	54.5	86.2	114	156	1240	975	272	340	660	592

The increased capacitance and inductance values lower the resonant frequency of the coil. The shape of the resonant peaks in this bode diagram suggest that there is a small range of frequencies where the V_{out}/V_{in} magnitude gain is greater than 1. For example, sensor UV-2 shows a gain ranging from 25 to 70 dB, which may be beneficial for improving the rise-time measurement of a faulty signal. The fast rise time of the partial discharge (PD) signal indicates that the signal has indeed different frequency components, up to 100 MHz, that define the shape of its rising edge. If the fault has moved some distance down the wire, or the higher frequency components have smaller magnitude, the amplification of the higher frequency components in the region defined above could help reconstruct the waveform to such an extent that the rise-times are comparable to the original PD signal.

It is worth drawing attention to the close agreement of table 4.1 and 4.2 in terms of the resonant frequencies that are observed for the sensor designs.

4.4.2 Step response

Table 4.3 summarises the main parameters of the step input response such as the sensor rise-time, peak response, % overshoot, and settling time. The order of these sensors is given in terms of the settling time, to within 2% of the final value. The sensors with the fastest rise-times are UV-7, UV-8, UV-11, UV-12, UV-10, UV-9, UV-2, UV-6, UV-5, UV-1, UV-4 and UV-3. Sensor UV-7 and UV-8 actually had the smallest geometrical sensing footprint yet had the fastest of rise-times.

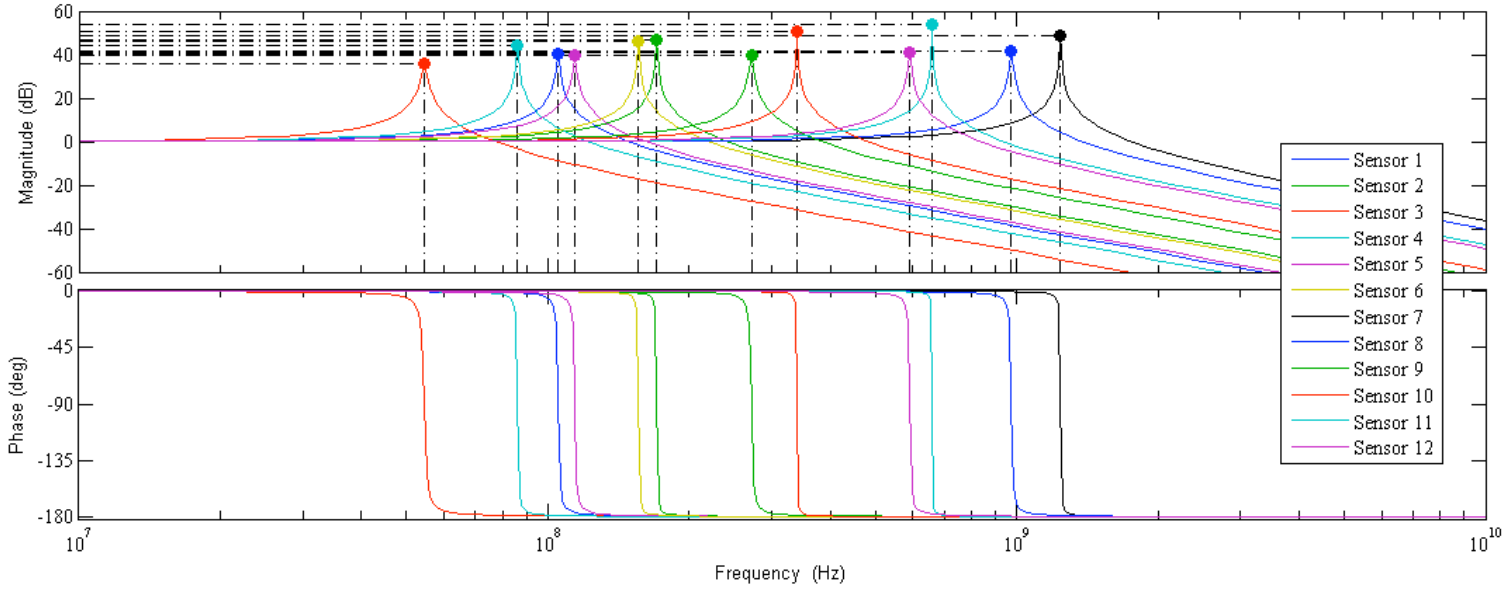

Figure 4.10 Bode response of UV-LIGA manufactured Rogowski coils. Sensors are in differentiating mode.

Sensors are in differentiating mode. Sensors 1 to 12 correspond to UV-1 to UV-12.

Table 4.3 Summary of step response characteristics of Rogowski coil sensors made by UV-LIGA in differentiating mode.

Sensor type	Rise time (ns)	Peak response (dB)	Peak response time (ns)	% Overshoot	Settling time (ns)
UV-1	1.58	1.985	4.75	98.5	1.2
UV-2	9.73	1.993	2.93	99.29	1.62
UV-3	3.06	1.974	9.17	97.4	1.38
UV-4	1.93	1.99	5.8	99	2.25
UV-5	1.46	1.984	4.38	98.4	1.04
UV-6	1.07	1.993	3.21	99.3	1.66
UV-7	0.134	1.994	0.404	99.4	0.265
UV-8	0.171	1.987	0.513	98.7	0.154
UV-9	0.613	1.984	1.84	98.4	0.445
UV-10	0.488	1.994	1.49	99.4	1.22
UV-11	0.259	1.997	0.758	99.7	0.927
UV-12	0.281	1.986	0.845	98.6	0.241

The sensors UV-11 and UV-12 have the same width as sensors UV-7 and UV-8 but double the length. The slowest sensors are UV-4 and UV-3, which corresponded to the 10 mm x 20mm sensors. In terms of the settling times, the smaller sensors tend to settle quickly to within 2% of its final value. The 2.5 x 5 mm designs used for design number UV-7 and UV-8 of Table 4.3 have settle times within 0.3μs of its resting magnitude. The larger coil designs such as UV-3 and UV-4 had the longer settling times, with the 20 x 10 mm sensors taking up to 2.25 μs to settle within 2 % of its final magnitude.

In the differentiating mode, the planar Rogowski sensors show a clear under-damped response to a step input. This is evident from the large overshoot for the sensors, the oscillatory response and the longer settling time. The step response of these sensors shows two components that are linked to the parameters of each sensor. The first component is the exponential decay seen in each plot that is in response to the real part of the complex pole. The second aspect of the step response is the oscillatory behaviour, which is governed by the natural frequency of each sensor design.

4.4.3 Root locus analysis

The root locus analysis is presented in figure 4.11. This analysis shows the relation between the damping factor ζ and the damped natural frequency ω_d whose roots are given

by equation 4.35. Sensor design UV-8 has the greatest amount of damping as shown by the dashed blue line in figure 4.11, but it also has the highest damped natural frequency, which results in the fastest rise-time. Sensor UV-7 has a similar geometrical footprint, but a different width of turns. This design can be seen in figure 4.11, where it lies to the immediate right of the real axis at the -1.5 scale. In figure 4.11, sensor designs 1-12 correspond to UV1-UV12.

Sensor design UV-7 has a shorter damping factor and a higher damped natural frequency than sensor design UV-8, and therefore a slightly slower rise-time. The other designs show that the damping factor ζ is much lower, but the damped natural frequency is also correspondingly much smaller. This is due to the designs having a greater amount of coil turns that lead to higher values of resistance, capacitance, inductance and mutual inductance. Overall, for the differentiating mode, the UV-LIGA sensors all show the ability to measure fast rise time signals.

The potential bandwidth of these sensors is very high, based on the relationship between rise-time and maximum bandwidth to be detected, being expressed in equation 4.43 as [4.23]:

$$Bandwidth = \frac{350}{T_r} \qquad \text{Eqn 4.43}$$

where T_r is the rise-time of the sensors.

4.5 Modeling of the UV-LIGA Rogowski coils in the self integrating mode

4.5.1 Bode response

The Bode response for sensor designs UV-1 and UV-2 (marked S1 and S2) is shown in figure 4.12, while the Bode figures for the rest of the sensor designs are located in Appendix 2. Figure 4.12 examines the Bode responses for these designs with the self-integrating impedance included (Z_L); the impact of this impedance is examined by varying its value. The values chosen were 0.1 Ω, 1 Ω, 10 Ω, 100 Ω and 1000 Ω, which correspond to Z1 to Z5 in the figure.

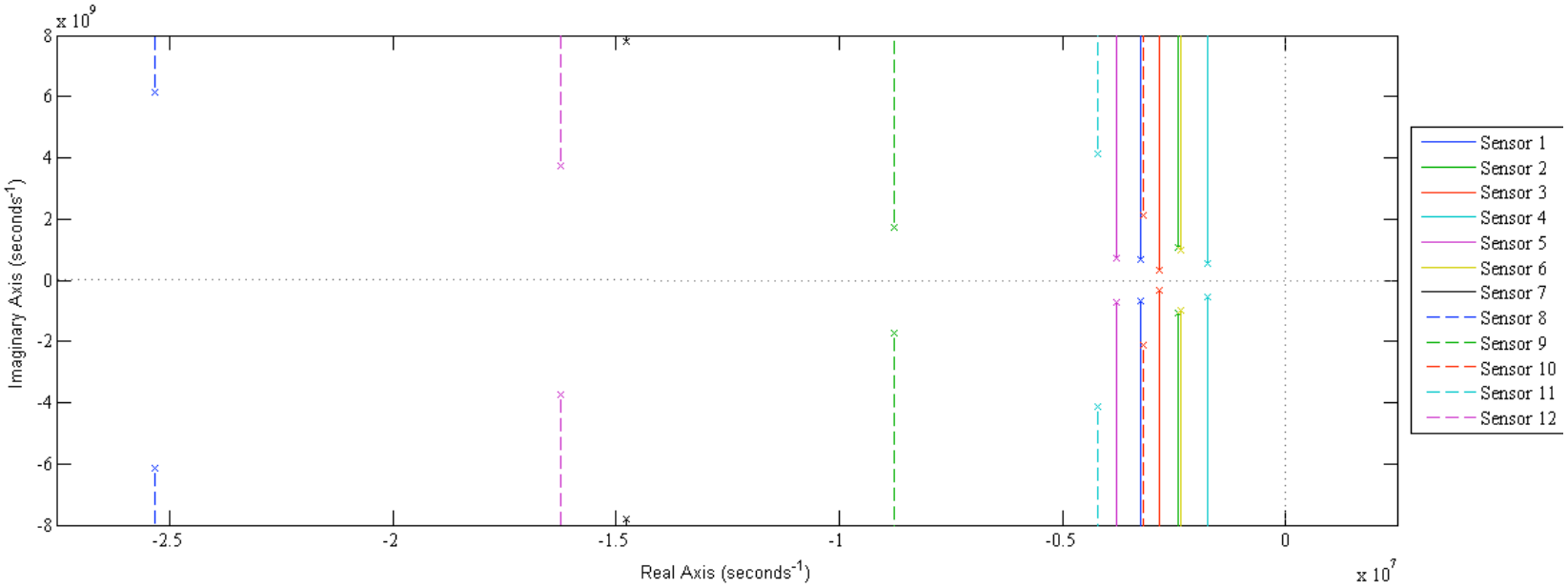

Figure 4.11 Root locus map of UV-LIGA manufactured Rogowski coils. Sensors are in differentiating mode.

Sensors 1 to 12 correspond to UV-1 to UV-12.

The Bode responses show that there is a trade-off between the magnitude of the response in terms of dB versus the phase response. Where the phase output is at -90°, the Rogowski sensors are operating in self-integrating mode [4.24]. At small impedances, the self-integrating mode of operation is valid from 3 MHz up to 8 GHz, but the magnitude response begins to decrease at around 1 MHz. For sensor design UV-3 with Z_L = 10 Ω, the magnitude response begins to decrease at around 10 MHz, yet the self-integrating mode exists further up the frequency range from 40 MHz to almost 200 MHz.

This is very close to the desired characteristics of the Rogowski coil for measuring PD signals. Sensor design UV-4 has a lower frequency at around 1 MHz where reduction in the output response begins to tail off, yet the sensor self-integrates from 4 MHz to 1 GHz. Even from lower than 1 MHz, the output response is lower than with other sensor and integrating impedance combinations. These combinations include design UV-5 with integrating impedance 100 Ω (S5, Z5). Although it has little reduction in the output response, there appears to be a very small range of frequencies where self-integration occurs. For example design UV-5 and design UV-6 (appendix) show self-integration to occur around 150 MHz. Sensor designs UV-9 and UV-10 (appendix) show a similar trade-off between output magnitude and the self-integrating region. The output response does not decrease till 30 MHz; the self-integrating region occurs around the 250 MHz range. The best trade-off appears to be those sensor designs with the impedance Z_4, which have small output attenuation at the low frequencies up to 40 MHz. The self-integrating region is much broader, ranging from around 100 MHz up to 2 GHz.

The Bode response for sensor designs UV-11 and UV-12 (appendix) also show similar behaviour. Designs UV-11 and UV-12 with impedance Z_4 both have magnitude responses that do not decrease until around 10 MHz. The self-integrating range seen in the phase diagram does not start to show until around 80 MHz and finishes at around 2 GHz. For all sensors, at small values of Z_L, the output response is much less than the input signal. It is as low as -50 dB for sensor UV-12 ($Z_L = Z_1$) and -60 dB for sensor UV-9 ($Z_L = Z_3$). For larger values of Z_L, the output response decreases very little when the impedances are in the range of Z_3 to Z_5. The self-integrating regions are very small, where the phase response decreases from 0° to -180° on an almost constant slope, passing through the -90° region.

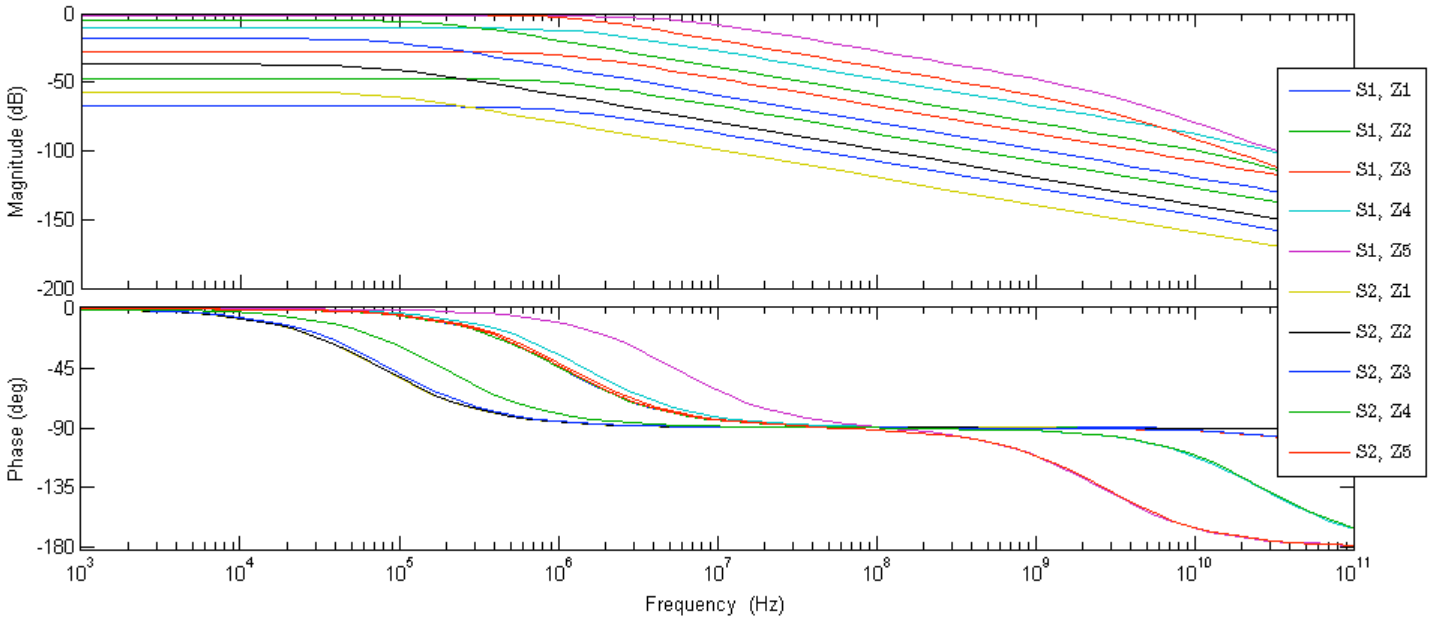

Figure 4.12 Bode response of sensor design 1 and 2 in integrating mode.

S1 = UV-1; S2 = UV-2; Z1 = 0.1Ω, Z2 = 1 Ω, Z3 = 10 Ω, Z4 = 100 Ω, Z5 = 1000 Ω.

The next aspect of simulation worth investigating further is to find whether there is a better range for Z_L. The most likely region will be where there is co-existence of good output response and reasonably broad self-integrating region is between Z_4 and Z_5.

4.5.2 Step response

The step response for sensor designs UV-1 to UV-6 is shown in the next two figures (4.13 and 4.14) for the condition that the self-integrating impedance is equal to 100 Ω or 1000 Ω. The remaining step response figures for all other sensor designs and self-integrating impedances are located in Appendix 2. The step response is for the other sensor designs (UV-7 to UV-12) and self-integrating impedance is located in Appendix 2, Integrating impedances of 0.1 Ω, 1 Ω, 10 Ω, 100 Ω and 1000 Ω are evaluated.

The output magnitude of all sensor designs to a step input signal is small when the Z_L is in the low region at around 0.1 Ω. For the sensor designs UV-1 to UV-6 with Z_L=100 Ω, the size of the magnitude response is 0.2-0.65 times the input signal. When Z_L is increased to 1000 Ω, the output of the sensors ranges from 0.7 (UV-3) to 0.95 times the step input.

The rise-times of these sensor designs range from 338 ns for UV-1 to around 633 ns for UV-4. The settling times for the step response for UV-1 to UV-6 show that the lowest settling time is UV-5 with 518 ns and the largest settling time is design S2 with 8.1 μs.
The magnitude of sensor output is, in increasing order, UV-6, UV-2, UV-4, UV-5, UV-1 and UV-3. Sensor design UV-6 has the smallest amount of turns yet has achieved the larger magnitude of 1.8 mV yet sensor design UV-3 has 69 turns and has the smallest output voltage of 0.2 mV.

Table 4.4 provides a summary of the step response characteristics which include the rise-time, peak response, peak response time, percentage overshoot and settling time. For each section in the table the sensors have been grouped according to being desireable (green), acceptable (orange) and not acceptable (red). For the section with settling time section, the outline is a dashed line. This reflects the final shortlist of sensors that give the best overall performance across all categories.

For designs UV-1 to UV-6, there are three designs that share the same sensing area (such as 10 mm x 10 mm for designs UV-1 and UV-2) with a low or high coil turns number for each design.

The designs with the higher amount of turns have the faster rise times. Sensor UV-1 has the higher amount of turns and also the fastest rise time; this is also repeated for sensor designs UV-3 and UV-5. The peak magnitude for these designs does not follow the same relationship as for the rise-time. Sensor UV-2 has a larger magnitude than UV-1; UV-3 and UV-4 do not follow this trend. Designs UV-3 and UV-4 have a sensing area that is double that of UV-1 and UV-2 (10 mm x 20 mm), so the total length of the coil turns is larger for this design. As a consequence, the capacitance, inductance and resistance of the sensor will increase, which impact on the output response to a step input signal.

The damping factor and natural damped frequency of the Rogowski sensors with different levels of capacitance, inductance and resistance will change according to the sensing area, the amount of turns and the width, height and spacing of turns. This explains why UV-3 is damped more than UV-4. UV-5 and UV-6 having a sensing area of 5 mm x 20 mm. Compared to UV-1 and UV-2, the area is the same, yet the resistance inductance and capacitance are less due to the amount of turns to be fitted while, at the same time, allowing enough space between the inner coil turns and the inner bond pad.

Filling the entire coil with turns would lead to a greater risk that one of the coil turns could be damaged by the wire bonding. UV-5 and UV-6 are configured so that the area of each coil turn can be aligned closer to the wire under test (WUT). The increase in length of the sensor allows a greater magnetic field density to be coupled compared to the 10 mm x 10 mm design. Settling times for the sensors UV-1, UV-3, UV-5 and UV-6 range from 500 to 900 ns.

For UV-2 and UV-4, the settling time is in the microsecond region. These designs have the two largest sensing areas but the smaller amount of turns and wider coil turn widths. For sensor UV-7 through to UV-12 and $Z_L = 0.1\Omega$, the output magnitude decreases from UV-7, UV-11, UV-10, UV-8, UV-12 to UV-9 and the settling times are all in the ns region (11 ns to 600 ns).

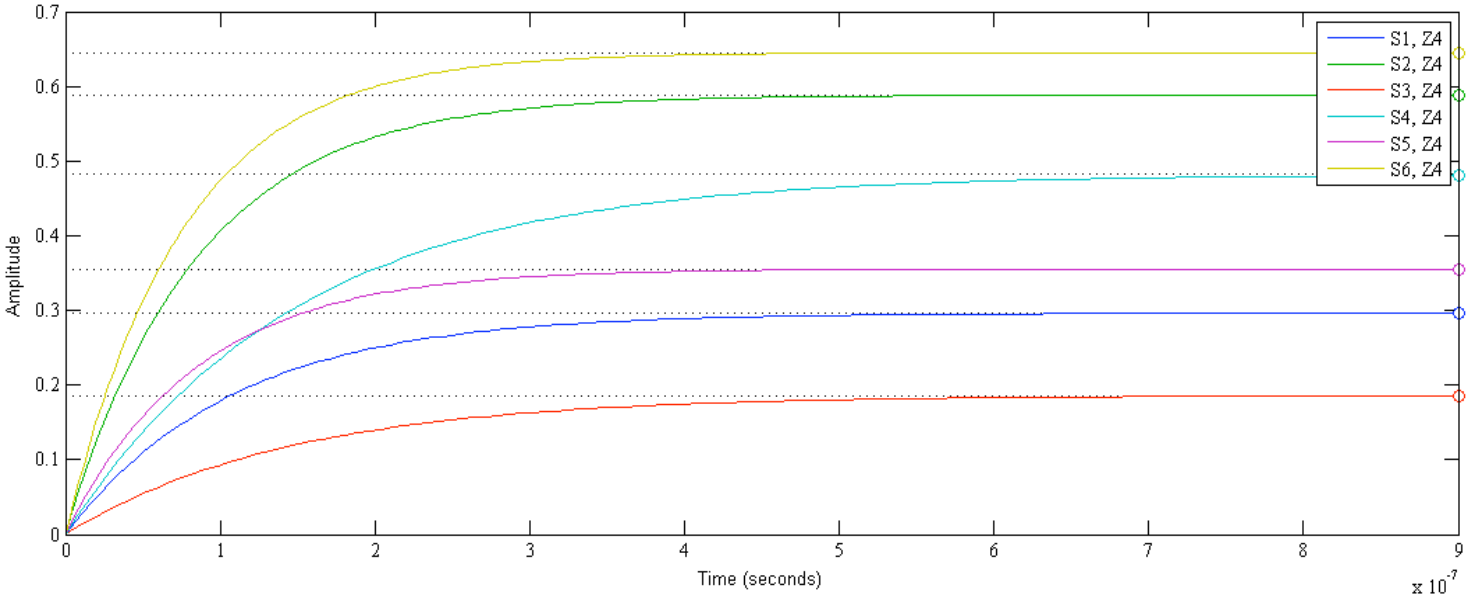

Figure 4.13 Step response of sensors 1 to 6 of the UV-LIGA manufactured Rogowski coils.

The integrating impedance is 100 Ω. Sensors 1 to 6 correspond to UV-1 to UV-6.

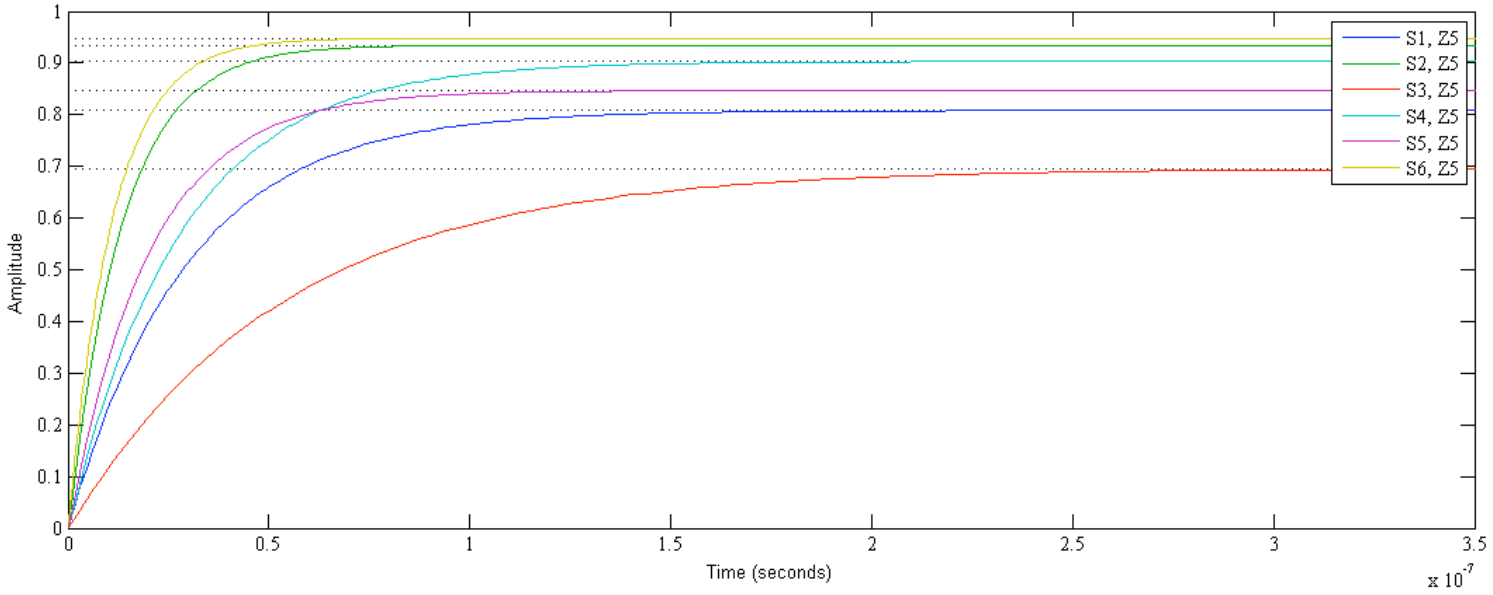

Figure 4.14 Step response of sensors 1 to 6 of the UV-LIGA manufactured Rogowski coils.

The integrating impedance is 1000 Ω. Sensors 1 to 6 correspond to UV-1 to UV-6.

This range of sensors has a smaller sensing area compared to UV-1 to UV-6, yet they manage to deliver faster rise-times and similar peak outputs in the mV region, which is similar to UV-1 to UV-6. The design with the smallest response is UV-9, which has a sensing area of 5mm x 10mm for an output of 0.86 mV.

Design UV-10 has a smaller amount of turns than UV-9 (23 vs. 37) yet presents a peak output of 3.6×10^{-3}, which is slightly more sensitive. This sensor is more under-damped than UV-9 meaning that it takes slightly longer to settle and possesses a slower rise-time. The rise-times decrease as Z_L increases from 0.1 Ω to 10Ω (Z1, Z2, and Z3). At low values of Z_L, the change in rise-time is small with decreases in the range of 14 to 70 ns for UV-1 to UV-6 and 7 to 90 ns for UV-7 to UV-12. There is no clear trend showing that choosing a maximum sensing area with maximum amount of turns provides a quicker rise-time as the integrating impedance is changed from Z1 to Z3.

UV-1 has more turns than design UV-2, yet UV-2 has a rise-time that decreases by around 50 ns from Z1 to Z3, compared to around 100 ns for UV-1. UV-6 has the smallest sensing area and the least amount of turns from UV-1 to UV-6, yet it has the largest decrease in rise-time of 70 ns. For UV-7 to UV-12, the designs that show the larger decrease in rise-time are UV-10 and UV-11. UV-10 has more turns than UV-9, yet shows the greatest decrease of 90 ns. UV-11 has a lesser amount of coil turns compared to UV-12 yet has a greater decrease in rise-time over the integrating range of interest (85 ns for S11, 9ns for UV-12). These designs have the smallest sensing area (5mm x 10mm for S9 and S10, 2.5mm x 10mm for UV-11 and UV-12). It appears therefore that the size and shape of the sensors, along with turns number, height of the coil turns and spacing between turns all contribute towards the rise-time of the sensor output when subjected to a step input signal.

All of the sensors analysed for the self-integrating condition show no overshoot, as the self-integrating impedances chosen are low enough to satisfy the condition $Z<Z_e$, where Z_e is expressed in terms of the inductance and capacitance of each Rogowski coil design ($Z_e = \sqrt{}$ (L/C).

4.5.3 Root locus analysis

The root locus diagram is a graphical plot of the loci of the roots of the characteristic equation as a function of a real parameter K. The parameter K of the system is otherwise known as the gain of the system; this is equal to one for the differentiating case whereas in self-integrating mode the gain of the system is a function of the self-integrating impedance Z_L. The root locus analysis is presented in figure 4.15, for the case of sensor UV-7 for Z_L ranging from 0.1 Ω to 1000 Ω. All designs are summarised in Table 4.5**,** which is located in Appendix 2.

The condition where $Z_L = 0.1$ (i.e. Z1) shows the highest amount of damping compared to designs Z2 to Z5. This means that the step output will decay over two times faster than the other self-integrating impedances. This is reflected in the bode figures of appendix 2.1 and 2.2 which show that as the self-integrating impedance increases, the damping decreases which results in less attenuation of the output signal. This behaviour is also summarized in Table 4.5.

To further study the trade-off between magnitude of the response and the region of self-integration, the gain factor (K) can be optimised to provide a specified damping ratio.

This is done by drawing a line from the origin at an angle of +/-θ with the negative real axis. The angle with the real axis can be translated into a specified damping ratio by the following equation:

$$\theta = \cos^{-1} \zeta \qquad \text{Eqn. 4.43}$$

It was suggested in [4.20,4.25] that an optimum damping ratio was 0.7, meaning that careful selection of the self-integrating resistance can tailor the output response of the sensor in mV while remaining in the self-integrating region.

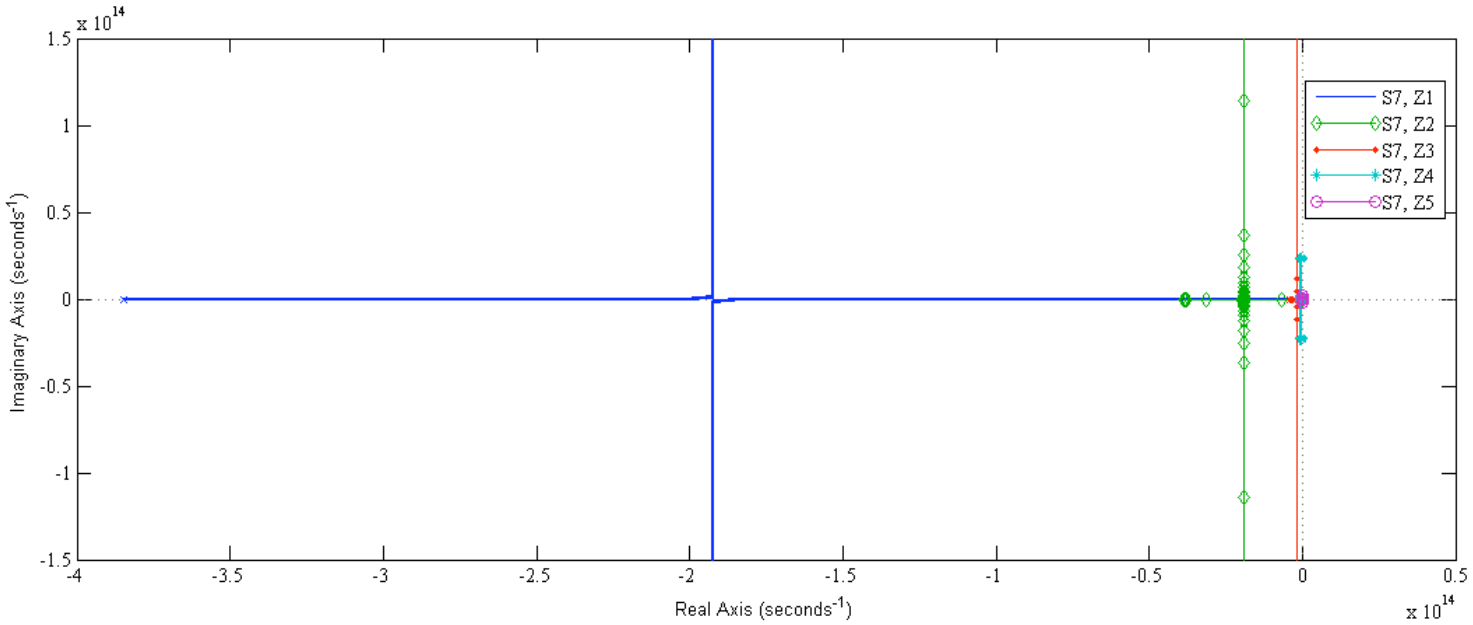

Figure 4.15 Root locus of sensor UV-7 of the UV-LIGA manufactured Rogowski coils.

Integrating Impedances used were Z = 0.1 Ω, 1 Ω, 10 Ω, 100 Ω and 1000 Ω. S7 = UV-7.

Table 4.4 Summary of step response of UV-LIGA Rogowski sensor in integrating mode.

Sensor type	Rise time (ns)					Peak response (x1000)					Peak response time (μ s)					Settling time(ns)				
	Z_L 0.1	Z_L 1	Z_L 10	100	Z_L 1000	Z_L 0.1	Z_L 1	Z_L 10	Z_L 100	Z_L 1000	Z_L 0.1	Z_L 1	Z_L 10	Z_L 100	Z_L 1000	Z_L 0.1	Z_L 1	Z_L 10	Z_L 100	Z_L 1000
UV-1	338	336	238	238	64.7	0.42	4.2	40.4	300	810	1.2	1.2	1.15	0.845	0.23	600	600	577	423	115.3
UV-2	451	449	398	187	297	1.4	14	125	590	934	16.2	15.9	14.2	6.67	1.06	8100	8000	7100	666	530
UV-3	389	387	380	316	118	0.228	2.3	22.3	186	700	1.38	1.38	1.35	1.126	0.4	692	690	677	563	210.4
UV-4	633	627.8	579.7	528.3	61.2	0.93	9.2	85	480	900	2.25	2.2	2.1	1.17	0.218	1130	1120	1030	585	109
UV-5	290.8	289.3	275.7	187.5	44.5	0.55	5.5	52	360	850	0.1034	0.1029	0.980	0.667	0.1583	518	515.2	491	333.9	79.3
UV-6	466.6	459	395.5	165.9	24.1	1.8	18	150	650	950	1.66	1.6	1.4	0.590	0.086	830.8	817	704	295.3	295.3
UV-7	74	70.65	48.5	117.5	1.31	5.3 X 10^{-3}	50.6 X 10^{-3}	0.35	0.84	0.98	0.263	0.251	0.172	0.0418	0.0041	1318	1258	86.4	86.4	2.36
UV-8	43.1	42.5	36.15	14.4	2	0.002	19.6 x10^{-3}	0.17	0.67	0.95	0.154	0.151	0.129	0.0514	0.00724	77.08	75.7	64.4	25.7	3.6
UV-9	125	124	115	67.2	14.1	8.6 x 10^{-4}	8.6 x 10^{-3}	0.08	0.46	0.98	0.445	0.442	0.410	0.239	0.0503	222	221	205	119.7	25.2
UV-10	342	332	252	74.1	9.1	3.6 x 10^{-3}	3.5 x 10^{-2}	0.27	0.78	0.97	1.2	1.18	0.896	0.264	0.0279	609.5	590	448.6	131.9	16.2
UV-11	259	242.5	145.5	29	3.1	7.9 x 10-3	7.4 x 10^{-2}	0.44	0.89	0.99	0.924	0.863	0.517	0.1035	0.00945	462.7	431.8	259.1	51.8	5.6
UV-12	67.5	66.3	56.3	22.5	3.1	2 x 10^{-3}	2 x 10^{-2}	0.17	0.67	0.95	0.240	0.236	0.200	0.0802	0.0128	120	118	100	40.2	5.6

4.6 The Qudos Rogowski sensor

4.6.1 Differentiating mode

Bode response

The characteristics of each sensor are summarised in Table 4.6 in terms of mutual inductance, inductance, resistance and capacitance. The values presented in this table were calculated using the equations presented earlier in this chapter for the mutual inductance. The other parameters were calculated using a similar technique as for the UV-LIGA manufactured sensors due to the sensor footprint being rectangular instead of the square design.

The table reveals that sensor 3 has the highest level of mutual inductance, inductance and resistance; the capacitance of this design is a close second to sensor 5.

Table 4.5 Design parameters for the Qudos manufactured Rogowski sensors.

	DESIGN Q1	DESIGN Q2	DESIGN Q3	DESIGN Q4	DESIGN Q5
Turn width (μm)	50	50	50	90	70
Turn Spacing (μm)	70	90	50	70	70

Table 4.6 Calculated value for the Qudos manufactured Rogowski sensors.

Sensor type	L_o (nH)	Mutual inductance (μH)	Resistance (Ω)	C_{TOTAL} (pF)	Resonant Frequency (MHz)	Magnitude (dB)
Q1	312.1	8.4	16	411.2	12.8	5.1
Q2	351.5	8.4	20	474.2	10.5	3.3
Q3	617.3	11.6	25	571.2	7.15	3.1
Q4	246.1	7.3	8.2	105.4	31	15.4
Q5	296.8	8.4	11.4	574.2	11.4	6.28

The sensor design with the smallest mutual inductance is design 4; the rest of the sensor parameters such as inductance, resistance and capacitance are lower than the other designs. It is intuitive to think of designing these sensors with a maximum amount of coil turns to maximize the mutual inductance between the sensor and wire under test, however, examination of the bode diagram shows that the magnitude response of sensor 3 starts to decrease at 50 MHz. In contrast, the magnitude response of sensor design 4 does not start to decrease from its resonant peak at 200 MHz.

Simply maximizing the sensor coil turns does not guarantee maximum sensitivity. The physical characteristics of the sensor design such as height of the coil turns, thickness of coil turns and spacing between coil turns have a secondary effect that results in the suppression of some frequencies within the range of interest.

Step response

The step response of the Qudos sensors is presented in figure 4.17; the performance of each sensor is summarized in Table 4.7. The results in this analysis are compared to the actual testing and characterization of the sensors that is presented in Chapter 7.

The step response shows that sensor Q4 has the fastest rise-time of 5.7 ns but the longest settling time of 228 ns. This is further explained by the overshoot being at 76.5 %, meaning that the settling time required for the oscillations to decay to within 2 % takes longer. Sensor design Q2 has the longest rise time of 18.4 ns but has a settling time of 139 ns; this is due to the overshoot being much less than sensor 4 at 27.4 % which means that a smaller time is required for the oscillations to decay.

Both Qudos and UV-LIGA sensors have similar rise-times in the ns range. UV-LIGA sensors UV-7 to UV-12 have sub ns rise-times and sensing areas that are larger than the Qudos designs. The main contributor to this difference is likely to come from the silicon substrate used on the Qudos designs and the return connection from the inner and outer bond pad being run underneath the coil sensing area, which would increase the capacitance for the sensors.

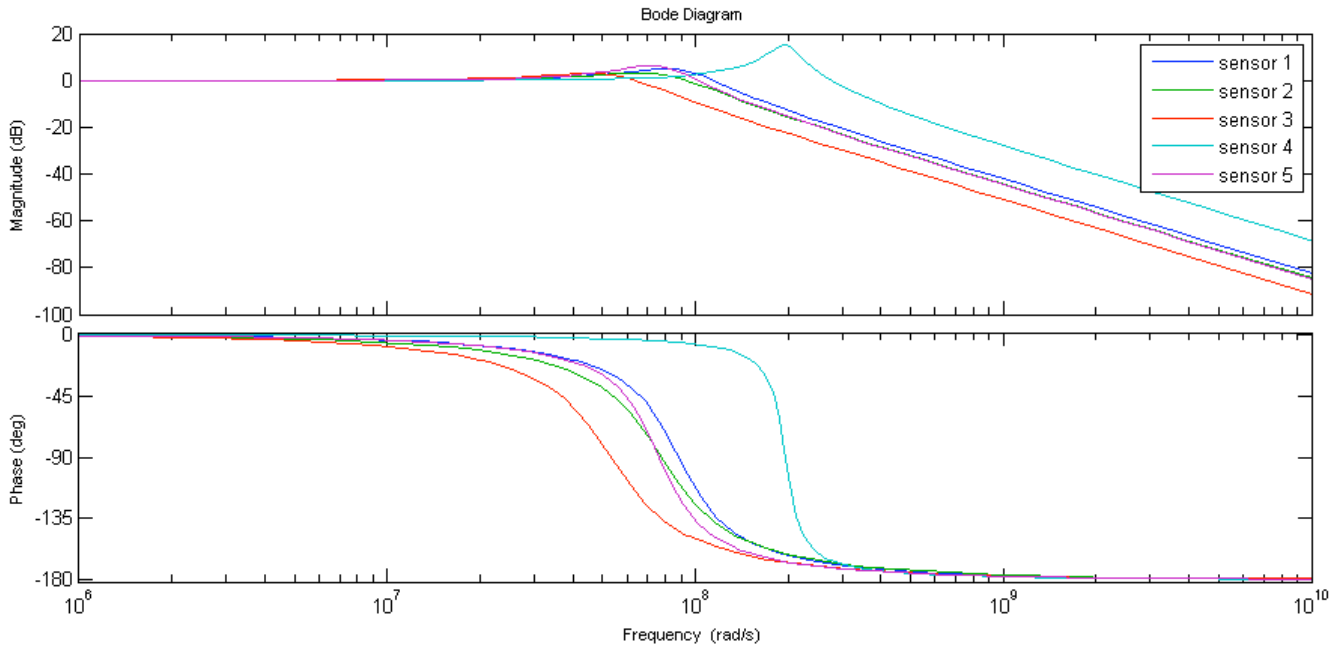

Figure 4.16 Bode diagram of the Rogowski coil manufactured by Qudos technology.

Sensors are in differentiating mode. Sensors S1 to S5 correspond to Q1 to Q5.

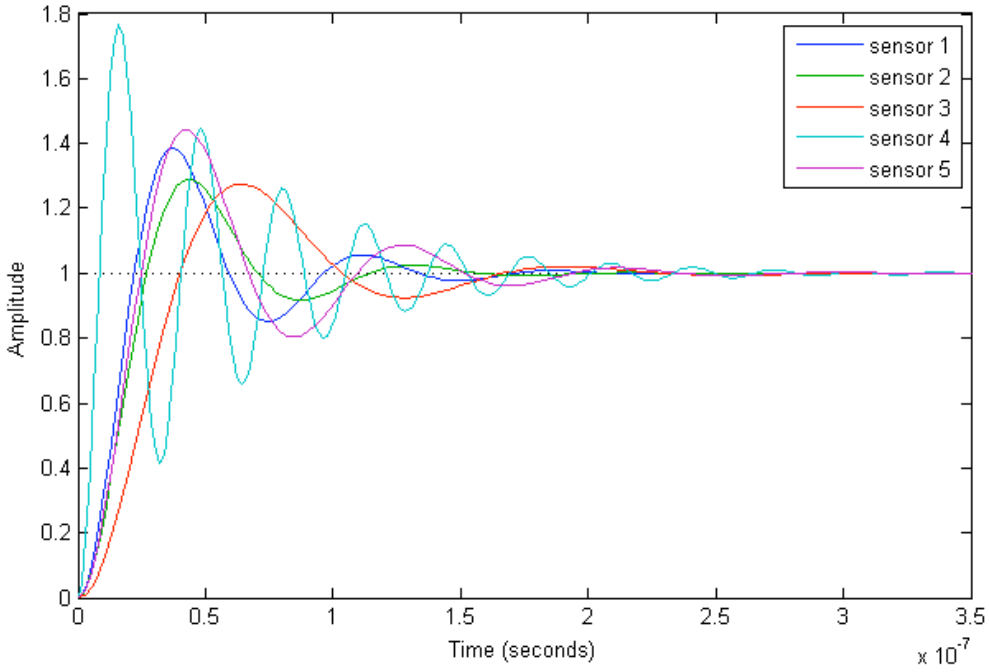

Figure 4.17 Step response of the Rogowski coils manufactured by Qudos Technology.

Sensors are in differentiating mode. Sensors 1 to 5 correspond to Q1 to Q5.

Table 4.7 Summary of step response analysis showing amplitude and time characteristics.

Sensor type	Rise time (ns)	Peak response	% Overshoot	Settling time (ns)
Q1	14.9	1.4	38.5	154
Q2	18.4	1.29	28.9	139
Q3	27	1.27	27.4	197
Q4	5.7	1.77	76.5	228
Q5	16.6	1.44	44.1	184

Root locus analysis

The root locus analysis of the Qudos sensors is presented graphically in Figure 4.18, with a summary of the real and imaginary components of each design presented in Table 4.8. Figure 4.18 shows that sensor Q4 is the closest to the intercept of the real and imaginary axis. The high imaginary component corresponds to the high oscillations seen in the step response analysis of the sensor, whilst the low real component is related to the level of damping the design provides to large overshoot and subsequent oscillations. Sensor Q2 has the largest real component of the root locus analysis, whereas the imaginary component is the second smallest of the designs.

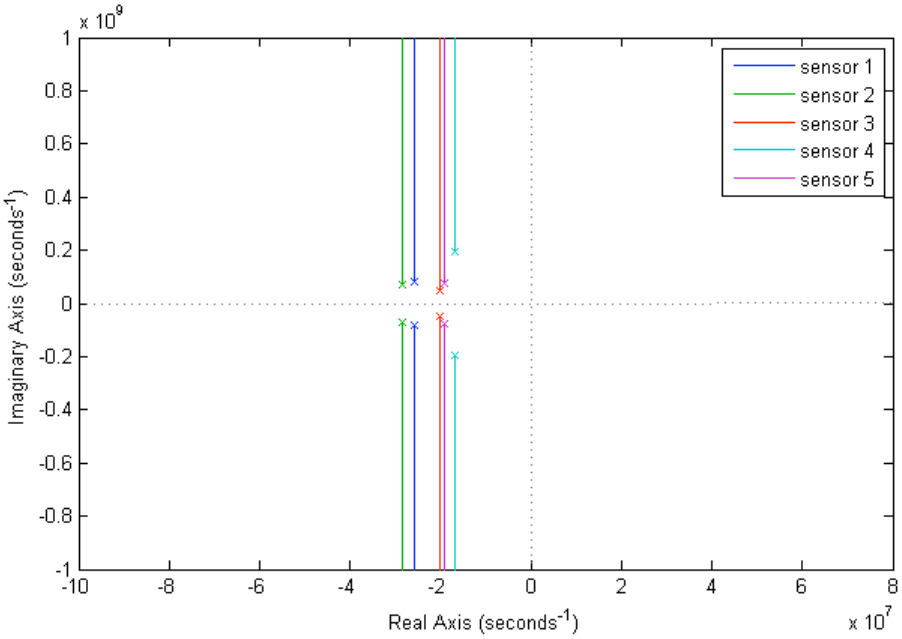

Figure 4.18 Root locus analysis of the Rogowski sensors manufactured by Qudos Technology.

Sensors S1 to S5 correspond to Q1 to Q5.

The small imaginary component explains the lower overshoot and the real component explains the higher level of damping to the oscillatory response of the sensor to a step input signal. The damping ratios and settling times of the poles are determined by their location on the root locus diagram. To achieve a settling time less than T_S, then real part of the poles must lie to the left of the point $4/T_s$. Drawing a line to the position of the pole and calculating the angle between the line and the real axis allows us to determine the damping

ratio for each of the poles. The damping ratio is calculated as $\zeta = \cos(\theta)$; poles that lie below the 45˚ line have damping ratios greater than 0.7.

Table 4.8 Poles of the transfer function for the Qudos manufactured Rogowski coils.

Sensors are operating in differentiating mode.

Sensor	Pole (Real Part)	Pole (Imaginary Part)
Q1	-2.6×10^7	$\pm j8.5 \times 10^7$
Q2	-2.85×10^7	$\pm j7.2 \times 10^7$
Q3	-2×10^7	$\pm j4.9 \times 10^7$
Q4	-1.66×10^7	$\pm j19.5 \times 10^7$
Q5	-1.92×10^7	$\pm j7.4 \times 10^7$

4.6.2 Integrating mode

Bode response

Compared to the UV-LIGA manufactured sensors, there is no bandwidth range where self-integration occurs. All sensors in the Bode response show that the phase change passes straight through -90° and onwards to 180° where the response flattens off. The bode response of design Q4 is presented in figure 4.19, which shows how the magnitude response and phase response changes as the self-integrating impedance (Z_L) changes from 0.1 – 1000 Ω. At smaller values of Z_L, the magnitude output is more attenuated and the phase response transitions over a smaller frequency range from 0 to 180 degrees. As Z_L approaches 1000 Ω, the magnitude response becomes less attenuated and the phase response requires a larger frequency range to transition from 0 to 180 degrees.

Step response

The step response shows some differences compared to the UV-LIGA manufactured designs. As figure 4.20 shows, the responses contain overshoot elements as the self-integrating impedance is varied from Z1 to Z5.

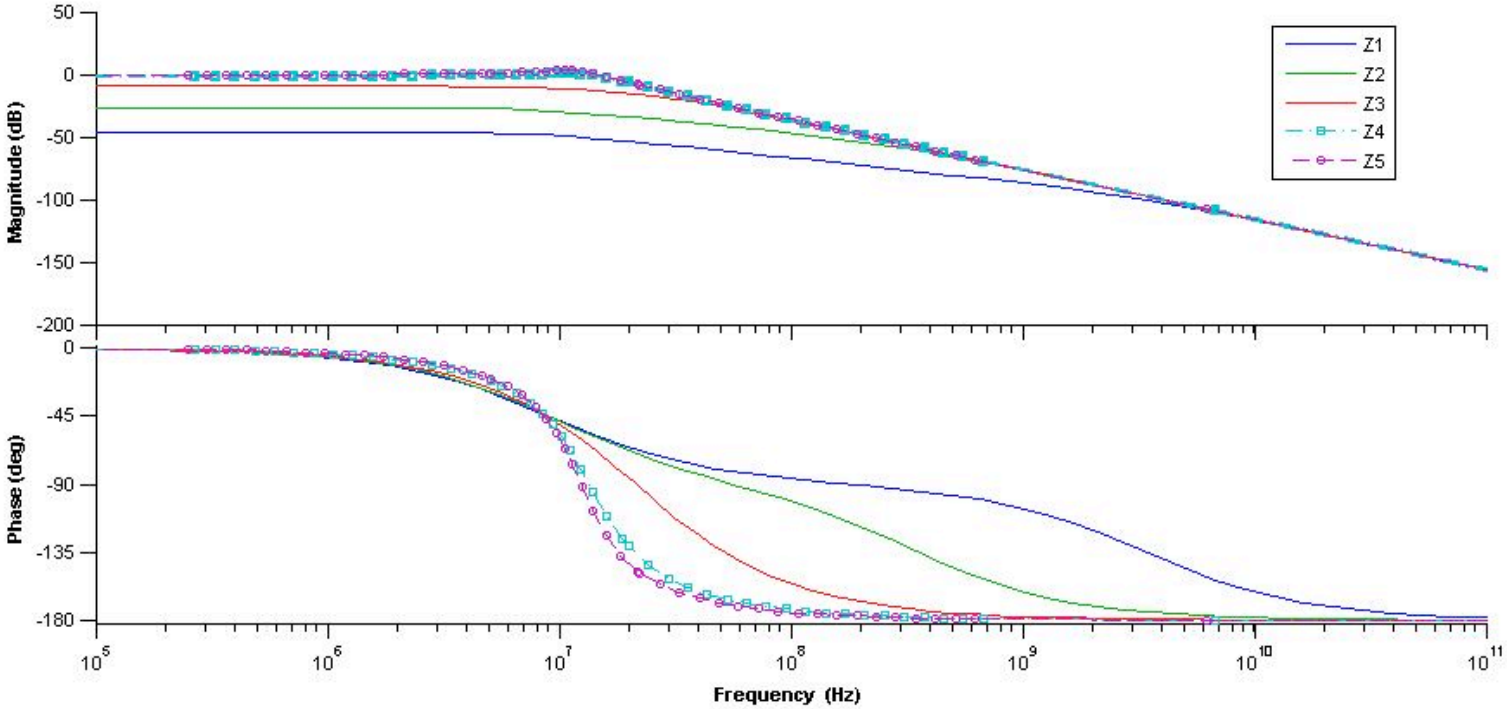

Figure 4.19 Bode diagram of the Rogowski coil manufactured by Qudos Technology.

Sensor is Q4 are in integrating mode. Z1=0.1Ω, Z2=1Ω, Z3=10Ω, Z4=100Ω and Z5=1,000Ω.

In addition to the level of overshoot in the step responses, there is a relation to the amount of damping that occurs in the output waveform. At Z_L = 1000 Ohms (Z5), the overshoot is the greatest; the settling time is also expected to be the longest as shown figure 4.20. Upon closer inspection of the settling times for these designs in Table 4.9, it appears that Z_L=1000 Ω does not have the longest settling time. The integrating impedances of Z4 and Z3 produce the longest settling times. Due to the level of overshoot seen in all of the Qudos sensors for the larger integrating impedances, further optimisation is needed to provide a suitable damping level that minimizes the overshoot yet maximizes the bandwidth where self-integration would occur.

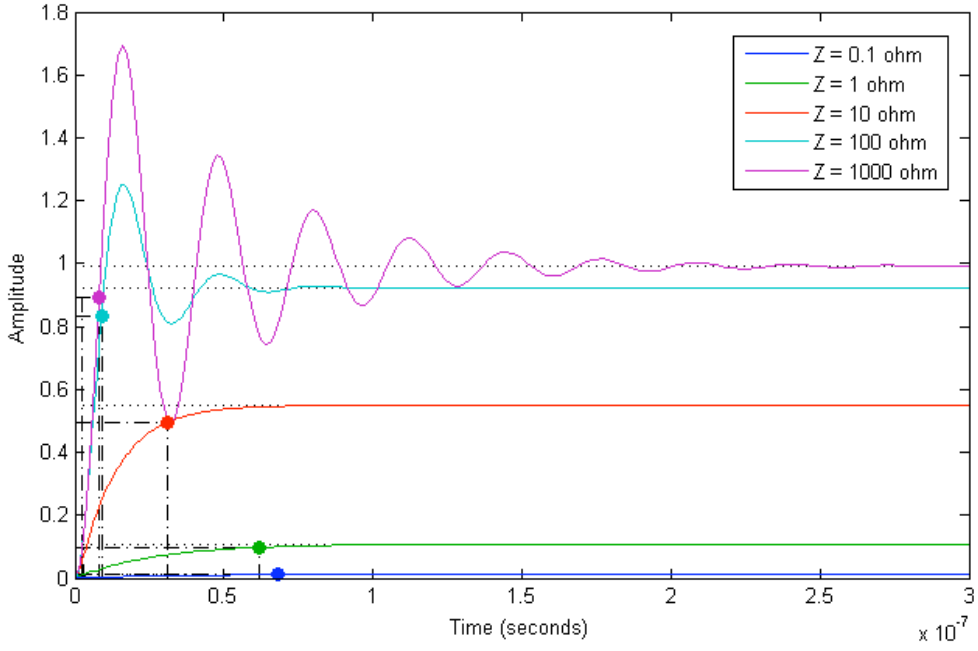

Figure 4.20 Step response of sensor Q4 manufactured by Qudos Technology.

Sensor is operating in integrating mode.

Root locus analysis

The root locus analysis of the Qudos sensors in self-integrating mode is summarised in **Appendix 2.15**. The table shows that, as Z_L is increased up to 1000 Ω, the real parts of the complex roots begin to decrease, such that less damping of the output signal occurs.

In addition to this change, there is an increase in the imaginary poles from zero to a magnitude that is comparable to the real part of the complex roots. This explains why there is a pronounced oscillation in the responses of these sensors to a step input signal. Further simulation of these sensors should be carried out to find the optimum self-integrating impedance for each design.

Table 4.9 Rise-time performance of Qudos manufactured Rogowski coils with self-integrating impedance connected.

Sensor type	Integrating impedance (Ω)	Rise-time (ns)	Peak amplitude	Overshoot	Settling time (ns)
Q1	0.1	42.6	0.00621	0	75.9
Q1	1	40.3	0.0588	0	72.1
Q1	10	24.8	0.385	0	43.7
Q1	100	15.5	1.35	37	88.5
Q1	1000	15.5	1.08	25.6	126
Q2	0.1	34.8	0.00498	0	68.5
Q2	1	36.8	0.0476	0	65.9
Q2	10	25	0.333	4.5e-13	43.3
Q2	100	18.4	0.997	19.7	98
Q2	1000	18.3	1.25	27.8	135
Q3	0.1	54	0.00398	0	96.3
Q3	1	52.2	0.0385	0	93.4
Q3	10	38	0.286	0	67.6
Q3	100	27.1	0.939	17.3	137
Q3	1000	27	1.23	26.2	156
Q4	0.1	65.2	0.012	0	116
Q4	1	58.8	0.109	0	105
Q4	10	28.6	0.549	1.01e-13	516
Q4	100	6.59	1.25	35.2	547
Q4	1000	5.67	1.7	70.9	179
Q5	0.1	56.7	0.0087	0	101
Q5	1	52.5	0.0806	0	94.1
Q5	10	27.8	0.467	0.00822	46.8
Q5	100	17.1	1.18	31.5	136
Q5	1000	16.6	1.41	42.8	182

4.7 Summary

This chapter presented the design and analysis of different Rogowski sensor designs: the UV-LIGA manufactured and Qudos manufactured versions. The range of performance available for micro-manufactured Rogowski sensors was examined through the design parameters used for both design variants.

UV-LIGA designs were evaluated by choosing different sizes of sensing areas while varying the coil turn widths from 20μm to 50μm with the spacing between turns kept constant at 30μm. The performance of the Qudos manufactured sensors was assessed by choosing a silicon substrate, while retaining the same sensing footprint across all design versions. Design variation was introduced through changing the coil turn widths and spacing. This version also aimed to show the impact of manufacturing Rogowski sensors on a common substrate where other sensors and on-board electronics could be combined onto one chip.

In terms of the best overall sensor design, the deciding factors are output magnitude, rise-time, settling time and cost per device; this is summarised in Table 4.10. For output magnitude, focus was on achieving the maximum amount of coupling between the sensor and the WUT. This would put UV-LIGA design UV-3 as the best candidate due to a mutual inductance of 80.9μH being achieved when there was a distance of 1mm between sensor and WUT.

When UV-3 is examined at a deeper level by creating a lumped parameter model of the sensor, the lumped parameter inductance, capacitance and resistance is used to derive the second order behaviour of the sensor. This allows the key parameters of the sensor to be examined, which are the signal magnitude at the output of the Rogowski sensor and the ability to react to fast rising transient signals. The transient response was examined by calculating the step response of the sensor. Results show that design UV-3 has very good rise-time and peak response characteristics, but the settling time is one of the largest out of the sensors selected in table 4.10. Sensor design UV-1 has better rise-time, peak response and half the settling time, but has less than half the mutual inductance of UV-3.

Design UV-3 in the differentiating condition did not possess the fastest rise-time. This was achieved with the smaller sensor designs UV-7 –UV-12, which delivered sub nano-second

rise-times. These designs also delivered the shortest settling times that were of sub-µs duration.

The Qudos manufactured sensors also delivered rise-times and settling times in the nano-second duration that were comparable to design UV-3, UV-7 and UV-8. The peak response output of the sensor was smaller, but this suggests that the sensor is less under damped than design UV-3. The settling times of the Qudos sensors are larger than the UV-LIGA sensors, which is attributable to the higher capacitance from the silicon substrate.
Due to the sensor footprints of UV-9 TO UV-12 and the Qudos sensors being smaller than design UV-3, this would allow a higher number of sensors to be produced per wafer. This results in a reduction of cost per sensor and an opportunity to increase the profit per sensor. The drawback of going with the smaller sensor designs is that the mutual coupling between wire and sensor at 1mm spacing is up to ten times smaller.

Table 4.10: Shortlist of UV-LIGA and Qudos Rogowski sensors in differentiating mode

Sensor type	Rise time (ns)	Mutual inductance (µH)	Overshoot	Settling time (ns)
UV-1	1.58	35.2	98.5	1.2
UV-3	3.06	80	97.4	1.38
UV-7	0.134	3.7	99.4	0.265
UV-8	0.171	7.1	98.7	0.154
UV-9	0.613	24.4	98.4	0.445
UV-10	0.488	15.3	99.4	1.22
UV-11	0.259	8.8	99.7	0.927
UV-12	0.281	13.7	98.6	0.241
Q1	14.9	8.4	38.5	154
Q2	18.4	8.4	28.9	139
Q3	27	11.6	27.4	197
Q4	5.7	7.3	76.5	228
Q5	16.6	8.4	44.1	184

In terms of the magnitude of the output, this is linked to the mutual inductance of the designs. For all sensors, the mutual inductance between WUT and sensor is much higher than discussed by other research for the conventional torroidal designed sensors. This is due to the coil turn windings being brought as close to the WUT as possible. Were these windings to be located at a larger radial distance from the WUT then the mutual inductance

would decrease from the micro-Henry region to the nano-Henry region.
The step response analysis showed the sensors contained a high amount of overshoot, which is attributed to the low level of damping that each sensor provides for these designs.

For the self-integrating condition, table 4.11 has a shortlist of the sensors that meet all of the criteria. Sensor design UV-3 displays a slower rise-time than UV-7 and UV-8 by almost a factor of one hundred. For the settling times, designs UV-7 and UV-8 settled up to one hundred times quicker than design UV-3. The Qudos designs were up to ten times slower that designs UV-7 and UV-8 with design Q4 having the fastest rise-time. This design had a much slower settling time than UV-7 and UV-8.

The design UV-7 had a greater coil turn width yet had the faster rise-time and settling times, meaning that we achieve the best performance sensor with some level of manufacturing robustness built in. This is due to it being easier to manufacture sensors with 50 um coil turns than the 20 um coil turns. This allows a greater device yield to be achieved during the manufacturing process.

Table 4.11: Shortlist of UV-LIGA and Qudos Rogowski sensors (self-integrating mode)

Sensor type	Rise-time (ns)	Peak response (x 1000)	Settling time (ns)
UV-1	64.7	810	115.3
UV-2	297	934	0.530
UV-3	118	700	210.4
UV-4	61.2	900	109
UV-7	1.31	0.98	2.36
UV-8	2	0.95	3.6
UV-11	3.1	0.99	5.6
UV-12	3.1	0.95	3.6
Q1	14.9	1.4	154
Q2	18.4	1.29	139
Q3	27	1.27	197
Q4	5.7	1.77	228
Q5	16.6	1.44	184

Although designs UV-7 and UV-8 were the best overall designs, the Qudos designs were still fit for purpose and could still catch fast rise time fault signals at a fast enough speed to

trip a circuit breaker if required. Further optimisation of the integrating resistance could be carried out to try and improve the rise-time and settling times of the designs. This would allow the integration of other sensors and on-board electronics in later design iterations that would provide a multi-sensor to be manufactured on the same substrate. The results of the characterisation and test later in this thesis will demonstrate that there is close agreement to these simulations.

References

[4.1] S.B. Bulumulla, N.A. Evers, "Flexible, lightweight sensor for monitoring wiring in aircraft", *2005 IEEE Sensors,* pp.790 - 793, Oct. 30 -Nov. 3, 2005.

[4.2] C. Qing and L. Hong-bin, "Design and Characteristics of Two Rogowski Coils Based on Printed Circuit Board". *IEEE Transactions on Instrumentation and Measurement,* vol. 55, no. 3, pp. 939 - 943, June 2006.

[4.3] B.G. Moffat and M.P.Y. Desmulliez et al, "Micro-fabricated current sensor for arc fault detection of aircraft wiring", *Proc. IEEE/CPMT 2nd International Conference on Electronic Systems Technology Integration (ESTC)*, 1- 4th September 2008, pp. 299 - 304.

[4.4] S. Takeuchi, N. Futai, et al, "Selective drive of electrostatic actuators using remote inductive powering", *The 14th IEEE International Conference on Micro Electro Mechanical Systems*, pp. 574 - 577, 25-25 Jan. 2001.

[4.5] J. Wu and V. Quin et al, "Powering efficiency of inductive links with inlaid electroplated micro-coils", *IOP Journal of Micromechanics and Microengineering*, vol. 14, no. 4, pp. 6, Feb 2004.

[4.6] H. Greenhouse, "Design of Planar Rectangular Microelectronic Inductors", IEEE *Transactions on Parts, Hybrids, and Packaging*, vol. PHP-10, no. 2, June 1974, pp. 101-109.

[4.7] F.W. Grover, "Inductance Calculations: Working formulas and tables", Dover Phoenix Editions, 28th May 2004.

[4.8] C.R. Neagu, H.V. Jansen and A. Smith et al, "Characterization of a planar micro-coil for implantable microsystems", *Sensors and Actuators A: Physical,* Volume 62, Issues 1–3, Pages 599-611, July 1997.

[4.9] N. Karrer, and P. Hofer-Noser, "PCB Rogowski Coils for High di/dt Current Measurement", *IEEE 31st Annual Power Electronics Specialists Conference,* vol. 3, pp. 1296 – 1301, 23 June, 2000.

[4.10] G. Robles, M. Argueso and J. Sanz et al, "Identification of Rogowski Coil Parameters for Partial Discharge Measurement", *IEEE Instrumentation and*

Measurement Technology Conference Proceedings, pp. 1 - 4, 1 - 3 May 2007.

[4.11] J. Zhang, "Flip Chip Assembled High-Q MEMS Inductors on Silicon for RFIC Applications", *PhD Thesis, Heriot-Watt University*, June 2007.

[4.12] V. Dubinkas and H. Edin, "High-Frequency Model of the Rogowski Coil With a Small Number of Turns," *IEEE Transactions on Instrumentation and Measurement,* vol. 56, no. 6, pp. 2284 - 2288, Dec, 2007.

[4.13] J. Peters, "Design of High Quality Factor Spiral Inductors in RF MCM-D", Masters Thesis, *Massachusetts Institute of Technology*, September 2004.

[4.14] B. Wang and D. Wang et al, "A Rogowski coil current transducer designed for wide bandwidth current pulse measurement". *IEEE 6th International Power Electronics and Motion Control Conference,* pp.1246 - 1249, 17-20 May 2009.

[4.15] J. DiStefano, A. Stubberud et al, "Schaums Outline of Feedback and Control Systems", 2nd Ed., Schaum's Outline Series.

[4.16] W. Bolton, "Control Systems", *Newes Publishing*, 30 Jan 2002.

[4.17] J.L. Lang and A. Argawal, "Foundations of Analog and Digital Electronic Circuits", Morgan Kaufmann Publishing, July 18, 2005.

[4.18] W. Li, "Study of the virtual instrumentation applied to measure pulsed heavy currents", *IEEE Instrumentation and Measurement Society*, pp. 284 – 288, 17 January 2005.

[4.19] W. Li, C. Mao and J. Lu, "Some considerations of designing a high performance Rogowski coil for pulsed current measurement", *IEEE Trans. Instrumentation and Measurement,* vol. 4, no. 1, pp. 284 – 288, 17 Jan., 2005.

[4.20] H. Yu and D. You et al "Study of a novel CT for short circuited current measurement", *IEEE/PES Transmission and Distribution Conference and Exhibition: Asia and Pacific,* pp. 1 – 5, 2005.

[4.21] C. Wang, Y. Chen et al, "Design of printed circuit Rogowski coil for highly accurate current measurement", *International Conference on Mechatronics and Automation*, pp. 3801 – 3806, 5-8 Aug. 2007.

[4.22] A. K. Mandal, "Modern Control Systems", *New Age International Pvt. Ltd Publishers,* December 1, 2008.

[4.23] Q Zhang, J Zhu and J Jia et al, F Tao and L Yang, "Design of a current transducer with a magnetic core for use in measurements of nanosecond current pulses", *Measurement Science and Technology*, vol. 17, no. 4, pp. 895 – 900, 23 March 2006.

[4.24] M. Argueso and G. Robles, et al, "Implementation of parameters of a Rogowski coil used for the measurement of partial discharges". *Review of Scientific Instruments*, vol. 76, no. 6, pp. 065107 – 065107, 7 June 2005.

[4.25] L.A. Kojovic, "Rogowski sensor for power grid travelling wave based fault location", IET *9th International Conference on Developments in Power System Protection*, pp. 438 - 443, 17-20 March 2008.

Chapter 5 UV LIGA process for the manufacture of the Rogowski sensor

5.1 Introduction

This chapter presents the UV-LIGA fabrication process of the planar Rogowski current sensor that is investigated in this thesis. Successful fabrication of micro-inductors has been demonstrated at the MIcroSystems Engineering Centre (MISEC) at Heriot-Watt University using this technique [5.1,5.2]. Packaging techniques such as flip chip bonding were used to connect torroidal windings for the pot core micro power inductor and produce the return path of a planar inductor. The focus for the manufacture of the sensor will move away from the flip chip approach for connecting the return path of the sensor to the outside contact pad. This is because the planar sensors being manufactured possess a much larger area than the work discussed by [5.2]. The resulting larger amount of coil turns means that there is greater difficulty in manufacturing the device due to the risk that there are broken coil turns and/or issues with overplating of the sensor pattern, leading to adjacent turns connecting with one another and shorting the sensor, rendering it useless. The process flow is presented in figure 5.1.

5.2 UV LIGA

There are two forms of LIGA micro-manufacturing techniques, which are X-Ray LIGA and UV LIGA. Erwin Willy Becker and Wolfgang Ehrfeld created the X-Ray LIGA technique in the early 1980s in response to the demand to be able to manufacture high-aspect-ratio structures of the order of 100:1 at micrometer precision for the mass production of micron sized nozzles for uranium-235 enrichment. Their research was carried out at the Institute for Nuclear Process Engineering (Institut fuer Kernverfahrenstechnik, IKVT) at the Karlsruhe Nuclear Research Centre (Forschungszentrum Karlsruhe), since renamed as the Institute for Microstructure Technology (Institut fuer Mikrostrukturtechnik). The high precision structures were realised by the highly collimated radiation emitted by the X-ray Synchrotron. LIGA stands for LIthographie, Galvanoformung, Abformung, which means Lithography, Electroplating and Replication. In this process, a polymer photoresist sensitive to X-ray radiation is applied to a conductive substrate, followed by the placement of a custom designed mask incorporating the desired pattern on it above the sensitive photoresist.

This permits the light to pass through areas of the structured pattern and into the sensitive photoresist layer. If the photoresist is a positive tone resist, areas exposed to X-Ray radiation will undergo a series of changes to its molecular structure. These exposed areas are now more susceptible to being dissolved in certain solutions; this allows the selective etching of the sensitive polymer such that the exposed region dissolves away leaving a patterned 3D imprint of the desired structure. If the resist is a negative tone resist then the area of the resist that is exposed becomes more resistant to dissolving in developing solutions; the unexposed regions will dissolve when placed in the developing solution.

Subsequent deposition of a metal in the mold after this step followed by removal of the polymer mold leaves a free standing replicate metallic structure; this may be used as a final part or as a mold insert for precision molding of batches of these structures. The generation of X-Ray radiation requires the use of a synchrotron machine, which is very expensive to procure and run; it is therefore not suitable for mass production. Another drawback is the cost of producing the masks that allow the transfer of the desired structures.

An alternative to X-Ray LIGA is the UV-LIGA process, which presents itself not only as a cheaper alternative to microstructure realisation, but is also integrateable with certain IC processes. In this process, an inexpensive light source such as a mercury lamp is used to produce ultraviolet light to expose the polymer photoresist. The complexity and intrinsic cost associated with X-Ray mask manufacture are also avoided by using a simpler and less expensive chromium mask. The only downside with this approach is that it is not as effective at producing high precision and high aspect ratio structures as the X-ray LIGA method.

This chapter presents the sequence of steps involved using this technique, as well as the design parameters that influence the profiles of the structures.

5.3 Fabrication process for planar Rogowski sensor

The cleanroom facilities at MISEC facilitate the manufacture of a planar Rogowski coil sensor using the UV-LIGA technique. Previous research has proven the feasibility of manufacturing and packaging planar micro-inductors [5.1,5.2]; planar inductor sizes in

this research were much smaller in terms of the outer diameter sizes [5.2] but comparable in the height and width of coil turns. The challenge for manufacturing the sensor is being able to transfer continuous coil turns without breaks in them. Discontinuities could arise from contamination of the photo-mask used to image transfer the sensor design onto the photoresist or trapped particles in the polyimide mould that stops the electroplating from occurring.

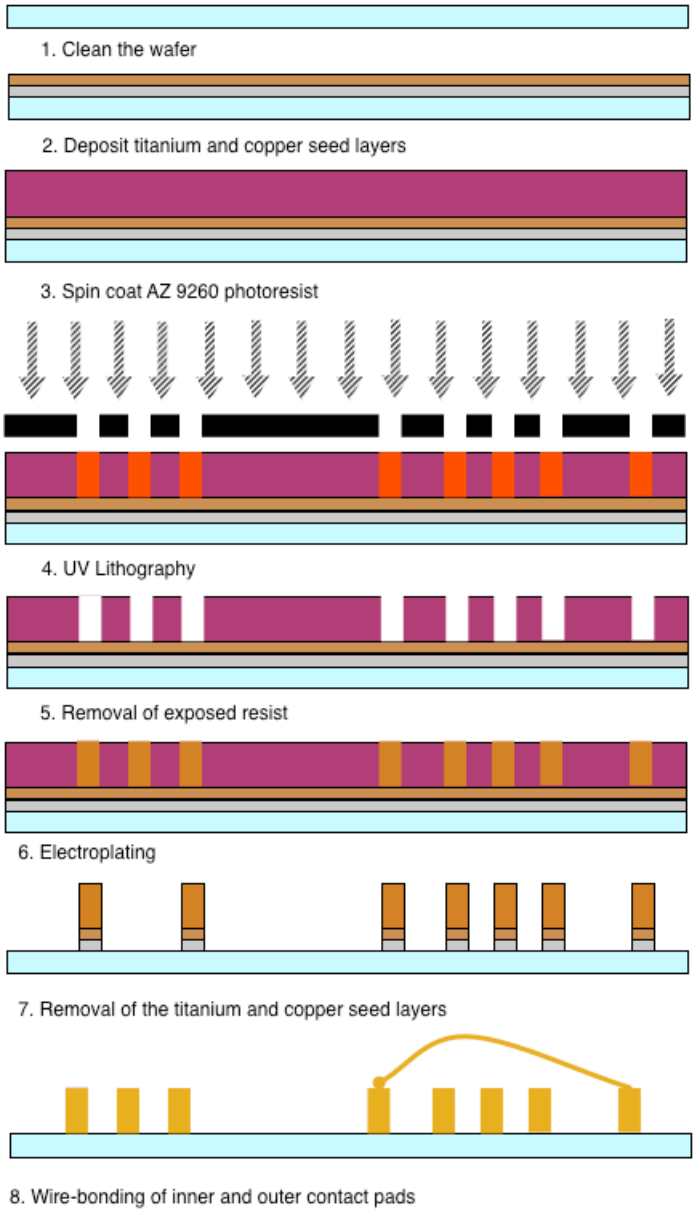

Figure 5.1 Process manufacturing steps for the UV-LIGA Rogowski sensor

5.4 Photomask design

For the fabrication of the current sensor by the UV-LIGA process, a photomask must ! rst be designed. The design of the mask incorporates the layout of the planar current sensor and the inner and outer bond pads for the electrical completion of the sensor circuit. The outer pads serve to allow probing of the sensor and also the connection of additional circuitry such as the integrating resistance.

Due to the cleanroom equipment being based on processing 3-inch wafers, the mask design will incorporate the sensor patterns within a 3-inch diameter area. The designs are created using a mask design software package called L-Edit from Tanner. The final mask structure is then exported to a suitable processing format, such as GDSII, for the mask vendors, such as JD Phototools, to create. The chosen polarity of the mask is clearfield, which means that the sensor design layout will be black and the background clear. The photomask used for the manufacture of the sensors is shown in figures 5.2a – 5.2f.

5.5 Substrate preparation

The correct preparation and cleaning of wafers prior to the manufacturing process steps are critical to achieving high device yields in MEMS and Integrated Circuit (IC) manufacture. It has been reported in [5.3] that 50 per cent of yield losses in IC manufacturing are attributed to contamination of the wafer surface by micro-particles due to poor cleaning procedures.

There is a two-stage preparation sequence for the manufacture of the 3-inch soda glass wafers. This ! rst stage of the process is critical in providing high yields and focuses on making the wafers free from surface defects and contamination such as grease. Such defects result in the affected area offering a poorer level of adhesion for both seed layers, which may also prevent the electroforming from occurring at the affected sites in later process steps.

To remove the contamination, the wafers are ! rst loaded in a wafer holder and then put inside a glass beaker and ! lled with de-ionised (DI) water and some Decon 90 cleaning agent. The beaker is then placed in an ultrasonic bath for around 90 minutes.

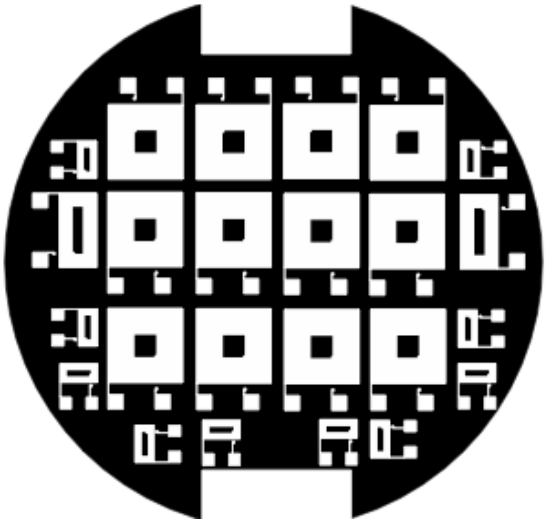

Figure 5.2a: 10 mm^2, 0.5 x 10 mm, 0.5 x 0.25 mm

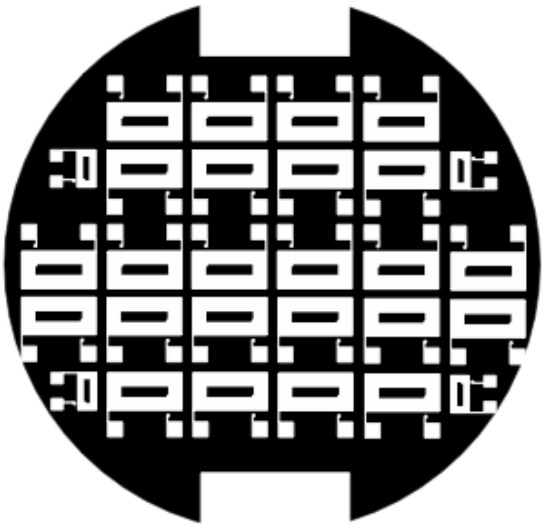

Figure 5.2b: 0.5 x 10 mm, 0.5 x 0.25 mm

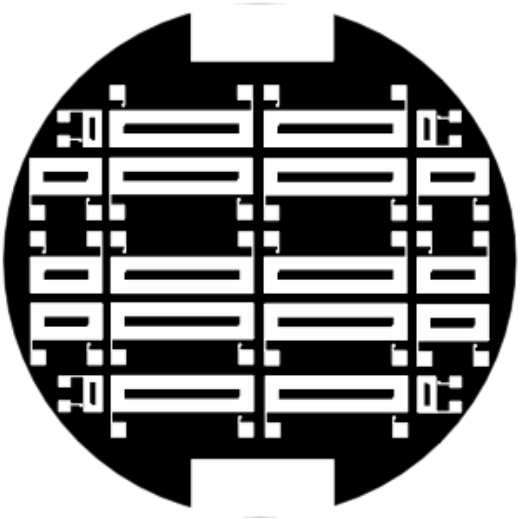

Figure 5.2c: 20 x 5 mm, 10 x 5mm, 5 x 2.5 mm

Figure 5.2d: 20 x 10 mm, 10 x 5mm, 5 x 2.5mm

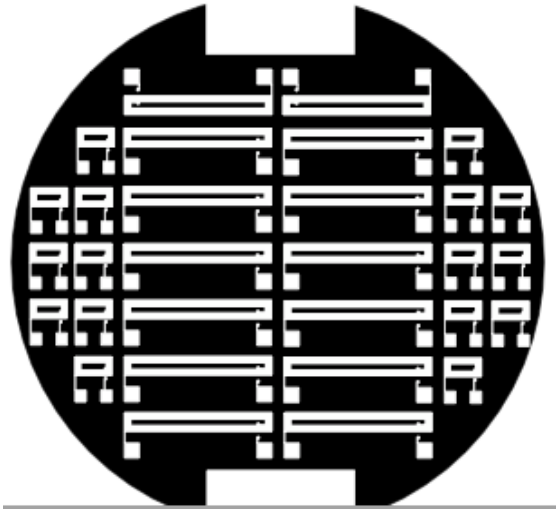

Figure 5.2e: 20 x 2.5 mm, 5 x 2.5 mm

Figure 5.2f: 20 x 2.5 mm, 5 x 2.5 mm, 20 x 10 mm, 10 x 5mm

Figure 5.2 Mask designs for manufacture of the UV-LIGA Rogowski sensors

This step should remove any grease and micro-particulates from the wafer surface. The second stage focuses on removing any leftover cleaning agent remaining on the wafer. The wafer holder containing the wafers is removed from the beaker and rinsed with DI water and set to the side of the work area. The beaker contents are emptied, and the beaker is rinsed a few times with DI water to make sure all remaining residue from the cleaning agent is removed. After this has been done, the wafer holder containing the wafers is put back in the beaker and filled back up with DI water. The beaker is then placed back in the ultrasonic bath for 60 minutes. After this has been carried out, the wafers are removed from the wafer holders and dried with pressurized nitrogen. They are now ready for the next stage, which is the deposition of the seed layers.

5.6 Seed layer deposition

Seed layers are an important foundation process step when micro-manufacturing devices that require electroplating to be performed during later process steps. Two very thin layers of metals of hundreds of nanometers thickness are deposited on the contaminant free glass wafer surface. The first of the metals to be deposited is Titanium, as it offers greater adhesion of the second metal to the glass surface. The second metal is used as a seed layer for electroplating and must possess a low sheet resistance to function as an electrode during electroplating. Titanium has a high electrical resistance and would produce an uneven current density [5.1] if used as an electrode resulting in electroplated structures of non-uniform thicknesses during electroplating.

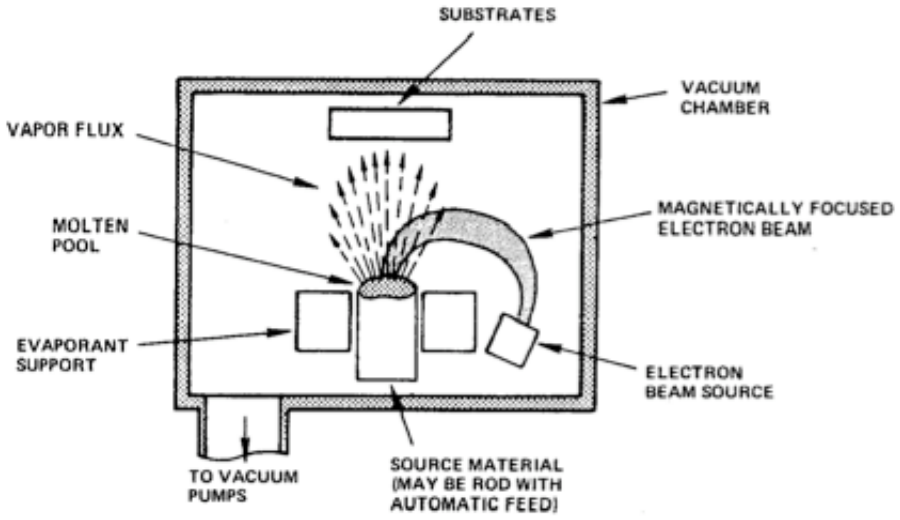

Figure 5.3 Operation of electron beam evaporator

Chromium is another option to be used as the first metal to be deposited, however it is more difficult to deposit using the equipment described in this section. Copper was chosen for the second layer. The process starts by loading five glass wafers on the wafer holder in the vacuum chamber. One slot in the wafer holder is left vacant as explained later. The wafer holder sits approximately 10 cm above the crucible that holds the metal slugs used for depositing the thin metal layers chosen in this fabrication sequence.

The deposition of the seed layers can be carried out by either Chemical Vapour deposition (CVD) or Physical Vapour Deposition (PVD). MISEC has the capability to deposit thin films by PVD using the electron beam (E-beam) evaporation apparatus. The primary mechanism of depositing thin films by E-beam evaporation is illustrated in figure 5.3; the electron beam is created by the thermionic filament that is heated to a high temperature by high AC current, followed by applying a bias of 7 kV. Electrons are emitted from the filament, which are directed to bombard the surface of the metal slug in the crucible. Direction is provided by an arrangement of permanent magnets and electromagnets that are controlled from outside the vacuum chamber.

The target metal is heated to melting point and starts evaporating. The role of the vacuum chamber in this process is to facilitate the transfer of the metal vapour to a cold surface such as the glass wafer. Once it has reached the wafer surface it condenses, hence forming the desired metal thin film. If the vacuum were not present then not much deposition would occur due to the heavy bombardment of air molecules. Removing the presence of the air molecules allows for free molecular flow of the metal vapour, and occurs at pressures below 10^{-6} bar. When starting to deposit the metal thin films, the current used for the e-beam is around 60 mA. The wafer holder is set so that the empty slot on the wafer holder is above the crucible, i.e. no wafer is available for any of the metal vapour to form on it. The crucible is allowed to heat up for a few minutes before rotating the wafer holder to present the first wafer to be covered by the titanium vapour. Around 30 seconds is enough to deposit around 60 nanometers, therefore after this time has elapsed the wafer holder is rotated once more to present the next wafer and this process is repeated till the vapour has covered all five wafers. Once this has been done the wafer holder is reset in the position that is vacant from holding a wafer. The e-beam current is decreased to zero and the crucible is rotated so that it presents the next metal to be deposited, which in this case is the copper slug. The e-beam current is then increased to around 30 mA for around a minute and then gradually

progressed to around 60 to 100 mA. This depends on how thick the oxide layer is on the copper slug and also why the temperature is increased to penetrate through this into the copper. The e-beam is usually left firing at the crucible for up to 5 minutes to make sure that the oxide layer and any contaminants have been removed from the copper slug. This can be viewed through the window in the vacuum chamber and usually there is a green tinge to the light from the burning away of the oxide layer. After this the copper layer should be bright orange in colour and ready for deposition to begin.

The first wafer is rotated into view of the vapour and left for around 90 seconds, which is enough to provide a thickness of 200-250 nanometers. Once all wafers have been subjected to the vapour coating, the vacant position of the wafer holder is moved above the crucible and the e-beam current is set back to zero. The e-beam is switched off and the chamber left to cool for up to an hour before bringing the chamber back up to normal pressure and opening it to remove the wafers; care should be taken not to open the chamber too soon as it can result in oxidation of the metal.

5.7 Photolithography

At this stage, the seed layers have been deposited and the wafer surface is ready to provide its function as an electrode in the electroplating process step. To enable the pattern transfer of the sensor design onto the seed layer, the photolithography processes outlined in figure 5.4 are followed.

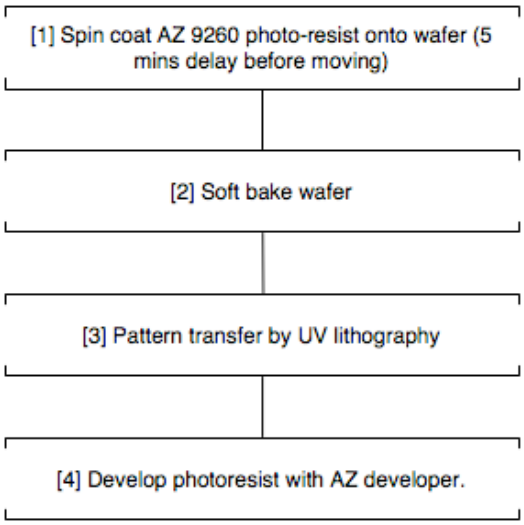

Figure 5.4 Process flow of UV Lithography

The proceeding sections provide an extensive background to the methodology and the trade-offs required in designing the process steps.

5.7.1 Photoresist and Spin coating

AZ Photoresist

AZ 9260 thick film photoresist, which is manufactured by Clairant under its 9200 product series, was used for the photolithography steps. The photoresist provides high resolution and good aspect ratio structures, and produces good sidewalls during development. In work by Brunet et al [5.5], planar micro-coils were micro-manufactured using AZ 9260 photoresist that produced aspect rations of 6:1 and thicknesses up to 81 μm. The photoresist also showed other advantages such as good adhesion to copper seed layers and ease of removal.

Spin coating

The spin coating of photoresist onto a glass wafer provides the material for transfer of the mask (sensor) image during the photolithography stage [5.6]. The rotational speed and ramp rate of the spin coater, the viscosity and time duration dictate the overall thickness of the polymer material used as a mold, dictating thereby the maximum thickness of electroplated metal. Although the plating rate is generally the same across the wafer, overplating can occur due to differences in the maximum height that can be plated without shorting out the coil turns. The spin coater comprises of a vacuum chuck that grips the glass wafer tightly prior to operating at high rotational speeds. Around 3 milli-litres are deposited on the wafer using a syringe, ensuring that no bubbles are created. If there are any bubbles, they can be removed by using a pipette to gently suck them out of the resist.

The sensor is to be electroplated to around 8μm in height, therefore the resist height was chosen to be around 15μm to enable the production of straight sidewalls, and to allow for any variations of resist height across the wafer surface. The spin coater is programmed to start at the spreading cycle followed by the coating cycle.

Table 5.1 Spin parameters for various AZ thicknesses [5.1].

	30 µm	**20 µm**	**5 µm**
Distribution of the AZ	30 Rev/sec	30 Rev/sec	30 Rev/sec
	70 rpm	70 rpm	70 rpm
	20 sec	20 sec	20 sec
Spread cycle for uniform wafer coverage	400 rpm	400 rpm	400 rpm
	100 Rev/sec	100 Rev/sec	100 Rev/sec
	20 sec	20 sec	20 sec
Cycle for final photoresist thickness	1000 rpm	1000 rpm	1000 rpm
	200 Rev/sec	200 Rev/sec	200 Rev/sec
	10 sec	10 sec	10 sec

The spreading cycle makes the photoresist to spread out from the middle towards the edges as a result of the centrifugal force. The spin parameters shown in table 5.1 were used to deposit a suitable photoresist thickness for electroplating the sensors. These parameters were also used in [5.1] to micro-manufacture a micro-inductor using UV-LIGA.

5.7.2 Soft bake

After the spin coating has been performed and the wafer allowed to settle for 5 minutes, the resist will still contain up to 15 per cent solvent [5.7]. There is also the possibility that the resist will contain built in stresses. For this reason, it is considered beneficial that a low temperature soft baking stage be performed at a temperature of around 75 to 100 °C for up to ten minutes duration. The corresponding baking times stated in [5.1] and [5.2] were followed to try and establish the best spin and soft bake parameters for accurately transferring the sensor design from the photomask into the resist. These parameters are summarised in Table 5.2.

Table 5.2 Soft bake parameters for various AZ thicknesses [5.1].

30µm	20 µm	5 µm
Temp: 110 °C	Temp: 110 °C	Temp: 110 °C
300 sec baking	180 sec baking	90 sec baking
1 hour delay	1 hour delay	1 hour delay

The major factor in choosing the process steps was whether there was any breaks in the coil turns once the UV exposure and development had been performed. In a majority of fabrication attempts, it was found that performing the spin and bake process steps in [5.2] produced a better fidelity reproduction of the sensor in the resist and less coil turns were broken.

5.7.3 Exposure and development of photo-resist

The purpose of the exposure and development stages is for the accurate transfer of the sensor image from the photomask onto the photoresist. The dosage of the UV exposure dictates how far the UV light penetrates into the resist: if the resist is not developed at the seed layer interface then residues of the photoresist are left behind. This presents a barrier stopping electroplating from occurring at the affected sites; breaks in the continuous coil turns appear and the device will show as an open circuit and is permanently damaged. This stage in the manufacturing process was one of the highest contributors to the poor manufacturing yield. To overcome this issue sensors were designed with conductor widths of 50 µm.

The simplest version of a UV exposure system consists of a UV lamp, which illuminates the resist-coated wafers by transmitting through the transmittable areas of the photomask. The required functionality of this process step is to deliver light with the adequate intensity, directionality, spectral characteristics and uniformity such that a near perfect replication of the mask design is transferred onto the photoresist. The incident dose of energy given in J/cm^3, is a product of the exposure time multiplied by the incident radiation.

The controller unit on the Tamarak UV system is set to around 1250 mJ energy for photoresist thicknesses of around 15µm. The photoactive compound in AZ9260 is DiazoNaphtoQuinone (DNQ), which is sensitive to the i-line (365 nm) and h-line (419 -

329 nm) wavelengths. UV exposure through i-line and h-line filters produces a photochemical effect in the exposed regions of photo-resist where the DNQ compound releases a nitrogen (N_2) molecule; the DNQ compound then absorbs a H_2O molecule, forming a carboxylic acid. This results in the changing of the cresol resin from hydrophobic to hydrophilic, which causes de-protolysis of the O-H group defining how soluble the photoresist becomes in aqueous solution.

The soft bake, UV exposure energy dose and developing time have an effect on the success of replicating the electroplating stage to high fidelity levels. If the photolithography parameters are incorrect then a host of problems such as radiation profile and pattern distortion occur. If the development stage is not performed for long enough then there will be residues left on the seed layer which will impede the electroplating from occurring at the affected site [5.8]. Electroplating that grows over these affected sites will result in loss of adhesion between the metal and seed layer.

5.8 Inspection

Examination of the mould, once revealed in the photoresist, is performed using a microscope and white light interferometer analysis [5.1], as shown in figures 5.5a - 5.5c. The initial microscope analysis shown in figure 5.5a provides a quick first pass check for signs of un-removed photoresist residue in exposed regions of the photoresist.

The next stage (figure 5.5b) is to look at the coil turns using the white light interferometer, which will show reflections in the exposed regions of the mold where the copper seed layer is present. If any residue is present on the copper layer then the software shows this in terms of a height change in the pattern. One example of this would be a bridge of photoresist connecting two adjacent coil tracks. In 5.5b, this would show up in red if the height was similar to the rest of the coil turns.

In addition to this inspection, the structures embedded in the resist were checked across the wafer for height profiles in the resist as shown in figure 5.5c. This provides information on regions of the photoresist that were thinner than others so that a decision could be made about what sensors could be successfully electroplated to the desired thickness.

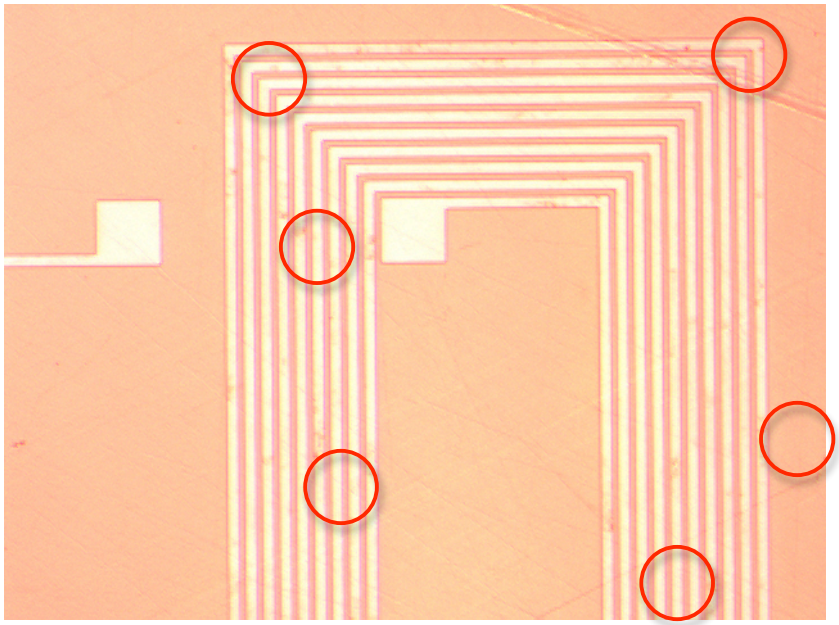

Figure 5.5A Microscope inspection of a 2.5 x 5 mm Rogowski sensor with residues left in some exposed coil turns.

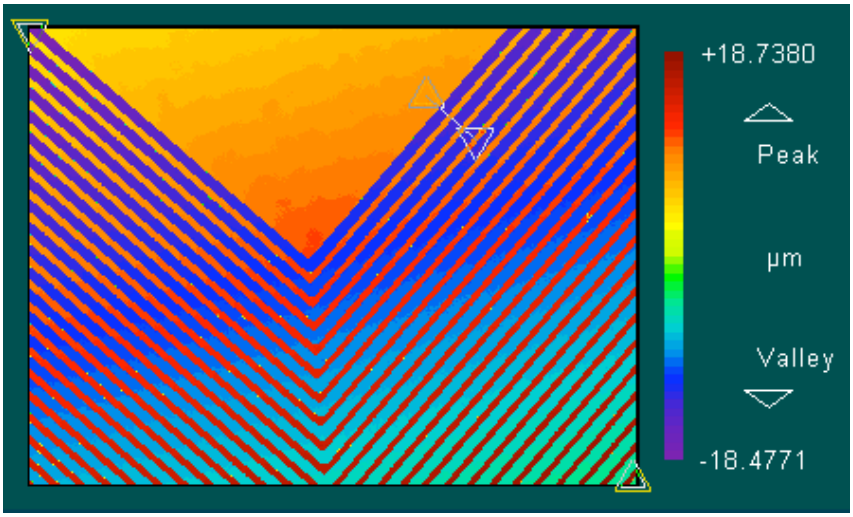

Figure 5.5B Inspection of the transferred sensor image into the photoresist using white light interferometry

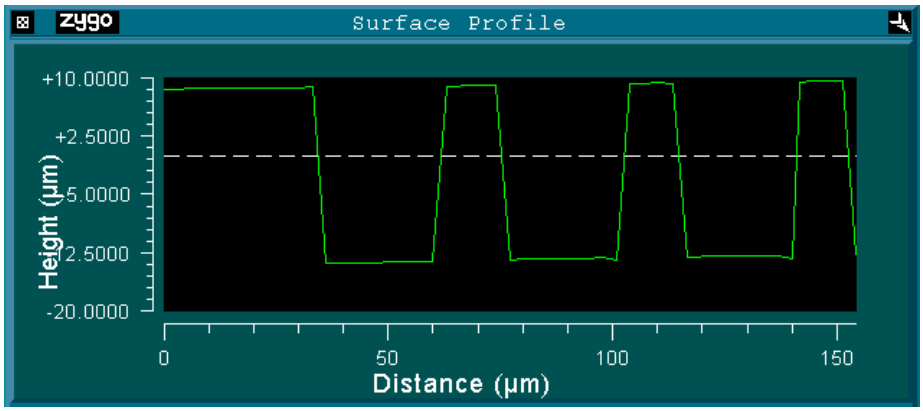

Figure 5.5C Inspection of the transferred sensor image into the photoresist using white light interferometry.

One of the main challenges with this manufacturing process was ensuring that no bridges between coil turns were present [5.9]. This is shown in figure 5.6.

A short-circuited coil turn would render the sensor useless during the electroplating step as it would replicate the mould with metal, reproducing the bridge in the process. The cause of such a defect arises from things such as over concentrated levels of developer solution or excessive developing times. This would cause small portions of photoresist to break away and/or thinning of the photoresist.

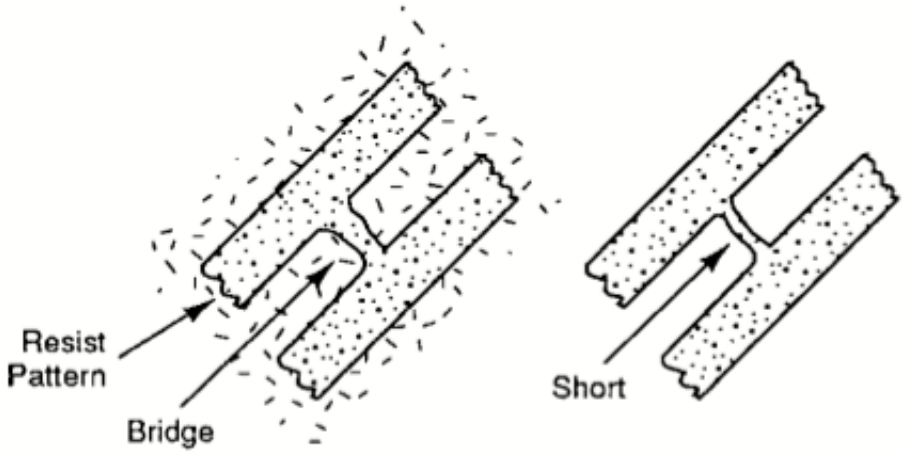

Figure 5.6 Bridging between coil tracks

5.9 Electroplating

Electroplating is the process step used in UV-LIGA to fill the exposed mould in the photoresist with conductive material to replicate a series of coil turns that make up the Rogowski sensor design. The setup for electroplating is shown in figure 5.7. It comprises of a bath of electrolyte that contains metal ions, two electrodes, and power supply. One electrode functions as a counter electrode (anode) and the other as a cathode. Deposition of the metal occurs when a voltage potential is set up between these electrodes that produces electric field in the electrolyte that attracts the positively and negatively charged ions in the solution to each electrode. The copper seed layer visible in the exposed regions of the photoresist covered wafer enables it to function as a cathode [5.10], therefore positively charged ions in the solution are attracted to the exposed regions of the seed layer on the wafer and the accumulation of metal occurs. This is described by equations 5.1 and 5.2.

Oxidation (Anode) $Me \rightarrow Me^{z+} + ze^{-}$ Eqn. 5.1

Reduction (Cathode) $Me^{z+} + ze^{-} \rightarrow Me$ Eqn. 5.2

where Me is the deposited metal at the cathode.

The metal chosen for the coil turns was gold as this is compatible with the gold wire bonding that is required to complete the sensor circuit at the last process step. The gold plating cell uses a Potassium Sulphite based [5.1] cyanide free solution (ECF 60) from Metalor Technologies (UK) Ltd. In addition to the electroplating setup shown in figure 5.7 a hotplate and magnetic stirrer setup based on Flynn et al [5.1,5.2,5.10] managed to successfully manufacture UV-LIGA DC-DC Converter and micro-coils. The hotplate and magnetic stirrer are required to maintain a constant temperature and agitation in the solution. The magnetic stirrer provides a uniform distribution of ions near the cathode, which should help provide the optimum rate of deposition across the wafer. As the ions deplete in the solution, the level of agitation has to be increased from 150 rpm to around 250 rpm.

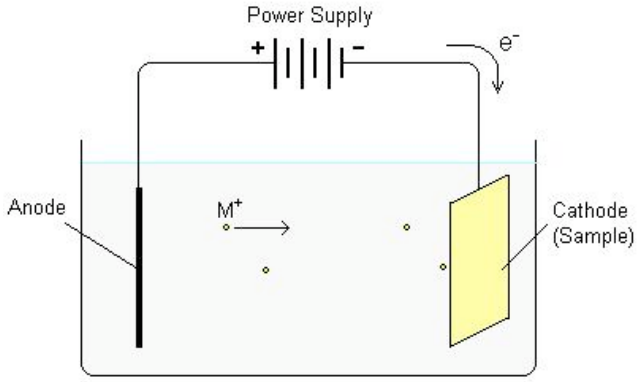

Figure 5.7 Schematic of DC electroplating setup.

Care is required when adjusting the speed of rotation to avoid introducing turbulent flow [5.1], which produces pitting in the metal. The temperature control also prevents pitting and promotes a uniform concentration of ions in the solution.

Faraday's Law in equation 5.3 calculates the amount of metal deposited at the cathode. It states that the amount of metal (M) deposited is dependent on time (t), applied current (I), molecular weight of the deposited metal (M), number of electrons involved in the reaction (Z) and the Faraday constant (F).

$$m = \frac{t \cdot M \cdot I}{Z \cdot F} \qquad \text{Eqn. 5.3}$$

Re-arrangement of the equation provides calculation of the height (h) of the electroplated film. The terms introduced into equation 5.4 are the area available for the electroplating to occur (A) and the volumic mass density (ρ) of the metal.

$$h = \frac{t \cdot M \cdot I}{\rho \cdot A \cdot Z \cdot F} \qquad \text{Eqn. 5.4}$$

Deposition of metal is faster for smaller aspect ratio patterns and the deposition rate changes dynamically as the mould fills up with metal. The aspect ratios of the micro-structures indeed decrease as the mould fills up, and the current distribution and subsequent mass distribution of the electrolyte change accordingly.

Success in fabricating micro-structures depends on the perfect replication of the polymer mould. The stages prior to electroplating determine the success of the electroplating stage: the seed layer(s) must provide good adhesion and low sheet resistance as a cathode. If the micro-patterns of the coil designs are not positioned uniformly over the wafer surface then there are enhanced levels of current densities at localised parts of the wafer. Localised current densities are not dependent just on the two-dimensional layout of the pattern; the resist thickness and associated aspect ratio control the current density. Areas in the polymer mould that are exposed to the electroplating process offer an ohmic resistance; smaller lateral dimensions result in a higher aspect ratio that results in an increased level of resistance to electroplating due to the increased size of diffusion layer generated by the increased difficulty in the convective flow reaching the bottom of high aspect ratio molds. As current will always move in the path of lesser resistance, lower aspect ratios will have greater current levels concentrated in these areas.

5.10 Removal of photoresist and seed layers

Once the gold electroplating of the coil turns has been performed, the next steps are the removal of the photoresist and the seed layers. Placing the wafer in a small beaker containing acetone and swirling this about to gently agitate the solution is sufficient to remove the photoresist. The wafer is then removed from the beaker and rinsed in deionized water on both sides of the wafer and dried in N_2 gas to ensure that all of the

photoresist has been removed. The presence of residues will affect the removal of the seed layers, therefore care is required at this stage.

The copper seed layer is removed using an ammonia persulfate solution. To avoid the uplift of the coil turns from the glass substrate, the wafer was placed in a beaker of deionised water, and the 10:1 diluted ammonia persulfate solution was added in small amounts and agitated gently until the copper seed layer was removed from the wafer. This could be identified visually by the change in colour of the seed layer. Once this stage has been reached the wafer was removed from the beaker, rinsed in deionised water, and dried with N_2. Another inspection of the wafer was performed using the white light interferometer to check that the entire copper seed layer had been removed. The titanium seed layer removal was performed by placing the wafer in a dilute solution of ammonia hydroxide. A similar process to the copper seed layer removal was followed. The wafer was again placed in a beaker filled with deionized water and the ammonia hydroxide solution added in small quantities while gently agitating the beaker.

The electroplated coils with the photoresist and seed layers removed are shown in figures 5.8 and 5.9. In figure 5.8, two bond pads need to be wire bonded to complete the electrical circuit of the Rogowski sensor. The sensor is checked beforehand for electrical continuity between the inner and outer bond pads by using a digital multimeter. The resistance check should be close to what was calculated for the modeling chapter minus the resistance of the wire bond.

5.11 Packaging of the sensor

The packaging of the sensor is focused on taking the Rogowski sensor in its die form and integrating it into a suitable package ready for testing it on a current carrying wire. The first aspect of the packaging involves the completion of any interconnections to communicate its measurement in a real world scenario. The main interconnect required at this stage is the connection of the inner and outer bond pad so that the spiral coil can function as a Rogowski sensor. After this has been completed, the final step is incorporating the sensor into a package that can clip around the wire under test (WUT).

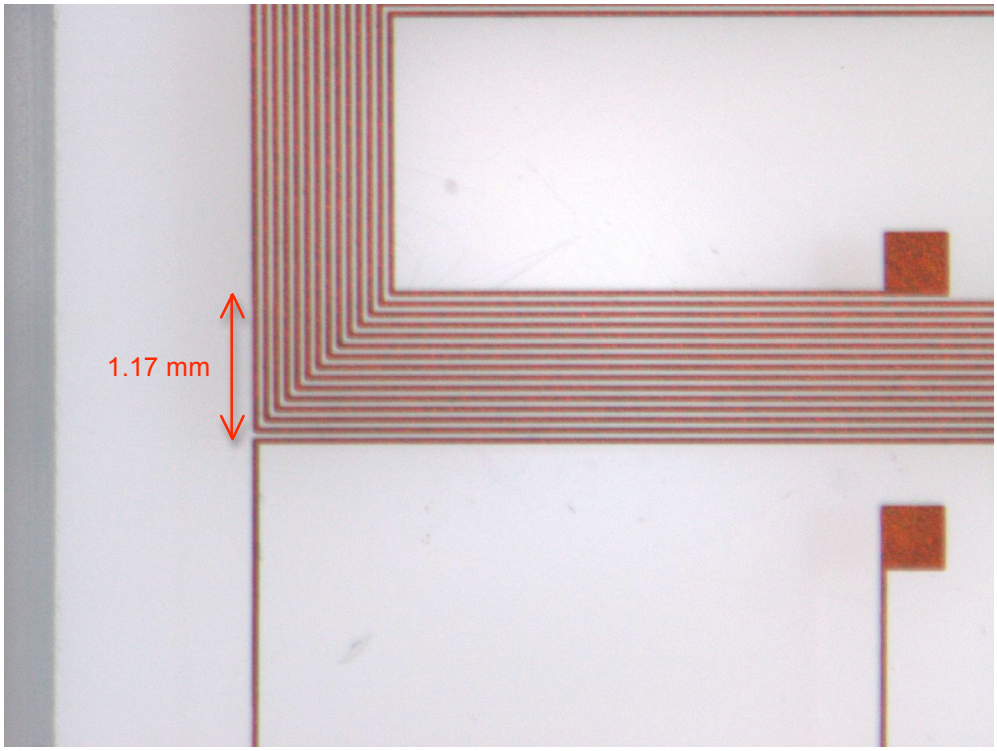

Figure 5.8 Rogowski sensor (5 x 2.5 mm) manufactured by UV-LIGA.
The inner and outer pads now require wire bonding to complete the sensor circuit.

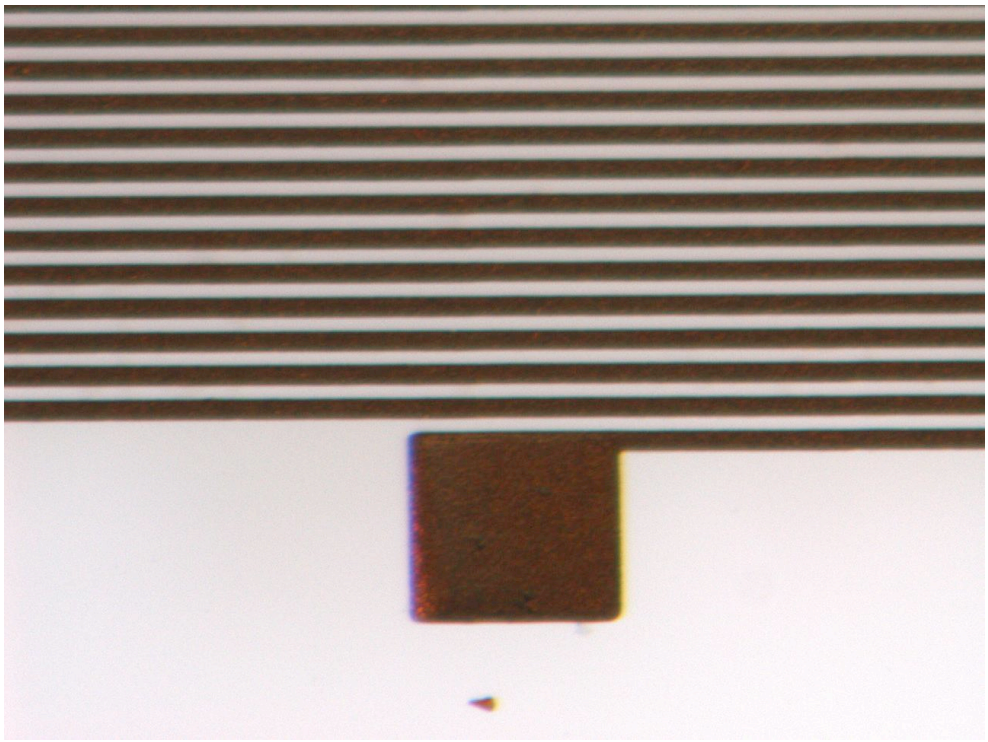

Figure 5.9 Close up view of the 10 x 20 mm Rogowski sensor.
Each conductor turn has a width of 50µm and spacing of 30µm.

5.11.1 Electrical completion of sensor circuit by thermosonic wire bonding

Connecting the inner and outer bond pads of the sensor together by wire bonding carries out the electrical completion of the sensor. The wire bonding is performed using the Kulicke and Soffa 4124 Thermosonic ball-wedge wire-bonding machine. This type of wire bonder uses ultrasonic and thermocompression bonding of gold wire with high automation capability due to the freedom of movement in any direction after the first bond has been made. Bonding parameters are pressure, temperature and ultrasonic energy.

A functional planar Rogowski sensor manufactured using UV-LIGA is shown in figures 5.10 and 5.11. The wire bond was started from the outside bond pad and completed in the inner bond pad. The loop of the wire bond over the coil turns of the sensor is shown in figure 5.11. The clearance of the wire bond over the coil turns stops the bond shorting out the coil turns. One way of stopping this occurring would be to apply a passivation layer over the coil turns to stop the bond wire causing a short circuit condition. The Qudos manufactured Rogowski sensors avoid this issue by burying the return wire underneath the coil turns and connecting to the bond pads using a microvia.

5.11.2 Custom packaging of the SEEDA current sensors

The Rogowski coil sensors fabricated by Qudos were cut into sensors by a diamond saw wafer cutter. Its outer dimensions were 0.4 x 1 cm; therefore, it was adequate to fit the sensor into a 28 pin Dual-In-Line Package (DIL) and have the sensor contact pads wiring the external pins of the DIL package. The wire bonding process used was similar to the LIGA Rogowski coils, except that the temperature was up to 160ºC for creating a strong enough bond to the aluminium contact pads of the Qudos current sensor.

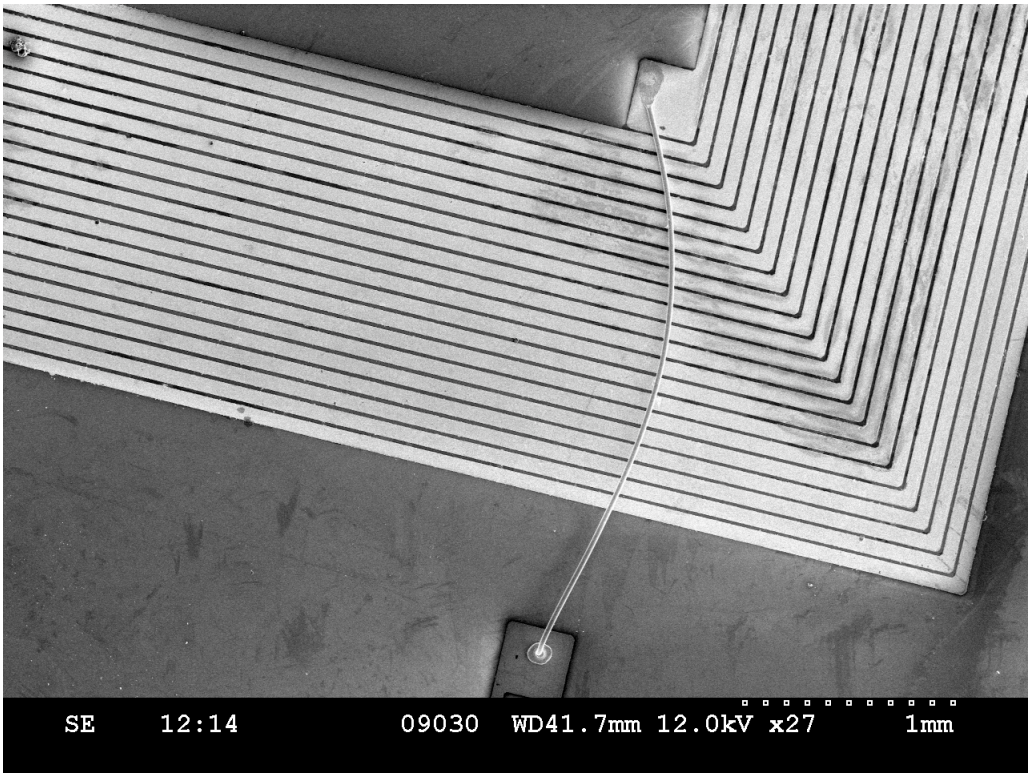

Figure 5.10 Side view image of the UV-LIGA manufactured Rogowski sensor taken on the SEM.

Coil turn width is 50μm and the inter-turn spacing is 30μm.

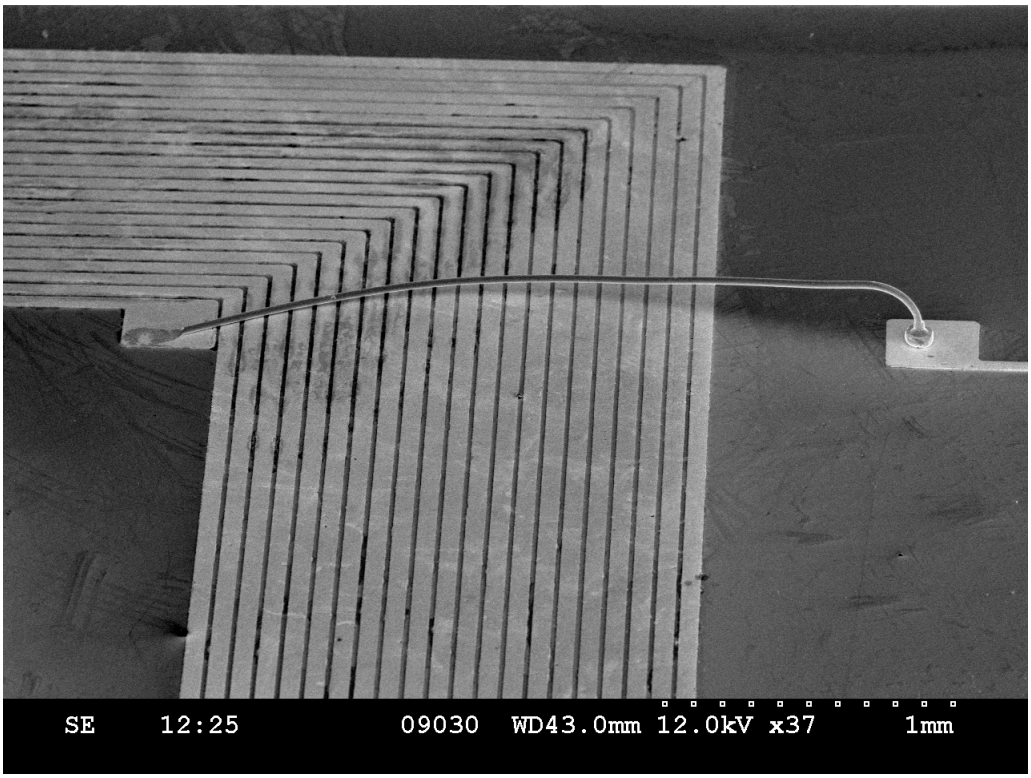

Figure 5.11 Top view of the UV-LIGA manufactured Rogowski sensor.

Coil turn width is 50μm and the inter-turn spacing is 30μm.

5.11.3 Fused Deposition Modeling (FDM) of package for wire testing and HUMMS sensor integration

Fused Deposition Modeling (FDM) was developed in the 1980s by Scott Crump and commercialised by Stratasys in the 1990s. After the stereolithography process, it is the most used method for rapid manufacturing. It is an additive process manufacturing technology, where layers of material are deposited layer by layer to produce a 3D reproduction of the CAD model.

1. Pre-processing. From the 3D CAD drawing, pre-processing software takes the 3D CAD drawing, slices it and calculates the required support structures to enable the part to be manufactured without falling over during the layer-by-layer deposition steps. The tool path for the nozzle to follow for each deposition layer are also calculated and optimised.
2. Production of parts. The 3D part is manufactured layer-by-layer. The dual extrusion heads lay down precisely the thermoplastic material and support material in each layer.
3. Support Removal. The temporary support structures are removed. The material used for the temporary supports are soluble in a water based solution.

Two prototypes were manufactured and are presented in figures 5.12a - 5.12c. The first prototype featured the company logo and measured 5 cm x 6 cm in footprint. The second prototype was 3.5 mm x 2.5 cm. Both prototypes were designed to fit the 2 cm x 1 cm Rogowski sensor inside and also clip around the wire to be tested, while maintaining a 1 mm separation.

5.12 Packaging of SEEDA sensor for wire monitoring test

The packaging used for testing the sensor on a wire is described in the characterisation section in Chapter 6 and utilises some of the design specification described in earlier sections. The main requirement is that the distance between wire and sensor must be kept at about 1 mm, which is the distance used in the calculation of the mutual inductance.

Other criteria considered was the package volume, which is around 1 cm^3. This prototype measured 1 cm x 2 cm x 0.5cm, which means that it can accommodate the sensor and a small electronics module capable of dealing with the signal processing and storage of data. A prototype laser cut package with the Qudos sensor positioned inside

is shown in figure 5.12d.

5.13 Manufacturing issues

For a simple design such as a planar Rogowski sensor presented in this thesis, a number of different challenges had to be overcome to obtain devices for testing and characterization. Issues were encountered when using the e-beam deposition equipment where the copper material was becoming oxidised in the chamber due to pumping down of the chamber too early. The copper layers formed on the wafers had higher levels of sheet resistance compared to prior processed wafers. This resulted in poor adhesion and higher stresses in the electroplated layer, which presented two varieties of device failure. The first failure mode was in the electroplating bath where the coil turns would pull away from the substrate whilst the electroplating was being carried out. Wafers with slightly lower sheet resistance also provided the second failure mode when the final packaging state of the sensor was performed.

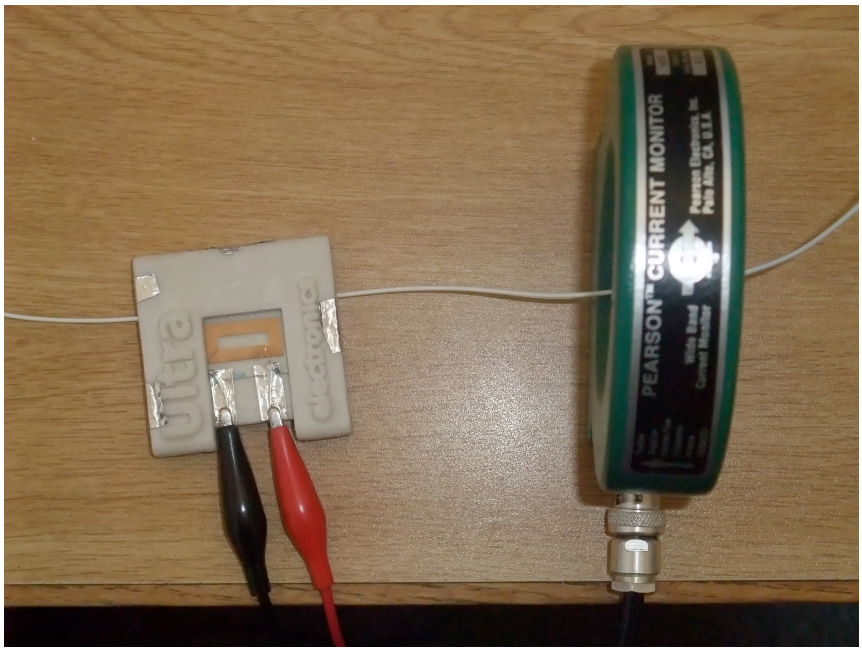

Figure 5.12A UV-LIGA sensor packaged in Concept 1 FDM packaged and clipped around WUT.

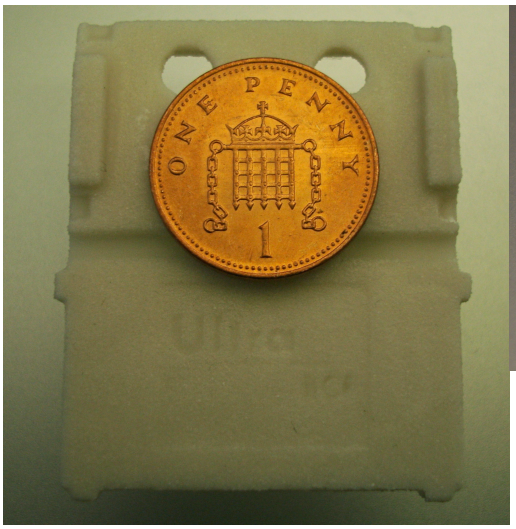

Figure 5.12B Concept 2 FDM package with smaller size.

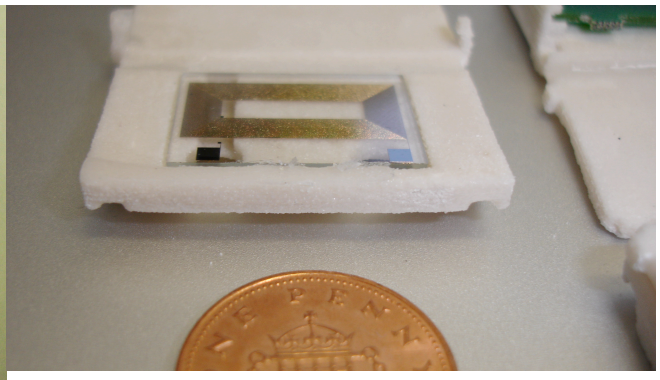

Figure 5.12C Concept 2 FDM package with smaller size with 20mm x 10 mm Rogowski sensor.

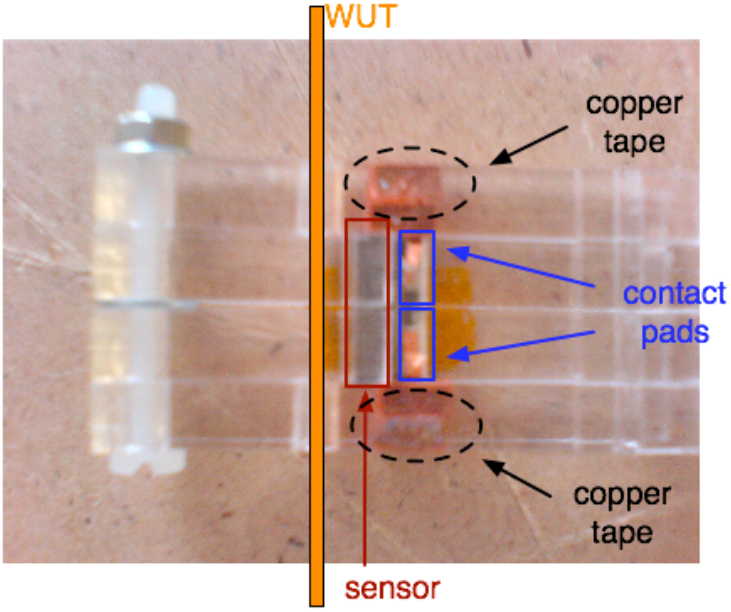

Figure 5.12D The Qudos sensor made out of laser cut sections.

Figure 5.13 Example of a non-sticking wedge bond.

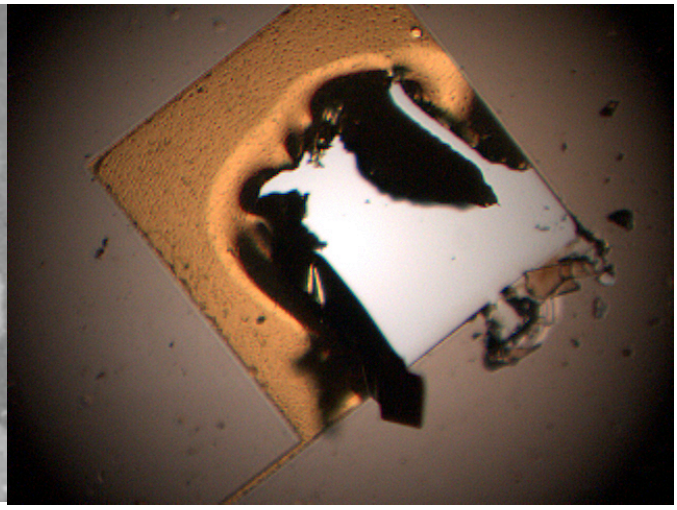

Figure 5.14 Damage induced to the bond pad during wire bonding.

During the wire-bonding step, the wire bond would pull away from the first bond pad and its connecting coil turn from the substrate. If the surface of the bond pads were contaminated and/or the temperature was not high enough then the wedge bond would not stick to the contact. This is shown in figure 5.13. On other occasions first part of the wire bond connection would rip/puncture the contact pad. This is shown in figure 5.14.

5.14 Summary

The manufacturing process and the associated steps have been presented and explained for the manufacture of the prototype planar Rogowski coil using the UV-LIGA process. Variations of sensor footprint have been manufactured according to the designs explored in the manufacturing chapter. The height of the coils was 8 µm and the majority of working sensors had 50 µm coil turn widths. This was due to the difficulty in manufacturing continuous coil turns widths of 20 µm. The laser cut and FDM manufactured packages allow the positioning of the sensor around the wire under test while maintaining a distance of no greater than 1mm. Future packaging will look at incorporating multiple sensors into the package.

The manufactured sensors have been tested and characterisation results are presented in Chapter 8 and compared to the theoretical models developed in the modeling chapter.

References

[5.1] David Flynn, "The manufacture and characterization of microscale magnetic components", PhD Thesis, *Heriot-Watt University, School of Engineering and Physical Sciences*, March 2007.

[5.2] J. Zhang, "Flip Chip Assembled High-Q MEMS Inductors on Silicon for RFIC Applications", *PhD Thesis, Heriot-Watt University*, June 2007.

[5.3] B.J. Chun, H.J. Song, and K.S. Lee. 'Surface Free Contaminants Cleaning Characteristics of Etched Si Wafer in SF/sub 6/ICP'. Plasma Science, 2003

[5.4] G.E. McGuire, "Semiconductor materials and Process Technology Handbook: For Very Large Scale Integration and Ultra Large Scale Integration", Noyes Publications, 1 June 1988.

[5.5] M. Brunet, T. O'Donnell and J. O'Brien et al, "Thick photoresist development for the fabrication of high aspect ratio magnetic coils", *Journal of Micromechanics and Microengineering*, vol. 12, no. 4, 22 March, 2002.

[5.6] J.J. Licari and L.R. Enlow, "Hybrid Microcircuit Technology Handbook", *Noyes Publications*, 1998.

[5.7] M.J. Madou, "Fundamentals of Microfabricaton", 2nd Edition, *CRC Press*, 2002.

[5.8] TP. Rai-Choudry, "The Handbook of Microlithography, Micromachining and Micro-fabrication: volume 2: Micromachining and Microfabrication",

[5.9] P.V.Zant, "Microchip Fabrication: A Practical Guide to Semiconductor Processing", Fifth Edition, *McGraw-Hill Publishing*, Chapter 9.

[5.10] D. Weiland, "Optical Fibre Array Manufacture using Microengineering Techniques", *PhD Thesis, Heriot-Watt University*, January 2007.

Chapter 6

Methodology for characterisation and test of Rogowski sensors

6.1 Introduction

The aim of this chapter is to present the methodology used to characterise the in-house manufactured UV-LIGA Rogowski sensors and the Rogowski sensors manufactured by Qudos Technology Ltd. The results of the characterisation will be compared to the modeling results carried out in Chapter 6 to see if there is agreement with the models developed. The physical properties of the sensors such as area, number of turns, turn/conductor width, inter-turn spacing and height allow the calculation of their electrical properties such as inductance, capacitance and resistance, which, in turn, allow the derivation of the sensor rise-time, phase shifts, and output magnitude of the sensors.

The sensors manufactured by Qudos have similar footprint but differ in the number of turns, the turn width and inter-turn spacing. A sensor layout of a fixed area is likely to increase the yield of the sensors, particularly when performing the electroplating process step in the device manufacture. This was observed during the UV-LIGA electroplating process step that produced a high amount of failures per wafer. This could be attributed to the localised areas on the chip with varying levels of current density present. As a result, there were more Qudos sensors produced for test and analysis than the UV-LIGA sensors.

The characterisation of the sensors is based not only on identifying the electrical parameters of the sensors as described above, but also to reproduce how the sensors interact being tested in an environment for which they are intended to be used. This chapter therefore presents the methodology for characterizing the R, L and C parameters of the Rogowski sensors and shows the test methods to assess the capability of the sensors to detect fast rise-time signals that are synonymous of arcing or partial discharges.

6.2 Test setup and methodology used to characterize Rogowski sensors R, L and C parameters.

Previous research has measured the inductance, capacitance and resistance of Rogowski coils [6.1-6.3] and micro-coils [6.4] to enable a comparison to be made between the calculated and physical parameters. These parameters can also be used to simulate the lumped parameter response of the sensors to verify if variation in the measured parameters has an impact on the response to fast rise-time signals.

The inductance and capacitance of Rogowski coils have small values compared to the resistance of the Rogowski sensors, so a 4-wire measurement method is often favored over the typical 2-wire measurement.

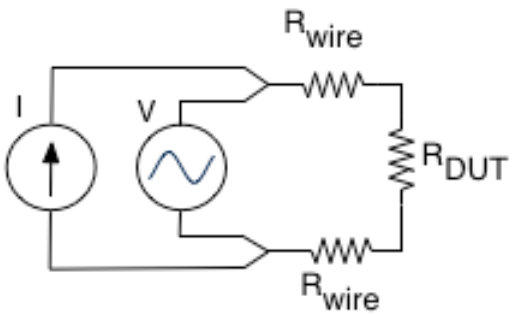

Figure 6.1a: 2-wire measurement of DUT

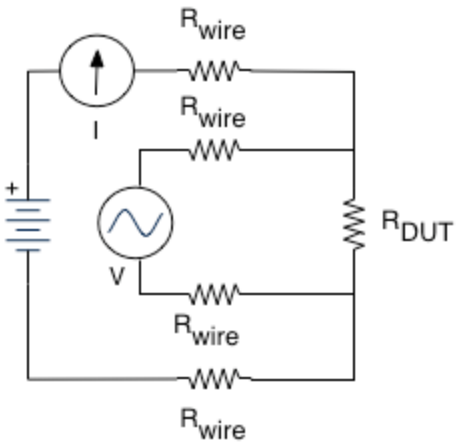

Figure 6.1b: 4-wire measurement of DUT

Figure 6.1 Circuit arrangements for 2 wire and 4 wire measurement of DUT

The 2-wire measurement method is shown in figure 6.1a and involves a multimeter using a constant current source (I) in series with the DUT. The voltage developed across the DUT is then measured by the voltmeter (V). The two wires used in this method possess a resistance that is added to the measurement of the DUT. This is illustrated in figure 6.1a. It is standard practice to use the 4-wire method to ensure that only that DUT is being measured and the influences of the test leads and fixture is minimised.

The 4-wire method is presented in figure 6.1b, and, as the name suggests it, uses 4 test wires to make a measurement of the DUT. The voltmeter has high input impedance, therefore current flowing through the test leads is very small in magnitude. The 4-wire test still involves the current source being used to force a test current through the DUT.

The test leads of the voltmeter are this time connected across the terminals of the DUT. This ensures that the measurement is that of the DUT without the contribution of the test leads.

Table 6.1 Equipment list for characterising the Rogowski sensors

EQUIPMENT LIST
1. HP 4192A LF Impedance Analyser
2. 4-wire measurement probe.
3. Digital Multimeter – Fluke 73-III

The inductance, capacitance and resistance values of each Rogowski sensor design were measured using the 4-wire technique with the HP 4192A LF Impedance Analyser. A digital multimeter was used to get resistance measurements from the sensors to show that the readings from the impedance analyser were within acceptable limits of each other. The experimental apparatus used for characterising the inductance, capacitance and resistance values is summarised in Table 6.1. In the test and analysis chapter, the data of both types of Rogowski sensors are checked against calculated values. Where applicable, a large number of sensors are measured and their variance measured to get an idea of how capable the manufacturing process is.

In the next section, the measured R, L and C parameters are substituted into the lumped parameter model to see how the differences in these parameters impact the capability to measure fast rise time signals. This involves performing bode and step response analysis and comparing with the measured data.

6.3 Test setup and methodology for evaluating capability to test fast rise-time signals.

In this section, an experimental setup was created that closely approximates the type of signals that would be present on aircraft wiring. These signals would be fast rising transient signals with rise-times of the order of nanoseconds and frequency content around 100 MHz. In [6.5], high precision Rogowski coils were manufactured on printed circuit boards to enable detection of fault generated travelling waves on power system transmission lines. The suitability of the sensor design was tested based on its ability to

detect travelling waves. Xianghu et al. use this experimental setup to validate suitability for high frequency testing as shown in figures 6.2 and 6.3 The Rogowski sensor is tested by inserting the wire through the PCB Rogowski sensor and connecting the wire to a travelling wave generator. A 3 Ω resistor is connected in series to this wire to limit the maximum current sent down the cable. The output of the Rogowski coil is connected to a 100 Ω resistance, which is, in turn, connected to channel 2 of an oscilloscope. Channel 1 of the oscilloscope displays the waveform of the impulse generator; the rise-time of the waveform is measured to be around 10 nano-seconds.

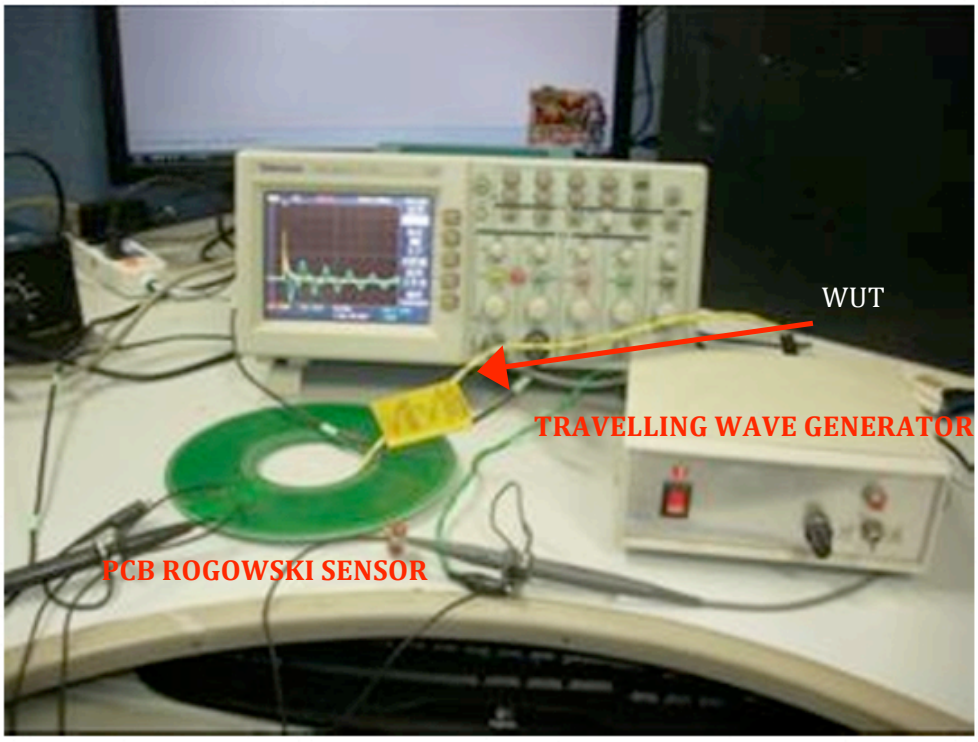

Figure 6.2 Test setup used for testing PCB Rogowski sensor

In [6.6], Orr et al. stated that the ability of Ultra High Frequency (UHF) sensors to provide a good response to the initial wavefront of a UHF signal has not been explored in detail. A sensor could have a low sensitivity but good initial response to a fast rise time signal as a result of a smaller propagation delay of the sensor. Conversely, a more complex designed sensor could result in a good sensitivity yet provide longer response time due to the higher propagation times of the sensor. The experimental procedure used to evaluate the sensors in this work was a step response, which is the normal method of determining the frequency response of the sensors using the Fast Fourier Transform processing. The output of the step response was captured using a digitising oscilloscope with a bandwidth of 3GHz and a sampling rate of 10 Giga samples per second.

In [6.7] Zhang et al. mention that, when a PD signal is captured by a wideband detector, the PD is not a single impulse but instead a series of oscillatory attenuation impulses [6.8]. This concept was incorporated into their test strategy by constructing a pulse generator that produced waveforms with rise-time of a few nanoseconds and duration of around 10 nanoseconds. Upon examination of the frequency spectra it was established that frequency components of up to 100 MHz were present. The experimental setup for testing the sensors is shown in figure 6.4.

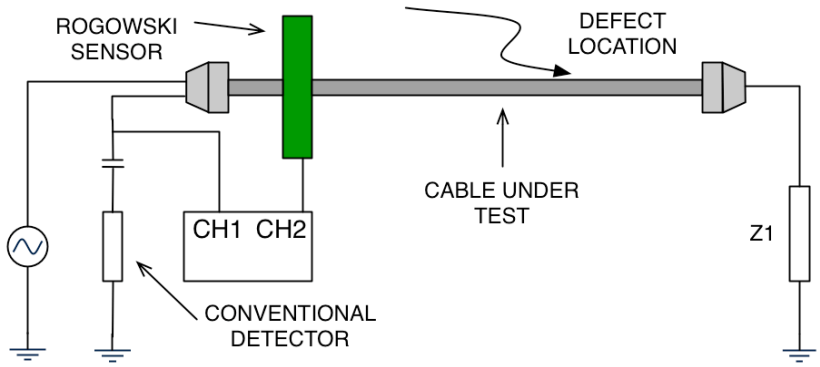

Figure 6.3 PD measuring circuit

The bode response of both types of Rogowski sensor will involve looking at the capability of each design to provide a wide measurement bandwidth, which will impact the ability of the sensor to detect fast rise-time signals.

Table 6.2 Equipment list for dynamically monitoring the Rogowski sensors

EQUIPMENT LIST
1. Tektronix AFG 3000 Function Generator
2. Tektronix 4000 wide band oscilloscope
3. Pearson Current Transformer – Model 6595
4. 2 x coax cables
5. Probe and clips

The wire under test (WUT) is threaded through the middle of the HFCT and is solder connected to a coaxial connector. The Qudos Rogowski sensor is positioned next to the WUT by inserting it into a laser cut package (figure 6.5) that holds the Rogowski sensor in a fixed position relative to the WUT.

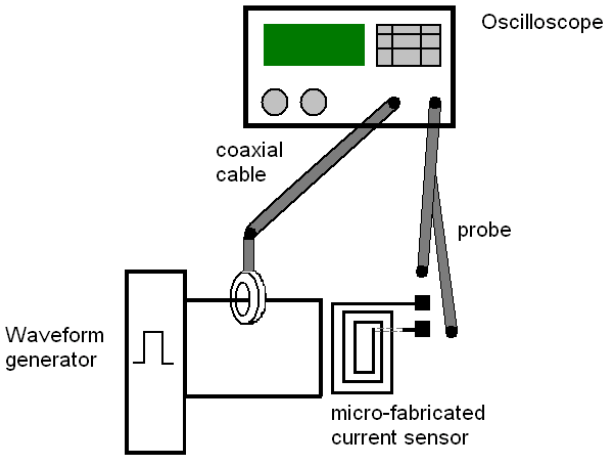

Figure 6.4 Test setup for dynamic measurement of the Rogowski sensors

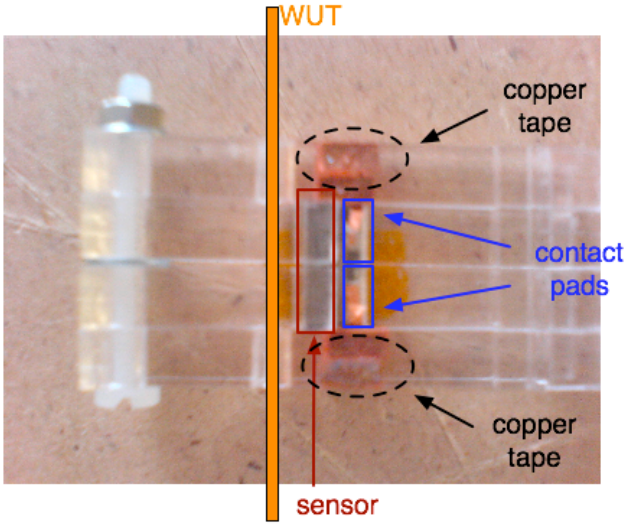

Figure 6.5 Laser cut package used for testing the Qudos manufactured Rogowski sensors

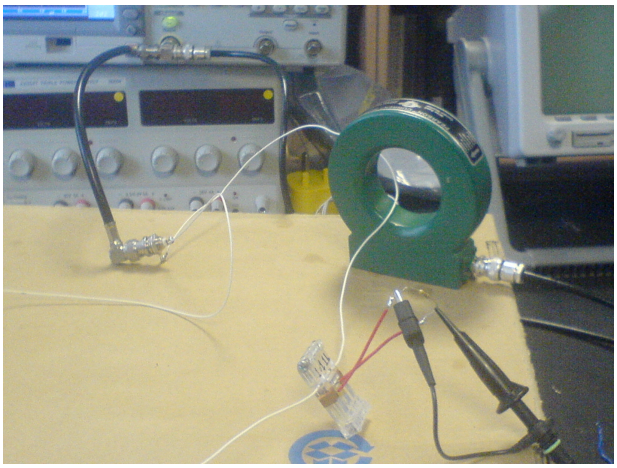

Figure 6.6 Test setup used for characterising Rogowski sensors in differentiating and self-integrating mode

Some conductive tape is connected from the output terminals of the Rogowski sensor to the outside of the laser cut package in order for the oscilloscope probe to be connected across it. The coax connection of the wire is connected to the Tektronix AFG 300 series signal generator and the coax output of the HFCT is connected to channel one of the wide bandwidth Tektronix 4000 series oscilloscope; channel two is connected to the probe used for measuring the Rogowski sensor output. For the UV-LIGA manufactured sensors, the sensor was placed right next to the wire under test. The wires soldered to the bond pads of the sensor were connected to the oscilloscope probe.

The protocol for testing involved sending sinusoidal waveforms from the signal generator onto the WUT and observing the resulting signal waveforms with the conventional Pearson high frequency current transformer and the Rogowski sensors discussed in this thesis. The frequencies chosen for this test ranged from 1MHz to 100 MHz and the amplitude of the signal was chosen as 10V Peak to Peak. The generation of sinusoidal waveforms with a 100 MHz bandwidth enabled a frequency response of the Rogowski sensors and the HFCT to be calculated in the form of a bode response. This also served as a good baseline for examining whether the manufactured Rogowski sensors performed better or worse than the current market offering. At the end of this process, the sensor was removed and swapped with another design until all the sensors had been characterised.

The signal waveform generator has the capability to send a variety of waveform types, onto the WUT and evaluated with the HFCT and the Rogowski sensors. These waveforms were sine waves and pseudo partial discharge signals that possess similar waveform shape and rise-times for which the Rogowski sensors could be evaluated against. Testing the sensors with pseudo partial discharge signals is discussed in the next section.

The sinusoidal waveform analysis will provide an idea of the sensor frequency response from 1–100 MHz, and enable a comparison between the calculated and measured frequency response of all the sensor designs to be evaluated. The results of this analysis is presented in the form of a bode response in the next section.

In addition to this, the resistance, inductance and capacitance measurements presented in the first section are to be used to recalculate the bode response of the Rogowski

sensor to compare how differences in measured values would impact its ability to detect high frequency signals.

6.4 Pseudo Partial discharge signal response

Although no actual measurements were taken by generating a pseudo partial discharge signal in the test setup for the differentiating case, it was still decided that it was worthwhile to understand the difference that the inductance, capacitance and resistance values have on the sensor rise-time. This involved performing a step response analysis using the resistance, inductance and capacitance values discussed in section 7.2 of chapter 7 and comparing to the step response analysis of chapter 5.

For the self-integrating analysis, the ability of both Rogowski sensor designs was evaluated against pseudo partial discharge-like signals. In research by [6.9] on the suitability of Rogowski sensors for partial discharge measurements or detection, the authors used either waveform generators or a partial discharge generator as part of their experimental apparatus. A digital waveform generator was available at Heriot-Watt University; therefore this was used to test the hypothesis that conventional Rogowski sensors could be miniaturized using micro-manufacturing processes and still be able to detect an arcing or partial discharge type signal. The experimental setup used for this test is identical to that used for generating sinusoidal waveforms with different frequencies in the MHz region. The difference between these tests was the waveform generator being programmed to produce 1 MHz charging and discharging signals that mimic the waveforms seen in partial discharge type signals. Both types of waveforms are sent down the WUT to test the Rogowski sensors response to a more realistic type of signal. The sensors were tested in the self-integrating condition and the results compared to the step response analysis in the modeling chapter. The UV-LIGA sensors tested in this section were designs UV-2 and UV-3 (designs 5 and 10 of modeling chapter), with the HFCT used to baseline the measurements against. All of the Qudos designs were tested and analysed.

The measured inductance, capacitance and resistance values acquired in the tests outlined in the beginning of the chapter were used to generate a new updated lumped model that can be further investigated to verify the impact of the difference between

measured and simulated values on the step response. This helped understand the impact on the sensors ability to detect fast rise-time signals.

6.5 Summary

This chapter has introduced the testing methodology used to verify the performance characteristics of Rogowski sensors by research carried out by research and academic groups. The methodology used involves measuring the lumped parameter values of the sensor such as the resistance, inductance and capacitance. These values are used to generate a second order lumped model response of the sensor and to understand the trade-off in the selection of the self-integrating impedance that can be connected across the sensor output terminal to reproduce the original PD signal.

Testing the sensors to a range of sinusoidal input signals on a wire and measuring the sensors response for the frequency range of interest can verify the sensor designs. This leads to the calculation of the bode response of the sensors. In addition to this, the sensor can be tested against a pseudo PD signal by injecting this onto the wire from a waveform generator and measuring the sensor response.

In the next chapter both the UV-LIGA and Qudos sensors were tested and analysed using these methods. Due to the high number of Qudos sensors presented for test, statistical analysis of the sensors inductance, capacitance and resistance values were performed to see how much the sensor measurements vary from sensor to sensor. Where there is a large difference between the measured and simulated values, further analysis was performed to establish the impact on the capability of each sensor design to measure fast rise time signals.

References

[6.1] G.M. Hashmi and M. Lehtonen, "On-line PD measuring system modeling and experimental verification for covered-conductor overhead distribution lines," *Mediterranean Conference on Control & Automation, 2007. MED '07.* pp. 1-6, 27-29 June 2007.

[6.2] B. Wang; D. Wang and W. Wu, "A Rogowski coil current transducer designed for wide bandwidth current pulse measurement," *IEEE 6th International Power Electronics and Motion Control Conference,* pp.1246-1249, 17-20 May 2009.

[6.3] L. Web, M. Changing and L. Jiming, "Study of a Novel CT used to measure the switch state current of RSD", Sensors & Transducers Magazine, vol. 68, issue 6, pp. 589-596, June 2006.

[6.4] C.R. Neagu, H.V. Jansen and A. Smith et al, "Characterization of a planar microcoil for implantable microsystems", Sens. Actuators A62 pp. 599–611. 1997.

[6.5] C. Xianghu; Z. Xiangjun and D. Feng et al. "Novel PCB sensor based on Rogowski coil for transmission lines fault detection," *IEEE Power & Energy Society General Meeting,* pp. 1 - 4, 26-30 July 2009.

[6.6] P.J.G. Orr, A.J. Reid and M.D Judd. "Sensor Response Characterisation for UHF Location of PD sources", *International Conference on Condition Monitoring and Diagnosis,* pp.1119 - 1122, 21-24 April 2008.

[6.7] Z.S. Zhang, D.M. Xiao and Y. Li. "Rogowski air coil sensor technique for on-line partial discharge measurement of power cables," *IET Science, Measurement & Technology,* vol.3, no.3, pp.187 - 196, May 2009.

[6.8] Y. Cheng and H. XIE, 'A physical model for nanosecond partial discharge'. *Proc. 6th Int. Conf. on Properties and Applications of Dielectric Materials,* 2000, vol. 2, pp. 697 – 700.

[6.9] Q. Zhang et al, "Design of a current transducer with a magnetic core for use in measurements of nanosecond current pulses", *IOP Measurement Science and Technology*, vol. 17, no. 4, pp. 895 - 900, 23rd March 2006.

Chapter 7 Test and characterisation of the Rogowski sensors

7.1 Introduction

This chapter presents the measurements and characterization of the Rogowski sensors based on the methodology outlined in the previous chapter. The inductance, resistance and capacitance results are introduced in section 7.2 alongside the assessment of the statistical variation of measurements performed on the Qudos sensors. These measurements are also used to re-simulate the Bode response in sections 7.3 and 7.4, and the step response analysis of the sensors in section 7.5. These sections also examine the sensors performance when tested in close proximity to a wire carrying different waveforms such as are sine waves ranging from 1-100MHz and pseudo-PD shaped waveforms.

7.2 Evaluation of R, L and C parameters

7.2.1 Qudos Rogowski sensors

The inductance, capacitance and resistance of the Qudos sensors were measured using the procedures described in the previous chapter. The sensor designs were manufactured over 4 wafer lots, labeled C12, C13, C14 and C15. The number of sensors presented for test for each wafer lot and sensor design is shown Table 7.1. Further information about each sensor design is indicated in Table 7.2.

Table 7.1 Amount of Rogowski sensors across each wafer

Wafer number	Sensor Q1	Sensor Q2	Sensor Q3	Sensor Q4	Sensor Q5	Sensor total
C12	10	10	10	10	10	50
C13	11	13	11	14	12	62
C14	4	4	4	5	6	23
C15	8	10	0	10	10	38

Table 7.2 Parameters for the Qudos manufactured Rogowski sensors

	Design Q1	Design Q2	Design Q3	Design Q4	Design Q5
Turn width (µm)	50	50	50	90	70
Turn spacing (µm)	70	90	50	70	70

Different yields for each design were observed due to the difficulties encountered during the manufacture of the sensors as explained earlier. The main issue observed during manufacture was the electroplating of the second metal coil turns layer of the Rogowski sensors. The first layer of the sensors was used as the underpass connection, shown in blue in figure 7.1, between the bond pad in the center of the Rogowski sensor and the outside of the sensor.

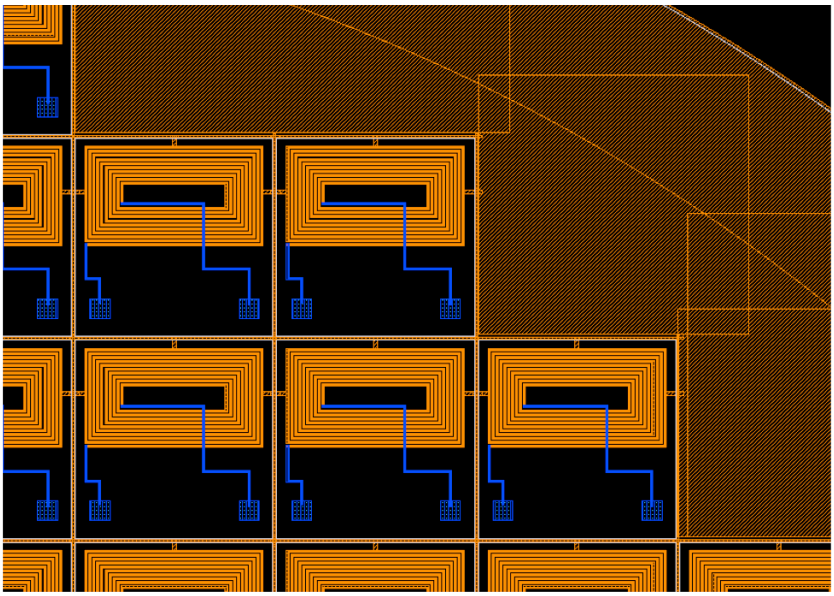

Figure 7.1 The different metal layers used by Qudos to manufacture the Rogowski sensor

This underpass connection removes the need for the wire bond connection used in the UV-LIGA manufactured Rogowski sensor. The second layer is for the coil turns. A number of manufacturing iterations were required to reduce the stresses in the metal coil turns such that they did not lift-off from the silicon substrate during the subsequent process steps. This involved the removal of the photoresist and further deposition and patterning of a polyimide passivation layer. In addition to mechanically holding down the coil turns onto the substrate, the passivation layer served to protect the coil turns from mechanical damage during handling and field use. Any scratches to the coil turns lead to a break in the continuity of one or more of the turns, resulting in an open circuit condition that rendered the sensor useless.

The measurement results for the sensors on each wafer were grouped by number and analysed statistically. This is presented in figure 7.2 in a histogram format, in solid lines for the measurements taken by the Impedance Analyser (IA), in a dotted line for those recorded by the Digital Multi-Meter (DMM). The histograms for both readings share a

similar mean and narrow standard deviation, which indicate that the IA is recording a true resistance reading for all the sensors.

The histogram analysis shows that the distributions of resistance for each sensor type are distinct from each other. Designs Q1 and Q4 have mean values that can be visually identified as being different from each other, but the dispersion of the distribution curve for both of these designs overlaps each other. If no prior knowledge about the measurement value and sensor design number was available, then it is highly probable an operator measuring these devices could identify them as the incorrect design type (i.e. mistakenly identify design Q1 as design Q4 and vice versa).

When the measured values of these sensors are compared to the calculated values in the modeling chapter, it shows that the majority of the resistance values are higher than anticipated. The probable cause for this is due to calculated values being based upon coil turns possessing a height of 10 μm, whereas the height of the devices manufactured is probably lower than 10 μm, causing thereby an increase in the resistance values. The origin of this height variation is most likely attributed to the lithography process. The spin coating parameters could have produced an uneven layer of photoresist across the wafer, leading to patterns across the wafer having different thicknesses from the top of the photoresist to the silicon wafer.

Another possible source of variation could be due to the position of the sensors across the mask. The different turn width and spacing of each sensor means that different times are required for the design to be fully replicated in the photoresist. Designs with wider coil turns will be fully developed much quicker than the designs with narrower coil turns. The wafer will require more time in the developer solution to remove the un-developed photoresist, reducing the overall photoresist thickness across the wafer as it is gradually etched away.

The variation in each sensor design is shown in Table 7.3 and their positioning across the mask layout is depicted in figure 7.4. The mask layout reveals that the sensors are repeated twice vertically across the wafer, but the designs vary horizontally across the wafer. In Table 7.3, the measurements for all sensor designs across wafers C12 - C15 are presented. This shows the average readings and the level of variation. It is apparent that there exists a level of variation from wafer to wafer and across each wafer.

In wafer C12 there is enough of each sensor design to gather this information, whereas all other wafers could only provide a selection of the designs for statistical analysis. This leads to the conclusion that there is further need to investigate the processing parameters used to manufacture these sensors and the relationship with the resistance, inductance and capacitance measurements.

In figure 7.3, a similar procedure to 7.2 is performed for the inductance measurements where the inductance readings across each wafer are grouped by design number and analysed statistically in histogram format. The results show that the mean of the readings are very close together, but the dispersion of the individual curves differs. For example, D1 has a medium dispersion of readings and designs Q2 and Q5 have curve dispersions that increase significantly for Q2 and then decreases for the measurements of Q5. On the other hand, Q3 and Q4 have similar means and very small dispersion of the curves. These most likely refer back to the manufacturing issues faced by Qudos that led to a low yield.

In Table 7.4, the average and standard deviation of inductance measurements for each sensor design and wafer batch is presented. Wafer C15 has averaged values that is out by a factor of ten, which is due to the variations in inductance measured across die to die. The other wafers have produced inductance values that are generally within the expected range of 246 nH to 617 nH. For the case of wafer C12, designs Q1 and Q3 are outside the calculated range. This is due to the large spread in inductance readings which skews the averaged and standard deviation calculations.

There was no Q1 type sensors on wafer 13, however all other designs show an average inductance reading within the range. The expected order of high inductance to low inductance values that correspond to each design in the modeling chapter is not replicated in the measurements. This again leads to concerns that the picking and grouping of the sensor die after manufacturing by Qudos has been done incorrectly. For wafer C14, only designs Q4 and Q5 were present for measurements. Again, the inductance values measured were within reasonable calculated ranges.

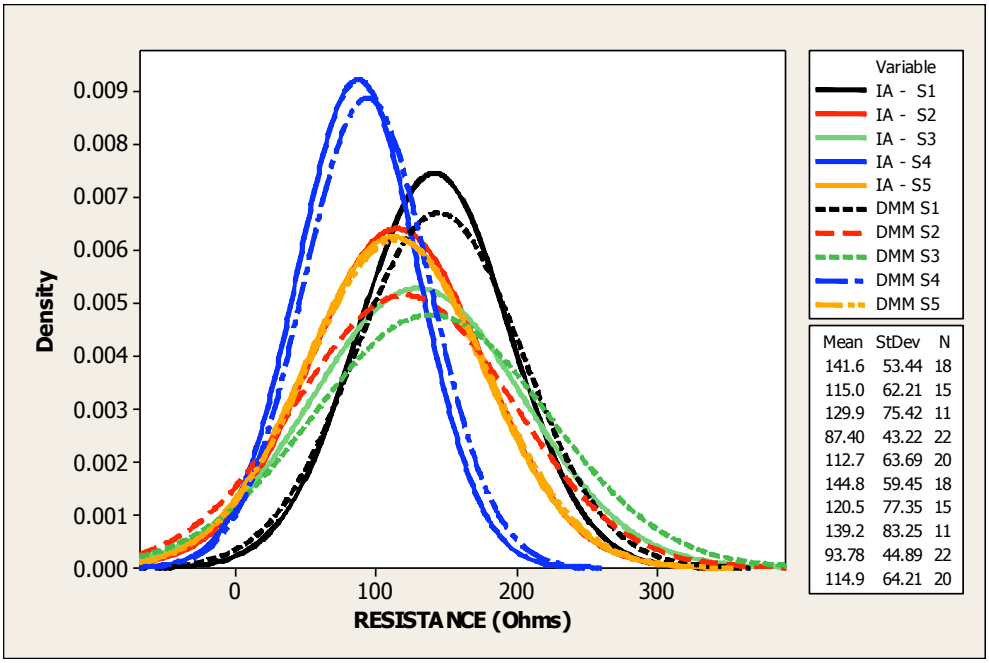

Figure 7.2 Histogram of sensor resistance measurements on both the impedance analyser and the DMM.

S1 to S5 correspond to Q1 to Q5.

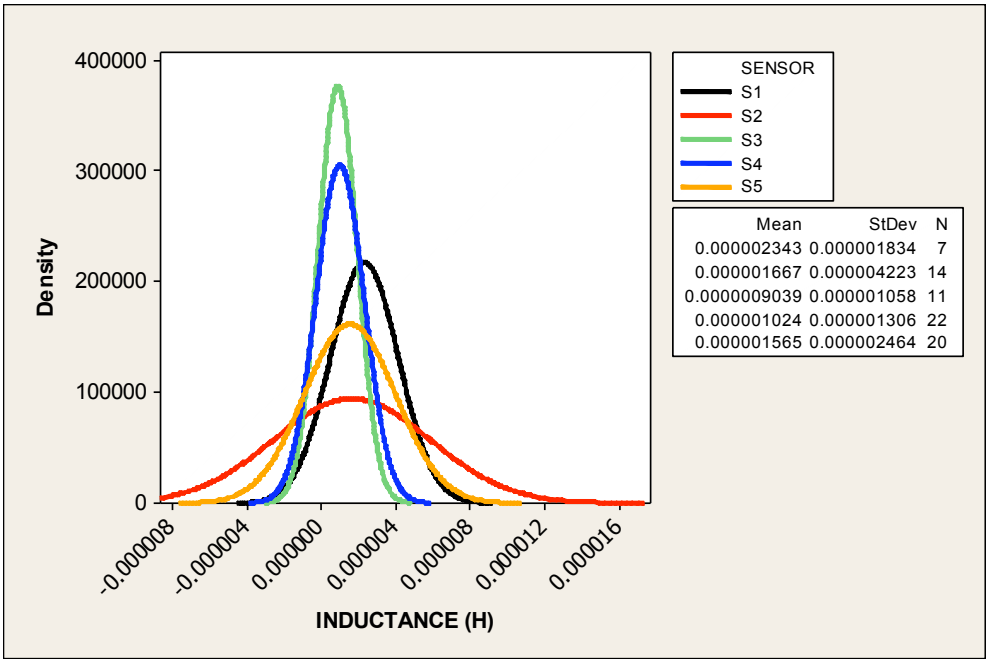

Figure 7.3 Histogram of sensor inductance measurements across all wafers.

S1 to S5 correspond to Q1 to Q5.

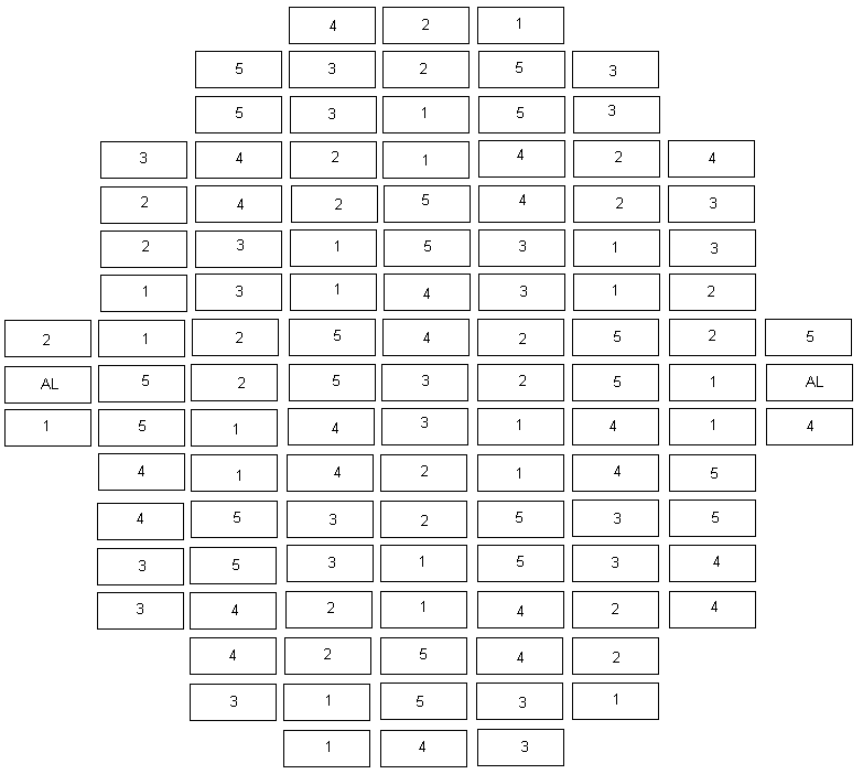

Figure 7.4 Mask design used for manufacture of Rogowski sensors by Qudos
The number indicated in the boxes refers to the design number.

They are slightly higher in value than expected, but the relationship of high to low inductance values for the simulated designs was repeated in the correct order for designs Q4 and Q5. The reason for this larger value of inductance could be attributed to the lithography steps used to produce the sensors. If the wafer is overdeveloped then the resist next to the unexposed regions will begin to erode. It is possible that erosion could occur to such an extent that the coil turns are closer to each other and the mutual inductance value between coil turns is increased greater than expected.

The capacitance measurements of the Rogowski sensors have the same large variations as the resistance and inductance measurements. The results presented in Table 7.3 show that the means range from 111 nF to 795 nF, indicating that the capacitance was out by around a factor of 100. The measurement data however looks closer to the values calculated in the modeling chapter. Generally, the capacitance test results for designs vary from the low nF range to 100s of nF's. In the modeling chapter, the capacitances were calculated to be in the region of 450 pF based on the equations discussed by Neagu et al [7.1]. This paper presented the manufacture of a planar micro-coil with a similar 2.5D structure on a silicon substrate as was manufactured by Qudos. The coil design was 4.5mm x 4.5mm with turn height of 1 μm, 112 coil turns, 10 μm width of each coil turn, and 6 μm spacing between each turn. This produced a capacitance of

around 120 pF. The Qudos manufactured sensors have much wider coil turns, ranging from 50 µm to 90 µm, and a larger sensing footprint (3.5mm x 9.5mm) which will result in a much higher capacitance between the coil turns to substrate. Additionally, the model used did not take into account the passivation layer applied to the top of the coil turns for mechanical protection. This increases the capacitance between coil turns, so that the overall value of the Qudos manufactured Rogowski sensors would be in the range measured.

A worthwhile exercise would have been to do a Measurement Systems Analysis (MSA) on the impedance analyser and the test method used to establish what the measurement error of the Qudos Rogowski sensor measurements was and the level of uncertainty this added to each measurement. This would involve the measurement of a range of reference capacitors from 1 pF up to the hundreds of nF range. The reference capacitors can be procured from Agilent technologies, but was not followed up due to the high cost ($6,000). These reference capacitors could be rented for one month for around £600. Measurements of these reference capacitors would be carried out between 30 – 50 times for each capacitance value, and ideally repeated by different people. The information provided by the MSA would identify what the measurement error is as well as identifying the sources of the measurement error. This would explain errors due to human interaction and also the measurement interaction with the measurement.

7.2.2 UV-LIGA Rogowski sensors

The measurement of the inductance, capacitance and resistance values of the Rogowski sensors manufactured by UV-LIGA was performed using the same method as described before. The numbers of sensors available to test was significantly less than the devices manufactured by Qudos. This was due to poor wafer yields in the manufacturing lab, sensors damaged during the wire bonding and assembly and also due to parts being damaged due to handling by other personnel. The sensors presented for test are listed in Table 7.4 along with the corresponding measurement results. Generally, the results for the UV-LIGA manufactured Rogowski sensors displayed similar trends to the measurements of the Qudos manufactured devices inasmuch as the inductance and resistance values are in close agreement to the values calculated in the modeling chapter, but there is a greater variation in the capacitance measurements and the calculated values.

For the inductance readings, sensor design UV-10 shows a reading of 3.95 μH versus a calculated value of 4.31 μH, sensor design UV-5 was measured to be 22.05 μH versus a calculated value of 24 μH and sensor design UV-2 was measured as 14.14 μH versus 14.5 μH.

Table 7.3 Measurement results of the UV-LIGA Rogowski sensors.

SENSOR DESIGN NO.	DIMENSIONS	INDUCTANCE (μH)	CAPACITANCE (nF)	RESISTANCE (Ω)
UV-2	1 cm x 1 cm	14.14	1.45	98.4
UV-5	0.5 cm x 2 cm	22.05	750	148.9
UV-10	1 cm x 0.5 cm	3.95	1.28	55.5

The resistance measurements for sensor UV-10 were 55.5 Ω versus 27.5 Ω, sensor UV-5 was 148.9 Ω versus 181.25, Ω and UV-2 was 98.4 Ω versus 70 Ω. Two process phenomena could explain these differences in the measurements. The first is that the height of each electroplated coil turn is greater than the calculations were based on (10μm) and the second is that the width of each coil turn is wider than originally designed. The first behaviour would explain the higher than expected resistance measurements (UV-10 and UV-2) and the second behaviour would explain the UV-5 resistance measurement being lower than the calculated value.

The source of these differences can be traced to the lithography process steps. With the different types of coil turn widths and spacing between coil turns, the development time of the photo-exposed resist would likely need to be increased for the larger sensor designs for which the unexposed photoresist has not been fully washed away from the unexposed photoresist. This increase of development time would broaden the coil turn width and decrease the spacing between coil turns resulting in an increase of the mutual inductance between coil turns of the sensor, and of the overall inductance. This is not reflected in the inductance measurements, which are all lower than the calculated values. We can therefore eliminate this process step as the source of the discrepancy in resistance value.

The likely reason the resistance measurements sit higher and lower than the calculated values is that there are variations in current densities across the wafer. Open sections on the wafer mold cause these variations in current densities. Differences to the dimensions

of each sensor such as the coil turn widths result in different growth rates of the electroplated gold from sensor to sensor. Subsequently, when the wafer was removed midway through the electroplating process step and inspected for the thickness of the electroplated material some sensors would have shown higher or lower thicknesses of deposited metal. It is likely that a sensor with smaller metal growth has been measured and a longer plating time has been provided to ensure that the sensor reached within the 8 – 10μm plating thickness. This would mean that the sensor designs with a faster plating rate would provide coil turn thicknesses higher than calculated and sensor designs with lower plating speeds would have a smaller than calculated thickness. Sensors UV-10 and UV-2 would appear to have a lower thickness and sensor UV-5 has a higher thickness, therefore the differences in height would serve to increase or decrease the cross sectional area used to calculate the resistance of a coil turn.

The capacitance measurements for the UV-LIGA Rogowski sensors follow a similar trend to the Qudos sensors in that the measurements are greater than the calculated values by a factor of 10,000. In addition to this, the measured values of capacitance do not present itself in the same order as the calculated values that were UV-2, UV-10 and UV-5 from lowest to highest capacitance value. Instead, the measured values were in reverse order from low to high capacitance values.

Understanding the source of the larger difference between calculated and measured values is made harder as not enough sensors samples exist to perform statistical analysis of the means and standard deviations of each sensor type. However, the UV-LIGA sensors possess a smaller value of capacitance than the Qudos manufactured sensors, which was expected due to the difference in substrates used for manufacturing the sensors. The UV-LIGA sensors are manufactured on a glass substrate, therefore the capacitance between coil turns and substrate is lower [7.2].

The capacitance between coil turns and the substrate is the main contributor to the higher sensor capacitance of the Qudos sensors. Further capacitance is introduced due to the addition of the polyimide based passivation material that lies above and between the coil turns. Overall, there is a difference of around 100 to 1000 between the Qudos and UV-LIGA manufactured Rogowski sensors. If the statistically calculated means of the Qudos designs are compared to the UV-LIGA sensors then the capacitance difference is up to 100 nF smaller for the UV-LIGA manufactured sensors.

Table 7.4 Analysis of the inductance, capacitance and resistance measurements of the Qudos Rogowski sensors.

Wafer #	Sensor #	Wafer Mean (μ) Resistance	Wafer Std. Dev. (σ) Resistance	Population mean (μ) Resistance	Population St. Dev. (σ) Resistance	Wafer Mean (μ) Capacitance (μF)	Wafer Std. Dev. (σ) Capacitance (μF)	Population mean (μ) Capacitance (μF)	Population St. Dev. (σ) Capacitance (μF)	Wafer Mean (μ) Inductance (μH)	Wafer Std. Dev. (σ) Inductance (μH)	Population mean (μ) Inductance (μH)	Population St. Dev. (σ) Inductance (μH)
12	1	151.9	124.6	*167.3*	*98.9*	0.0048	0.033	*0.34*	*0.43*	1.52	3.4	*2.3*	*1.8*
	2	114	63.7	*114.6*	*61.4*	0.105	0.083	*0.27*	*0.47*	0.78	0.82	*1.7*	*4.2*
	3	373.7	361.4	*239.6*	*271*	0.0031	0.0051	*0.111*	*0.17*	60.5	98	*0.9*	*1.1*
	4	114.7	64.5	*95.3*	*50.8*	0.45	0.0042	*0.39*	*0.55*	0.83	0.77	*1*	*1.3*
	5	93.4	52.3	*106.7*	*60.2*	0.13	0.22	*0.8*	*0.55*	0.5	0.415	*1.6*	*2.5*
13	1	NA	NA			NA	NA			NA	NA		
	2	91.4	32			0.11	0.06			0.27	0.21		
	3	117.9	67.5			0.13	0.129			0.62	0.54		
	4	64.5	22.4			0.21	0.19			0.32	0.12		
	5	78.7	35			0.325	0.4			0.34	0.19		
14	1	NA	NA			NA	NA			NA	NA		
	2	NA	NA			NA	NA			NA	NA		
	3	NA	NA			NA	NA			NA	NA		
	4	76.3	47			NA	NA			0.83	0.53		
	5	113.2	47.1			NA	NA			0.93	1.3		
15	1	200.1	46			0.863	0.24			2.7	1.7		
	2	175.1	92.6			1	0.76			5.2	7.4		
	3	NA	NA			NA	NA			NA	NA		
	4	129.7	38.4			0.11	0.55			2.2	1.8		
	5	169.2	75.8			2.39	3.2			4	3.4		

This is despite all of the UV-LIGA designs possessing a footprint which is 2 to 4 times greater. The impact of a silicon substrate, the oxide layer between the silicon substrate and metal layer of the coil turns along with the capacitance of the return metal path that lies between the coil turns and substrate has resulted in a much higher capacitance.

7.3 Bode analysis - Differentiating behaviour

7.3.1 Bode response of the Qudos Rogowski sensors

The Bode response using the measured values obtained in the earlier section is presented in figure 7.5. The response starts to drop at around 1 kHz for sensor Q1 followed by Q2 and Q4 at 5 kHz. The remaining designs (Q3 and Q5) begin to tail off at around 10 kHz.

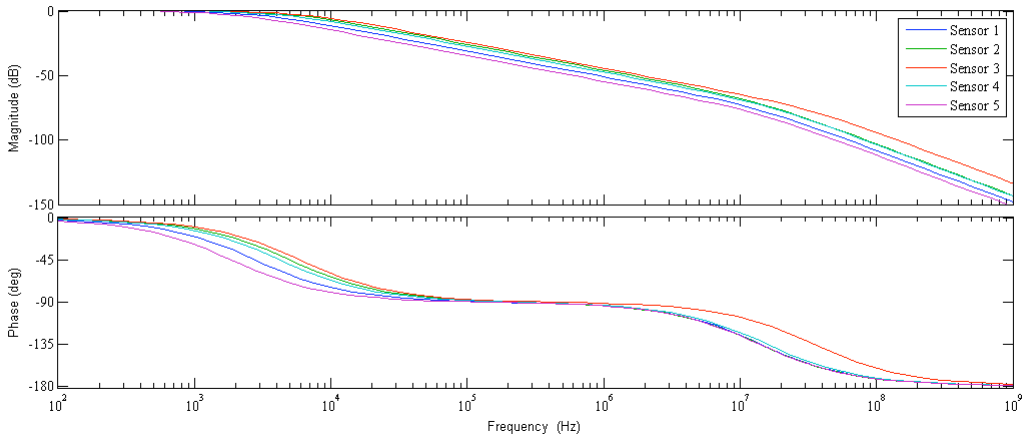

Figure 7.5 Bode response simulation using measured values

For the frequency range of interest (1–100 MHz), the output signal of the Rogowski sensors ranges from -40 to -70 dB down, which is a significant drop from the original calculated Bode response in the modeling chapter. The phase response portion of the bode analysis shows that design Q1 is -90° out of phase from around 8 KHz to 1.5 MHz. Sensor D2 has -90° phase change from 70 kHz to around 5 MHz, design Q3 from 70 kHz to 10.5 MHz, design Q4 from 70 kHz to 150 kHz and design Q5 from 100 kHz to 2 MHz. The magnitude and phase elements of the Bode analysis show that the output signal is attenuated far more compared to the original calculations in the modeling chapter. It can be concluded that the mean values calculated from the sensor measurements were skewed from measurements

possessing large variances in value. The Bode analysis gained from measuring the sensor output from 1 – 100 MHz is provided in figures 7.6 and 7.7.

The magnitude response for all of the sensors and the High Frequency Current Transformer (HFCT) is provided in figure 7.6 and shows that initially the HFCT provides a greater signal output at 1 MHz than the other sensors. The output of the HFCT starts decreasing from 5 MHz to 25 MHz by 20 dB; beyond this point the attenuation increases at a greater rate to a minimum at 42 MHz. At this point it is attenuated by a further 34 dB from the output signal measured at 1 MHz.

The Qudos sensors begin to equal the output magnitude of the HFCT in the order of Q5 (1.7 MHz), Q3 (1.8 MHz), Q4 (2.8 MHz) and Q1 (5 MHz). At 9 MHz, designs Q2, Q3, Q4 and Q5 provide an output signal that is almost one order of magnitude higher than the HFCT. Design Q1 shares the same output magnitude at 9 MHz, however after this point its output begins to increase upward to its maximum value of -17.2 dB at around 28 MHz. The sensor displays its first resonant peak before decreasing to -34dB at 34 MHz. After this point, it drops to its minimum value of -52 dB before increasing back up to its maximum value of -18.5 dB at 82 MHz. Design Q3 follows a downwards trajectory after 9 MHz till it provides an output slightly less than the HFCT from 10 to 10.5 MHz. After this point, it displays a similar form as sensor Q1 in that it rises up to a peak maximum of -31 dB before sharply declining to its minimum at 36 MHz. After this point, the output increase sharply beyond its lower MHz output to a maximum of -17.1 dB at 80 MHz.

Sensor Q2 has the poorest low frequency performance out of all the sensors at frequencies starting from 1 MHz and stopping at 4 MHz. After this point Q2 follows the output of the HFCT from 4 MHz to 9 MHz before increasing upwards to its first peak at 28 MHz; at this point the gain is -19 dB. Apart from a smaller resonant dip at 40 - 45 MHz, the higher frequency output of this design increases back up to what appears to be a second resonant peak.

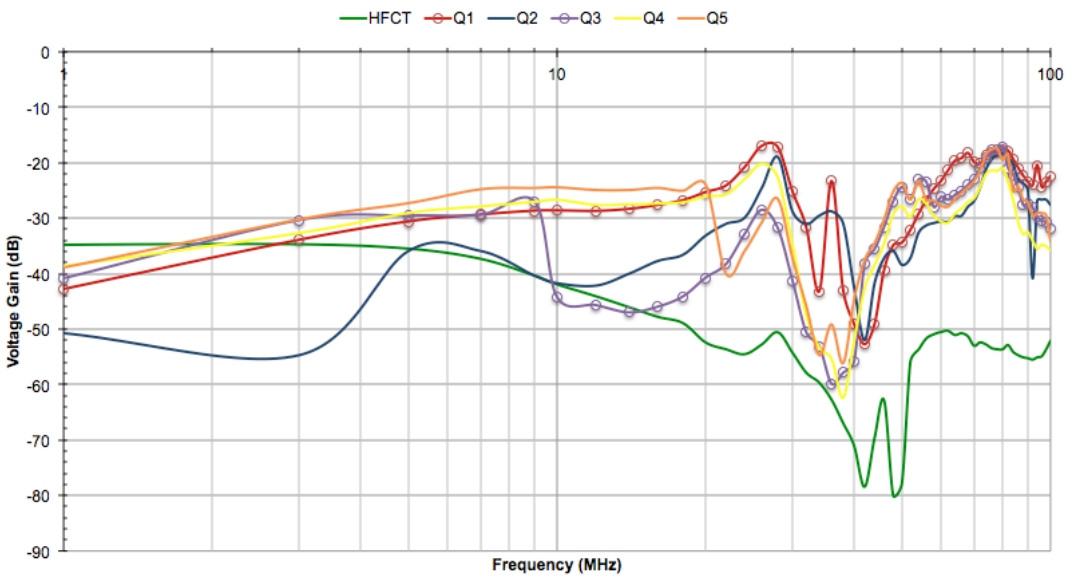

Figure 7.6 Magnitude response of Qudos Rogowski coils in differentiating mode

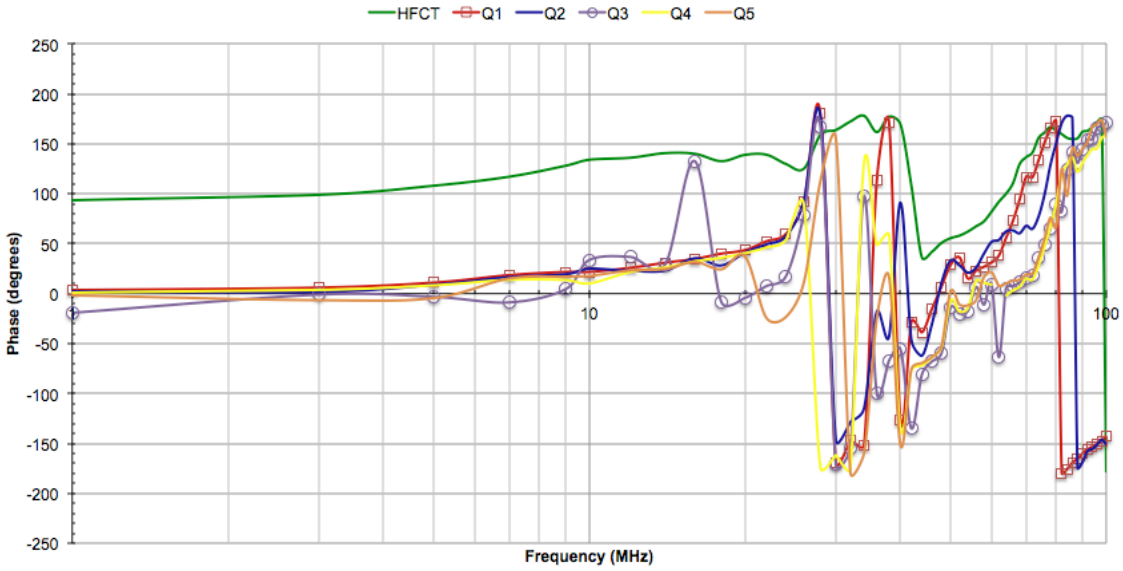

Figure 7.7 Phase response of Qudos Rogowski sensors in differentiating mode

Designs Q4 and Q5 follow a similar output beyond 9 MHz as design Q1. Design Q4 almost reaches a similar resonant peak of -20.8 dB at 25 MHz before falling sharply to -62 dB at 38 MHz. This design has the lowest output response. Design Q5 displays a minimum at 22 MHz (-40 dB) and 38 MHz (-56 dB).

The measured Bode response shows that the sensors perform better at MHz frequencies which contrasts to the simulated bode response (using the R, L and C measurements). It is possible that the measured capacitance has an influence on the high frequency behaviour, therefore it should be much smaller than the measurements indicate.

7.3.2 Bode analysis of UV-LIGA Rogowski sensor in differentiating mode

The results of the sensor performance are indicated in figures 7.9 to 7.11. The growth rates reflect that sensor UV-5 reaches higher maxima of -8.4 dB at its first resonant peak, whereas sensor UV-2 reaches a resonant voltage output of -19.8 dB.

The response of UV-2 to a 100 MHz sine wave on the WUT is shown in figure 9.8. The signal trace of the Rogowski sensor is shown in purple, the trace for the HFCT is shown in green and the trace of the supply voltage is shown in yellow.

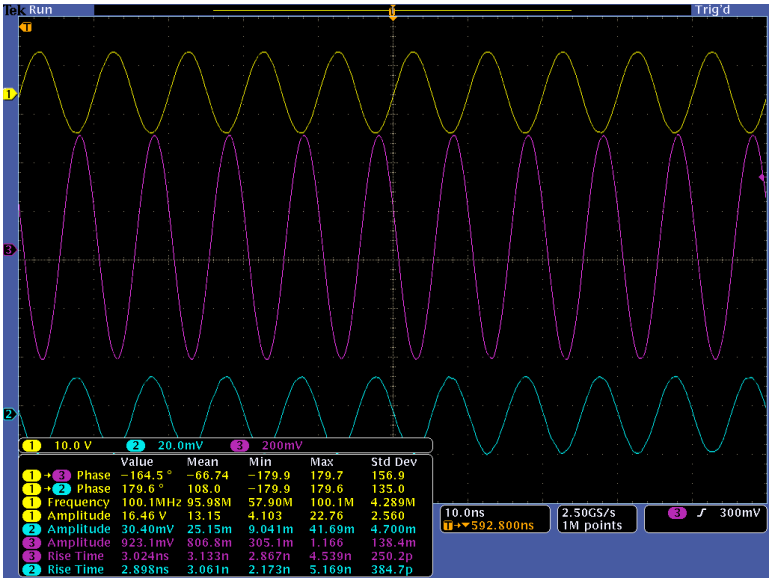

Figure 7.8 Response of the UV-LIGA Rogowski sensor in differentiating mode to a sine wave

The graph shows UV-2 with amplitude of 923.1 mV at 100 MHz, whereas the commercial HFCT has an output voltage of 30.4 mV. The overall performance of HFCT and UV-LIGA sensors in terms of magnitude and phase is shown in the Bode response in figures 7.9 and 7.10. The first figure is magnitude response, which shows similar behaviour in the low MHz range in that the commercial HFCT provides a slightly higher output voltage from 1 MHz to 2 MHz. In this frequency range, the output of the HFCT is -34 dB, whereas UV-2 produces -38 dB and UV-5 produces -40 dB. At 2 MHz, the output of all the sensors are -30 dB with the HFCT maintaining this output to 4 MHz before it decreases to -40 dB by 10 MHz. After this point it decreases at a rate of 0.5 dB/MHz up to around 26 MHz. After this point up till around 36 MHz, its output decreases at a rate of 0.8 dB/MHz; beyond this point it continues decreasing till it reaches the minimum output of -80 dB. In contrast, with the UV-LIGA manufactured sensors, both sensors experience increases in their voltage output from 3 MHz to 10 MHz at a rate of 0.9 dB/MHz. The increase in output continues until around 15 MHz, before dipping slightly in output at 18 MHz to -38 dB. After this point it increases at a higher rate up until 27 MHz with a growth rate of 3 dB/MHz for UV-5 and 1.8 dB/MHz for UV-2. After these resonant peaks, both sensors decrease sharply to lower minima at 38 MHz than at 18 MHz. After these points the output rises sharply again to 46 MHz for UV-5 and 48 MHz for UV-2. At this point UV-2 produces a slightly greater output than the UV-5 of -15 dB versus -17.5 dB.

The Bode response shows that as the frequency increases from 10 MHz upwards, the UV-LIGA sensors produce an output that ranges from 60 to 200 higher than the commercial HFCT. The Bode response shown in figure 7.11 is produced from the measured inductance, capacitance and inductance values discussed earlier in this chapter. The re-simulated response shows that the magnitude response begins to decrease beyond 1 MHz. The only parameter that has changed is the capacitance (inductance and resistance were in agreement with original estimates), which is larger than originally estimated. High capacitances decrease the bandwidth lower down the frequency range. Due to the excellent performance beyond 10 MHz, it is fair to conclude that the actual capacitance must be much smaller than that measured with the LCR meter.

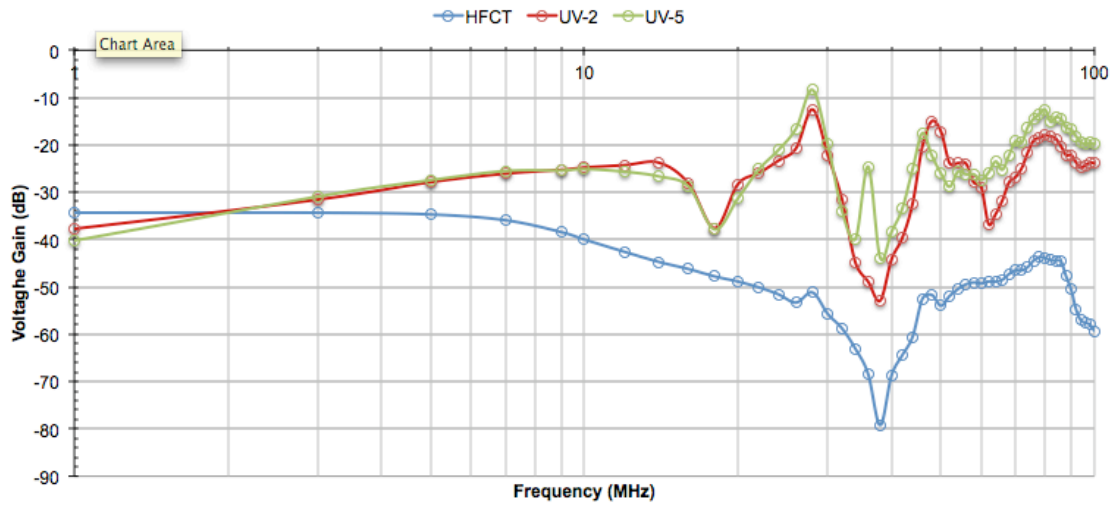

Figure 7.9 Magnitude response of UV-LIGA Rogowski sensor in differentiating mode

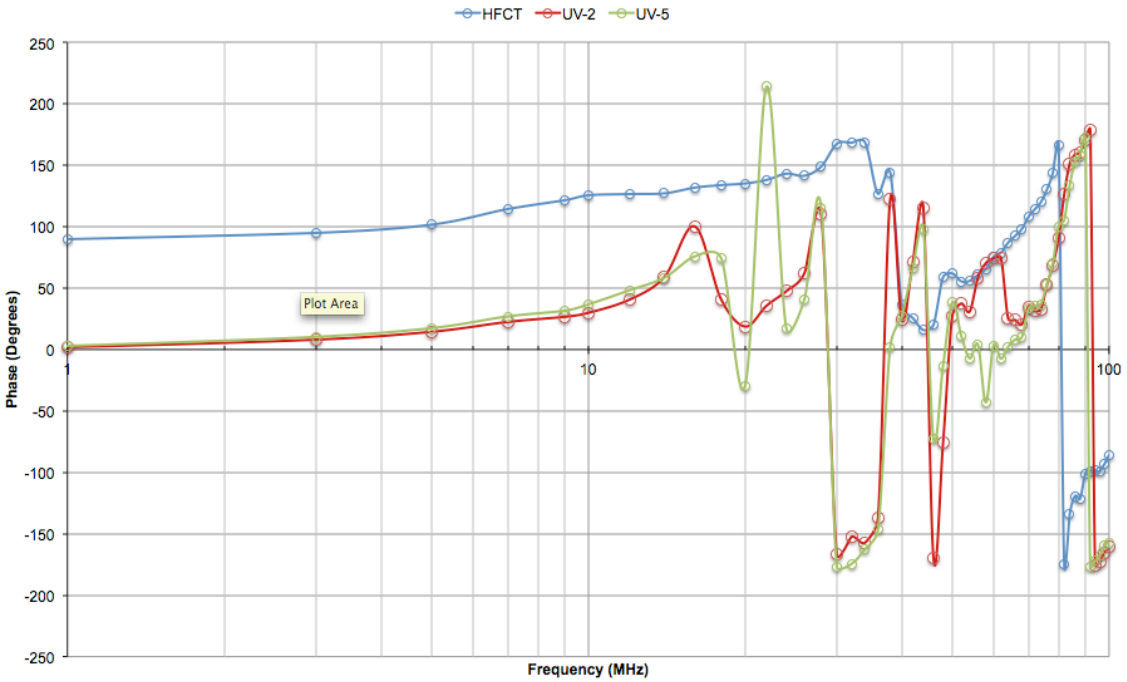

Figure 7.10 Phase response of UV-LIGA manufactured Rogowski sensor in differentiating mode

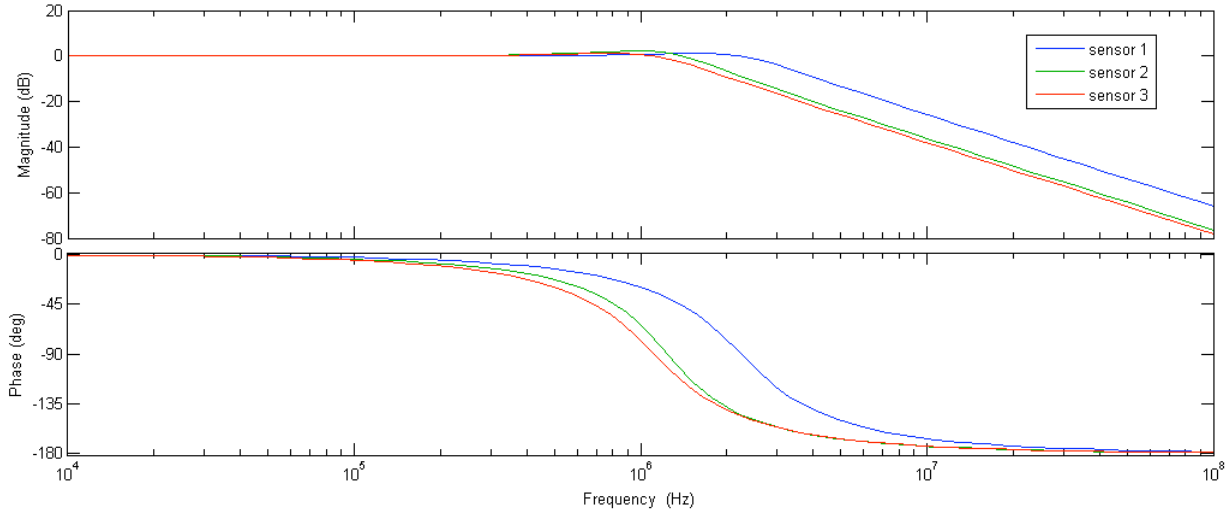

Figure 7.11 Bode response of UV-LIGA manufactured sensor in differentiating mode using measured R, L and C values.

In terms of capability for measuring fast rise times signals with enough clarity to perform multi-resolution analysis at a later stage, the UV-LIGA sensors are far more capable of resolving the higher frequency details of a partial discharge signal. In terms of further validation work, the origin of the minima observed in the magnitude response (figure 7.9) should be investigated further.Both the UV-LIGA and the Qudos sensors display minima in the Bode response at similar frequency locations as the commercial HFCT. This might be the result of reflections along the cable attenuating the voltage along the WUT. This could be verified further by choosing different lengths of cable to function as the WUT.

Additionally, the impact of varying the distance of the sensor along the cable should also be investigated. Due to the superior high frequency performance, there is however sufficient evidence that these sensors may be able to detect arcing signals over a longer distance than the commercially available HFCTs.

7.4 Bode analysis of the sensors in self-integrating mode

7.4.1 Bode response of Qudos sensors in self-integrating mode

The results of Qudos manufactured sensors to sinusoidal waveforms are illustrated in the magnitude and phase graphs in figures 7.12 and 7.13. The HFCT shows a higher magnitude than sensor Q1 between 1 and 5.5 MHz, sensor Q4 from 1 to 4.5 MHz and sensor Q5 from 1 to 5 MHz. Sensors Q2 and Q3 start with higher output magnitudes than the HFCT from 1 to 1.75 MHz. After this point, Q2 fluctuates at this value until it increases to similar levels as the HFCT. From 10.7 MHz its magnitude increases further until it reaches 26 MHz. After this point it starts to decrease rapidly, reaching its minimum value at 36 MHz, just before the HFCT reaches its minimum.

After this point it starts to ascend quickly, producing an output far higher than the HFCT from 40 MHz until 60 MHz where it briefly dips below the output of the Pearson sensor before rising quickly again increasing the sensor output to its highest levels between 65 to 100 MHz. The HFCT has reached its maximum output at around 3.5 MHz before decreasing all the way up until 38 MHz.

After this point it begins to increase upwards to 90 MHz before starting to decrease once more. In terms of the phase response of the sensors, there was no defined region where the phase response remained at -90° which was predicted in [7.2]. Instead, the response remained at a steady rate of increase to 20 MHz then it began to oscillate from 180 to -180° up until 100 MHz. This behavior was reported in [7.3] along with an output response that contained oscillations in the impulse response test. The simulated Bode response is given in figure 7.14. It shows that the response starts to decrease between 1 and 5 kHz, which is sufficiently less than shown in figure 7.12.

7.4.2 Bode response of UV-LIGA Rogowski sensors in self-integrating mode

The behaviour of the UV-LIGA manufactured Rogowski sensors to the same range of frequencies as the earlier sections is presented and discussed through figures 7.15 to 7.17. The output voltage of design UV-5 and UV-2 is presented in figure 7.15, which shows that the output voltage is -21 dB at 100 MHz, compared to -19.5 dB for the differentiating case. This is the result of a modification of the damping coefficient by introduction of the self-integrating resistance, which was 1,000 Ω for this measurement.

The other contrast between the results of the responses is that for the Qudos sensors, there is a more pronounced difference between the output of the sensors for the self-integrating and differentiating frequency response. The UV-LIGA manufactured sensors show similarity in output for the differentiating and self-integrating condition.

This is presented in figure 7.17, which shows that UV-5 and UV-2 have a magnitude response that begins to decrease at 1 MHz. Sensor design UV-10 begins to decrease in magnitude after 2 MHz, therefore this design has a slightly larger bandwidth before the magnitude begins to decrease beyond -3 dB. The shape of the sensor output waveforms that were presented in the Bode response of figure 7.12 share a lot of similarity with the responses presented in [7.4], [7.5] and [7.6].

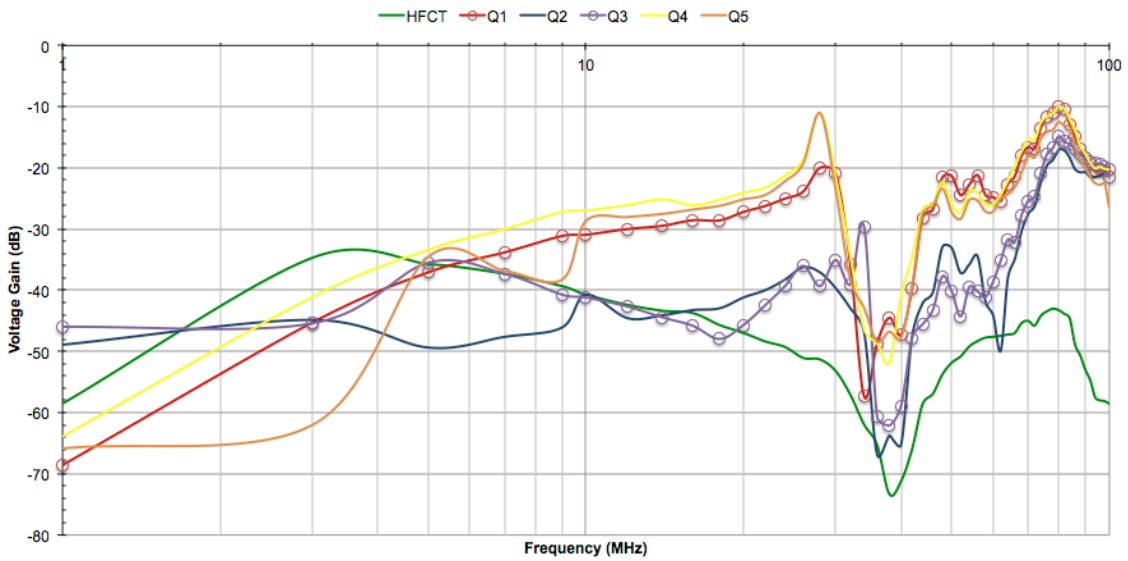

Figure 7.12 Qudos sensor Bode response in self-integrating mode

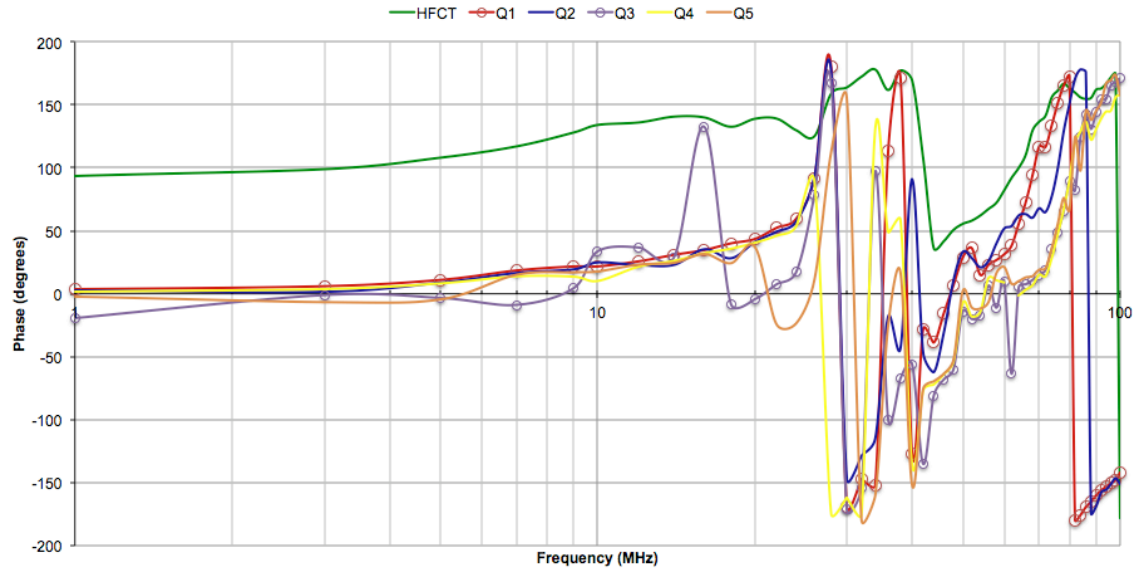

Figure 7.13 Qudos sensor phase response in self-integrating mode

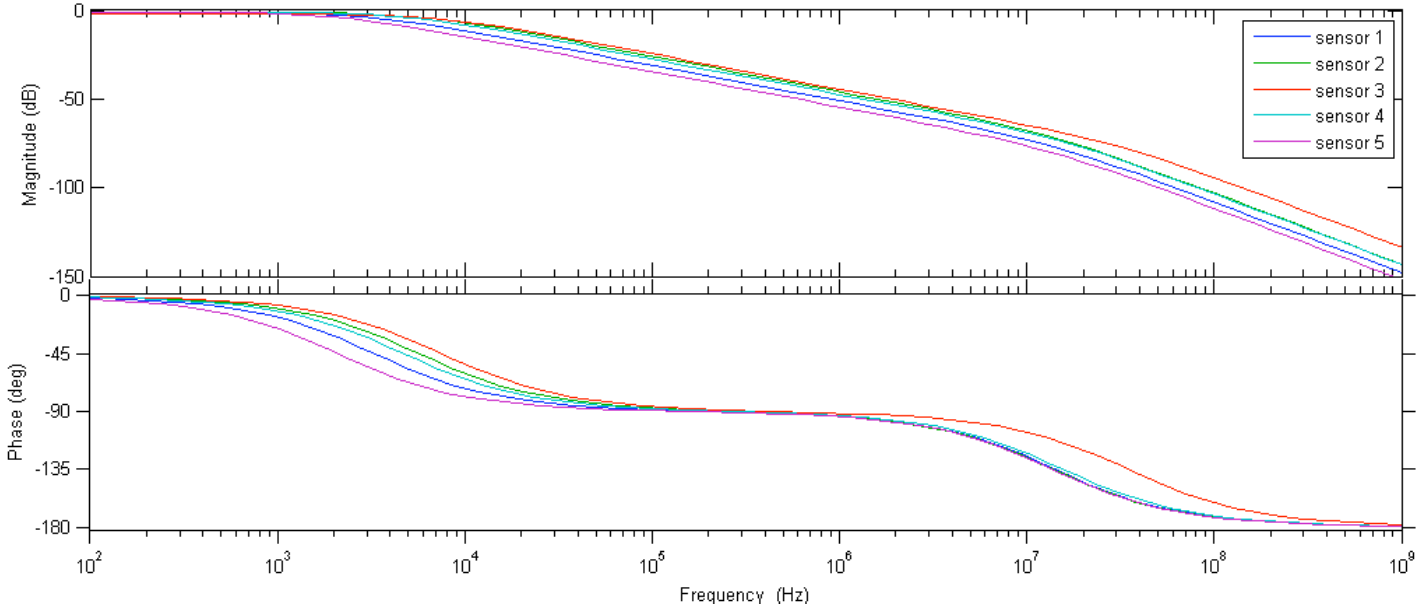

Figure 7.14 Simulated Bode response of Qudos sensors in self-integrating mode with 1,000 Ω impedance.

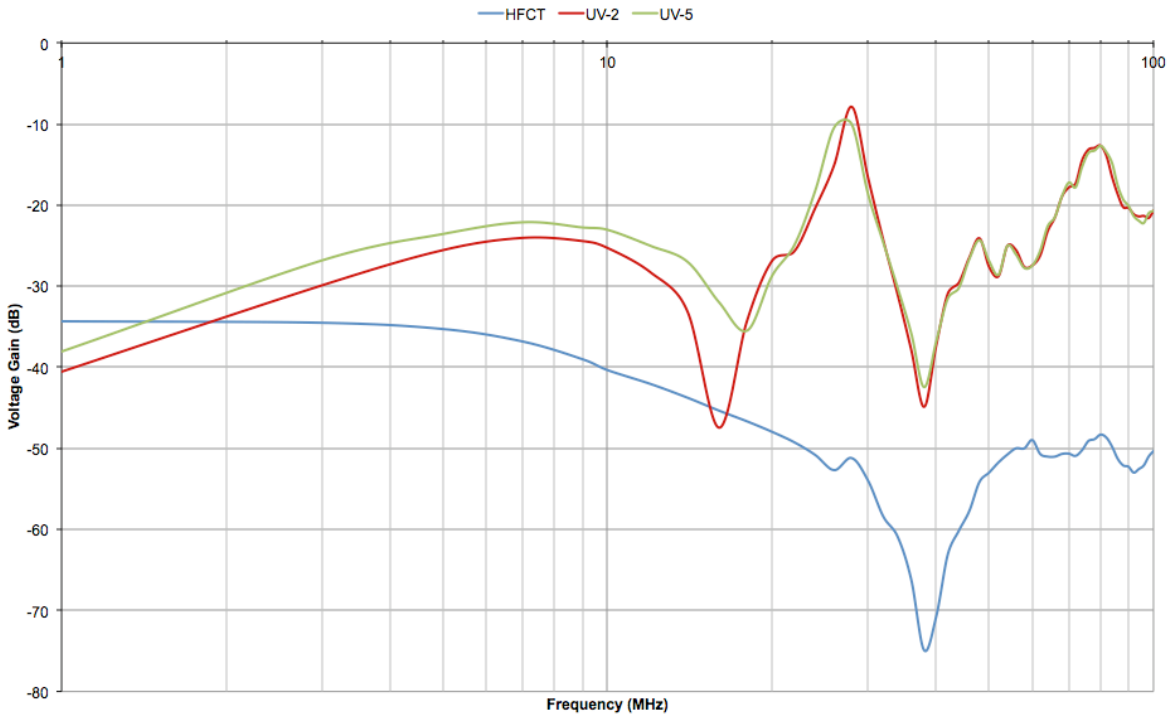

Figure 7.15 Magnitude response of the UV-LIGA Rogowski sensors in self-integrating mode

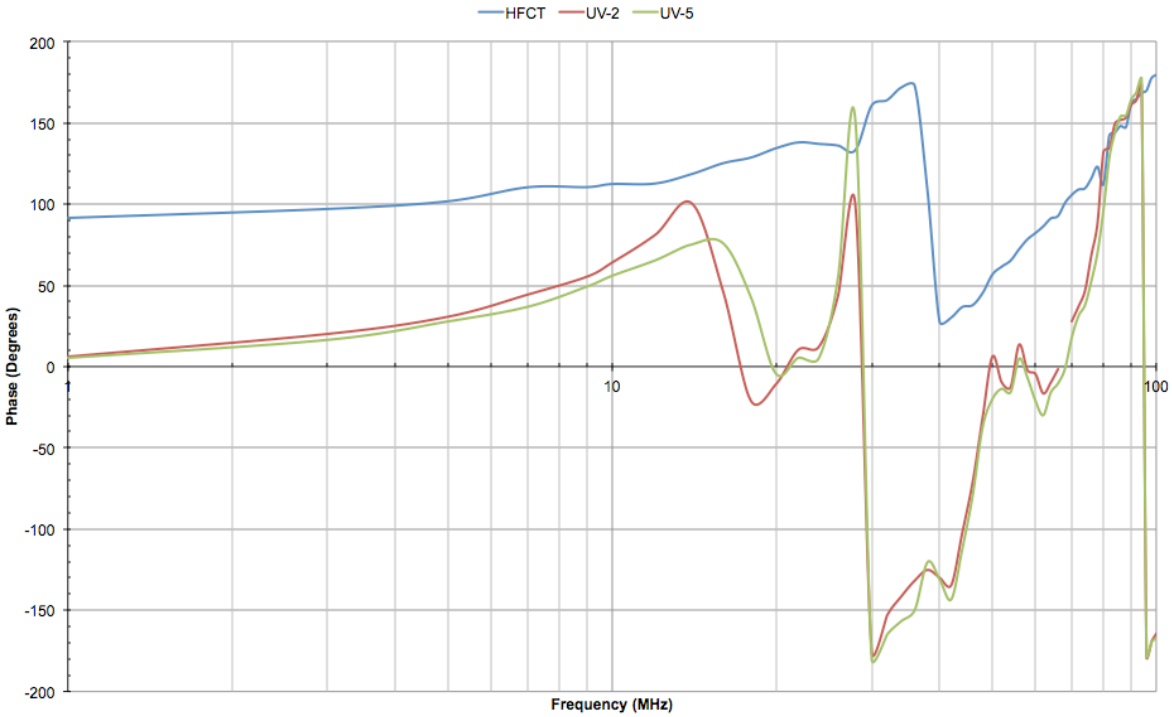

Figure 7.16 Phase response of UV-LIGA Rogowski sensors in self-integrating mode

In figure 7.18 [7.7], the magnitude response is initially shown as having a flat response with a number of discrete notches at 50 MHz and 160 MHz and two small spikes around 100 MHz and 135 MHz. The RHS of figure 7.18 shows the actual measured transfer impedance. This has a reasonably flat response up to 70 MHz before the shape changes to contain a level of peaks and nulls in the output beyond 100 MHz. This behaviour is explained in [7.7] and [7.8] as a high frequency effect where the Rogowski sensor is modeled as a transmission line with one end short circuited and discrete notch frequencies at these higher frequencies occur where the output tends to zero. This is described in equation 7.1, where k = 1 is the first discrete notch zero. The size of the notches is related to the value of integrating impedance used on the Rogowski sensor [7.7]. Higher values of integrating impedance result in a more pronounced deep notch in the Bode response of the sensors.

Therefore there is a trade-off with using a lower value integrating impedance and smaller notches and lower sensitivity to high frequency signals. The discrete notch effect is reproduced in the Bode response when the model is changed from the lumped model discussed in Chapter 5 to a distributed high frequency model shown in [7.7] and [7.8].

Simulating a model in this way would require changing the voltage gain transfer function used in chapter 5 to a transfer impedance model [7.7].

$$f_r = \frac{k}{2\sqrt{L_0 C_0}} \qquad \text{Eqn. 7.1}$$

The voltage gain transfer function examined the relationship between V_{out}/V_1 whereas the transfer impedance model examines the relationship between V_{out}/I_1.

For the phase response, the sensors show 0° phase shift up to 200 KHz; beyond this point all the sensor designs begin to change phase at a different rate. The first sensor to produce a -90° phase shift is design UV-2, which occurs at 1 MHz. Sensor design UV-5 occurs shortly afterwards at around 1.5 MHz. Design UV-2 is the last sensor to move away from 0° to 90° phase change at 2.5 MHz. In contrast, the phase diagram constructed with the measurements presented in 7.2 show that the change of phase from 0° to -90° occurs between 1 – 10 MHz and continues up until 1 GHz for some sensors designs.

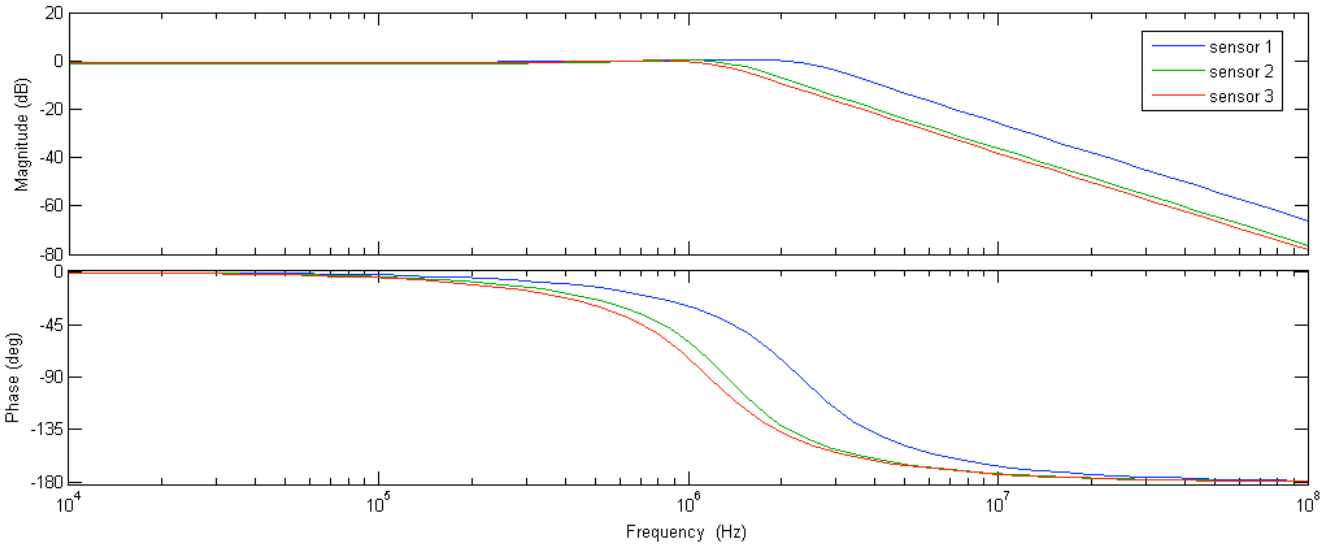

Figure 7.17 Simulated Bode response of UV-LIGA sensors in self-integrating mode using measured R, L and C parameters.

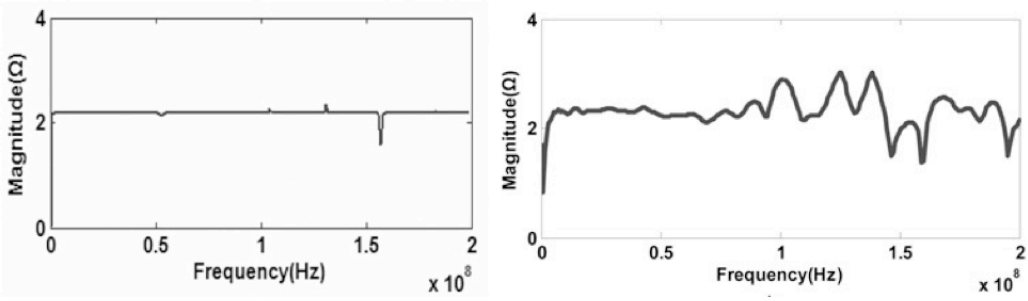

Figure 7.18 Simulated transfer impedance of Rogowski sensor. LHS is simulated transfer impedance and the RHS is the measured transfer impedance [7.7].

This is explained from the differences in the calculated R, L and C values and the values measured in this chapter. Additionally, in [7.2] the author states that self-integration will occur where the condition $Z_{int} < Z_e$. The parameter Z_e is expressed in the equation below as:

$$Z_e = \sqrt{\frac{L_l}{C_l}} \qquad \text{Eqn. 7.2}$$

Since there is a big change between the measured and simulated capacitance it is likely that this will have some effect on the above equation, meaning that the integrating impedance chosen (Z_{int}) of 1000 will be too high for the self-integrating condition to occur.

The shape of the phase waveform in figure 7.16 is similar to that shown in [7.9], [7.10], [7.3] and [7.4], therefore the fast switching of phase at the higher frequencies is likely to be down to the same reasons as the phase change.

7.5 Pseudo PD signal analysis

7.5.1 Qudos sensor in differentiating mode

Although no actual measurements were taken by generating a pseudo-partial discharge signal in the test setup for the differentiating case, it was still decided that it was worthwhile to understand the difference that the inductance, capacitance and resistance values have on the sensor rise time. For the self-integrating analysis, the ability of both Rogowski sensor designs was evaluated against pseudo-partial discharge like signals.

The step response analysis based on the measurements obtained earlier in the chapter presents rise times that are larger than originally predicted. The step response is summarized in Table 7.5. When the step response is compared to the modelled step response in Chapter 4 (Table 4.7) it is evident that the modelled response possesses a higher rise time at the expense of many oscillations in its response. The original results show rise times in the regions of tens of ns and settling times in the order of hundreds of ns. The updated results show rise times in the order of tens or hundreds of μs and settling times in the order of hundreds of μs. The other difference between these results is that there is no overshoot in the response of the updated calculations compared to the original model. This is likely to be attributed to the higher values observed for the resistance, inductance and capacitance values measured in section 7.2.

Table 7.5 Summary of simulated step response of the Qudos sensors in differentiating mode using R, L and C values

Sensor type	Rise time (μs)	Peak Response	Settling time (μs)
Q1	355	1	632
Q2	101	1	180
Q3	51.4	1	91.5
Q4	109	1	195
Q5	29.7	1	52.9

The combination of slightly higher inductance and resistance values coupled with the much higher capacitance reading has increased the damping factor (ζ) of the second order transfer function which results in a higher level of damping.

The order of the sensor designs with the fastest rise time and settling time differs from that calculated in section 4.6.1 of Chapter 4. This is likely to be due to the values used in this model being the average of all sensor readings for each design. The large variance in some of the measurements and the higher averaged values for each parameter leads to a nonlinear increase in the resistance, inductance and capacitance values used in the calculations for each sensor design. The results for the sensors in self-integrating mode presents an opportunity to see if the sensors display behaviour closer to the original simulated values in Chapter 4 or if they are closer to the behaviour expected from the measured values earlier in this chapter.

7.5.2 Qudos sensors in self-integrating mode

The response of sensor Q2 to discharge type signals is shown in figures 7.19 and 7.20. A summary is provided in Table 7.6 of the performance of all sensor designs to the pseudo-partial discharge signals. The results for these designs show that the smaller Rogowski sensors manufactured on silicon are a viable option for measuring partial discharge signals when compared to the UV-LIGA sensors. The sensor designs show rise times that range from 1.7 – 18.3 ns, which is within the calculated range of the rise-times quoted in Table 4.9 of the modeling chapter. The order of sensor designs with the fastest rise time to the slowest rise time in these measurements is not the same as was calculated in Table 4.9 of the modeling chapter. This is attributed to the differences in measured capacitance values to those calculated in Chapter 4. The different capacitance values measured will alter the rise times due to its impact on the second order differential equation that describes the sensor behaviour across the frequency response and step response analysis. The settling time for sensor design Q2 can be taken from the screenshot taken of the oscilloscope trace. It shows around 3 – 3.5 time divisions, resulting in a settling time of around 600 - 700 ns, which, if taken to mean a value ±2 % of steady state value, is slightly less than the HFCT. The oscillations shown in 7.19 and 7.20 are similar to those reported in [7.11] and [7.3]. It is explained as under-damped behavior of the sensor and can be resolved by modifying the damping of the sensor through a selection of the damping factor to around $\zeta = 0.7$.

In terms of the magnitude output of the sensors, all of the Qudos manufactured sensors produce a voltage output that is higher than the commercial HFCT. The range of voltage outputs from low to high start with design Q2 followed by Q3, Q1, Q5 and Q4. There is a trade-off between the sensor providing the highest output voltage and the shortest rise time and settling time. Design Q4 would be chosen based on this compromise as a rise-time in the order of 30 ns and an output voltage of the sensor of 330 mV is a signal that can be easily processed without further amplification.

Figure 7.19 Sensor Q2 response to a discharge signal in self-integrating mode

Figure 7.20 Sensor Q2 response to a charging signal in self-integrating mode

Table 7.6 Response of Qudos sensors to rising and falling PD signals in self-integrating mode. (Z_L=1000 Ω).

Sensor	Discharging signal			Charging signal		
	Magnitude (mV)	Rise-time (ns)	Settling time (ns)	Magnitude (mV)	Rise-time (ns)	Settling time (ns)
Q1	315.9	21	1400	353.2	5.2	1000
Q2	201	5	900	217.9	1.7	900
Q3	213.9	17.8	1000	208.2	1.86	950
Q4	337	31	2900	386.6	18.31	3200
Q5	331.7	27	3000	397.2	14.25	2900
HFCT	68.9	35.8	1800	70.9	222.7	1400

Table 7.7 Re-calculated step response of Qudos manufactured Rogowski sensor in self-integrating mode.

Sensor type	Integrating impedance (Ω)	Rise-time (μs)	Peak amplitude	Settling time (μs)
R1	0.1	0.08	5.97e-4	0.15
R1	1	0.74	0.0059	1.30
R1	10	0.70	0.056	12.5
R1	100	47	0.3740	83
R1	1000	107	0.8563	190
R2	0.1	0.068	8.7e-4	0.12
R2	1	0.60	0.0086	1.10
R2	10	5.5	0.08	9.80
R2	100	32	0.467	57
R2	1000	62	0.897	11
R3	0.1	0.027	4.17e-4	0.049
R3	1	0.24	0.0042	0.43
R3	10	2.3	0.04	4.10
R3	100	17	0.294	30
R3	1000	47	0.806	83
R4	0.1	0.090	0.001	0.16
R4	1	0.85	0.01	1.5
R4	10	6.5	0.08	12
R4	100	42	0.51	74
R4	1000	745	0.91	130
R5	0.1	0.18	9.35e-4	0.32
R5	1	1.7	0.009	3.10
R5	10	7.45	0.04	13
R5	100	90	0.48	160
R5	1000	170	0.9	300

The PD performance was also evaluated by substituting the measured R, L and C measurements into the second order lumped model and performing a step response analysis. The results are summarised in Table 7.7, which show that the rise time performance has increased from the original model.

7.5.3 UV-LIGA manufactured sensor response to partial discharge in differentiating mode

The step response analysis for the UV-LIGA sensors is presented using the same methodology discussed for the Qudos sensor in the differentiating mode. The simulated results that are displayed in Table 7.8 show step responses with an element of overshoot. The reason that this behaviour occurred for the UV-LIGA sensors is that the measured resistance and inductance values for these parts were in a closer range to the calculated value, whereas the capacitance was slightly larger that predicted.

Table 7.8 UV-LIGA manufactured Rogowski sensors (differentiating mode using measured R, L and C values).

Sensor type	Rise time (μs)	Peak Response	% Overshoot	Settling time (μs)
UV-2	0.234	1.164	16.4	0.23
UV-5	0.195	1.22	22	1.08
UV-10	0.117	1.16	16.32	0.575

This meant that overall the parts behaved more closely to what was expected in terms of producing a response that comprised a level of overshoot and fast rise-times and settling times. The re-simulated values show that the increase in capacitance and resistance values has increased the rise time by a factor of 1,000 for UV-1, 100 for UV-2 and 100 for UV-3. The settling times are faster by a factor of 10 for UV-10, almost unchanged for UV-5 and faster for UV-2. This corresponds with an 80 % reduction in the overshoot in the response signal so it appears that the combination of increases in capacitance and resistance have increased the damping ratio for all the manufactured devices. This increase in damping has reduced the level of oscillations in the response of the sensor to a step input signal, therefore it settles within 2% of its steady state value much more quickly.

7.5.4 UV-LIGA Rogowski sensor in self-integrating mode

The sensors tested in this section were designs UV-5 and UV-2, with the HFCT used to benchmark the measurements. These waveforms are located in the Appendix A2 and summarised in table 7.9. The results of these tests confirm that not only can a micro-manufactured 2.5D Rogowski sensor be used to measure this type of waveform, but it also possesses a faster rise time than the HFCT in response to these signals. In Table 7.9, design UV-2 shows a rise time of around 52.7 ns in comparison to the 222.7 ns for the HFCT. Design UV-5 produced a rise-time of 51.6 ns, which is marginally faster than design UV-2. Inspection of the time period per division (400 ns), the oscilloscope shows that this is within the expected figure.

Table 7.9 Summary of the pseudo falling PD test on UV-LIGA Rogowski sensors

Sensor (cm)	Discharge Signal Magnitude (mV)	Discharge signal rise-time (ns)	Charging signal Magnitude (mV)	Charging signal rise time (ns)
UV-2	475	30	479	52.7
UV-5	580	25	428.1	51.6
HFCT	68.9	35.8	70.9	222.7

The output magnitude of the sensors is 479 mV for design UV-2 and 428.1 mV for the design UV-5. The HFCT produces 70.9 mV, which are six or seven times smaller than what is produced by the UV-LIGA sensors. Closer inspection of these graphs show that the output of the Rogowski sensors could be higher than the figure quoted. The waveform shows a lot of overshoot, with the peak reaching almost 1.5V before oscillating above the x-axis in the positive direction. Clearly the sensor displays complex roots due to the operating integrating resistance as the settling time required to reach the zero output is very long. Based on the 400 ns per time division setting, it shows that the sensor requires 2 μs of settling time. This could be improved further by optimizing the integrating resistance to a point where it suitably damps the oscillations to decrease the settling time, whilst preserving the high sensor output magnitude.

Table 7.10 Summary of step response of UV-LIGA manufactured Rogowski sensor using measured parameters

Sensor type	Integrating impedance (Ω)	Rise-time (μs)	Peak amplitude	Overshoot (%)	Settling time (μs)
UV-2	0.1	0.315	0.001	0	0.56
UV-2	1	0.313	0.01	0	0.56
UV-2	10	0.286	0.092	0	0.52
UV-2	100	0.218	0.53	0	0.61
UV-2	**1000**	**0.23**	**1.04**	**14.6**	**1.06**
UV-5	0.1	0.33	6.7E-4	0	0.58
UV-5	1	0.32	0.0067	0	0.58
UV-5	10	0.304	0.063	0	0.55
UV-5	100	0.207	0.406	0	0.32
UV-5	**1000**	**0.193**	**1.023**	**17.5**	**0.98**
UV-10	0.1	0.16	0.0018	0	0.278
UV-10	1	0.15	0.0177	0	0.274
UV-10	10	0.133	0.153	0	0.24
UV-10	100	0.11	0.7	0	0.34
UV-10	**1000**	**0.109**	**1.09**	**15.3**	**0.55**

For the charging PD waveform, the oscilloscope readings show that the rise times were 899.8 ns for design UV-2 and 831.5 ns for design UV-5. Comparison of this figure with the prior figure shows that both readings share the same time period per division (400 ns) and the same fast response to the peak sensor output that is a fraction of a time division. Both waveforms should therefore have a rise time that is below 35.8 ns instead of only the one waveform showing this and the other apparently showing a rise-time close to 1 μs (899.8 ns). Clearly the response times of both sensors is below ten μs but display a much longer settling time; this is evident from the large oscillations about the x-axis.

The magnitude output of the sensor designs for this input waveform is measured as 475 and 580 mV. However, closer inspection of the peak of the waveform versus the 16 voltage divisions reveals the peak voltage to be closer to 1.6 V. When compared to the prior figure, the peak outputs are similar. In appendix A2 and Table 7.10, the results are presented for the simulated step response based on the R, L and C measurements that were discussed earlier in this chapter. The simulation looks at the step response of the Rogowski sensors with integrating resistances of 0.1, 1, 10, 100 and 1,000 Ω. Of relevance to the

measurements discussed in this thesis are the results of the sensors for the 1,000 Ω integrating resistance and the impact on the rise-time, peak amplitude, overshoot and settling time. For the simulated values shown in Table 7.10, the rise times are much higher than measurements indicate. Values of rise times range from 110 ns to 230 ns, whereas the measured values are less than 30-50 ns. For the peak amplitudes, the level of overshoot ranges from 14.6 to 17.5% higher than would be expected if the R, L, C and Z_{INT} values had been optimized to provide a critically damped output. This is likely to be attributed to the higher than expected capacitance of the Rogowski sensor when compared to the simulated values reported in Chapter 4.

Since the R and L values of the sensor are in close agreement to one another this seems a logical conclusion to the results seen here. The calculated settling times of the Rogowski sensor is less than the measured values by around a factor of 10; this again is likely to be attributed to the differences in measured capacitance versus the calculated capacitance values. This means that higher values of capacitance reduce the settling time of the sensor. Similar results are presented in the work referenced [7.11], [7.7], [7.3], [7.4], [7.12] and [7.13] that examine the Rogowski coils ability to detect partial discharge signals by measuring real life partial discharges or a pseudo PD signal using a waveform generator.

Both UV-LIGA and Qudos sensor designs demonstrate improvements over the conventional HFCT to measure fast rise-time signals in a quicker time and to output a higher voltage. Such designs could be mass-produced to provide a sensor that costs far less than the £800 HFCT. Additionally, the size and weight of these devices is much lower than the HFCT by at least two orders of magnitude, which indicates it as being a suitable portable sensor for monitoring PD signals on EWIS.

7.6 Summary

The test and analysis of UV-LIGA Rogowski sensors and Qudos Rogowski sensors have been introduced in this chapter, which allowed investigation and clarification into the trade-offs between sensor size and substrate choice.

The first set of measurements focused on acquiring the inductance, capacitance and resistance values of each sensor design. Observations between measured and simulated results have been reported. The large number of sensors manufactured by Qudos provided an opportunity to analyse the variation within and between designs. The statistical analysis showed larger than expected variation within each sensor design that is thought to originate from variations in the manufacturing process rather than variation from the instrument. The capacitance measurements for the Qudos sensors showed the greatest difference to the simulated values in the modeling chapter.

For wafer 12, the capacitances readings were in the hundreds of nF range instead of being hundreds of pF. Further root cause analysis revealed that the equation used for calculating the capacitance does not include the use of passivation material on top of the coil turns. The material used was a polymer therefore this would introduce a relative permittivity into the calculation of around 3.5. The introduction of a passivation layer on top of the coil turns accounts for some of the additional increase in capacitance. Deviation to the manufacturing specifications would be the introduction of a thinner oxide layer between the coil turns and substrate that would present an increase in parasitic capacitance.

The inductance and resistance measurements of each UV-LIGA design were very close to the calculated values. This adds a level of confidence that the equations used could accurately predict the parameters of each sensor. The equations for inductance and resistance are therefore accurate for calculating the sensor lumped parameters and also that the impedance analyser can accurately measure these parameters. The capacitance measurements still showed a large difference between predicted and measured values. The measured values differed by a factor of 1,000, indicating an error in the capacitance calculation and/or variation in the measurement of capacitance. This could be further investigated by testing the impedance analyser against a range of small reference capacitors to see if it was accurately measuring these values.

To rule out the measurement system as being the source of error, some accredited capacitors could be bought that covered a range of values in the nF and pF range for testing the measurement system against. A number of measurements could be made of each part to see what the accuracy and precision of the measurement was. If the system accurately measures these parts then the source of variance of the measurements would be attributed to the sensors. If this were to occur then further root cause analysis would be required for the Qudos parts. This would involve examining the sizes of the key parameters that influence the capacitance of each sensor.

The secondary aspect of the testing examined the sensor designs ability to detect a range of high frequency sine waves that we sent down a wire and also a pseudo partial discharge waveform. The performance of the sensor designs was benchmarked against a commercial high frequency current transformer (HFCT).

At the higher frequency range above 10 MHz, the Qudos Rogowski sensors in self-integrating mode delivered a higher magnitude response than the HFCT. This will allow the higher frequency portions of a PD signal to be amplified, therefore helping to retain information about a PD signals rise-time. The HFCT only showed a higher output at 1 MHz before all the Qudos manufactured designs began to output higher voltages. Both devices appeared to show discrete notch frequencies between 30 – 50 MHz, which is a common effect reported when testing Rogowski sensors against high frequency signals.

The UV-LIGA sensors produced similar characteristics when tested versus the HFCT. These sensors provided a higher voltage output than the HFCT above 10 MHz, therefore both designs are acceptable to use for testing high frequency signals.

The rise-time and magnitude performance of the Rogowski sensors were examined when a pseudo PD signal was sent down the wire. Both the UV-LIGA and Qudos sensors show faster rise times than the HFCT and produce a greater magnitude output. The rise-times were in the order of 1.7-18.3 ns and the magnitudes were around 210-400 mV.

In terms of optimum sensor design selection, the Qudos manufactured sensors show the best results while retaining a smaller footprint and a passivation layer. If the passivation layer were not present then this may further increase the rise time performance of the

sensors. Additionally, the manufacture of the Rogowski sensors on silicon could allow the manufacture of a selection of sensors on a common substrate such as humidity, temperature and Rogowski sensor. If two Rogowski sensors were to be included in this arrangement, then one sensor could be covered in the polyimide passivation and used to measure humidity by measuring the capacitance change according to changes in the relative humidity.

The benefit of this design is that is can be installed in areas where space is a premium due to the sensor being fitted with the thinner dimension protruding radially out from the wire and the longer side of the sensor lying parallel to the WUT.

References

[7.1] C.R. Neagu et al. “Characterisation of a planar microcoil for implantable microsystems”. *Proceedings of Eurosensors X, Sensors and Actuators A: Physical,* vol. 62, pp. 599 – 611, July 1997.

[7.2] G. Robles and M. Argueso et al, “Identification of parameters in a Rogowski coil used for the measurement of partial discharges”, *IEEE Instrumentation and Measurement Technology Conference Proceedings,* pp.1 - 4, 1-3 May, 2007.

[7.3] “On-line PD Measuring System Modeling and Experimental Verification for Covered-Conductor Overhead Distribution Lines”, *2007 Mediterranean Conference on Control and Automation*, pp. 1 – 6, July 27 – 29.

[7.4] V. Dubickas, H. Edin, "High-Frequency Model of the Rogowski Coil With a Small Number of Turns," *IEEE Transactions on Instrumentation and Measurement,* vol. 56, no. 6, pp. 2284 - 2288, Dec. 2007.

[7.5] Q. Zhang et al, “Design of a current transducer with a magnetic core for use in measurements of nanosecond current pulses”, *IOP Measurement Science and Technology*, vol. 17, no. 4, pp. 895 - 900, 23rd March 2006.

[7.6] N. Karrer and P. Hofer-Noser, "PCB Rogowski coils for high di/dt current measurement," *IEEE 31st Annual Power Electronics Specialists Conference,* vol.3, pp.1296 - 1301, 18 – 21 June 2000.

[7.7] Z.S. Zhang, D.M. Xiao and Y. Li. "Rogowski air coil sensor technique for on-line partial discharge measurement of power cables," *IET Science, Measurement & Technology,* vol.3, no.3, pp.187 - 196, May 2009.

[7.8] Valentinas Dubickas, “Development of on-line diagnostic methods for medium voltage XLPE power cables”, Ph.D. thesis, ETK, School of Electrical Engineering, Royal Institute of Technology (KTH), Stockholm, February 2009.

[7.9] G. M. Hashmi, M. Lehtonen and M. Nordman, “Modeling and experimental verification of on-line PD detection in MV covered-conductor overhead networks”, *IEEE Transactions on Dielectrics and Electrical Insulation,* vol. 17, no. 1, pp. 167 – 180, Feb. 2010.

[7.10] G. M. Hashmi “Partial Discharge Detection for Condition Monitoring of Covered-Conductor Overhead Distribution Networks using Rogowski Coil”, *PhD Thesis*, 2008.

[7.11] C. Xianghu; Z. Xiangjun and D. Feng et al. "Novel PCB sensor based on Rogowski coil for transmission lines fault detection," *IEEE Power & Energy Society General Meeting,* pp. 1 - 4, 26-30 July 2009.

[7.12] L. Dalessandro, N. Karrer and M. Ciappa et al. "Online and Offline Isolated Current Monitoring of Parallel Switched High Voltage Multi-Chip IGBT Modules", *IEEE Power Electronics Specialists Conference, 2008. PESC 2008.* , pp. 2600 - 2606, 15-19 June.

[7.13] K.J. Khor and K.L. Wang. "Partial Discharge Sensing in Overhead Distribution Line", *2008 Australian Universities Power Engineering Conference*, pp. 14 – 17, 14 – 17 Dec. 2008.

Chapter 8 Characterisation and testing of a humidity sensor

8.1 Introduction

This chapter covers the work done on the design, manufacture and test of a polyimide covered interdigitated sensor commissioned by the South East of England Development Agency (SEEDA).

As explained previously, different levels of humidity can exist throughout the airplane and at different times. As the aircraft moves from one location to another, humidity conditions can be sufficiently high that a drop in temperature in parts of the aircraft will result in condensation of water on the cooler surfaces. Water might appear on polymer wiring looms and, in the long term, inside the wiring interconnect. Discussions with experts in the field of humidity and moisture measurement [8.1] indicate that it is feasible to create a small, low cost humidity sensor with fast response to detect moderate levels of moisture in a gas or within hermetically sealed in electronic devices. There is also the possibility that these MEMS humidity sensors can be designed to operate better over a narrower range of humidity in order to detect moisture leaks. This chapter presents therefore preliminary work carried out to manufacture such a sensor.

The chapter starts with a presentation on the fundamentals of humidity sensing and the rationale that led to the choice of the sensor. The procedures used for characterising the humidity sensors manufactured by Qudos Technology are presented along with experimental setup and characterisation results. A summary of further development and test work to be carried out on the sensor is given along with a possible test setup.

8.2 Humidity – some definitions

Humidity is defined as the presence of moisture, which is water vapour present in air or in a gas [8.2]. When the partial pressure of water vapour is compared to the total atmospheric pressure, it is possible to derive the absolute quantity of moisture in air. To further understand this concept, consider a closed volume of air that sits above water at a certain temperature. There will be water molecules leaving the water to the air and some water

molecules in the air going back to the water. The balance at which the water leaves and enters the air will at some point reach equilibrium; at this stage, the water vapour content in the air and water vapour pressure become constant. This condition is known as the Saturation Water Vapour Pressure, which increases and deceases in proportion to temperature [8.3]. The saturated vapour pressure is the maximum amount of moisture that can be held at a certain temperature.

Absolute Humidity is the mass (m) of water vapour in a unit volume of gas (v); it can also be considered in terms of its corresponding density of water vapour, d_w. It is mathematically described as follows [8.4]:

$$absolute\ humidity\left(\frac{g}{m^3}\right) = \frac{mass\ of\ water\ vapour}{volume\ of\ air} \qquad \text{Eqn. 8.1}$$

From this equation, the absolute humidity will change as the volume of air changes, which makes it a less suitable method for measuring the humidity in air [8.4].

Relative Humidity (%RH) at any specified temperature is the ratio of partial vapour pressure, e, above water in air to the saturated vapour temperature, e_w, at the same temperature above water:

$$\%RH = \frac{actual\,vapour\,pressure\,in\,air}{saturated\,vapour\,pressure}\cdot 100 = \frac{e}{e_w}\cdot 100 \qquad \text{Eqn. 8.2}$$

Saturation vapour pressure varies with temperature, so relative humidity changes with the amount of water vapour in air and temperature [8.4]. Another way of expressing relative humidity is by considering it in terms of the mole fraction of water vapour in a closed space to the mole fraction of water vapour at saturation in the same closed space.

Dew point measurement: This is the temperature where a gas will deposit water on a cool surface by condensation reaction at a constant pressure [8.2,8.3]. At this temperature the gas is fully saturated (100 % relative humidity) [8.3]. Dew point can also be defined as the temperature that the air must be at to hold the maximum possible amount of moisture [8.4]. Translation from Dew Point, T_d, to saturated vapour pressure in Pascals, $e_w(T)$ is achieved through modification of the Magnus Formula [8.5]. At temperature T (in ˚C), the saturated vapour pressure over liquid water is expressed in hectoPascals (hPA) as:

$$e_w(T) = \alpha \cdot e^{\left(\frac{\beta \cdot T}{\lambda + T}\right)} \qquad \text{Eqn. 8.3}$$

where α = 6.112 hPA, β = 17.62 and λ = 243.12 ˚C.

Re-arranging the above equation by taking the natural logarithm leads to the following expression of the Magnus formula [8.5]:

$$\ell n\ e_w(T) = \ell n\ 611.2 + \frac{17.62 \cdot T}{243.12 + T} \qquad \text{Eqn. 8.4}$$

8.3 Types of humidity sensors

The humidity sensor market offers solutions ranging from die level to integrated packaged solutions consisting of the humidity sensor die and on-board signal processing electronics. Sensors can also be integrated into probe solutions that are aimed at industrial applications in the energy, industrial and healthcare markets [8.3,8.6]. The main types of humidity sensors considered for integration in a health and usage monitoring system are based on changes to the resistive, mass, capacitive, thermal conductivity and optical properties of the sensor sensitive material.

8.3.1 Chilled Mirror Hygrometers

Also known as the condensation hygrometer, the chilled mirror hygrometer is the most accurate and reliable hygrometer. It is widely used as a calibration standard for humidity sensors and probes at the National Physical Laboratory (NPL), England and the National Institute for Standards and Technology (NIST).

The measurement principle of this device is based on maintaining the temperature of a mirror surface at the dew/frost point temperature as water vapour moves across it, resulting in the production of a thin layer of dew or frost. A beam of light from a light source such as a Light Emitting Diode (LED) is aimed at the mirror surface and a photo-detector monitors the reflected light. When there is no dew or frost on the mirror surface, the reflection of light is at its greatest. When the temperature of the mirror is cooled by a thermoelectric cooler such as a Peltier device to less than or equal to the dew/frost point, the formation of

a thin frost or dew layer forms which scatters the light being reflected by the mirror. This causes the light detected by the photo-detector to decrease, indicating the onset of dew or frost point.

The largest source of measurement error in these devices comes from measuring the surface of the mirror when the dew or frost point occurs. To resolve this, the temperature of the mirror is closely monitored by a NIST traceable platinum thermometer embedded close to the mirror surface. The mirror itself is generally constructed from materials that have good thermal conductivity, such as silver or copper. It is also plated with an inert material such as nickel or gold to stop tarnishing and oxidation. The output signal from the photodetector is used as a feedback signal to maintain a thin layer of dew or frost on the mirror. A separate light source and detector are used to compensate errors arising from the optical elements. Both elements are arranged in a bridge circuit containing an adjustable balance that controls the Peltier element and therefore the mirror temperature.

The other source of measurement error is from calculating the dew point based on water forming on the mirror when it is actually frost forming. Below 0ºC, water can exist as ice or supercooled water so the correct equations must be used for calculating the dew point.

8.3.2 Resistive humidity sensors

Resistive humidity sensors measure the change in the electrical impedance of a hygroscopic material such as a conductive polymer or salt. They are manufactured by the deposition of interdigitated electrodes using standard IC manufacturing techniques or wire wound electrodes in a glass or plastic cylinder, as shown in figure 8.1. The physical structure of interdigital electrode resistive humidity sensors is shown in figure 8.2.

The sensor detects humidity through the absorption and adsorption of water vapour in the hygroscopic material leading to the dissociation of ionic functional side groups of the molecular chain. These sensors show an inverse exponential relationship to humidity; changes to the ionic functional groups result in a change in conductivity that is converted to humidity. The response time of these sensors to reach 63 % of its maximum value is between 10 to 30 seconds; the impedance of these sensors changes from 1kΩ to 100 MΩ. Modified polymer materials can be used for resistive humidity sensors; polyelectrolytes are

used to modify the chemical structure of the polymer, where an ionic radical group is attached to specific regions of the repeat unit belonging to the polymer backbone. This results in the polymer becoming a conducting material.

Figure 8.1 Selection of different resistive humidity sensors [7].

An example of polyelectrolyte materials (PE) is sulfonated polysulfone, which contains groups of sulfate groups along the polymer backbone. The diffusion of moisture into this material whilst an electric field is present across the sensor will hydrolize the ionic groups creating a flow of ions. As humidity levels rise, the conductivity of the material will decrease. A majority of resistive type humidity sensors use AC excitation with no DC bias to prevent polarization of the sensing material [8.4]. Further signal conditioning is applied to change the AC signal to a DC signal that is scaled, amplified and converted to digital format.

This type of sensor has the advantage to be interchangeable to within a range of ± 2 %, allowing calibration of the sensor to be carried out using a resistor at a fixed % RH set point. This sensor type uses coatings, however, that are slightly water soluble and can shift values when left exposed to condensation. Additionally, resistive sensors are temperature dependent when exposed to environments where the temperature can fluctuate by 10 ºC.

These sensors are designed to operate in the -40 to 100 °C temperature range, but are vulnerable to chemical vapour and other contaminants that exist within the environment. Consequently the lifetime of resistive humidity sensors is around 5 years.

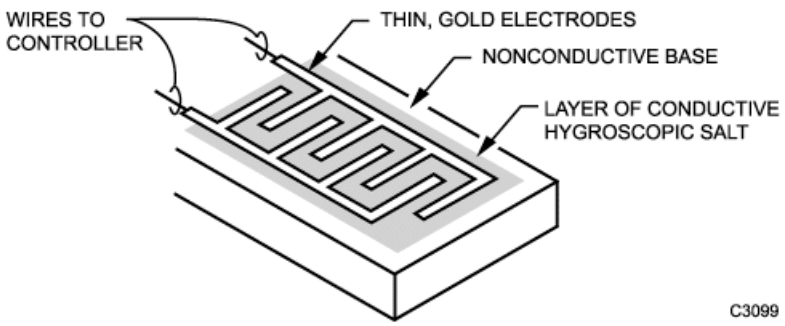

Figure 8.2 Resistive humidity sensor consisting of interdigital electrodes and conductive polymer [8.8].

Recent developments in resistive humidity sensor technology have focused on ceramic coatings to overcome condensation issues. This type of sensor is based upon a ceramic substrate that is patterned with interdigitated electrodes; these are then covered with a ceramic binder and conductive polymer mixture. The final assembled sensor is installed in a plastic housing that has a dust filter, which is composed of hydroscopic treated material.

8.3.3 Mass sensitive sensors

This type of sensor measures humidity according to the resultant mass change of a moisture sensitive material. The device features a mechanical structure that vibrates at its natural resonant frequency. As the device absorbs or desorbs moisture from its environment, there will be changes to its mass that is detected through changes in its natural vibrating frequency [8.9-8.13]. This mode of operation is used for Quartz Microbalance (QM) devices and Bulk (BAW) and Surface Acoustic Wave (SAW) Sensors. SAW sensors feature interdigitated electrodes on a piezoelectric substrate that is sensitive to surface perturbations due to the acoustic energy of the emitted surface waves being confined to the surface region. One type of SAW sensor is reported in [8.11,8.13], whereby surface acoustic waves are launched across the polyimide film by the reverse piezoelectric effect. An RF signal is generated at the operating frequency of the sensor; the signal is transported from the interdigitated transducer IDT to the polymer film and out to the output IDT. The velocity and amplitude of the signal are then measured. Water vapour absorbed by the polymer will affect the transmission time of the acoustic wave and therefore the frequency, amplitude and phase of the acoustic waveform. Equation 5 below expresses the change in

velocity of the signal after passing through the lossless film of the sensor surface by [8.7,8.9,8.11,8.13]:

$$\frac{\Delta V_R}{V_R} = (k_1 + k_2) fh\rho = \frac{\Delta f}{f} = \frac{\delta\varphi}{\varphi} \qquad \text{Eqn. 8.5}$$

8.3.4 Thermal conductivity humidity sensors

Thermal conductivity sensors measure absolute humidity through differentiation of the thermal conductivity of dry air and that of air containing water vapour. When air or gas such as nitrogen is dry it has greater ability to sink heat than more humid environments, as the gas contains greater amounts of water vapour. Thermal conductivity sensors typically consist of two identical thermistor sensors that are connected in a bridge circuit configuration. When current is passed through these thermistors the sensors are heated through Joule losses, at temperature rises greater than 200°C. It is the heat dissipation from these thermistors that gives an indication of the humidity. The sealed thermistor shown in figure 8.3 will have a greater temperature dissipated than the exposed one due to the difference in thermal conductivity of the water vapour compared to that of the nitrogen. The Joule heat generated will cause different temperatures and therefore provide different values of their respective resistances, which are proportional to the absolute humidity. Calibration of these sensors is done by placing the sensor in moisture free air or nitrogen and adjusting the respective output to zero.

Figure 8.3 Thermal conductivity humidity sensor

This type of sensor is very durable and can operate up to temperatures as great as 300°C as well as being resistant to chemical vapours. As greater resolution can be achieved at higher

temperatures than capacitive and resistive sensors, they are more suitable to more hostile environments. Typical accuracy is +3g/m^3, which can be approximated to around ± 5% R.H at 40°C and ± 0.5 % R.H at 100°C, which is unsuitable for the intended application. Other technologies such as polymer capacitive sensing can achieve accuracy of ± 2 % R.H. This is the target specification for humidity sensors explored in this thesis.

8.3.5 Advanced resistive humidity sensing

Usually when polymer materials are used for relative humidity sensing applications, the mechanism for transduction is via capacitive or resistive changes in the polymer thin film. In [8.14,8.15] an advanced resistive sensing mechanism has been developed to sense moisture using a different property of the polyimide. This sensor works by monitoring the swelling of the polymer as it absorbs greater amounts of water vapour**.** The behaviour of this class of RH sensors is analogous to a traditional bimorph cantilever structure responding to a temperature gradient where differences in material thermal expansion coefficients cause a deflection.

Polymers show changes in electrical, dielectric and mechanical properties as it absorbs moisture; the polymer swells as water molecules are absorbed and diffuse into the bulk polymer material. The dielectric constant of the polymer will change in accordance to the volumetric fraction of water that enters the film. During this process there will be conformational and configurational (shape and orientation) changes in the polymer backbone. This results in dimensional changes in the polymer film, which results in swelling of the polymer in proportion to the volume of water uptake.

Buchol [8.16] developed a humidity sensor that detected the swelling of the polymer by using a design that included piezoresistors to detect the swelling of the polyimide. The design consisted of a diaphragm made of silicon that had polyimide placed on top; by placing the piezoresistors on the diaphragm, the bending of the diaphragm as a result of the swelling of the polyimide could be detected. A humidity sensor similar to the diaphragm type designs used in piezoresistive pressure sensors was proposed by Garlach [8.17] at Dresden University. The size of the diaphragm was 0.6 mm x 1.8 mm in area and 12 μm thickness, with the polyimide placed on top of thickness 12 μm. Within the diaphragm

there are four piezoresistors located in a Wheatstone bridge arrangement to detect the diaphragm deflection and convert it into a relative humidity reading. The piezoresistors, polysilicon bridge circuit traces and the polyimide are electrically isolated by thermal oxide and silicon nitride passivation layers as it was reported in [8.18] that humidity dependant changes in polymer sensing films could strongly impact the accuracy and long term stability of capacitive sensors when the film is in electrical contact with the electrodes. The sensor design produced a sensitivity of 25 μV/%RH and a response time of 25 seconds.

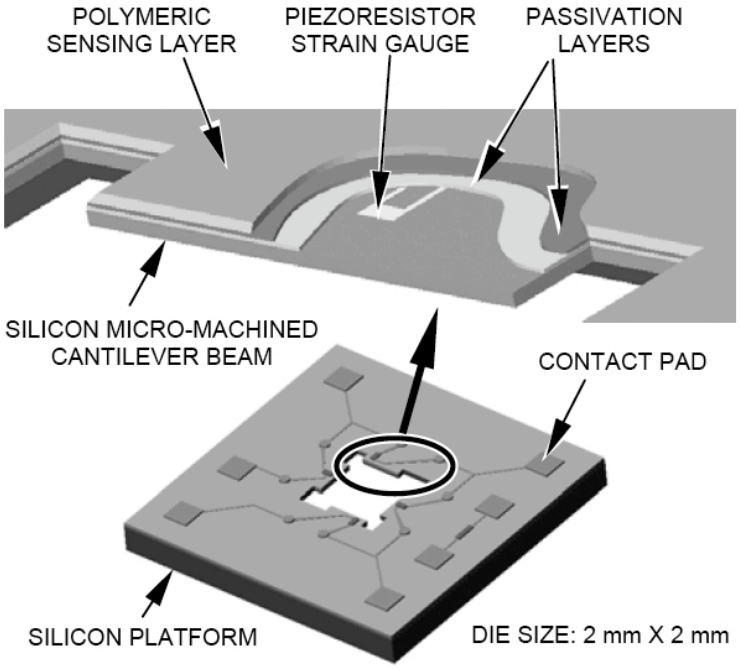

Figure 8.4 Hygrometrix shear-stress based resistive relative humidity sensor.

Hygrometrix went on to commercialise and patent a similar design to Garlach known as the HMX 2000, which is shown in figure 8.4. The sensor chip is 2mm x 2mm in area and the design consists of four cantilever beams covered with humidity sensitive polyimide in a Wheatstone bridge arrangement. The cantilever structures are created in the silicon substrate by bulk micromachining; this allows the cantilever beams freedom to deflect under application of strain. Each cantilever beam has a semiconductor strain gauge that measures the deflections by the piezoresistive effect. The strain gauges are formed by ion implantation and thermal diffusion of the silicon substrate of the cantilever beams. Like Garlach, [8.17] this design incorporated silicon nitride passivation to isolate the polymer film from the metallisation and the strain gauges. A thermistor is also included in the sensor

to calibrate for temperature errors in the relative humidity measurement. This device has a tenth of the output signal of conventional crystalline structure strain gauges, yet has a sixty times faster response speed at around 5 seconds. The output signal is very linear and has excellent temperature sensitivity. The device has also a very good chemical resistivity in [8.19] and recovers from chemical contaminant by rinsing the sensor in isopropanol and deionised water. Parallel plate capacitive humidity sensors did not recover as well in identical tests in terms of chemical resistivity and recovery of the contaminated polyimide. This supports the theory that the top electrode affects the long-term drift of commercially available humidity sensors.

8.3.6 Capacitive polymer humidity sensors

This type of humidity sensor makes use of the change in relative permittivity in polymers as the % RH is being changed in the surrounding environment. These types of sensors are used in a wide range of industrial applications such as windshield defoggers [8.20], HVAC, weather stations, food processing, textiles and environmental test chambers.

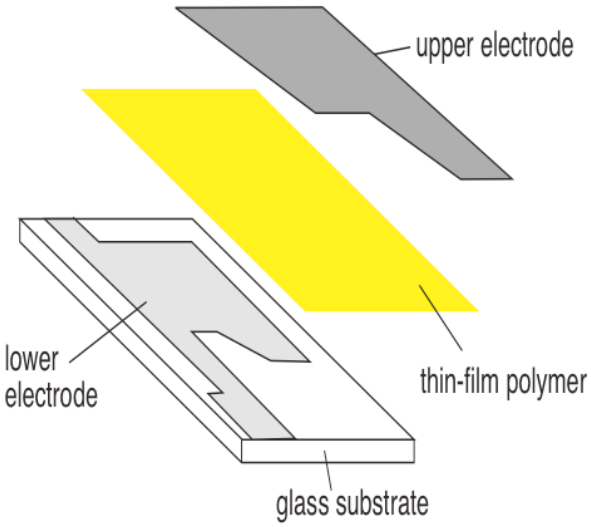

Figure 8.5 Capacitive humidity sensor with porous upper electrode [8.8].

The bulk capacitance value offered by the manufacturers of these sensors is between 4-500 pF at 50 % RH and 25°C; the typical changes in capacitance for 1%RH change is between 0.2 - 0.5 pF. The reasons for the variations in capacitance are down to the footprint of the

sense die, the thickness of the sensing polymer and the geometric details of the electrode layout and configuration.

Micro-manufactured humidity sensors can be categorised according to the transduction mechanism for sensing relative humidity; the main types of sensor are shown in figures 8.5 and 8.6. These sensors are known as interdigitated electrode and parallel plate polymer capacitive humidity sensors. Both types of sensor rely on the change in dielectric constant of the polymer as water vapour diffuses into the polymer. In a dry state (0% RH) the relative permittivities of polymers are around 3.

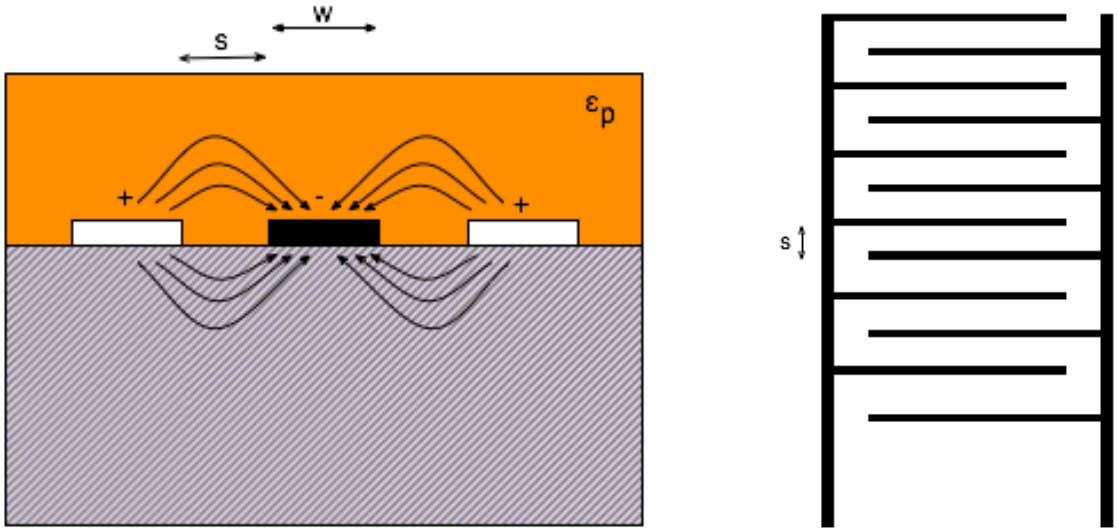

(A) The E-Field between electrodes *(B) Layout of IDT*

Figure 8.6A and 8.6B: IDT humidity sensor

The permittivity of water is around 80, so as the polymer absorbs water vapour, the relative permittivity of the water filled polymer increases. As the relative humidity increases the polymer will continue to absorb water vapour till it is fully saturated. When the sensor is operating in its intended environment, water vapour will continue to be transferred from the ambient environment to the polymer until steady state conditions are reached where the vapour conditions are similar.

Looyenga's equation states [8.14] that the change in dielectric constant of a polymer material with volume uptake of water in the following equation.

$$\varepsilon = \left(\upsilon_2\left(\varepsilon_w^{1/3} - \varepsilon_p^{1/3}\right) + \varepsilon_p^{1/3}\right)^3 \qquad \text{Eqn. 8.6}$$

where n_2 is the fractional volume uptake of water, ε_w is the permittivity of water and ε_p is the permittivity of the polymer.

Absorbed water in a polymer exists in three states, which are chemisorbed, physiosorbed and condensed states. For the first state, water molecules are chemically bound to the surface layer of the polymer due to the highly polar water molecules being attracted to key locations of the polymer side chains through weak attractive forces. In the second state, they are held together by surface forces; in the third state, water will condense inside pores or micro voids in the polymer chain – this is also known as clustering, which is thought to be the major source behind the hysteresis of these sensors. Below a certain pore radius (r_k), water will start condensing inside the pores. This is called Capillary Condensation and the critical radius is expressed as follows:

$$r_k = \frac{2\gamma M_n}{\rho RT \ell n(p_s / p)} \qquad \text{Eqn. 8.7}$$

where γ = surface tension, M_n = molecular weight of water, ρ = density, R = universal gas constant, T= temperature, p_s = saturated pressure and p =pressure.

The parallel plate setup usually involves using silicon or glass as the substrate, followed by the deposition of a bottom electrode, the sensing polymer and a top electrode, which is usually a porous thin film. In some versions of this design, a further polymer layer is deposited on top of the porous upper electrode to protect it from damage. The capacitance of a porous plate capacitive humidity sensor is given as:

$$C(\%RH) = \varepsilon_r(\%RH)\varepsilon_0 \frac{A}{g} \qquad \text{Eqn. 8.8}$$

Where C is the capacitance at a particular %RH set-point, e_r is the permittivity of the polymer sensing material at a particular % RH set-point, e_0 is the permittivity of free space, A is the area of the electrodes and g is the thickness of the polymer or distance between the electrodes.

Substitution of equation 7 into e_r will allow calculation of the full range capacitance change across the full humidity range. The sensitivity of the humidity sensor is expressed in terms of its at dry (0% RH) capacitance versus its maximum capacitance defined usually at 100 % RH [8.21], although its not uncommon for some manufacturers of humidity sensors to specify this as 80 or 90 %.

$$\alpha_H = \frac{\Delta C}{\Delta \%RH} \qquad \text{Eqn. 8.9}$$

Figure 8.6 shows the interdigitated electrode configuration humidity sensor, which consists of two overlapping sets of finger shaped electrodes that are covered with moisture sensitive polymer. The electric field lines generated between adjacent finger electrodes penetrates into the polymer by a finite distance that depends of the spacing between opposing electrodes. There is therefore a trade-off between the optimum thickness of the sensing polymer and the electrode spacing. For optimum selectivity of vapour measurement using an IDT sensor, the electrode periodicity is chosen so that 95 % of the electric field lines are within half the distance of the electrode periodicity.

In addition to the electric field lines extending into the polymer above the electrodes, the field also extends downwards into the substrate. This produces a capacitance between the electrodes and substrate when the electrodes are partially or fully covered by an oxide layer. Such a layer is provided for various reasons such as stopping the water corroding the metal electrodes and also diffusion of the water vapour into the substrate. This parasitic capacitance does not vary with humidity, therefore the change in capacitance is only half the amount that can be achieved by the electric field that is set up between electrodes. Consequently, the sensitivity of IDT sensors is smaller than can be achieved with the porous electrode parallel plate version.

8.4 Design of humidity sensor

The IDT versions of the capacitive humidity sensor are preferred over the parallel plate design because the electrode configuration is planar and does not obstruct the diffusion of water vapour through the polymer film. Additionally, it is likely that sensors with all of the polymer in contact with the environment recover from exposure to chemicals that are likely to be present on EWIS. In tests [8.19], parallel plate humidity sensors did not recover from chemical exposure even after being rinsed in deionised water. In contrast, a humidity sensor with all of its sensing material in direct contact wit the environment managed to recover from exposure to chemical spillage once it has been rinsed in deionised water.

A variety of designs were selected for manufacture through variation of the sensor parameters responsible for changes in capacitance variation across a certain sensing area. These parameters are summarised in Table 8.1. According to [8.22, 8.23] the standard equation for capacitance of a parallel plate humidity sensor (equation 8.10) can be modified to account for the interdigital design, which is presented in equation 10.

$$C = \frac{2 \cdot n \cdot \varepsilon \cdot w \cdot (L - x)}{d} \qquad \text{Eqn. 8.10}$$

where n is the number of electrode fingers, $\varepsilon = \varepsilon_r \varepsilon_0$ where ε_0 is the permittivity of free space and ε_r is the relative permittivity of the sensing polymer above the electrodes. w is the width of the electrode fingers, L is the length of the finger electrodes, x is the difference between L and the finger overlap length (100 m) and d is the spacing between electrode fingers.

Table 8.1 Sensor designs using designs of experiments methodology

SENSOR DESIGN	H1	H2	H3	H4	H5
Sensing area (mm^2)	9	11.25	6.75	9	9
Finger width (μm)	6	6	6	6	6
Finger spacing (μm)	3	3	3	9	6
Finger pitch (μm)	9	9	9	15	12
Finger length (μm)	3112	3460	2704	3100	3100
Finger overlap (μm)	3012	3360	2604	3000	3000
No. of fingers	332	372	288	200	250

8.5 Humidity sensor modeling

To gain an understanding between the various design parameters, a Finite Element Analysis of the structure was first carried out. The software used for this analysis was Comsol Multiphysics. The method of carrying out this analysis is to solve the electrostatics equations for the model, resulting in the energy stored in the two-finger model of the IDT capacitor.

The Maxwell equation for the electric flux density, D (C/m^2), was solved in this software:

$$\nabla \cdot D = \rho \qquad \text{Eqn. 8.11}$$

where ρ is the electric charge density (C/m^3). The Poisson equation allows the determination of the electric field intensity E (V/m). For a linear medium, this is expressed as follows:

$$D = \varepsilon_0 \varepsilon_r E = \varepsilon E \qquad \text{Eqn. 8.12}$$

Combining these two equations leads to the following derivation:

$$\rho = \nabla \cdot D = \varepsilon_0 \varepsilon_r \nabla \cdot E \qquad \text{Eqn. 8.13}$$

The electric field intensity, can be re-written so that it is the gradient of a scalar potential in the form of $E = -\nabla V$, where V is the electrical potential, such that:

$$\rho = \varepsilon_0 \varepsilon_r \nabla \cdot E = -\varepsilon_0 \varepsilon_r \nabla \cdot \nabla V = -\varepsilon_0 \varepsilon_r \nabla^2 V \qquad \text{Eqn. 8.14}$$

This last equation forms the basis of the Poisson's Equation. To analyse the humidity sensor in Comsol, the solver used in Comsol is the electrostatics module; it attempts to solve Poisson's equation for the case where the charge density equals zero. This reduces Poisson's Equation to the Laplace equation:

$$\nabla^2 V = 0 \qquad \text{Eqn. 8.15}$$

Solving this equation provides a measure of the electric field intensity at all points though the model. This information allows the derivation of the electric energy density, W_{stored}, calculated by integrating the above equation:

$$W_{stored} = \frac{1}{2} CV^2 = C = \frac{2W_{stored}}{V^2} \qquad \text{Eqn. 8.16}$$

Comsol can solve this equation for the model implemented, and provide a capacitive representation of the sensor model. This is presented as follows:

$$W_{stored} = \frac{1}{2} CV^2 = C = \frac{2W_{stored}}{V^2} \qquad \text{Eqn. 8.17}$$

Where V is the potential across the sensor and C is the capacitance of the sensor.

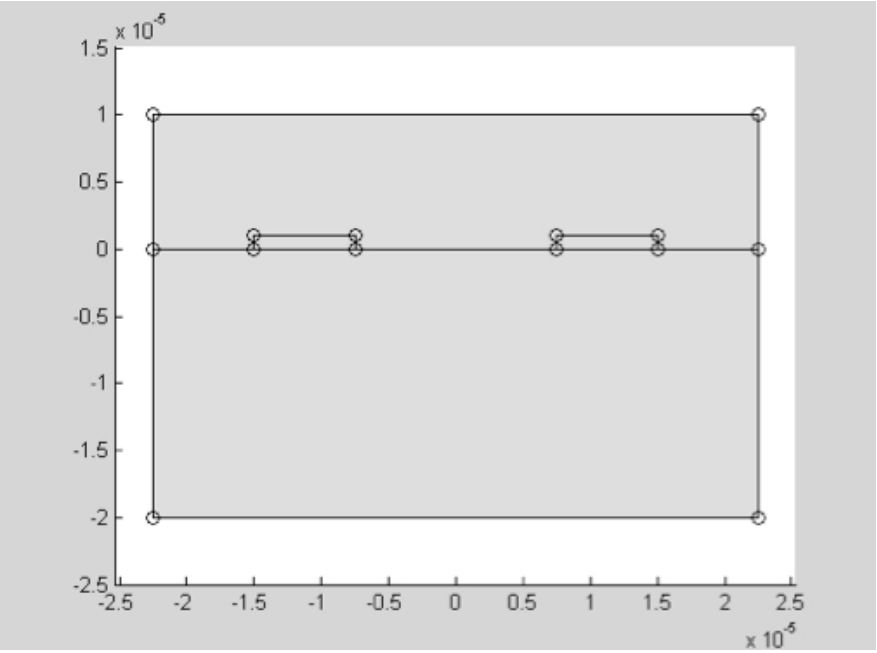

Figure 8.7 2D model of inter-digitated electrodes used to simulate IDT humidity sensor

To solve all of the above equations within the electrostatics module of Comsol Multiphysics, there must first be a model built which correctly reflects the physical structure of the sensor yet simple enough for it to avoid being computationally expensive, resulting in long simulation times. The structure used in the simulation is a 2D representation of the sensor, as shown in figure 8.7 above. It is the side view of the sensor, providing a view of the silicon substrate, the finger electrodes and the moisture sensitive material on top. The finger electrodes are of width, w and a spacing of 2w. The effects of introducing a layer of passivation under the electrodes are presented later.

Before the simulation can start, the boundary conditions of the model must be fully defined. For this model, the boundary conditions are set up so that the outer boundary has zero charge $n \cdot D = 0$. The remaining boundaries are set to "continuity" in the form of $n \cdot (D_1 - D_2) = 0$. The model can now be solved and run without errors, establishing the electric field for all points of interest.

The first set of simulations examined the effect of polymer height on the sensor capacitance for a fixed electrode width of 10 um, which is shown in figure 8.8a. The second simulation

examined the impact of the pitch on the capacitance for a fixed 2 µm thickness of BCB. This is presented in figure 8.8b. The results of these simulations confirm that the model is working as intended; in figure 8.8a the capacitance of the IDT sensor increases with polymer thickness. At around 15 µm thickness, the increase in capacitance appears to be slowing to a settled value.

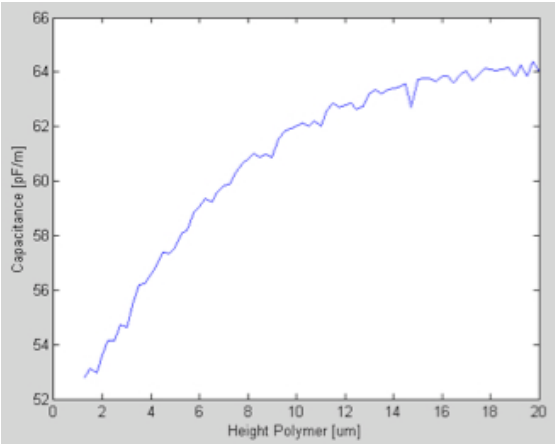

[a]: Capacitance per unit length of an IDT sensor with electrode width of 10 µm

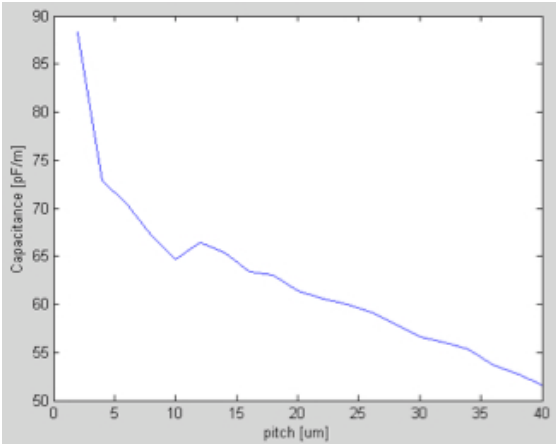

[b]: Capacitance per unit length of an IDT humidity sensor with 2 µm thick BCB layer

Figure 8.8 Effects of varying the pitch for constant material thickness

The electrode width is 10 µm and the spacing between electrodes is twice this figure (20 µm). The overall pitch is 30 µm, so the optimum thickness is half the pitch as this contains a high proportion of the electrostatic field lines that emanate from the electrode fingers into the polymer.

For the case of fig 8.8b, the capacitance starts to decrease as the pitch size increases. The standard model of a capacitor will show a decreasing capacitance as the gap between electrodes increases; since the pitch is getting bigger with electrode width remaining constant, the gap between the electrodes is getting larger. For the case of fig 8.9, the electrode width remains at 10 µm and the polymer thickness remains constant at 2µm. The pitch varies for a total sensing area of 3mm x 3mm. If the normal model of the parallel plate humidity sensor is used then the increase in the dielectric thickness would decrease the capacitance of the humidity sensor.

Table 8.2 Matrix showing sensor output capacitance at 0 and100 %RH for the BCB covered sensors.

The effect of the electrode thickness is evaluated from 1 - 10 um.

Sensor design	Q1 (pF)	Q2 (pF)	Q3 (pF)	Q4 (pF)	Q5 (pF)
T = 1 (0%RH)	15.6	19.5	11.7	3.1	5.9
T = 1 (100%RH)	20.4	25.4	15.3	4.1	7.6
T = 2 (0%RH)	31.2	39.1	23.4	6.2	11.7
T = 2(100%RH)	40.7	51	30.6	8.1	15.3
T = 3 (0%RH)	46.8	58.7	35.1	9.4	17.6
T = 3 (100%RH)	61.1	76.5	45.9	12.2	22.9
T = 4 (0%RH)	62.4	78.2	46.8	12.5	23.5
T = 4 (100%RH)	81.4	102	61.2	16.3	30.6
T = 5 (0%RH)	78	97.8	58.5	15.6	29.4
T = 5 (100%RH)	101.8	127.5	76.5	20.4	38.2
T = 6 (0%RH)	93.6	117.3	70.2	18.7	35.2
T = 6 (100%RH)	122	153	91.8	24.4	45.8
T = 7 (0%RH)	109.2	136.9	81.9	21.8	41.1
T = 7 (100%RH)	142.5	178.5	107.1	28.5	53.5
T = 8 (0%RH)	124.8	156.4	93.6	25	47
T = 8 (100%RH)	163	204	122.4	32.6	61.1
T = 9 (0%RH)	140.4	176	105.3	28.1	52.8
T = 9 (100%RH)	183.2	229.5	137.1	36.6	68.8
T = 10 (0%RH)	156	195.5	117	31.2	58.7
T = 10 (100%RH)	203.6	255	153	40.7	76.4

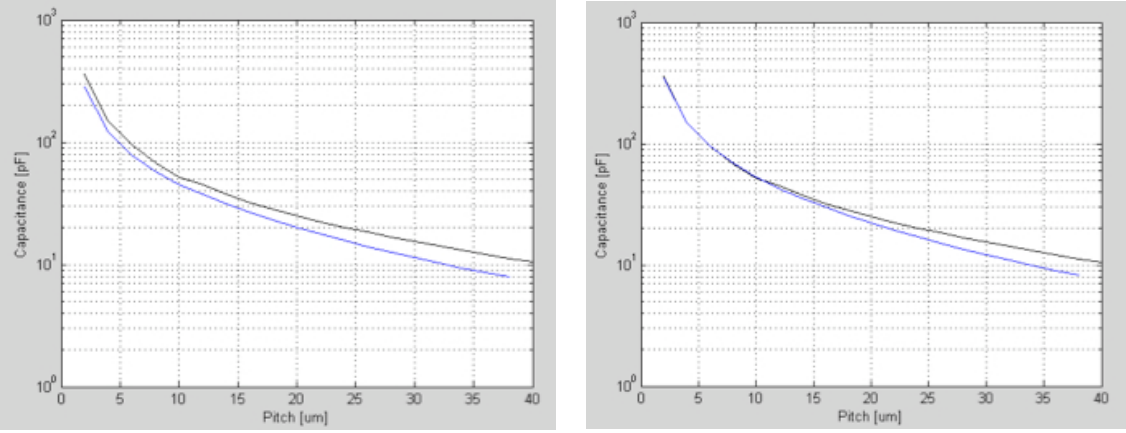

[a] *0.1 μm thick silicon oxide layer* [b] *0.4 μm thick silicon oxide layer*

Figure 8.9 Capacitance of an interdigital humidity sensor with a BCB layer

The graphs examine the responses when introducing different thicknesses of passivation. Sensor was 2 μm thick and had a total available sensing layer of 3mm x 3mm.

Since this sensor is based on IDT electrodes, the field lines from electrode to electrode bend into the moisture sensitive polymer. The depth that the field lines penetrate into the material depends on the width and spacing of the electrodes; typically the pitch between electrodes should be less than or equal to the sensing film thickness. If the film thickness is less than the pitch then a greater percentage of the field lines will emanate past the sensing material and into the surrounding air; this will decrease the maximum possible capacitance that can be attained. For the condition that the sensing material is thicker than the pitch of the electrodes, there will be an increase in the maximum attainable capacitance.

The impact of interdigital electrode thickness is analysed in Table 8.2. Its shows the variation in capacitive output for thicknesses ranging from 1 μm to 10 μm. As the thickness is increased, the capacitive output of the sensor designs increases. Figure 8.9 shows the change in capacitance of the sensor as an oxide insulator layer is introduced. Layer thicknesses of 0.1 and 0.4 μm were introduced to the model and showed little overall change in the capacitance of the sensor. This layer is often used to stop moisture from entering the silicon substrate when functioning as a humidity sensor.

The next step was to use equation 8.10 to examine the actual design parameters chosen for the manufactured humidity sensors, which is presented in table 8.1. The impact of the electrode thickness was evaluated on the range of capacitance change for each sensor design.

8.6 Manufacture of the humidity sensor

The manufacture of the humidity sensor was carried out by Qudos Technology ltd, located in Oxford, England. Figures 8.10 show the side profile and layout of the sensor. The sensors were manufactured on 4 inch <100> p-type silicon wafers with 1 µm pre-coated thermal oxide layer on top. The next step was the deposition of photoresist, lithography and the deposition of the metal 1 layer. This produces multiple electrodes that create the interdigital electrode fingers.

A passivation layer is then deposited, which is a 1 µm silicon dioxide layer deposited through PECVD. This layer is then etched to remove the passivation lying on top of the contact electrodes and the sensing electrodes.

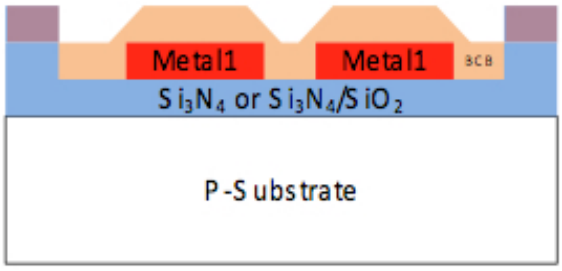

[a] Cross section of the IDT humidity sensor being manufactured

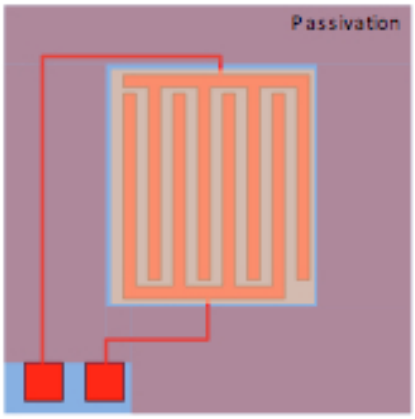

[b] Design and layout of the IDT humidity sensor

Figure 8.10 The design and layout of IDT sensors fabricated by Qudos technology Ltd.

The final steps involve the application of the humidity sensitive material over the electrodes; Benzocyclobutene (BCB) or Polyimide (PI) of thickness 2 µm was selected for this application. The curing process times used for changing the phase of the material to a solid were not given, nor is it known if the materials were pre-imidised prior to the curing stage. If the material is not pre-imidised then the curing profile used will have an effect on the sensitivity and hysteresis performance of the sensors. After the spin coating and curing stages have been carried out, the wafer is then diced into 5 mm^2 chips; they are then inspected and sent on to Heriot-Watt University for packaging and testing.

8.6.1 Packaging of the humidity sensor

To facilitate the testing and characterisation of the humidity sensor, the sensor die shown in figure 8.11 first needs to be packaged so that it can be interfaced with measurement equipment. The packaging of the sensor is achieved through the procurement of custom-manufactured 28 pin DIL packages from a company called IC Proto. The chip support paddle area is 5mm^2, which provides enough area to glue the sensor die. High temperature resistant glue is used to enable adhesion to the package during the higher temperature thermosonic bonding stage. During bonding, the glue is first deposited on the paddle area and then gently dabbed with some tissue to enable no glue moves around the sides of the die and on top of the gold contacts of the package. The die is placed in this space using tweezers, and gently pressed on the corners of the die to enable a strong enough bond to be created.

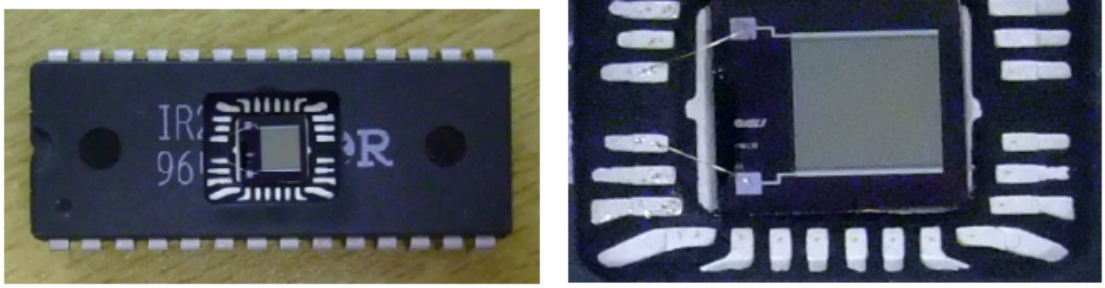

[a] *Humidity sensor wire bonded in 28-pin DIL package.*

[b] *Close up view of wire bonded humidity sensor die to the DIL package.*

Figure 8.11 Packaged humidity sensor

The sensor die was wire bonded to pins 1 and 28 of the DIL package, and this was followed for all other sensor die that were packaged. To enable the testing of the sensors in an environmental chamber without having to open the chamber again and reconnect the next sensor, a PCB board was created that had DIL connection points in the board. This meant that the PCB board could be connected to cabling that would run out of the environmental chamber to the test equipment.

8.7 Test methodology of humidity sensor

The test setup of the humidity sensors is shown in figure 8.12. The original idea for characterisation of the humidity sensors was to measure the device characteristics at a number of humidity set-points so as to gather information on the offset (capacitance at 0% RH), sensitivity (pF/%RH) and hysteresis of the humidity sensors. This information is important in later development work aimed at integrating the humidity sensors into a multi sensor unit. Interfacing of the capacitive humidity sensor to electronics will require the conversion of the capacitive output sensor reading to a digital format alongside other types of sensor.

Manufacturers of humidity sensors will specify the performance of their sensors over a specified temperature and relative humidity operating range. This is typically achieved by recording the sensor performance across increasing and decreasing values of relative humidity for certain temperatures; alongside such measurements will be an industry standard humidity and temperature probe that has been calibrated to national and/or international standards.

Table 8.3 Relative humidity above saturated salt solutions at various temperatures.

Salt/Temperature (˚C)	5	10	15	20	25
Lithium chloride	11.3	11.3	11.3	11.3	11.3
Magnesium chloride	33.6	33.5	33.3	33.1	32.8
Potassium carbonate	43.1	43.1	43.1	43.2	43.2
Sodium bromide	63.5	62.2	60.7	59.1	57.6
Sodium chloride	75.7	75.7	75.6	75.7	75.3
Potassium chloride	87.7	86.8	85.9	85.1	84.3
Potassium sulphate	98.5	98.2	97.9	97.6	97.3

The primary standard for humidity measurements is the chilled mirror hygrometer, therefore this was identified and used for the measurements. The model used was a Michelle instruments Optidew Precision with Pt100 Platinum resistance temperature sensors. Due to the time needed to carry out such measurements, a single temperature was chosen to simulate the different humidity conditions. A temperature close to room temperature such as 25°C was chosen, after which rising and falling humidity set-points would be selected. Various publications have characterised humidity sensor performance using a humidity generator or salt bath solutions [8.24-8.26]; the former would use 0% RH to 90% RH in 10% RH increments for the rising set-points followed by 10% RH decrements starting from 90% RH down to 0% RH for the falling set-points. The typical set points that could be used for different temperatures and the salt solutions are presented in table 8.3.The profile for testing the sensors in this work was 0% RH to 90% RH, followed by 90% RH down to 0% RH with 10% RH increments/decrements. The equipment used for this characterisation is outlined in figures 8.12 and 8.13. The testing was carried out at the environmental test facilities at Ultra Electronics in Cheltenham, UK. An environmental test chamber by Unitemp (based in High Wycombe, Buckinghamshire) was provided for this testing.

There was no automated data logging equipment provided for interfacing with the humidity sensors via the access point to the side of the chamber. Such equipment would have enabled the benefit of regular automated acquisition of each sensors output capacitance over specified time intervals and humidity set points. These readings could also be collected in tandem with information of the chamber real time performance, resulting in further information about the accuracy and precision of the chamber in relation to the sensor performance. The other challenge faced with using this equipment was that the chamber itself could not be automated to run the characterisation profile, which meant that an operator had to be available to change the chamber settings, record the sensor data, record the chamber performance and also record the humidity and temperature information from the higher accuracy humidity and temperature transmitter. Other drawbacks included being unable to program the chamber to run characterisation profiles over extended time durations, which would have been beneficial for characterising the long-term stability. This is an important measure of both capacitive and resistive humidity sensors that use polymer films which are known to suffer from long-term drift [8.27-8.29].

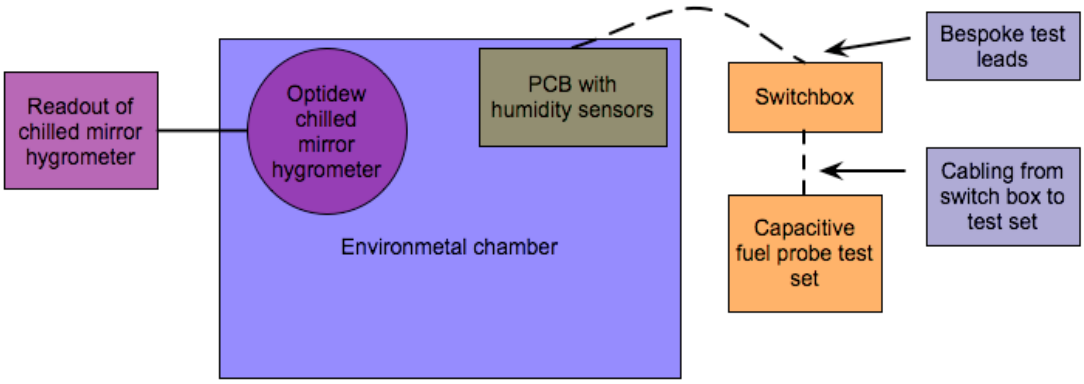

Figure 8.12 Characterisation setup of the humidity sensor.

[A]: Capacitive fuel probe test set *[B]: Switch box used with the capacitive test set*

Figure 8.13 Capacitive fuel probe test equipment used in characterisation of humidity sensors

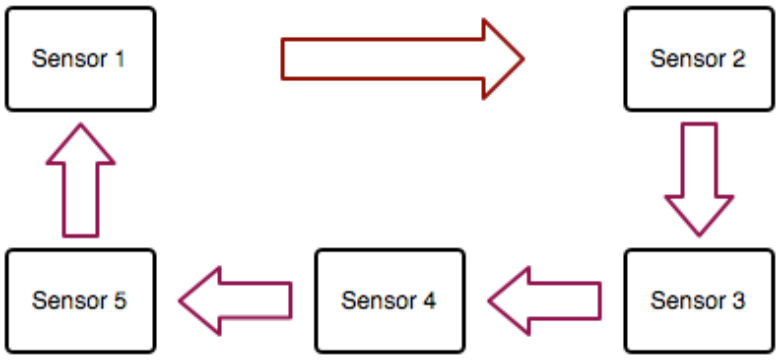

Figure 8.14 Order for sampling the humidity sensors.

The initial challenge was to locate a suitable instrument for measuring the capacitive output of the different humidity sensors. Measurement of capacitance down at the pico-farad range normally requires equipment such as an LCR meter, which would have been fine for a single sensor measurement but time intensive for multiple measurements in the time available. These measurements require open and short measurements to be carried out so that the parasitic impedances introduced by the fixture can be removed from the sensor data.

Since the sensors had been packaged in open topped packages, the best route to testing the sensor would be to design a PCB that would connect the output pins of the packaged sensor to the output measurement device. Since Ultra Electronics has access to capacitance fuel probe measurement technology, modifications to the test equipment were performed to read the capacitance of each humidity sensor on the PCB by manual selection of each sensor using the switchbox belonging to the test equipment. The capacitance fuel probe and switch box is shown in figures 8.13a and 8.13b. Under normal operating conditions, the test equipment can measure down to 1 pF with a resolution of 0.01 pF. Custom test leads were manufactured in-house to connect the output socket of the PCB board to the switch-box; after this point the switch box would be connected to the capacitance test measurement device. However the same challenge of compensating the additional capacitance introduced by the sensor packaging, cabling and test fixtures needed to be resolved.

The test equipment includes functionality aimed at removing the additional capacitance of the wiring and interconnect using in-built software features that nullify the effects of the test fixture. For further improvements in measurement accuracy, this process could have been repeated at all humidity set-points used in the characterisation. The process used for the test is to start the chamber of at 0% RH and increase the relative humidity in 10% RH steps up to 90% RH, after which the relative humidity content is decreased in decrements of 10% RH. At each relative humidity set-point, the switch box position would be set to interrogate the capacitive output of the sensors followed by recording the relative humidity and temperature readings of the chamber and probe. The time duration for each set point was 30 minutes so that the chamber and sensors could settle before measurements commenced. The order of recording the sensors values is shown in figure 8.14; measurements are taken from sensors 1-5 for the BCB covered sensors followed by sensors 1-5 for the PI covered versions.

8.8 Discussion of results

The results for the performance of both humidity sensors is presented in figures 8.15 and 8.16, which show the capacitive output of the sensors at various relative humidity set points for the BCB covered sensors followed by the polyimide covered sensors. The shape of the sensors output is first captured via boxplots to illustrate the spread in measurements and the level of variance for each sensor. The shape of the output for sensors 1 and 5 is similar to that reported in [8.30,8.31] which also uses an interdigitated humidity sensor with either low k dielectrics or BCB as the humidity sensitive polymer. The response of the BCB covered sensors is shown in figure 8.15, which show some of the sensors decreasing in capacitance and others increasing in capacitance as the relative humidity increases inside the chamber. Examples of sensors showing increased capacitance with increasing relative humidity are sensors 1 and 5; sensor 1 shows increases in capacitance until 80% RH then does not increase beyond this.

Sensor 5 shows increases in capacitance as the relative humidity increases until 80% RH where there is a larger change in capacitive output from 80% RH to 90% RH. Literature and patents such as [8.30, 8.31] tend to show that this capacitance increase occurs at a medium level of relative humidity such as 60% RH, then there is a sharp increase in capacitance change all the way up till 90% RH. This effect is more pronounced when the surface of the polymer has been subjected to an oxygen plasma treatment, resulting in a rough surface finish that increases the surface area of the sensing film. Polymers such as BCB possess a lower uptake of water at low relative humidity set points, as a result of moisture entering the polymer by diffusion and there being a smaller free volume within the material. At higher relative humidity set points, moisture will start condensing inside the porous structure of the polymer film and be driven further inside the material. A majority of the water uptake will be due to water entering and remaining in the film in bulk form; the rest of the water will exist by different types of chemical bonding between the polarised side chains of the polymer. Although sensor 1 shows increases to the capacitive output as the relative humidity increases, there is no further increase at 90%RH. The explanation for this is that not enough time has been allowed for the chamber to reach the 25 °C operating temperature and the 90% RH set point.

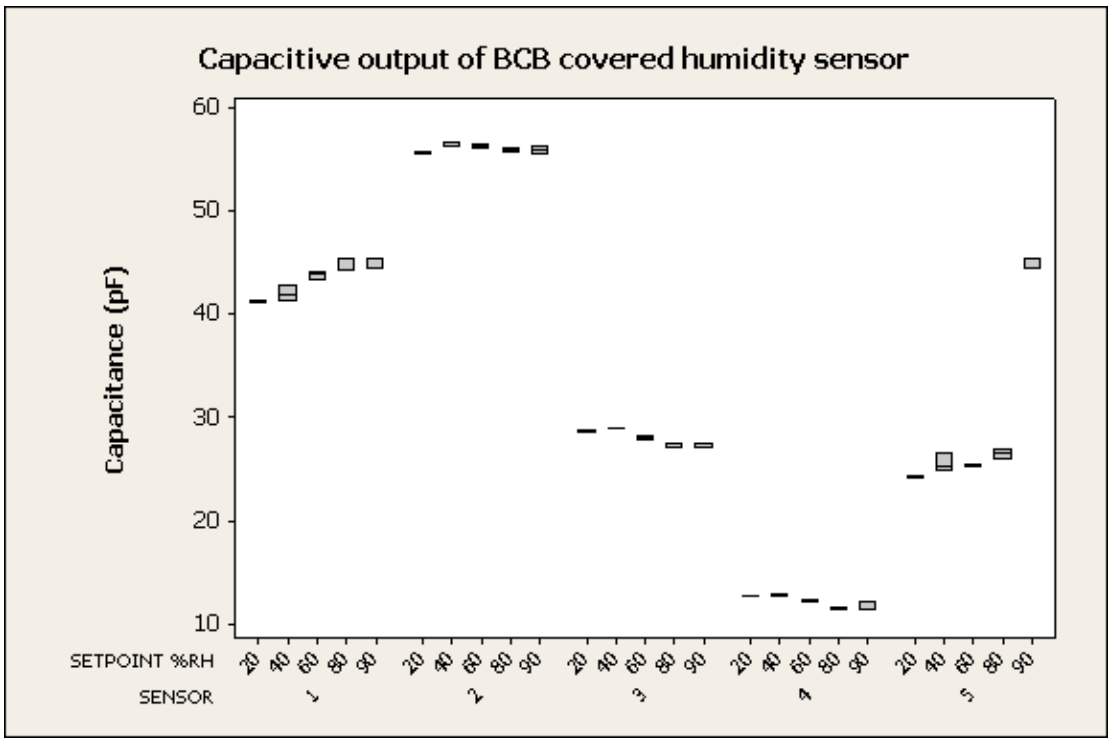

Figure 8.15 Boxplot of capacitance vs. humidity for BCB covered humidity sensors.

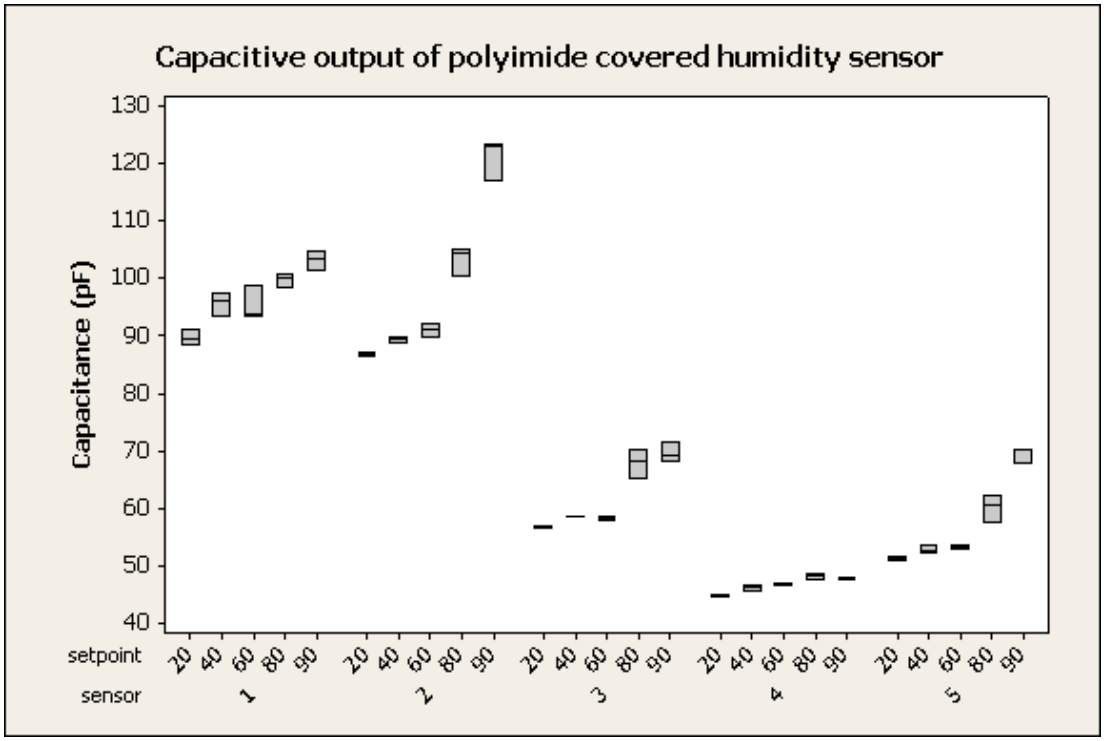

Figure 8.16 Boxplot of capacitance vs. humidity for polyimide covered humidity sensors.

Another explanation is that the capacitance of the PCB test board has not been fully compensated, resulting in capacitance fluctuations being introduced into the measurement.

Closer inspection of the chilled mirror data (temperature and humidity) obtained during the BCB measurements is shown in figures 8.17 and 8.19. They show on figure 8.17 that the 80% RH set point that the temperature is closer to the 25°C than when the chamber is set at 90% RH. These measurements had temperatures that ranged from 24.7-24.8 °C, whereas at 90% RH the temperatures ranged from 24.4 and 24.6 °C. When the chamber is at a lower temperature (such as 24.4 °C) and showing 90% RH, the air can hold less water vapour in fully saturated (100% RH) state than at 24.8 °C and fully saturated. This means the sensor is holding less water vapour at 90% RH than at 80% RH; consequently, the capacitance output of the sensor should be less. If the chamber had been allowed more time to stabilise at a higher temperature such as 24.8 °C then the capacitance would most likely have been higher; the graph would then show an increase in capacitance at every relative humidity set point.

For insight into the behavior of the PI covered sensors, figures 8.18 and 8.20 show the differences in temperature and relative humidity of the chamber and the chilled mirror hygrometer for each relative humidity set point.

At the 20% set point that was programmed into the chamber, there is an error between the chamber and CMR ranging from 0.9–2.9°C across the chamber readings. The error starts of largest at the beginning of the measurements and trends downwards to a lower value of error. At 40% RH the error trends between 0.6–1.6°C; it does not appear to be settling down to a steady state value. The next set point (60% RH) looks like it is settling to a steady state value, with errors ranging from -0.3 to 0.7°C. The 80% RH set point ranges from 0.6 to -0.1°C and the 90% RH set point ranges from 0.8 to 0°C.

In addition to the chamber failing to reach the desired temperature, the program of relative humidity set points which comprise of 20% RH, 40% RH, 60% RH, 80% RH and 90% RH were not reached and failed to settle at a steady state value. In figure 8.21, the plot examines the relative humidity error between the chamber and the chilled mirror hygrometer (CMR). At the 20% RH set point, the error between the chamber and CMR ranges from 28% RH to 7% RH.

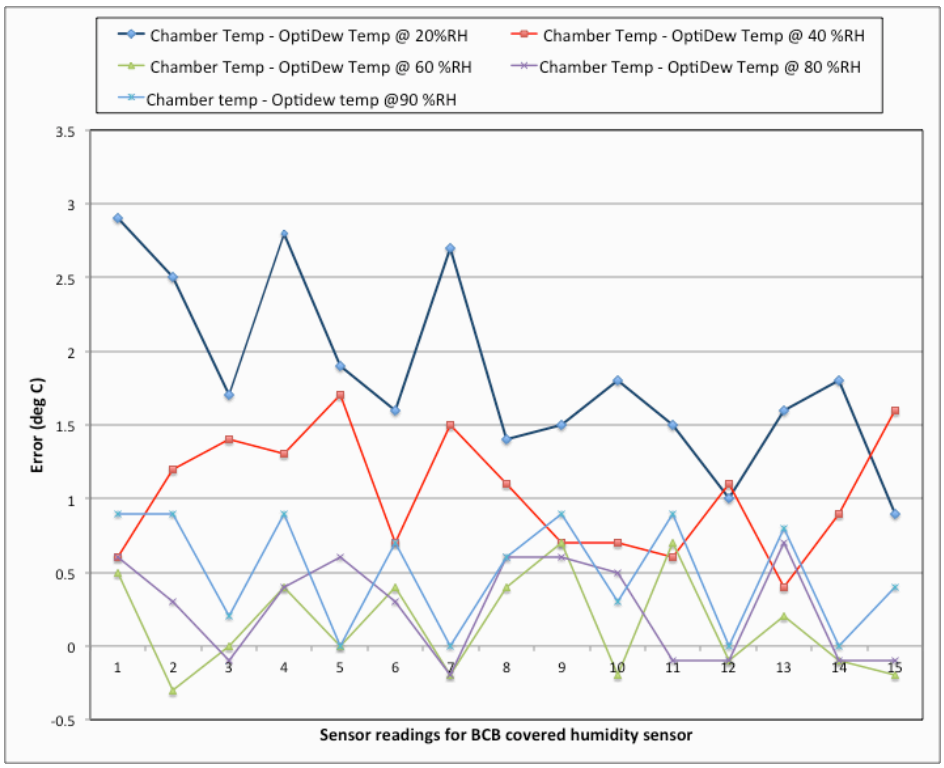

Figure 8.17 Errors in the chamber temperature when compared to the chilled mirror hygrometer for four %RH setpoints. Samples used were the BCB sensors.

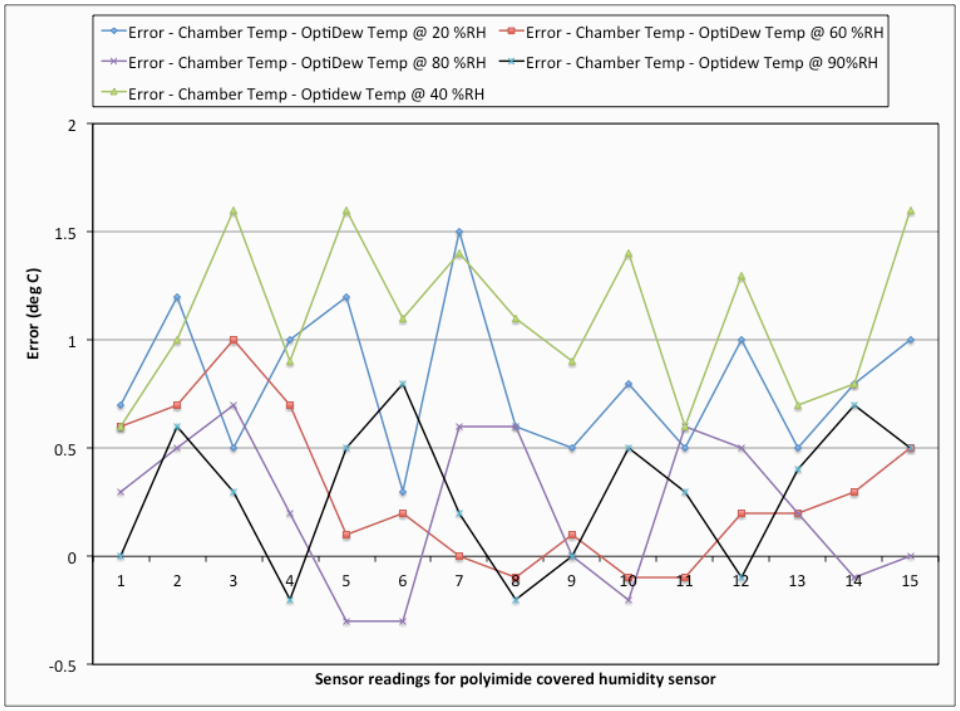

Figure 8.18 Errors in the chamber when compared to the chilled mirror hygrometer for four %RH setpoints. Samples used were the PI humidity sensors.

At 40% RH, the error has decreased slightly to between 4.5–14% RH. Both results suggest that the chamber is having difficulty reaching such low levels of humidity in the time available.

It is likely that an in-built humidity sensor such as a wet bulb hygrometer is used in a part of a feedback loop to control the humidity being generated and circulated within the chamber. This type of hygrometer is known to suffer from larger measurement error due to the wet sock element becoming contaminated. This contamination was not verified at the time due to not being aware of the issue; it is identified visually by examining the color or the wet sock. In a perfect state, it is a brilliant white colour; when the sock begins to degrade due to contamination it turns a greyish white colour. The wet bulb hygrometer uses two thermometers to make a relative humidity measurement. One bulb is covered with a moist wick (which is where the term wet sock or wet bulb comes from) and the other bulb is left bare (called the dry bulb). Airflow of a specified velocity is focused on the wet bulb, which results in evaporation of water vapour from the wick. The evaporation causes a reduction in the temperature reading. The readings of both bulbs along with a pressure reading provide the data needed to calculate the relative humidity.

Additionally, due to the chamber size being larger than modern systems such as a Thunder Scientific environmental chamber, a larger period of time is required for the volume within the chamber to stabilise thermally and for the relative humidity to circulate properly so that constant relative humidity is achieved within this volume. All systems are known to suffer from an issue known as dead volume, which is where there is temperature and relative humidity gradients within the chamber.
This phenomenon occurs at the corners of the chamber due to the air not properly circulating at these points and also because air is a poor thermal conductor. Allowing longer periods of time for the chamber to settle at a particular temperature and relative humidity should improve the issue, however in a commercial environment this introduces additional costs for calibrating the device. Introducing an air circulator into the chamber can improve this, though there should be an awareness of the localised heat being generated by the device in terms of the overall measurement uncertainty. In an ideal case, a time period of 3 hours should be provided at each relative humidity setpoint before acquiring measurements from the sensors.

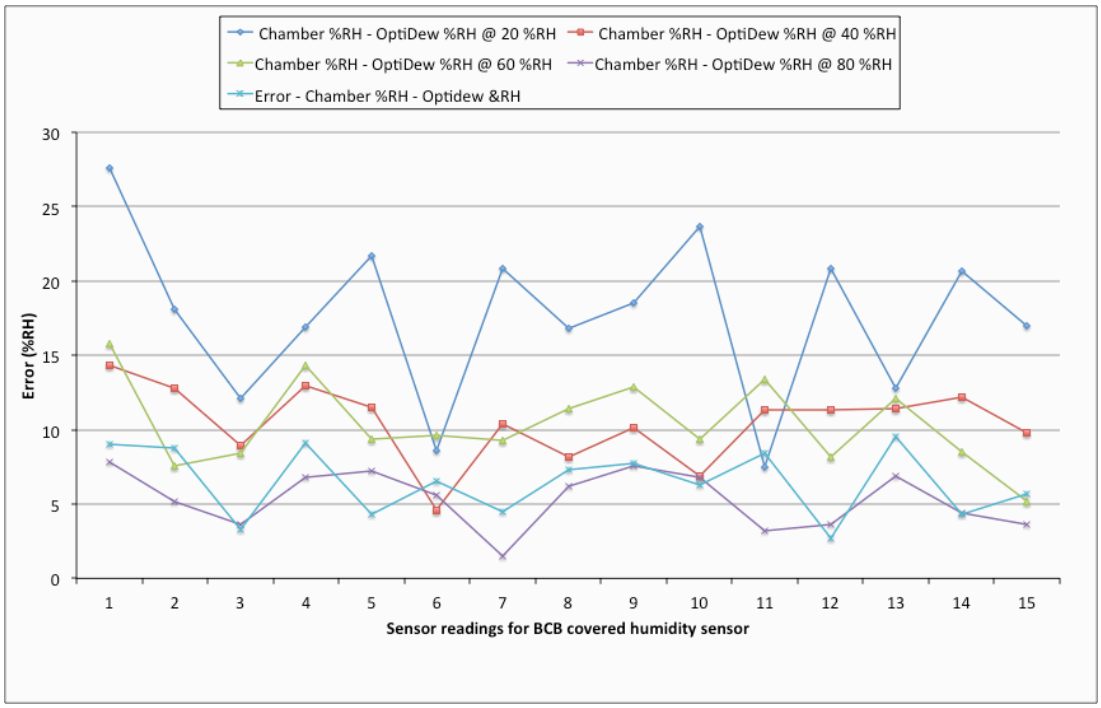

Figure 8.19 Error in the chamber %RH measurement when compared to a chilled mirror hygrometer (Optidew). Samples were the BCB humidity sensors.

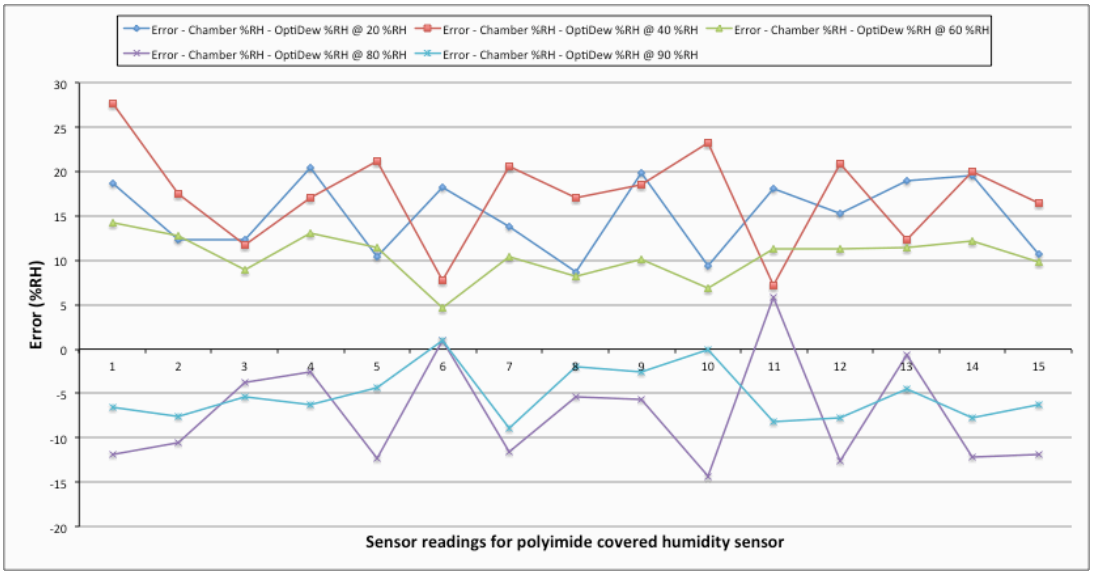

Figure 8.20 Error in the chamber %RH measurement when compared to a chilled mirror hygrometer (Optidew).

The performance for the polyimide covered humidity sensors are presented in a boxplot in figure 8.16, and the temperature and humidity errors are presented in 8.18 and 8.20. Overall, these sensors show a better performance than the BCB covered sensors due to the sensors showing an increase in capacitance as the relative humidity increases from the 20% RH set point up to 90% RH. Sensor 1 displays this behavior in terms of overall trend, though on closer inspection reveals that the boxplots for each set point has quite a large variance when compared to the boxplots of the other sensors, such as sensor 4. The 60% RH set point for sensor 1 shows that the median of the 3 sensor measurements is located around 92 pF; instead, the median should be located closer to the midpoint of the boxplot, which is around 95 pF. The capacitance of sensor 1 is also higher than expected, which can be explained more clearly if figure 8.18 is consulted. This figure examines the temperature errors for all the set points that were programmed into the chamber. It shows for the 40% RH set point that the temperature error ranges from 0.6 to 1.6°C. The 60% RH set point shows errors ranging from 1°C to -0.15°C, whereas at 80% RH the error is from 0.7°C to -0.3°C. For 80% RH, the temperature error appears to be decreasing overall and converging to a steady state value, yet the 90% RH set point ranges from 0.75°C to -0.2°C but does not appear to be settling to a steady state. This behavior requires further analysis that could be gathered through acquiring information about the temperature error from low to high relative humidity, followed by high to low relative humidity. This has a significant impact on when the sensors should be sampled in the future for their capacitance; the dew point hygrometer should be used as the indicator that the environment has reached 25 °C temperature and either 80% RH or 90% RH set points. When the chamber is programmed at the desired set points of 25 °C temperature and relative humidity of 80% RH and 90% RH, the humidity levels are achieved by holding a certain amount of water vapour relative to the maximum amount that can be held at 25 °C. The relative humidity is calculated by the ratio of the observed vapour pressure to the maximum vapour pressure at this temperature. If the relative humidity of the chamber was to be recalculated for the sensor measurements with the condition that a similar water vapour content remained at the time of sensor measurement and the temperature either increased/decreased to 25°C, there would be a reduction/increase of the relative humidity measured in the chamber. At temperatures higher than 25°C, there would be a greater amount of water vapour required to reach the 80% RH/90% RH set points as opposed to the water vapour required at temperatures below 25°C.

Table 8.4 Response of the humidity sensors covered with BCB dielectric.

Sensor	Equation	Offset (pF)	Sensitivity (pF/%RH)
1	0.0764 *% RH + 39.2	39.2	0.0764
1	0.0559 *% RH + 40	40	0.0559
1	0.0459 *% RH + 40.6	40.6	0.0459
2	0.0091 *% RH + 55.6	55.6	0.0091
2	0.0036 *% RH + 55.9	55.9	0.0036
2	0.0003 *% RH + 56	56	0.0003
3	29.6 – 0.0290 *%RH	29.6	– 0.0290
3	29.5 – 0.0241*% RH	29.5	– 0.0241
	29.5 - 0.0240 *% RH	29.5	- 0.0240
4	13.4 – 0.0224 *% RH	13.4	– 0.0224
4	13.5 – 0.0229 *% RH	13.5	– 0.0229
4	13.4 – 0.0208 *% RH	13.4	– 0.0208
5	23.2 + 0.0424 *% RH	23.2	0.0424
5	21.6 + 0.0654 *% RH	21.6	0.0654
5	24.6 + 0.0199 *% RH	24.6	0.0199

As the temperature is reduced towards 25°C with the same vapour content, the relative humidity content is recalculated to show a much higher value. Conversely, at lower temperatures, a lesser amount of water vapour is needed to reach the desired humidity set point. As the water vapour content is held constant and the chamber temperature increased up to 25°C, the actual recalculated relative humidity value is lowered. This means that the capacitance readings of the sensors when the chamber was set to 90% RH are much lower than expected. Even though the chilled mirror hygrometer shows slightly higher relative humidity values in the chamber, the temperature is lower than for the 80% RH case. It is likely then that the actual vapour content in the chamber is at similar levels. If the chamber was allowed longer than 30 minutes, then what should occur is that the temperature should reach 25°C and the vapour content should increase so that a true 90% RH measurement is achieved with the sensors. Once the analysis of chamber performance is applied to the measurements for sensors 2-4 an understanding as to why the sensors display decreasing capacitance as the relative humidity is increased.

Table 8.5 Response of the humidity sensors covered with polyimide dielectric.

SENSOR	EQUATION	OFFSET (pF)	SENSITIVITY (pF/%RH)
1	0.135 *%RH + 87.8	87.8	0.135
1	0.571 *% RH + 58.5	58.5	0.571
1	0.166 *% RH + 86.7	86.7	0.166
2	0.293 *% RH + 78.6	78.6	0.293
2	0.206 *% RH + 81.9	81.9	0.206
2	0.267 *% RH + 79.3	79.3	0.267
3	0.202 *% RH + 51	51	0.202
3	0.170 *% RH + 52	52	0.170
3	0.125 *% RH + 53.5	53.5	0.125
4	0.0497 *% RH + 44	44	0.0497
4	0.0607 *% RH + 43.3	43.3	0.0607
4	0.0525 *% RH + 44.2	44.2	0.0525
5	0.1494 *% RH + 46.95	46.95	0.1494
5	0.1423 *% RH + 47.26	47.26	0.1423
5	0.1624 *% RH + 46.95	46.95	0.1624

At the 20% RH set point, temperature has not reached the 25°C value. Instead, it ranges from 22.1 to 23.6°C meaning that there is a 3 to 5.5% RH measurement error. Furthermore the chamber fails to settle on the 20% RH set point, instead varying from 23.4 to 40% RH. This will impact the sensors 3 and 4 the greatest because the base capacitance for these sensors is the smallest, plus there is a smaller change in capacitive output as the relative humidity changes.

The stability of the chamber has the greatest impact on the measurements of the BCB covered sensors compared to the polyimide covered sensors due the lower dielectric constant of the BCB and the smaller amount of water that is absorbed by the material as the relative humidity is increased. The data obtained for the sensors show that the relative humidity in the chamber was creeping upwards, thereby corrupting the measurement for this set point. The measurements were attempted a number of times but no improvement in chamber performance could be achieved in the time frame available. This stopped measurements being carried out for decreasing humidity set points. Calculations of hysteresis for the BCB and polyimide covered sensors could not therefore be achieved.

The capacitive output across the sensors as the relative humidity set-points change is very small, changing from tenths to hundredths of a pico-Farad. The resolution/discrimination of the measuring equipment is very important, which is usually why measurement systems analysis should be performed to see if the instrument is suitable for the intended measurements. Although the instrument can accurately measure down to 1 pF, there is no knowledge of the repeatability of the instrument, meaning there could be a large variation in the measurements that affect the overall accuracy. Sensors 2, 3 and 4 show different profiles compared to sensors 1 and 5; as the set points increase for these sensors there is some change in capacitance upwards. In other occasions the capacitance change stays constant or even decreases which indicates an issue with the measuring equipment. Linear regression analysis was performed on the sensor data to provide information on the sensitivity of the sensors and the offset (capacitance at 0% RH). This is summarised and presented in tables 8.4 and 8.5. The summary for the BCB sensors is shown in table 8.4, which show that sensitivities of 0.076 pF/%RH was the highest sensitivity for sensor 1 and 0.065pF/%RH for sensor 5. The sensitivity for sensors 2, 3 and 4 show negative values because the capacitance output of the sensors decreases as the relative humidity increases. Although the data for the both sensors is likely to be corrupted by fluctuations in the chamber temperature and relative humidity, the BCB design's offset capacitance trended from high to low in the order H2, H1, H3, H5 and H4. This was similar to the order presented in table 8.2 earlier in this chapter. The sensitivity of the BCB sensors that displayed a positive trending best-fit line ranged from 0.004 pF per % RH to 0.07 pF per % RH. Design H2 had the largest variation between the three readings for this design. For the polyimide covered humidity sensors, offset capacitance followed a similar trend to the BCB sensors. The designs H2 and H1 had offsets that were closer than expected, with design H2 having a larger variance between readings than H2. The sensitivity of the polyimide sensors ranged from 0.05 pF per % RH to 0.571 pF per % RH, which was greater than the BCB designs. The order of sensitivity was H2, H3, H5 and H4.

The sensor structures were evaluated to see if there was justification for lower capacitance readings than expected. The close up images taken from the microscope in Figure 8.21 reveal that a number of the conductive tracks that form the interdigitated electrodes have breaks in them at a number of points. This results in decreasing the capacitance between the finger electrodes, depending on where along the length of the electrode the breakage has occurred. If the breakage has occurred along the end of the

finger then there is smaller reductions to the capacitance; if the breakage has occurred closer to the start of the finger electrodes then there will be a larger decrease in the capacitance. The number of breakages in the electrode fingers appeared across all designs, suggesting that there was an issue with the reproduction of the electrode pattern in the photoresist. This may also be a contributory effect as to why there was a noted variance in the offset of the sensors and why there was a variation in the readings.

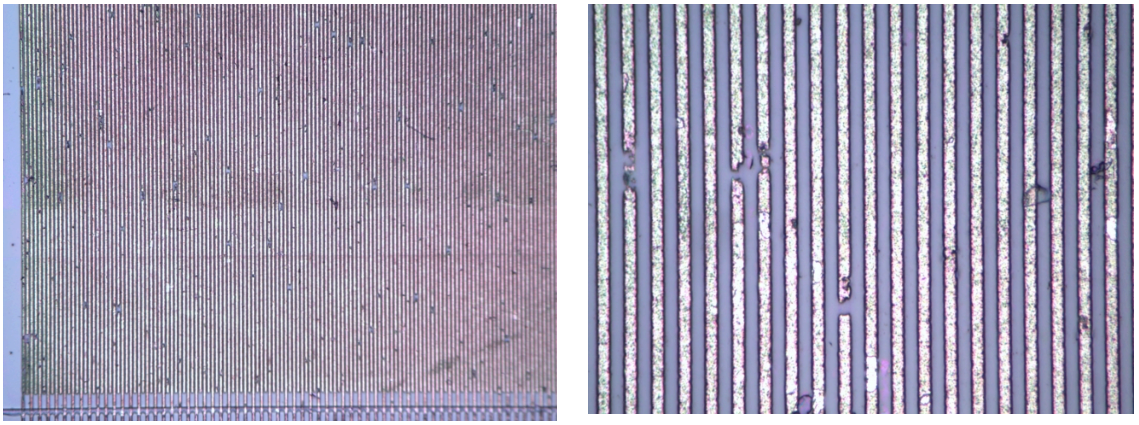

[a] *Humidity sensor H1* [b] *Humidity sensor H5*

Figure 8.21 Defects in the interdigitated electrodes.

A number of conductive tracks have breaks in them that will decrease the sensitivity of the measurement.

8.9 Summary

This chapter has introduced a background in humidity sensing and a selection of the methods to detect humidity. The design selected for manufacture and future integration into a multi-sensor application was the interdigitated electrode polymer capacitive humidity sensor. This was preferred over the parallel plate version, as despite possessing a higher capacitance per unit area, the sensor does not recover well from exposure to chemical contaminants. Sensor designs that leave the polymer fully open to react with the environment tend to recover when rinsed in deionised water. Aircraft wiring bundles are likely to suffer spillages from a range of aircraft fluids that could affect the long term performance of a humidity sensor, so the IDT design is particularly well suited on this occasion.

A range of humidity sensor designs were presented that examined the trade off between the design parameters and the capacitance measured across the whole relative humidity

range. The electrode finger width was a factor that was kept constant at 6 μm, which was due to the difficulties with reproducing the electrode pattern successfully in the photoresist. Other parameters such as the spacing between the finger electrodes, pitch and area were varied.

The designs that used polyimide as the moisture sensitive layer and the plasma treatment exhibited a response that is typical of this type of design such as a greater sensitivity at high relative humidity and low sensitivity at low relative humidity. The oxygen plasma treatment appeared to enhance this effect. The design that provided the highest base capacitance (offset) was design H2. This also had a smaller variation between offset and sensitivity. The next steps would be to resolve the lithography problems that contribute to the broken electrodes and establish if another process was available to make the electrode width and pitch smaller. This would allow a smaller sensor footprint and decrease the cost per die.

The chamber was unable to stabilise at lower relative humidity settings such as 0% RH, 10% RH, 20% RH, 30% RH and 40% RH in the 30 minute settling time that was allocated for each set-point. At these set points, the humidity readings from the chamber controller showed that the relative humidity was continuing to climb past the set point programmed into the controller. The chamber could maintain a constant humidity until further up the relative humidity range such as 50% RH. Additionally, there were differences in the temperature and humidity measured by the sensors belonging to the chamber control unit and the measurements of the chilled mirror hygrometer.

To carry out better characterisation of the humidity sensors, the chamber must be evaluated to see if it can stabilise at lower humidity values if longer time duration is provided. This will involve evaluating the temperature and humidity throughout the chamber at different locations, preferably with a number of temperature probes positioned across the chamber. Although the water vapor content of air is assumed uniform throughout the chamber, this does not necessary mean that relative humidity is also uniform. For the most reliable measurement, dew point measurements are the best because they are directly related to vapor pressure and are not affected by the temperature like relative humidity sensors/probes. Measuring the temperature at different position would therefore allow calculation of the shift in relative humidity across the chamber as a result of different temperatures present.

Future work would look at testing the capability of the fuel probe test system against reference capacitors to see how capable the system is in repeatability and reproducibility of measurements. Other test methods such as using an LCR meter may be a more suitable option. Due to the difficulties with measuring such small capacitances, another option would be to integrate the humidity sensor with a capacitance to voltage ASIC as this would allow the sensor voltage to be read out more accurately and without the challenge of minimizing the introduction of additional capacitance to the measurement.

References

[8.1] L. Cadenhead J. Skardon and E. Zdankiewicz, "Trace moisture leak detection using MEMS sensor", *5th International Symposium on Humidity and Moisture*, May 2006.

[8.2] Ian R. Sinclair, Editor. "Sensors and Transducers", *Newes*, 3rd Ed., chapt. 7, pp. 172 – 176, 2001.

[8.3] J. Fraden, "Handbook of Modern Sensors, Physics, Designs and Applications", *Springer*, 3rd Ed., pp. 393 – 404.

[8.4] H. Johari. "Development of MEMS Sensors for Measurements of Pressure, Relative Humidity and Temperature", *PhD thesis*, Worcester Polytechnic Institute, April 2003.

[8.5] Sensirion application note: Dew Point Calculation "A Guide to the measurement if humidity".

[8.6] B. Okcan. "Humidity sensors using MEMS and standard CMOS technologies". *Master's thesis*, Graduate School of Natural and Applied Sciences of Middle East Technical University, 2003.

[8.7] D.K. Roveti, " Choosing a humidity sensor: A review of three sensing technologies" *Sensors Magazine*, vol. 18, no. 7, July 2001.

[8.8] Honeywell Manual of Automatic Control, Honeywell Building Solutions. http://www.buildingcontrolworkbench.com/

[8.9] H. Wohltjen. "Mechanism of operation and design considerations for acoustic wave device vapor sensors". *Sensors and Actuators*, vol. 5, no. 4, pp. 307-325, July 1984.

[8.10] P.Veradi V.I. Anisimkin, S.A. Maximov and E. Verona. "Effect of humidity on SAW devices", *IEEE Proceedings of Ultrasonics Symposium,* vol.1, pp. 409 - 413, 5 - 8 Oct 1997.

[8.11] V.K. Varadan, V.V. Varadan and X.-Q. Bao, "Integration of interdigital transducers, MEMS, and antennas for smart structures", *Proceedings of The International Society for Optical Engineering*, pp. 95 – 106, 1996.

[8.12] E. Verona C. Caliendo and V.I. Anisimkin. "Surface acoustic wave humidity sensors: A comparison between different types of sensitive membrane", *IOP Smart Materials and Structures*, vol. 6, no. 6, pp. 707 - 712, 1997.

[8.13] K.A. Vetelino D.W. Galipeau, P.R. Story and R.D. Mileham. "Surface acoustic wave microsensors and applications", *IOP Smart Materials and Structures*, vol. 6, no. 6, pp. 658 - 662, 1997.

[8.14] R. Fenner and E. Zdankiewicz. "Micromachined water vapor sensors: A review of sensing technologies", *IEEE Sensors Journal,* vol.1, no. 4, pp. 309 -317, Dec 2001.

[8.15] Hygrometrix Inc., “A comparison of humidity sensing technologies”. *Application Note 2004-2*.

[8.16] R. Buchhold A. Nakladal and G. Gerlach *et al.*, “Mechanical stress in micromachined components caused by humidity-induced in-plane expansion of thin polymer films,” *Thin Solid Films*, vol. 312, pp. 232 – 239, 14 Jan. 1998.

[8.17] G. Gerlach and K. Sager, “A piezoresistive humidity sensor,” *Sensors and Actuators A: Physical*, vol. 43, Issues 1–3, pp. 181-184, May 1994.

[8.18] N. Yamazoe and Y. Shimizu, “Humidity sensors: Principles and Applications”, *Sensors and Actuators*, vol. 10, pp. 379 – 398, 1986.

[8.19] Q.A. Shams, C.G. Burkett and T.S. Daniels et al, “Characterization of Polymer-Coated MEMS Humidity Sensors for Flight Applications”, NASA/TP-2005-213770.

[8.20] J. Fraden, “Handbook of Modern Sensors: Physics, Designs and Applications”, *Springer Pubishing*, 3rd Ed., 1993.

[8.21] C.-Y. Lee, A. Su and Y.-C. Liu et al, “Sensor Fabrication Method for *in Situ* Temperature and Humidity Monitoring of Light Emitting Diodes”, *MDI Sensors Journal*, 7th April 2010.

[8.22] S. Lee C. Lee and G. Wu. “In situ measuring of temperature and humidity within the membrane electrode assembly by micro-sensors”, *Proceedings of the 35th International MATADOR Conference,* pp. 377–380, June 2007.

[8.23] S. Lee C. Lee and G. Wu. et al, “in situ measuring of temperature and humidity within the membrane electrode assembly by micro-sensors”. In Proceedings of the 35th International MATADOR Conference, pp. 377–380. June 2007.

[8.24] Institute of Measurement and Control, “A Guide to the Measurement of Humidity”, 1996. ISBN 0-904457-24-9

[8.25] A. Carotenuto and M. Dell’Isola, “An experimental verification of saturated salt solution-based humidity fixed points,” *Int. J. Thermophys.*, vol. 17, pp. 1423–1439, 1996.

[8.26] U. Kang and K.D. Wise, "A high-speed capacitive humidity sensor with on-chip thermal reset," *IEEE Transactions on Electron Devices,* vol.47, no.4, pp.702-710, Apr 2000.

[8.27] Y. Sadaoka, “Capacitive-Type Relative Humidity Sensor with Hydrophobic Polymer Films”, Solid State Gas Sensing, Chapter 3.

[8.28] M. Matsuguchi, Y. Takahashi and T. Kuroiwa et al, “Effect of Sensing Film Thickness on Drift Phenomenon of Capacitive-Type Humidity Sensors,” Journal of the Electrochemical Society, pp, 192 – 195, 2003.

[8.29] A.R.K Ralston, C.F. Klein and P.E. Thoma et al, “A model of the relative environmental stability of a series of polyimide capacitive humidity sensors”, *Sensors and Actuators B: Chemical*, vol. 34, Issues 1–3, Pages 343 - 348, August 1996.

[8.30] US Patent 8007167, “Integrated electronic sensor”, 30 Aug 2011.

[8.31] C. Laville and C. Pellet, "Comparison of three humidity sensors for a pulmonary function diagnosis microsystem," *IEEE Sensors Journal,* , vol.2, no.2, pp. 96 - 101, Apr 2002.

Chapter 9 Conclusions and Future Work

9.1 Conclusions

The main objective and contribution of this thesis was to design, micro manufacture and test a planar Rogowski sensor that could be inserted within key areas of aircraft electrical wiring and interconnect systems (EWIS). The UV-LIGA process was used to develop a series of different sensors that could be benchmarked against a commercial high frequency current transducer (HFCT) and compared to a planar Rogowski sensor manufactured on a silicon substrate by Qudos technology Ltd. The constraints of weight, size and space were overcome through the creation of a high density of sensor coil turns over a small sensing footprint, to create a high magnetic coupling between the device and a wire under test (WUT). The small space constraint required that the sensor be placed as close as possible to the WUT, which in itself results in an increase in the mutual inductance.

Chapter one introduces a brief background to the challenges faced with maintaining legacy aircraft electrical wiring and interconnect systems and the design brief of the sponsoring company (BCF Designs Ltd.) to design a multi-sensor system that is capable of monitoring the EWIS in real time, in situ and capable of being easily placed in key problem areas of the aircraft where EWIS has a highly intermittent fault rate. Such a system has to be small in size and weight due to constraints imposed by the location of the wire bundles and also by the aerospace industry, which require such systems to be a low weight burden to the aircraft once the sensors are scaled up in number to various other locations. This solution takes the form of multiple integrated MEMS sensors, capable of monitoring the ageing and fault parameters. The advantages of MEMS sensors is that they are small in size and low in cost, while outputting data that can be used in prognostics and health monitoring systems.

Chapter 2 provides an in-depth review of ageing and failure mechanisms of aircraft wiring and interconnects systems. The ageing and failures are addressed through breaking down the problem into various chemical, mechanical and electrical failures, which are summarized by a FMEA. This work used real world data that was shared from a wiring survey maintenance report for Tri-Star aircraft carried out by the RAF at Norton Brize. The key failure of EWIS was partial breakdowns or arcing of the wire cable bundle, which presents itself as a high-energy flashover with temperatures

reported in 1000 °Celsius and above. This leads to damage to adjacent wires in the cable bundle and potentially the outbreak of fire. These faults carry an electrical signature in the form of a fast rising transient waveform that has frequency components of up to 100 MHz and beyond.

The arcing fault signals are affected by these variables, with the electrical signatures changing between high and low altitudes. This justifies the inclusion of a pressure sensor to identify the likelihood of certain forms of arcing occurring and which faults are most likely to self-extinguish.

Chapter 3 presents an introduction to the customer requirements for this project, along with an introduction to Health and Usage Monitoring Systems. This type of system is the basis from which a Health and Usage Monitoring Microsystem (HUMMS) is formed using smart sensors. These sensors are micro-manufactured thin film sensors capable of detecting all the parameters that contribute to the ageing and the failure predictors of EWIS. The FMEA presented in chapter 1 showed that temperature and humidity variations accelerate the ageing of the wire insulation. Additionally, humidity can promote arcing so there is a requirement to be able to monitor these environmental parameters as well as detecting the current signature. The sensors chosen in this thesis are focused on monitoring and detecting these parameters and events. Other sensors such as pressure sensors and accelerometers enable vibration to be detected and the likelihood of arcing from sustaining itself.

Techniques in the high voltage industry for identifying and locating faults on electrical wiring are also discussed. These techniques use high frequency current sensors that are located at various positions to enable location of the fault as well as its detection. Placing the sensors at both ends of the cable bundle enables the location of the fault to be identified when an arcing condition is detected.

A review of current sensing technologies that meet the customer requirements as well as being capable of detecting arcing faults is provided. This concludes that a high frequency sensor such as a Rogowski sensor has the greatest potential to detect high frequency signals such as arcing, whilst, at the same time, meeting the customer requirements. Conventional Rogowski sensors are normally quite large, possess smaller coupling between the wire under test and the sensor and suffer from non-linearities as a result of incorrect positioning and also due to the imperfect positioning of the coil turns

that make up the sensor. The novelty of the work presented in this thesis is that the designs help to reduce these effects through using micro-manufacturing techniques.

The operation of the Rogowski sensor when manufactured as a 2.5D planar device is provided in chapter 4. The chapter begins by introducing the Rogowski sensor as a second order lumped parameter model that is comprised of mutual inductance, inductance, capacitance and resistance. These parameters are related to the size of the sensor footprint and also on the coil turns that make up the sensor. The lumped parameters model enables the second order behaviour of the sensor to be explored via Bode analysis, the step response analysis and the root locus analysis. Such an analysis enables insight into the behaviour of the sensor to be further explored when the sensor is operated in differentiating or self-integrating mode.

UV-LIGA manufactured Rogowski sensors and Rogowski sensors manufactured on silicon substrates by Qudos Technology Ltd. were analysed using these methods to establish which design looked the most capable at detecting fast rise time signals. The UV-LIGA designs had more freedom in terms of the size of the sensing area that could be incorporated into each wafer mask design. The designs ranged from large (2 x 1 cm) to small (0.5 x 0.25 cm), with coil turn widths of 20μm and 50μm used with a standard coil turn spacing of 30μm. The Qudos sensors have a fixed sensing area (0.5 x 0.35cm), but have different amounts of coil turns, coil turn widths and coil turn spacing. For the differentiating case, the UV-LIGA Rogowski sensors have a greater peak magnitude at the self-resonant frequency. The self-resonant frequencies were much higher, with most frequencies extending beyond 100 MHz upwards. The bandwidth of the UV-LIGA Rogowski sensors therefore appears more suited for measuring fast rise-time arcing waveforms.

For the self-integrating case, the Bode response shows that there is a trade-off between the sensor output magnitude and the frequency range where self-integration of the Rogowski sensor output is performed. As the self-integrating resistance is varied from a low to a high value, the output magnitude increases while the self-integrating bandwidth decreases. This behaviour can be observed for all Rogowski sensors.

The UV-LIGA designs explored the effect of increasing the sensing area to accommodate more coil turns so that a greater amount of magnetic field can be coupled to each coil turn of the sensor. As the coil turns are increased, the resistance, capacitance and inductance increase. This therefore impacts the second order behaviour

of the sensor, which governs the rise-time response, the level of signal overshoot and the settling time. The larger sensors possessed larger rise-times compared to the smaller sensors for both the differentiating and self-integration mode of operation. The settling times followed a similar trend.

The capacitance of the sensors increase with the silicon substrates and result in slower rise-times and settling times when compared to UV-LIGA sensors of similar sizes. The larger UV-LIGA sensors generally had comparable rise-time and settling times. The peak amplitudes experienced by both sensors were similar in size when a self-integrating resistance of 1000 Ω was used. The best design was UV-LIGA design 7 with optimum characteristics of rise time and settling time. The larger coil turn width (50μm) is easier to manufacture than the 20μm designs. The Qudos designs were adequate enough to do the required detection of fast rising signals, and have the benefit that they could be manufactured on a common substrate with a humidity sensor and/or other sensors.

Chapter 5 introduces the UV-LIGA manufacturing processes used to micro-manufacture the UV-LIGA Rogowski sensor. Planar Rogowski sensors were fabricated with gold coil turns created during the electroplating of the lithographically patterned wafer. Custom packaging of the Qudos Rogowski sensors is also discussed in this chapter, along with fused deposition modeling of a package to hold the UV-LIGA Rogowski sensor and a wire under test (WUT) within a close distance to one another. This would allow the maximum coupling to be achieved between the sensor and the WUT. Manufacturing issues experienced included the coil turns peeling away from the substrate as a result of high stresses in the electroplated metal and poor adhesion to the substrate.

Chapter 6 provides an introduction to the methodologies used to characterize and test the Rogowski sensors. The methodology includes a test setup for measuring the inductance, capacitance and resistance. A large number of the Qudos Rogowski sensors were available for testing, which provided an opportunity to perform a statistical analysis of the characteristics of the sensors. This allowed a review of how capable the processes used by Qudos were to make sensors of a given specification. A low number of UV-LIGA sensors were available to carry out a similar statistical analysis.

The last test setup discussed was focused on the sensors ability to detect high frequency waveforms and is broken down into two sections. The first section described the sensor

close to the wire under test (WUT) and the range of high frequency sine waves sent down the wire using a waveform generator. The output of the sensors was recorded on a wide bandwidth digital oscilloscope and the magnitude and phase were recorded. The second part of the test involved using repeating the characterisation with the exception that charging and discharging signals were sent down the WUT and their response noted. This included the rise-time, settling time and magnitude of the signal. Similar information was recorded for the commercial high frequency current transducer (HFCT) and used to establish where the planar designs had merit over a more expensive counterpart.

Chapter 7 presents the analysis and discussion of the test and characterization of the Rogowski sensors. The measurements of the UV-LIGA sensors showed close correlation to the simulated values of chapter 4 for the inductance and resistance. The capacitance measurements were out by a factor of 10,000. The likely cause is measurement error from the LCR meter. The inductance and resistance measurements for the Qudos sensors show large variation within each design. The values measured were up to ten times higher than the model estimated, which leads to the conclusion that the thickness of the coil turns is smaller than 10 μm. The mean of the inductance measurements was poor for wafers 12, 14 and 15. Wafer 13 appeared to have values very close to the modeled values from designs two to five. There were no sensors from design one available to test due to poor yield.

The capacitance measurements were different from the modeled values by up to a factor of 1,000. Some sensors on wafer 12 were different by a factor of ten. Due to the high differences, the root cause could be attributed to a number of things. The first issue could be with the LCR meter. The other source of error could be down to the calculations used, but this seems unlikely due to the close correlation observed for the UV-LIGA measurements. The most likely issue is attributed to the processing of the sensors, which Qudos accepted that there had been challenges experienced with micro-manufacturing the sensors without the coils peeling away from the substrate.

The Bode analysis of the sine wave frequency sweep from 1-100 MHz showed that both the UV-LIGA and Qudos sensors provided higher magnitude outputs than the commercial HFCT beyond 3 MHz. This means that both designs show better potential for detecting fast rise time signals than the HFCT. This was verified when testing the sensors with charging and discharging waveforms from the signal generator. Both designs showed faster responses to these signals and also output voltages. All designs

feature a large amount of oscillations in the output that indicates that the sensors are not adequately damped. The Qudos sensors appeared to have faster rise times than the UV-LIGA sensors due to the sensors being smaller, which is in agreement with the modeling chapter. The simulated Bode response of the Qudos designs using the measured values shows a poorer high frequency response. Due to the good response to the high frequency signals, it is likely that the major component of error in the capacitance measurements comes from the LCR meter.

Chapter 8 presented the design, modeling and test of humidity sensors manufactured by Qudos. An overview of the different types of humidity sensors and rationale for the design selected in this research was given. The polymer capacitive humidity sensor with interdigital electrodes was chosen ahead of the parallel plate design because it is able to recover from contamination more easily. The physics of operation and the chemistry that defines the interaction between moisture sensitive material and water vapour were introduced.

A total of ten designs evaluated, which covered five electrode configurations and two types of moisture sensitive material. The electrode configurations examined the effect of variation to the sensing area, electrode finger spacing, finger length, finger overlap and the number of fingers. The moisture sensitive material used was BCB and polyimide. A 3D finite element model was used to examine the relationship between capacitance of a sensor versus polymer height for fixed finger electrode width and also capacitance versus pitch. Once a polymer reaches a thickness that is half the pitch of the electrodes, most of the electrostatic field lines are contained within the polymer. If the thickness is too low then more of the field lines pass through the material and sensitivity is lost.

Sensors were presented for test using a setup that involved a specialized fuel probe test set, which was designed for measuring small capacitances in the picoFarad range. The humidity chamber provided by the company struggled to stabilize at low relative humidity setpoints, so some of the sensor readings may have been reading a higher level of capacitance because of this. The BCB covered humidity sensors take up a smaller amount of water vapour than the polyimide covered sensors. This results in a smaller increase in capacitance as humidity is increased. Some of the sensor responses show negative sensitivity that is attributed to the humidity shifting beyond its target setpoint.

The polyimide covered humidity sensors absorb a greater amount of water vapour as the relative humidity is increased and also possess a higher relative permittivity than BCB. This results in a higher base capacitance (offset) and also a higher sensitivity, which is reflected in the graphs showing positive sensitivity.

Examination of the interdigitated structures revealed a lot of broken electrode fingers, which will result in the base capacitance being lowered. This may be one of the reasons why some of the variation exists between sensor readings. Additionally, it suggests that the processes used by Qudos to manufacture both the humidity sensors and the Rogowski sensors were not fully optimized or controlled adequately during manufacture.

9.2 Future work

The next stage for testing the Rogowski sensors should focus on testing a wire harness from aircraft and inducing a real arcing signal in a section by connecting it to a metallic surface and removing it gradually. The acquired sensor data could be recorded using a fast sampling computer. This would allow further investigation into the characteristics of the arcing waveform. Once this has been completed, more parameters that influence the arcing waveform can be introduced, such as vibration, pressure, temperature and humidity.

A measurement system evaluation of the LCR meter and the BCF fuel probe test system should be carried out. This evaluates the level of accuracy of the measurements and the Gauge Repeatability and Reproducibility (GR&R) of a measurement system. For the LCR meter in particular, this will help understand if the accuracy and GR&R of the meter is attributed to the large difference between modeled and observed results.

The accuracy of the measurement relates to how close the measurement result is with the reference measurement. Accuracy is broken down into three components that are bias, linearity and stability. For bias, a number of measurements are carried out and the mean of the measurements is compared to the reference value. Linearity examines the bias across a range of measurements. For the LCR this would be looking at how bias varies as the test frequency for the LCR meter is varied. Stability looks at the change in bias over a long time period. GR&R is made up of two components that examines the consistency of repeated measurements of a randomly selected part using the same

equipment and different appraisers. The two components are repeatability and reproducibility. Repeatability is concerned with repeating measurements on randomly selected parts with the same operator and measurement equipment. It is often referred to as Equipment Variation (EV) or "within system variation" and is an estimate of the standard deviation of the variation caused by repeatability. Reproducibility is also known as Appraiser Variation (AV) and is focused on the relationship of measurement error with different appraisers.

Reference capacitors by Agilent Technologies can be rented for £600 per month that consist of a range of capacitors in the pF range. The LCR meter could be evaluated across a range of frequencies while doing these measurements to better understand how the measurement error varies. The same procedure could also be carried out with the BCF fuel probe test system.

The test should be repeated with a more stable humidity chamber that is capable of providing low humidity. With such a chamber, an accurate collection of capacitance data could be gathered from low to high humidity and back down to low humidity. This will allow assessment of the sensor hysteresis, which is a function of the sensing material. Such information will provide a greater opportunity to understand which sensing polymer is best out of the BCB and polyimide.

The next test to be carried out would be long-term drift, which is performed by leaving the sensor to settle for a specific number of hours at each setpoint.

Such timely testing would require a test system that could log data without human involvement, therefore one option for a test system is to use the capacitance measuring capabilities of the LCR meter and automating it by reading out the data using software such as Labview. A chilled mirror hygrometer should still be used to given an accurate indication of the chamber temperature and humidity. This by default will allow accuracy and precision measurements to be made with confidence.

APPENDIX 1: FMEA Taxonomy

Appendix 1.1 Taxonomy of faults related to chemical failure modes

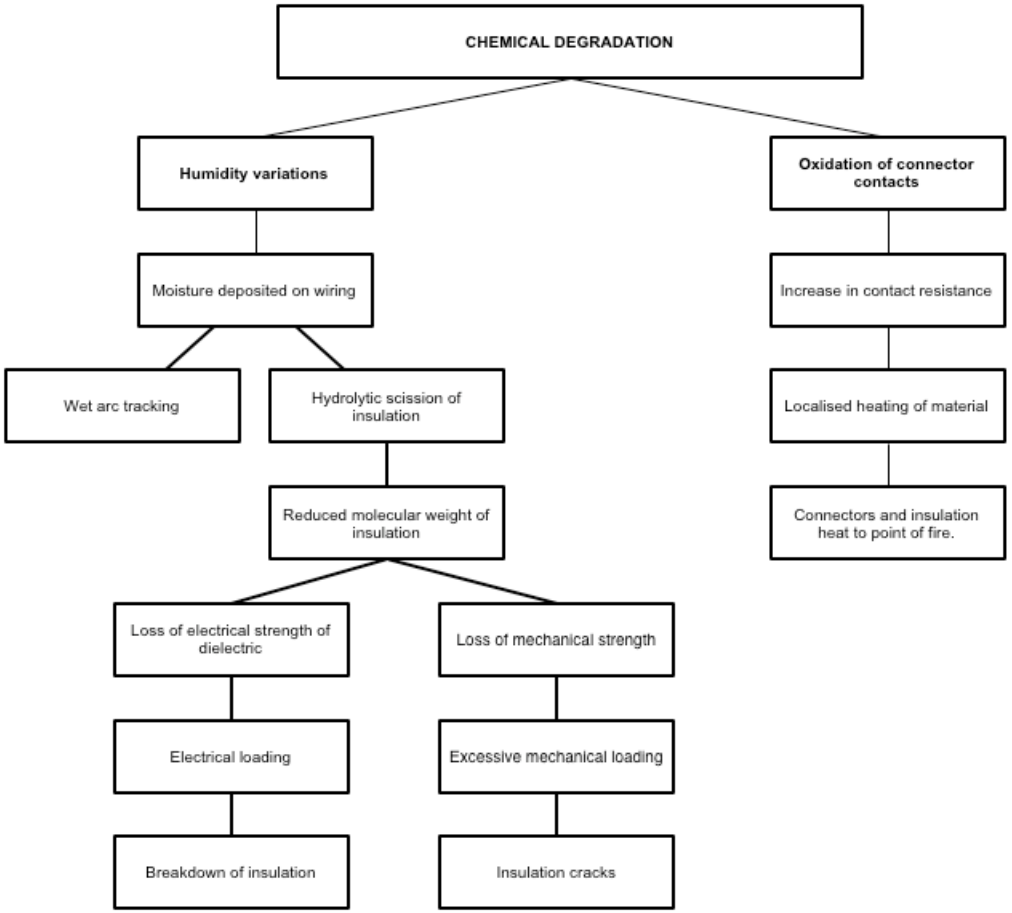

Appendix 1.2 Taxonomy of faults related to electrical failure modes.

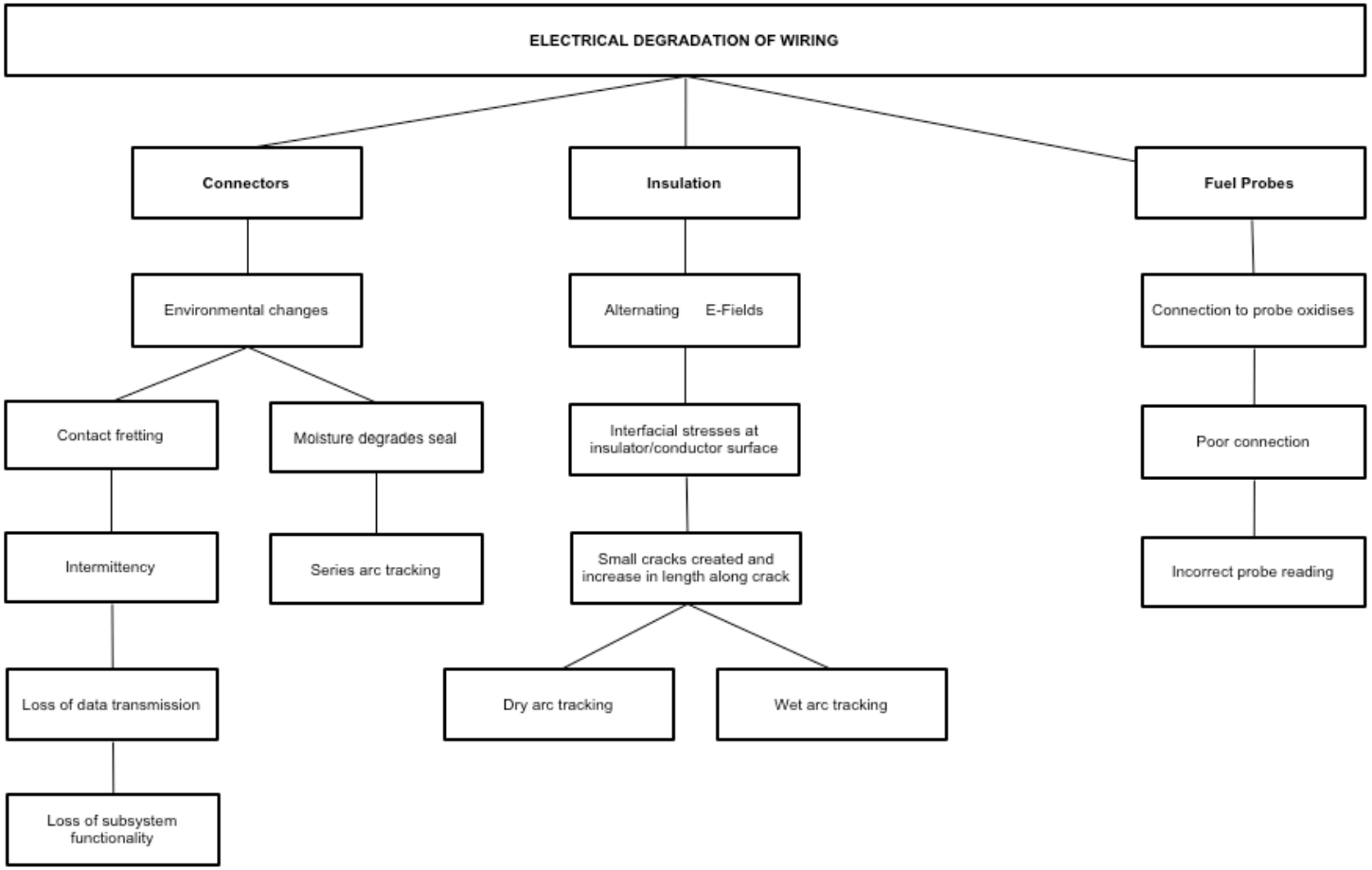

Appendix 1.3 Taxonomy of faults related to mechanical failure modes.

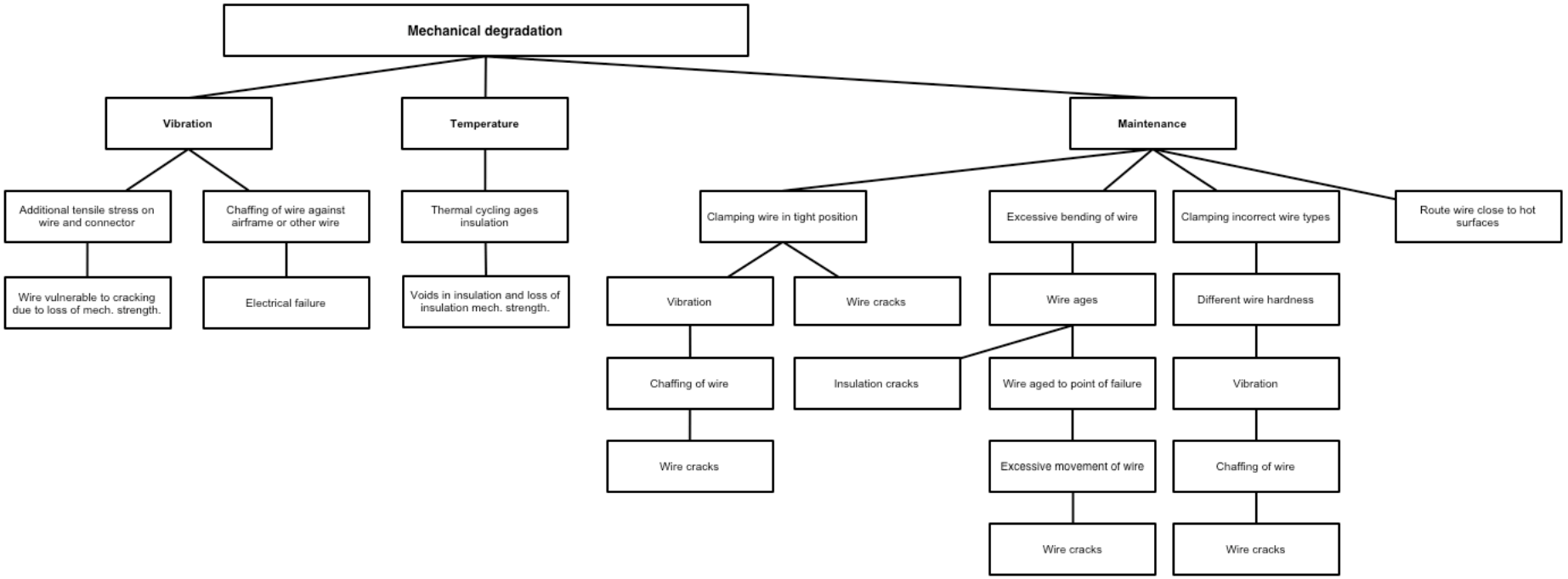

Appendix 1.4. FMEA

Device: Aircraft Wiring									
Item/ Function	Potential failure mode	Causes of failure	Effects of failure	Detect	Local effect	Effect on unit	Severity	Occurrence	RPN
Insulation	Interfacial Tension	A.C E-Field	Voids/ Cracks progress to arcing events	9	Aging effect/ Insulation cracks	Aging/ Failure	7	4 - 6	252 - 378
	Lowering of mechanical strength of insulation	Exceeding Max bend radii/wire in strained position/ Vibration/ scission	Voids/ Cracks/micro discharge/ Arcing (more probable where moisture is)	5	Cracks appear in insulation earlier than estimated	Aging/ Early failure	7	7	245
	Fatigue/ maintenance errors	Large variations in temp/ wire mechanically strained.	Cracks appear/ insulation will crack on next mech. Loading	6	Material becomes stiffer/ages. Cracks will start to move	Aging/ Early failure	8	8	384
	Swelling of insulation/ Insulation subjected to varying levels of humidity/ temperature	High humidity	Hydrolytic scission of insulation/ loss of physical strength/ corroded conductors	7	Standing waves (for high freq. wiring), increased conductance of insulation, heating of insulation, accelerated hydrolytic scission/ eventual arcing	Premature aging/ Early failure/ catastrophe	9	9	567
	Hydrolytic scission	Moisture	Decrease in molecular weight/loss of physical properties	1	Loss of material strength, cracks start, arcing probable	Cracks appear early	9	9	81
	Wet Arc Tracking	Moisture/ cracks/ dry tracks on insulation	Flashover /Carbon deposits/fire	9	Burnt insulation, Which carbonizes, allowing higher energy arcing/fire	Loss of aircraft control/ fire	10	9	810
	Dry Arc Tracking	Exposed conductor touches aircraft or other wires	Flashover /Carbon deposits/fire	1	Burnt insulation, Which carbonizes, allowing higher energy arcing/fire	Loss of aircraft control/ fire	10	7	630
Connector	Series arc tracking	Corrosion in pin socket/ loose connection in series with load	Flashover, i^2R heating of surrounding area, pyrolysis	6-8	Burnt/smoldering insulation, smoke, loss of signal transmission	Loss of aircraft control/ fire	10	7-9	420-720
	Contact Fretting	Vibration induced movement of conductor interface	Corrosion, increase in contact resistance, loss of electrical contact	8-10	Loss of signal transmission, series arc tracking	Loss of aircraft control and/or fire	10	6-8	480-800

Appendix 1.4. (cont'd)
Classification of Severity, occurrence and Detection.

Severity Rating

1: No impact on wire/interconnect

2 – 3: Very little impact on wire/interconnect

4 – 6: Some impact on wire/interconnect

7 – 8: Critical on wire/interconnect

9 – 10: Very critical on wire/interconnect

Occurrence

1 Unlikely to occur

2 – 3: Seldom occurs

4 – 6: Probable

7 – 8: Likely

9 – 10: Very probable

Detection

1: Easy to detect by existing methods whilst aircraft is not in flight.

1: Easy to detect/ can be detected whilst the aircraft is in flight OR easier to detect in flight with non-invasive detection techniques if available.

1 – 3: Likely to detect by existing methods whilst aircraft is not in flight

2– 3: Likely to detect in flight/ more likely to detect whilst the aircraft is in flight if non invasive detection methods available.

4 – 6: Probable detection with existing methods whilst aircraft is not in flight.

4 – 6 : Probable detection whilst in flight/probable if non invasive detection methods available.

7 – 8 Seldom detected by existing methods.

7 – 8: Seldom detected whilst aircraft is in flight/or with aid of non invasive measurement techniques.

9 – 10: Unlikely to detect whilst the aircraft is not in flight.

9 –10: Unlikely to detect in flight or with aid of non-invasive measurement technique.

APPENDIX 2: Modeling of Rogowski sensors

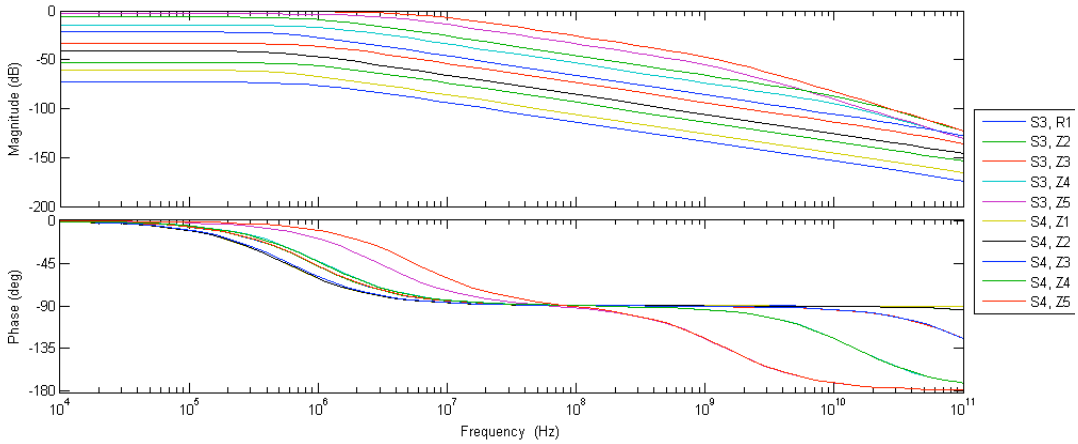

Appendix 2.1: Bode response of sensor designs 3 and 4 in self-integrating mode.
S3 = sensor design; S4 = sensor design 2; Z1 = 0.1 Ω, Z2 = 1 Ω, Z3 = 10 Ω, Z4 = 100 Ω, Z5 = 1000 Ω.

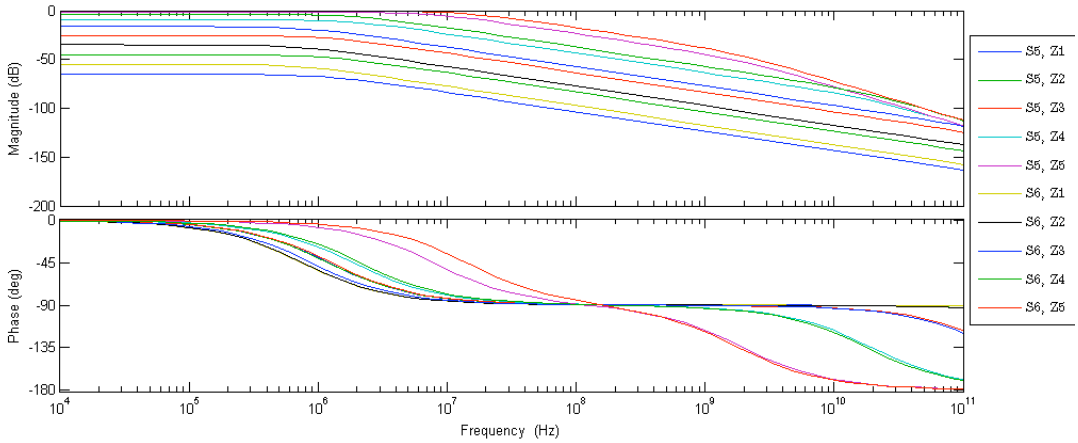

Appendix 2.2: Bode response of sensor designs 5 and 6 in self-integrating mode.
S5 = sensor design; S6 = sensor design 2; Z1 = 0.1 Ω, Z2 = 1 Ω, Z3 = 10 Ω, Z4 = 100 Ω, Z5 = 1000 Ω.

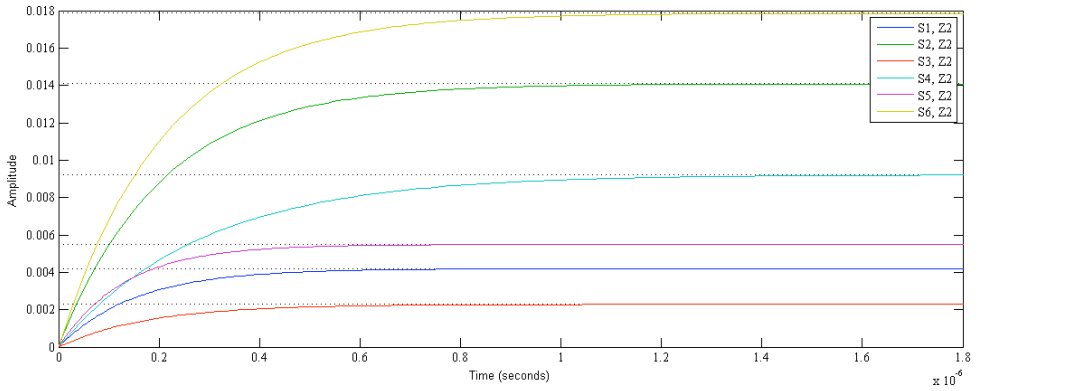

Appendix 2.3: Step response of sensors 1 to 6 of the UV LIGA manufactured Rogowski coils.
The integrating impedance is 1 Ω.

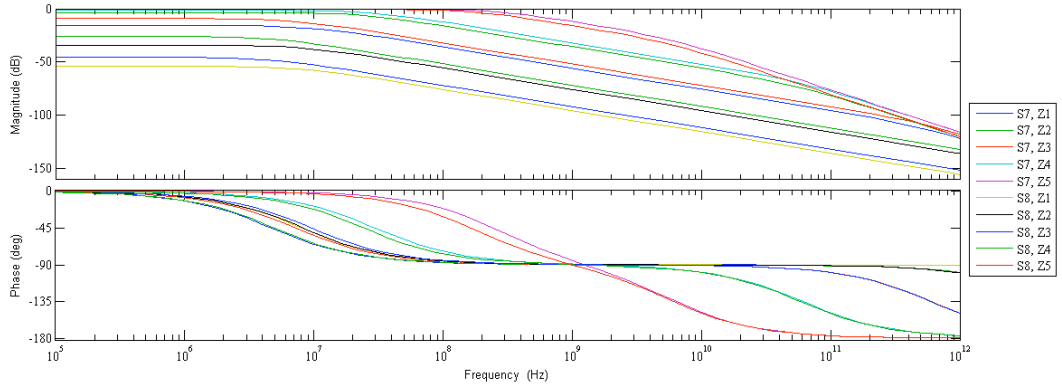

Appendix 2.4: Bode response of sensor designs 7 and 8 in self-integrating mode.
S5 = sensor design; S6 = sensor design 2; Z1 = 0.1 Ω, Z2 = 1 Ω, Z3 = 10 Ω, Z4 = 100 Ω, Z5 = 1000 Ω.

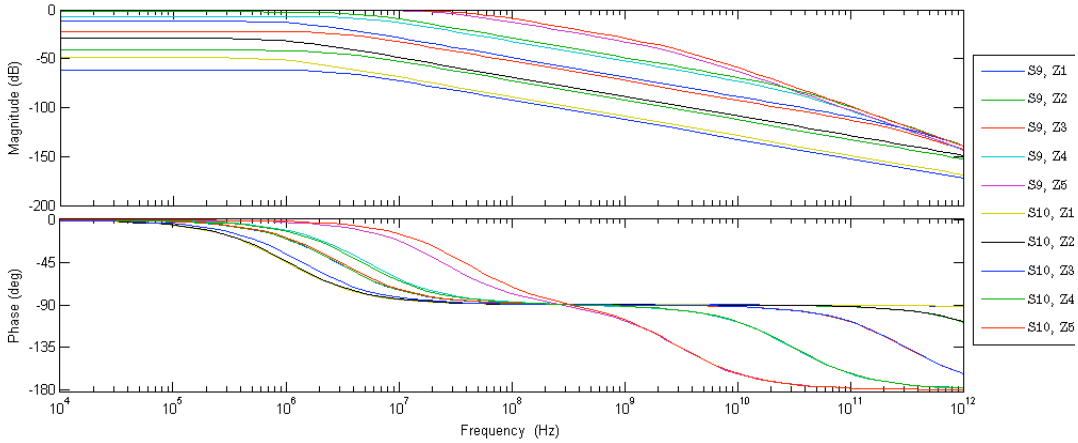

Appendix 2.5: Bode response of sensor designs 9 and 10 in self- integrating mode.
S9 = sensor design 9; S10 = sensor design 10; Z1 = 0.1 Ω, Z2 = 1 Ω, Z3 = 10 Ω, Z4 = 100 Ω, Z5 = 1000 Ω

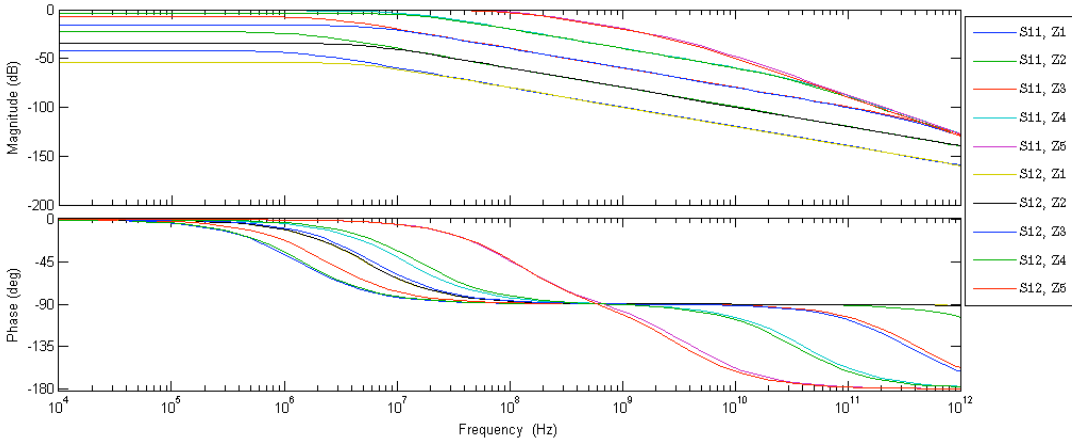

Appendix 2.6: Bode response of sensor designs 11 and 12 in self-integrating mode.
S11 = sensor design 11; S12 = sensor design 2; Z1 = 0.1 Ω, Z2 = 1 Ω, Z3 = 10 Ω, Z4 = 100 Ω, Z5 = 1000 Ω.

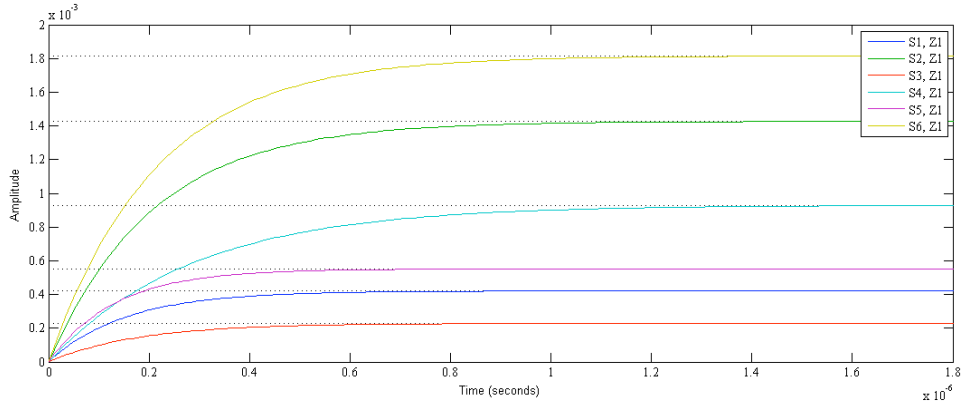

Appendix 2.7: Step response of sensors 1 to 6 of the UV LIGA manufactured Rogowski coils. The integrating impedance is 0.1 Ω.

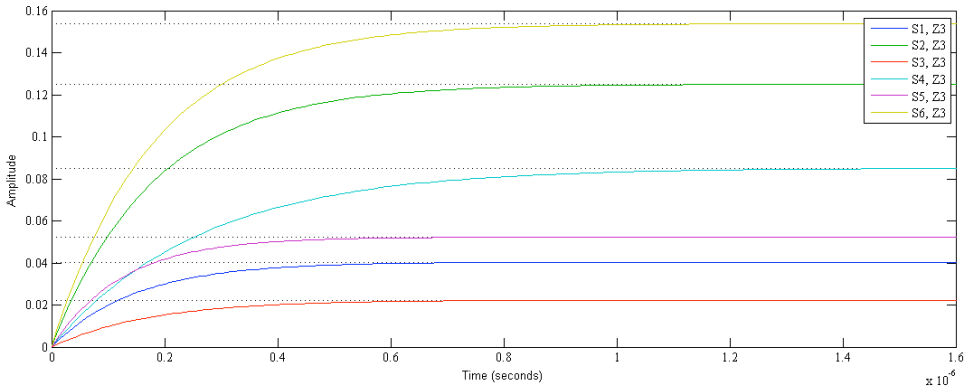

Appendix 2.8: Step response of sensors 1 to 6 of the UV LIGA manufactured Rogowski coils. The integrating impedance is 10 Ω.

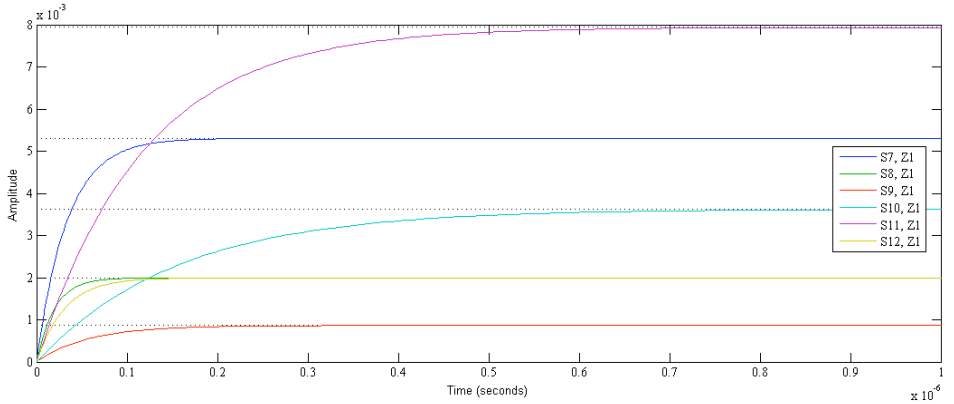

Appendix 2.9: Step response of sensors 7 to 12 of the UV LIGA manufactured Rogowski coils. The integrating impedance is 0.1 Ω

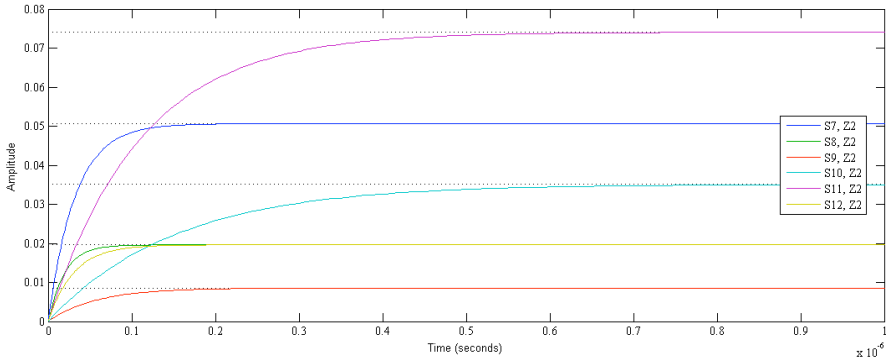

Appendix 2.10: Step response of UV-7 to UV-12 of the UV LIGA Rogowski coils. The integrating impedance is 1 Ω.

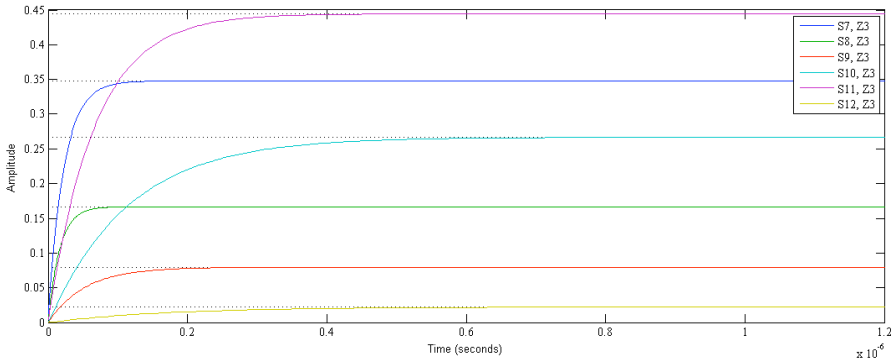

Appendix 2.11: Step response of sensors UV-7 to UV-12 of the UV LIGA manufactured Rogowski coils. The integrating impedance is 10 Ω.

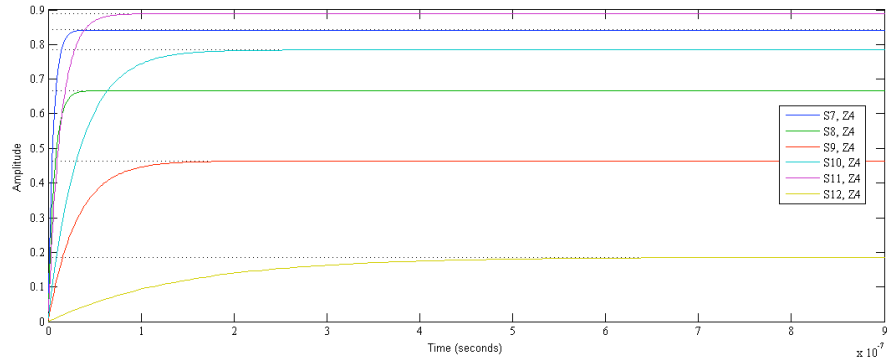

Appendix 2.12: Step response of sensors UV-7 to UV-12 of the UV LIGA manufactured Rogowski coils. The integrating impedance is 100 Ω

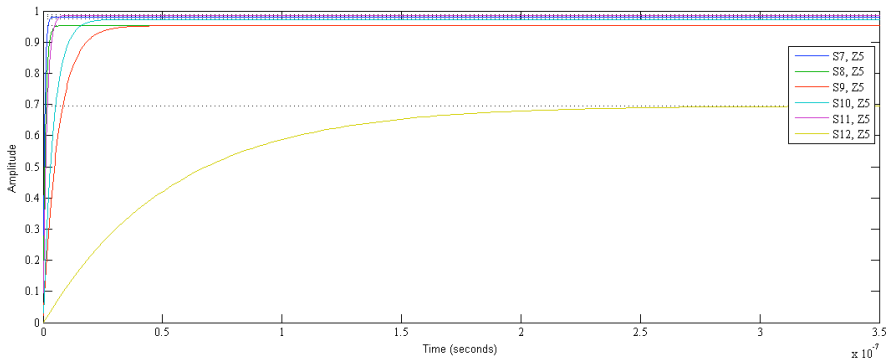

Appendix 2.13: Step response of sensors UV-7 to UV-12 of the UV LIGA manufactured Rogowski coils. The integrating impedance is 1000 Ω.

Appendix 2.14: The roots of the characteristic equation for each Rogowski sensor design.

Sensor type	Real	Imaginary	Sensor Type	Real	Imaginary
S1, Z1	-1.59×10^{14}	0	**S7, Z1**	-3.85×10^{14}	0
S1, Z2	-1.59×10^{13}	0	**S7, Z2**	-3.85×10^{13}	0
S1, Z3	-1.59×10^{12}	0	**S7, Z3**	-3.85×10^{12}	-0.0001
S1, Z4	-1.59×10^{11}	0.0001	**S7, Z4**	-3.84×10^{11}	-0.0024
S1, Z5	-1.59×10^{10}	0.0034	**S7, Z5**	-3.68×10^{10}	-0.18
S2, Z1	-1.66×10^{14}	0	**S8, Z1**	-3.7×10^{14}	0
S2, Z2	-1.66×10^{13}	0	**S8, Z2**	-3.7×10^{13}	0
S2, Z3	-1.66×10^{12}		**S8, Z3**	-3.7×10^{12}	0
S2, Z4	-1.66×10^{11}	0.0001	**S8, Z4**	-3.7×10^{11}	-0.0012
S2, Z5	-1.65×10^{10}	-0.0074	**S8, Z5**	-3.6×10^{10}	-0.106
S3, Z1	-9.09×10^{13}	0	**S9, Z1**	-1.9×10^{14}	0
S3, Z2	-9.09×10^{12}	0	**S9, Z2**	-1.9×10^{13}	0
S3, Z3	-9.09×10^{11}	-0.0001	**S9, Z3**	-1.9×10^{12}	0
S3, Z4	-9.09×10^{10}	-0.0007	**S9, Z4**	-1.9×10^{11}	-0.0003
S3, Z5	-9.08×10^{9}	-0.0186	**S9, Z5**	-1.9×10^{10}	-0.0155
S4, Z1	-9.09×10^{13}	0	**S10, Z1**	-1.96×10^{14}	0
S4, Z2	-9.09×10^{12}	0	**S10, Z2**	-1.96×10^{13}	0
S4, Z3	-9.09×10^{11}	0	**S10, Z3**	-1.96×10^{12}	0
S4, Z4	-9.09×10^{10}	-0.0007	**S10, Z4**	-1.96×10^{11}	-0.0003
S4, Z5	-9.059×10^{9}	-0.0359	**S10, Z5**	-1.94×10^{10}	-0.024
S5, Z1	-1.235×10^{14}	0	**S11, Z1**	-2.56×10^{14}	0
S5, Z2	-1.235×10^{13}	0	**S11, Z2**	-2.56×10^{13}	0
S5, Z3	-1.235×10^{12}	0	**S11, Z3**	-2.56×10^{12}	0
S5, Z4	-1.235×10^{11}	-0.0001	**S11, Z4**	-2.56×10^{11}	-0.0008
S5, Z5	-1.23×10^{10}	-0.0049	**S11, Z5**	-2.50×10^{10}	-0.07
S6, Z1	-1.124×10^{14}	0	**S12, Z1**	-2.13×10^{14}	0
S6, Z2	-1.124×10^{13}	0	**S12, Z2**	**-2.13×10^{13}**	0
S6, Z3	-1.124×10^{12}	0	**S12, Z3**	-9.1×10^{11}	-0.0001
S6, Z4	-1.124×10^{11}	-0.0001	**S12, Z4**	-9.1×10^{10}	-0.0007
S6, Z5	-1.112×10^{10}	-0.0091	**S12, Z5**	-9.08×10^{9}	-0.019

Appendix 2.15: Analysis of the roots of the Qudos Rogowski sensor in the self-integrating condition.

Sensor	Integrating Impedance	Poles (real)	Poles (Imaginary)
1	Z1	-5.2×10^{7} to -2.43×10^{10}	x
1	Z2	-5.5×10^{7} to -2.43×10^{9}	x
1	Z3	-1.1×10^{10} to -1.85×10^{10}	x
1	Z4	-3.8×10^{7}	$\pm j8.7 \times 10^{7}$
1	Z5	-2.7×10^{7}	$\pm j8.5 \times 10^{7}$
2	Z1	-5.7×10^{7} to -2.1×10^{10}	x
2	Z2	-6×10^{7} to -2.1×10^{9}	x
2	Z3	-1.34×10^{10}	$\pm j8.2 \times 10^{6}$
2	Z4	-3.9×10^{7}	$\pm j7.5 \times 10^{7}$
2	Z5	-2.95×10^{7}	$\pm j\ 7.25 \times 10^{7}$
3	Z1	-4.1×10^{7} to -1.75×10^{10}	x
3	Z2	-4.2×10^{7} to -1.75×10^{9}	x
3	Z3	-6.7×10^{7} to -4.49×10^{10}	x
3	Z4	-2.9×10^{7}	$\pm j\ 5.2 \times 10^{7}$
3	Z5	-2.1×10^{7}	$\pm j\ 4.96 \times 10^{7}$
4	Z1	-3.4×10^{7} to -9.48×10^{10}	x
4	Z2	-3.74×10^{7} to -9.48×10^{10}	x
4	Z3	7.76×10^{7} to -9.04×10^{10}	x
4	Z4	-6.4×10^{7}	$\pm j1.94 \times 10^{8}$
4	Z5	-2.14×10^{10}	$\pm j1.95 \times 10^{8}$
5	Z1	-8.5×10^{7} to -1.74×10^{10}	x
5	Z2	-9×10^{7} to -1.69×10^{9}	x
5	Z3	-1.06×10^{8}	$\pm j\ 9.6 \times 10^{7}$
5	Z4	-2.8×10^{8}	$\pm j\ 8.1 \times 10^{7}$
5	Z5	-2×10^{7}	$\pm j7.49 \times 10^{7}$